View metadata, citation and similar papers at core.ac.uk

brought to you by CORE

provided by UNT Digital Library

A Comprehensive Statistically-Based Method to Interpret Real-Time Flowing Measurements

Final Report

Period Start August 2003
Period End January 2007

By

Keita Yoshioka, Pinan Dawkrajai, Analis A. Romero,
Ding Zhu, A. D. Hill, and Larry W. Lake
January 2007

DOE Award Number; DE-FC26-03NT15402

The University of Texas at Austin
Texas A&M University

Disclaimer

This report was prepared as an account of work sponsored by an agency of the United States Government. Neither the United States Government nor any agency thereof, nor any of their employees makes any warranty, express or implied, or assumes any legal liability or responsibility for the accuracy, that its use would not infringe privately owned rights. Reference herein to any specific commercial product, process, or service by trade name, trademark, manufacturer, or otherwise does not necessarily agency thereof. The views and opinions of authors expressed herein do not necessarily state or reflect those of United States Government or any agency thereof.

Abstract

With the recent development of temperature measurement systems, continuous temperature profiles can be obtained with high precision. Small temperature changes can be detected by modern temperature measuring instruments such as fiber optic distributed temperature sensor (DTS) in intelligent completions and will potentially aid the diagnosis of downhole flow conditions. In vertical wells, since elevational geothermal changes make the wellbore temperature sensitive to the amount and the type of fluids produced, temperature logs can be used successfully to diagnose the downhole flow conditions. However, geothermal temperature changes along the wellbore being small for horizontal wells, interpretations of a temperature log become difficult. The primary temperature differences for each phase (oil, water, and gas) are caused by frictional effects. Therefore, in developing a thermal model for horizontal wellbore, subtle temperature changes must be accounted for.

In this project, we have rigorously derived governing equations for a producing horizontal wellbore and developed a prediction model of the temperature and pressure by coupling the wellbore and reservoir equations. Also, we applied Ramey's model (1962) to the build section and used an energy balance to infer the temperature profile at the junction. The multilateral wellbore temperature model was applied to a wide range of cases at varying fluid thermal properties, absolute values of temperature and pressure, geothermal gradients, flow rates from each lateral, and the trajectories of each build section.

With the prediction models developed, we present inversion studies of synthetic and field examples. These results are essential to identify water or gas entry, to guide flow control devices in intelligent completions, and to decide if reservoir stimulation is needed in particular horizontal sections. This study will complete and validate these inversion studies.

Table of Contents

Lists of Graphical Materials

Table

Figure

CHAPTER 1

INTRODUCTION

1.1 BACKGROUND

In the past decades, thousands of wells have been drilled horizontally and in multiple directions to obtain larger contact with the reservoir. Because of the growing complexities of the recent well trajectories, running conventional production monitoring tools on appropriate locations has become difficult and costly. Flow rate, pressure, and temperature are the principle parameters to be measured through production logging. Continuous profiles of pressure and temperature measurements in a complex well can be obtained accurately and inexpensively using the advanced technology of fiber optics. Since the first fiber optic sensor was implemented in a well in Shell's Sleen Field in 1993 (Kragas, 2001), the use of distributed temperature sensors (DTS) and distributed pressure sensors (DPS) has become increasingly common for monitoring producing sections of horizontal wells.

For multi-phase flowing wells, despite the recent advancements in technologies and equipments, a comprehensive solution to measuring flow rates and holdups of the phases is evasive (Falcone *et al.*, 2002). However, to take full advantage of intelligent wells, which can control inflow capacities from different producing sections without interventions, real-time monitoring of the downhole flow conditions such as flow rate profiles and locations of excessive water or gas influx is essential. Therefore, to realize the value of intelligent wells, downhole flow conditions are either measured or interpreted from measurable parameters (*e.g.* density, pressure, and/or temperature) in horizontal, multi-lateral, or multi-branching wells.

Temperature logs have been interpreted successfully in vertical wells to locate water or gas entry zones, casing leaks, and inflow profiles (Hill, 1990). Recently, interpretations of temperature profiles in horizontal wells have been reported to be useful to identify types of fluid flowing to a wellbore (Tolan *et al.*, 2001; Brown *et al.*, 2003; Foucault *et al.*, 2004). However, the inferences described above require a model to translate temperature information into flow information. Although several wellbore temperature models are available for vertical wells, there has been little work on the thermal modeling of horizontal producerbores.

The main difference between vertical and horizontal wellbore models lies in the variation of temperature and pressure. In vertical or near vertical wells, the wellbore pressure is usually dominated by a hydrostatic difference, and the wellbore temperature by the geothermal temperature, causing both wellbore temperature and pressure to change with depth. If a vertical well produces fluid from different depths, the fluids have different inflowing temperatures because of the geothermal temperature variation with depth. This difference in inflowing temperature can cause clear changes on a temperature log, which can be interpreted to infer the downhole flow conditions.

The geothermal temperature variation along a horizontal well is very small. To identify the causes of a measured temperature variation, reservoir and wellbore temperature models are required to relate a measured temperature to the inflow profile of the well. These models must account for all the subtle thermal energy effects including Joule-Thomson expansion, viscous dissipative heating, and thermal conduction.

1.2 LITERATURE REVIEWS

One of the earliest works on temperature prediction was done by Ramey (1962). Ramey's method approximates the pressure gradient of vertical wellbores by the hydrostatic difference, neglecting frictional pressure drop, and assumes steady-state heat transfer inside the wellbore and transient conduction from the reservoir. The solution was obtained semi-analytically under these assumptions. His temperature prediction model works for either a single-phase incompressible liquid or a single-phase ideal gas in vertical injection and production wells. Sagar (1991) extended Ramey's work to inclined wellbores. Hasan *et al.* (1998) applied an energy equation for multi-phase flow and calculated temperature profile and history numerically. Hagoort (2004) revisited Ramey's equation and compared it to the rigorous solution. He confirmed that Ramey's equation works for broad situations except for early periods of production, and also determined the periods for which Ramey's approximate solution could be applied.

For horizontal or near-horizontal wells, the hydrostatic difference is zero or very small. Dikken (1990) presented a coupled reservoir and wellbore equations to simulate horizontal well production. In developing the model, he considered wellbore pressure as a function of wellbore and reservoir pressures, and flow rate of the well. He also showed that neglecting wellbore pressure drop could result in errors in estimating production rate profiles. Hill and Zhu (2006) introduced a dimensionless number that represents the relative importance of the horizontal wellbore pressure drop to the reservoir pressure drawdown and categorized the situations where the wellbore pressure could be regarded as constant.

When the wellbore is continuously receiving mass from the formation (radial influx), the frictional pressure drop is different from that which occurs in pipe with no inflow along it.. Yuan *et al*. (1998) and Ouyang *et al*. (1998) conducted horizontal wellbore flow experiments to estimate the pressure drop caused by radial influx in a porous pipe and correlated new friction factors for horizontal producerbores.

Stone *et al*. (2002) proposed a thermal simulation model with multi-segment wells. They applied nodal analysis to the coupled problem and solved the equations segment by segment. Ouyang and Belanger (2006) presented an inversion study of DTS data. They concluded that flow rate could be properly estimated based on DTS data for wells oriented from vertical to 25^o and also stated that the inversion would not be performed in the wells inclined closer to horizontal than this limit by showing numerical experimental results from the model they developed. However, the theoretical details of the study were not revealed.

1.3 OBJECTIVES

The primary objective of this study is to develop an interpretation method of temperature and pressure data from horizontal or near-horizontal wellbores. There are three significant differences in concepts from vertical wells. First, the geothermal temperature that surrounds the horizontal wellbore is almost constant. Second, the frictional pressure drop is the dominant effect on the pressure profile while in vertical wells the gravitational pressure drop is the most important term. Finally, because of much longer exposed length to the formation, the wellbore continuously gains or loses convective energy from or to the formation as well as mass along its path.

Except for the production system that is stimulated by thermal method (wellbore heating, hot-fluid injection, or combustion), the isothermal system has been assumed in petroleum engineering applications. However, to identify the causes of a measured temperature variation in the normal horizontal well production system, we must consider subtle temperature behaviors in the wellbore and the reservoir.

In this project, we derive the governing equations for the wellbore and the reservoir then combine the equations. The derived equations also work for inclination wells including vertical wells. The coupled equations are solved simultaneously for flow rate, pressure, and temperature profiles along the wellbore by applying successive substitution. Using the temperature and pressure prediction model developed, we infer the features and sensitivities of temperature or pressure profiles under various production scenarios, such as water entry.

This research also proposes an interpretation method of temperature and pressure profile data to downhole inflow conditions. We set the parameters to be estimated as productivities or inflow rates of each segment. From continuous temperature and pressure data along the well, we invert them into the parameters by applying the Levenberg-Marquardt algorithm.

CHAPTER 2

EXECUTIVE SUMMARY

The increasing deployment of distributed temperature and pressure measuring devices in intelligent well completions provides a means to monitor the inflow profiles without any well intervention. If the profiles of pressure and/or temperature are affected by the inflow profiles of the various phases being produced, we would be able to estimate these flow profiles by inverting measured temperature and pressure profiles. This inversion is particularly challenging for horizontal wells because the pressure drop along the well is usually small, and temperature changes, which are primarily caused by Joule-Thomson effects, are also small.

The objectives of this research are twofold. The first goal is to develop a comprehensive prediction model of temperature and pressure behavior in horizontal laterals, build sections, and junctions. Second, we develop an interpretation method of distributed temperature and pressure data into downhole flow conditions.

This report first presents a simple and comprehensive model for predicting the temperature profile in a horizontal well during normal production (steady state flow). Prediction of the wellbore temperature profile requires modeling of all thermal effects occurring in the reservoir and in the wellbore itself. For the reservoir temperature model, we couple mass and energy balances of fluid flow in a permeable medium in a rectangular homogeneous reservoir with no flow boundaries at the top and bottom of reservoir. For the two flow regions (radial and linear) considered in the reservoir, the equation is solved analytically in one dimension. This analytical solution is then coupled with a wellbore temperature model using a multi-segment technique to obtain the fluid temperature profile along the wellbore. The wellbore model presented here accounts for Joule-Thomson effects, and convective and conductive heat transfer from the formation. It can model both compressible and incompressible single/multi phase flow in a wellbore with an arbitrary inclination.

The primary results of the model are estimates of the extent of temperature change during flow. Results show that temperature changes on the order of a few degrees are possible and temperature changes of this magnitude are certainly detectable with current technology. A second result is a demonstration of the inference of a single phase and multiphase flow profiles from a synthetic case. Sensitivity studies with the model illustrate the flow conditions that cause measurable temperature changes or anomalies that could be recognized in an analysis of distributed temperature measurements.

We further developed a numerical temperature model of a bottom water drive reservoir to demonstrate the uses of temperature profiles in detecting water entries driven by water coning. Water in this numerical model is initially located in a warmer zone below a horizontal well. Results show that oil or water can enter the wellbore 2-3 ^{o}F higher, while gas can enter with 5-6 ^{o}F lower, than the geothermal temperature. Inflow temperature causes the slope of the wellbore temperature profile to change notably, depending on the flow rates and types of fluid entering.

We also present an inversion method that interprets distributed temperature and pressure data to obtain flow rate profiles along horizontal wells. The inversion method, which is based on the Levenberg-Marquardt algorithm, is applied to minimize the differences between the measured profiles and the profiles calculated from a forward model of the well and reservoir flow system. The minimization was accomplished by adjusting the well's inflow profile.

We present synthetic and field examples in this report to illustrate how to use the inversion model to interpret the flow profile of a horizontal well. The synthetic examples show that even with single-phase oil production, the inflow profile can be estimated, in many cases, with the inversion method developed. The method is even more robust when water or gas is produced along discrete intervals in an oil production well because of the unique temperature signature of water or gas production. We applied the inversion method to temperature and pressure profiles measured with production logs in a North Sea horizontal oil producer. The method successfully determined the profile of oil and water entry in a region of large water influx; the profile determined compared well with a flowmeter derived profile.

Finally, we show a temperature estimation model for build sections and junctions. The model predicts the temperature profiles in the build sections connecting the laterals to one another or to a main wellbore, accounting for the changing well angle relative to the geothermal temperature profile. In addition, energy balance equations applied at each junction predict the effect of mixing on the temperature above each junction. The sensitivity studies in the build section and junction are shown in this report.

CHAPTER 3

RESERVOIR MODEL

3.1 INTRODUCTION TO THERMAL RESERVOIR MODEL

In most thermal vertical wellbore models, the fluid is assumed to arrive at the wellbore with the same temperature as the geothermal temperature. Some authors included warming or cooling effects near the wellbore vicinity before the fluid enters the wellbore (Ouyang and Belanger, 2006; Maubeuge *et al.*, 1994). However, these warming or cooling effects resulted from the Joule-Thomson effect (see Appendix A) are relatively small compared to the temperature variation in depth caused by geothermal temperature gradient. Therefore, these effects are in general negligible in vertical wellbore modeling.

Under the condition of normal production, a temperature difference on the order of a few degrees Fahrenheit from the geothermal temperature can possibly occur through the transport in porous media (Dawkrajai *et al.*, 2006; Dawkrajai, 2006). These temperature changes, which are often neglected in vertical well modeling, would play an important role in horizontal well modeling since there would be little differences in geothermal temperature along horizontal wells. Hence, to develop a prediction model for horizontal well interpretations, we also need equations for the reservoir flow and have to couple them with the wellbore equations.

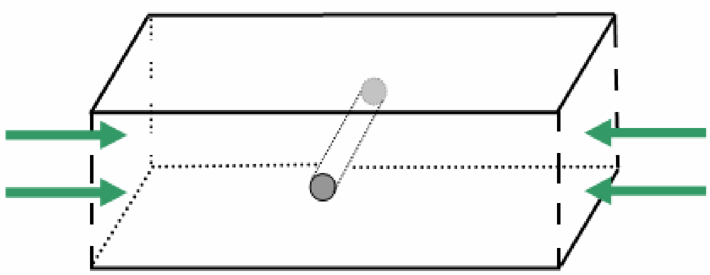

Fig. 3.1 Box-shaped reservoir with constant fluxes from the sides.

3.2 WORKING EQUATIONS FOR RESERVOIR FLOW

We consider a box-shaped reservoir fully penetrated by a horizontal well as depicted in **Fig. 3.1** with no-flow lateral boundaries and constant fluxes from the sides. The fundamental equations describing fluid flow in a reservoir are mass balances, Darcy's law, and energy balance. These equations are very general and used in many engineering applications. They are discussed and formulated to fit the scope of this study.

3.2.1 Mass balance

A starting point for studying fluid flow is the mass balance. It is the conservation of mass that transports through a unit area in unit time. By understanding the mechanisms of mass flow, we can infer the velocity or pressure distribution of the fluid in a reservoir. The velocity or pressure distribution is then coupled with the energy equation to obtain temperature profiles in the reservoir.

The general form of the mass balance that can apply directly to fluid flow in permeable media for any number of components, phases, and chemical reactions is explained in Chapter 2 of Lake (1989). It is simplified here for single phase and steady-state flow condition.

$$\phi \frac{\partial \rho}{\partial t} = -\nabla \cdot (\rho \mathbf{u}). \tag{3.1}$$

where $\mathbf{u}$ is the Darcy velocity ($\mathbf{u} = \mathbf{v}\phi$) and the relationship between the pressure is given as,

$$\mathbf{u} = -\frac{\mathbf{k}}{\mu} \cdot (\nabla p + \rho \mathbf{g}) . \tag{3.2}$$

where $\mathbf{k}$ is the permeability and μ is the viscosity. The mass balance (Eq. 3.1) is typically expressed in terms of pressure by substituting Darcy's law (Eq. 3.2). Dropping time derivative term, we obtain

$$\begin{aligned} 0 &= -\nabla \cdot (\rho \mathbf{u}) \\ &= \nabla \cdot \left(\rho \frac{\mathbf{k}}{\mu} \cdot (\nabla p + \rho \mathbf{g}) \right) . \end{aligned} \tag{3.3}$$

For an isotropic and homogeneous reservoir, neglecting gravity, Eq. 3.3 becomes

$$0 = \rho \nabla^2 p + \nabla \rho \cdot (\nabla p). \tag{3.4}$$

Dividing by ρ and expanding $\nabla \rho$ yield

$$\begin{aligned} 0 &= \nabla^2 p + \frac{1}{\rho} \frac{\partial \rho}{\partial p} \nabla p \cdot (\nabla p) \\ &= \nabla^2 p + c \nabla p \cdot (\nabla p) \end{aligned} , \tag{3.5}$$

where c is the compressibility of the fluid. The second term is usually negligible for a slightly compressible fluid.

3.2.1 Energy balance

A brief derivation of the thermal energy balance is presented here. Rigorous detail is in Bird *et al.* (2002) and Sandler (1999). First, we start from the flowing fluid.

$$\frac{\partial}{\partial t}(\rho \mathbf{v}) = -\nabla \cdot \rho \mathbf{v}\mathbf{v} - \nabla p - \nabla \cdot \boldsymbol{\tau} + \rho \mathbf{g}\,, \qquad (3.6)$$

where $\boldsymbol{\tau}$ is the shear stress tensor.

The momentum is usually viewed as a force, thus; multiplying force by velocity gives the mechanical energy. Knowing that, we can take the dot production of the velocity vector, **v**, with the momentum balance in Eq. 3.6. The result is the mechanical energy balance shown in Eq. 3.7.

$$\frac{\partial}{\partial t}\left(\frac{1}{2}\rho v^2\right) = -\nabla \cdot \left(\frac{1}{2}\rho v^2 \mathbf{v}\right) - \nabla \cdot p\mathbf{v} - p(-\nabla \cdot \mathbf{v}) - \nabla \cdot (\boldsymbol{\tau} \cdot \mathbf{v}) - (-\boldsymbol{\tau} : \nabla \mathbf{v}) + \rho \mathbf{v} \cdot \mathbf{g}\,. \qquad (3.7)$$

The general form of the total energy balance includes kinetic energy, internal energy, heat conduction, work done on the flowing fluid by pressure forces, external forces (gravity) and viscous forces. This total energy balance can be written below.

$$\begin{aligned}\frac{\partial}{\partial t}\left(\frac{1}{2}\rho v^2 + \rho U\right) = -\nabla \cdot \left[\left(\frac{1}{2}\rho v^2 + \rho U\right)\mathbf{v}\right] + \nabla \cdot K_T \nabla T - \nabla \cdot p\mathbf{v} \\ - \nabla \cdot (\boldsymbol{\tau} \cdot \mathbf{v}) - (-\boldsymbol{\tau} : \nabla \mathbf{v}) + \rho \mathbf{v} \cdot \mathbf{g}\end{aligned}\,, \qquad (3.8)$$

where U is the internal energy and K_T is the total thermal conductivity of rock and fluid. Subtracting the mechanical energy balance in Eq. 3.7 from the total energy balance in Eq. 3.8 yields the thermal energy balance from which temperature of fluid can be obtained as

$$\frac{\partial}{\partial t}(\rho U) = -\nabla \cdot (\rho U \mathbf{v}) + \nabla \cdot K_T \nabla T - p \nabla \cdot \mathbf{v} + (-\boldsymbol{\tau} : \nabla \mathbf{v})\,. \qquad (3.9)$$

Eq. 3.9 is one of the most useful forms of the microscopic energy balance in engineering thermodynamics and fluid mechanics. The left side describes the accumulation of internal energy per unit volume. The transport terms on the right side are the internal energy changes caused by convection, conduction, fluid expansion, and viscous dissipation, respectively. For steady-state flow, the time derivative is dropped. The equation is in the following form.

$$0 = \nabla \cdot (\rho U \mathbf{v}) + p \nabla \cdot \mathbf{v} - \nabla \cdot K_T \nabla T - (-\boldsymbol{\tau} : \nabla \mathbf{v})\,. \qquad (3.10)$$

To express the thermal energy balance in terms of measurable (sensible) quantities (p , T), we substitute the definition of enthalpy, H, which is given by

$$H = U + \frac{p}{\rho}\,, \qquad (3.11)$$

Substituting Eq. 3.11 into Eq. 3.10 gives

$$0 = \nabla \cdot (\rho \mathbf{v} H) - \nabla \cdot (p\mathbf{v}) + p\nabla \cdot \mathbf{v} - \nabla \cdot K_T \nabla T - (-\boldsymbol{\tau} : \nabla \mathbf{v}) . \qquad (3.12)$$

Expanding the first term on the right side, we have

$$0 = (\rho \mathbf{v}) \cdot \nabla H + H\nabla \cdot (\rho \mathbf{v}) - \nabla \cdot (p\mathbf{v}) + p\nabla \cdot \mathbf{v} - \nabla \cdot K_T \nabla T - (-\boldsymbol{\tau} : \nabla \mathbf{v}) . \qquad (3.13)$$

Assuming spatially constant porosity, the mass balance (Eq.3.3) becomes

$$\begin{aligned} 0 &= \nabla \cdot (\rho \mathbf{u}) \\ &= \phi \nabla \cdot (\rho \mathbf{v}) \end{aligned} . \qquad (3.14)$$

Therefore, the second term on the right side of Eq. 3.13 is zero. We obtain

$$0 = (\rho \mathbf{v}) \cdot \nabla H - \nabla \cdot (p\mathbf{v}) + p\nabla \cdot \mathbf{v} - \nabla \cdot K_T \nabla T - (-\boldsymbol{\tau} : \nabla \mathbf{v}) . \qquad (3.15)$$

Enthalpy is a function of temperature and pressure and can be expressed as

$$dH = C_p dT + \frac{1}{\rho}(1 - \beta T) dp , \qquad (3.16)$$

where C_p is the heat capacity, and β is the coefficient of isobaric thermal expansion defined as

$$\beta = -\frac{1}{\rho}\left(\frac{\partial \rho}{\partial T}\right)_P . \qquad (3.17)$$

From the relationship in Eq. 3.16, Eq. 3.15 becomes

$$\begin{aligned} 0 &= \rho \mathbf{v} \cdot \left[C_p \nabla T + \frac{1}{\rho}(1 - \beta T)\nabla p \right] - \nabla \cdot (p\mathbf{v}) + p\nabla \cdot \mathbf{v} - \nabla \cdot K_T \nabla T - (-\boldsymbol{\tau} : \nabla \mathbf{v}) \\ &= \rho C_p \mathbf{v} \cdot \nabla T - \beta T \mathbf{v} \cdot \nabla p - \nabla \cdot K_T \nabla T - (-\boldsymbol{\tau} : \nabla \mathbf{v}) \end{aligned} . \qquad (3.18)$$

The $(-\boldsymbol{\tau} : \nabla \mathbf{v})$ term is the viscous dissipation heating that describes the irreversible degradation of mechanical energy into thermal energy. The research and discussion on it is ongoing. This term is sometimes viewed as an entropy generation in thermodynamics, which means that it is always positive (heating) for a Newtonian fluid. For special fluids, the term can be negative because some energy may be stored as elastic energy (Bird *et al.*, 2002). $(-\boldsymbol{\tau} : \nabla \mathbf{v})$ is commonly substituted by $(-\mathbf{v} \cdot \nabla p)$ for a flow governed by Darcy's law; see Ingham *et al.* (1990) and Al-Hadhrami *et al.* (2002) for details. This substitution makes Eq. 3.18 become a complete energy balance of steady-state flow.

The heat conductivity is the effective heat conductivity, K_T, which combines both fluid and rock conductivity. Empirical expressions for K_T can be found in the literature (Lake, 1989). For a fluid filled consolidated sandstone, an example expression is given as

$$K_T = K_d \left\{ 1 + 0.299 \left[\left(\frac{K_{fl}}{K_a} \right)^{0.33} - 1 \right] + 4.57 \left[\frac{\phi K_{fl}}{(1-\phi) K_d} \right]^{0.482} \left[\frac{\rho}{\rho_s} \right]^{-4.30} \right\}. \qquad (3.19)$$

where the subscripts *fl*, *a*, and *d* refer to fluid, air and dry respectively. K_T depends weakly on temperature and is treated as a constant here. The main assumption is that the temperature of flowing fluid is identical to the temperature of the rock. This assumption is valid for continuous flow (steady-state) because changes in a flow rate are much slower than the response time of any sensor. Finally, replacing the interstitial velocity, **v,** with the Darcy velocity, **u**, the equation becomes

$$0 = \rho C_p \mathbf{u} \cdot \nabla T - \beta T \mathbf{u} \cdot \nabla p - \nabla \cdot K_T \nabla T + \mathbf{u} \cdot \nabla p . \qquad (3.20)$$

The first term is thermal energy transported by convection. The second term is thermal energy (cooling) caused by fluid expansion. The third term is thermal energy by heat conduction, and the last term represents viscous dissipation.

3.3 INFLOW TEMPERATURE ESTIMATION

Inflow temperature can be estimated by solving the equations derived in the previous section. For the reservoir with horizontal well shown in **Fig. 3.1**, the pressure drop in the reservoir can be obtained by integrating Darcy's law along the streamline. Furui *et al.* (2003) investigated the geometry of streamlines from a finite element simulation and approximated the pressure profile in the reservoir by a composite of 1D radial flow near the well and 1D linear flow farther from the well as drawn in **Fig. 3.2.** They estimated the distance from the wellbore where linear streamlines become radial as *h*/2. Their solution corresponds to the analytically derived solution by Butler (1994).

We solve the reservoir equations following the streamline geometry shown in **Fig. 3.2**. Firstly, we solve the equations analytically and then approximate the solution to a simpler expression that gives almost an identical answer to the rigorous solution.

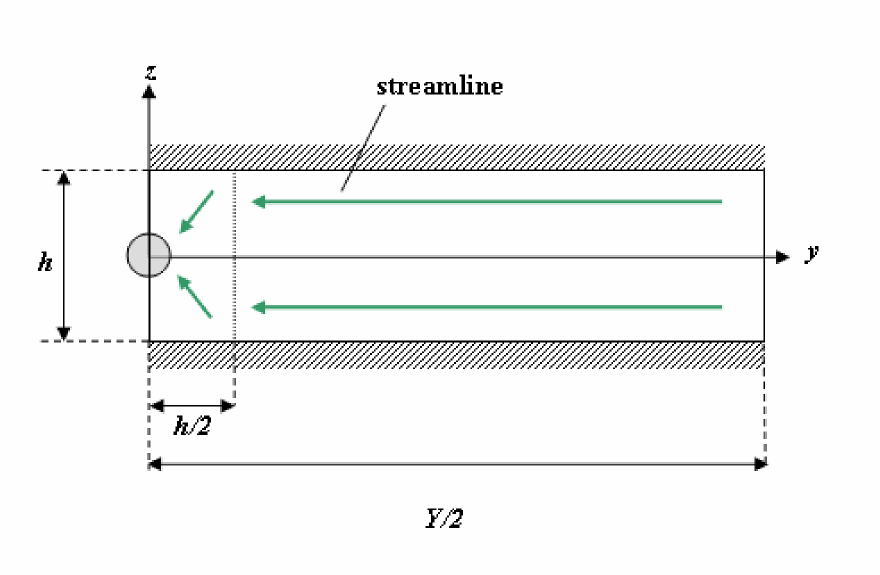

Fig. 3.2 Geometry of the streamlines.

3.3.1 Analytical solution

Following the reservoir streamline geometry, the pressure relationship in a 1D Cartesian coordinate (y-direction) is described by Darcy's law as

$$u_y = -\frac{k}{\mu}\frac{dp}{dy}, \tag{3.21}$$

In term of the volumetric flow rate, Eq. 3.21 becomes

$$\frac{q}{2Lh} = -\frac{k}{\mu}\frac{dp}{dy}, \tag{3.22}$$

where *q*, *L*, and *h* are the flow rate, the length of well, and the thickness of the reservoir respectively. In linear coordinate, the energy balance becomes

$$\rho C_p u_y \frac{dT}{dy} - \beta T u_y \frac{dp}{dy} - K_T \frac{d^2T}{dy^2} + u_y \frac{dp}{dy} = 0\,. \tag{3.23}$$

Substituting Eq. 3.22 into Eq.3.23 and rearranging yield

$$\frac{d^2T}{dy^2} - \frac{\rho C_p}{K_T}\left(\frac{q}{2hL}\right)\frac{dT}{dy} - \frac{\beta\mu}{kK_T}\left(\frac{q}{2hL}\right)^2 T + \frac{\mu}{kK_T}\left(\frac{q}{2hL}\right)^2 = 0\,. \tag{3.24}$$

Solving the second-order ordinary differential equation, we obtain

$$T = L_1 e^{m_+ y} + L_2 e^{m_- y} + \frac{1}{\beta}, \tag{3.25}$$

where

$$m_{\pm} = \frac{q}{4hL}\left[\frac{\rho C_p}{K_T} \pm \sqrt{\left(\frac{\rho C_p}{K_T}\right)^2 + \frac{4\beta\mu}{kK_T}}\right]. \tag{3.26}$$

L_1 and L_2 are integration constants to be determined by boundary conditions.

Similarly, we have for the radial flow portion,

$$\frac{q}{2\pi rL} = -\frac{k}{\mu}\frac{dp}{dr}. \tag{3.27}$$

In radial coordinates, the energy balance becomes

$$\rho C_p\, u_r \frac{dT}{dr} - \beta T\, u_r \frac{dp}{dr} + u_r \frac{dp}{dr} - K_T \frac{1}{r}\frac{d}{dr}\left(r\frac{dT}{dr}\right) = 0. \tag{3.28}$$

Substituting Eq. 3.27 into Eq. 3.28 gives

$$-\frac{2\pi L\, K_{Tt}}{q} r^2 \frac{d^2T}{dr^2} + \left(\rho C_p - \frac{2\pi L\, K_T}{q}\right) r\frac{dT}{dr} + \frac{\mu q\beta T}{2\pi kL} - \frac{\mu q}{2\pi kL} = 0. \tag{3.29}$$

Solution to this second-order differential equation is given by

$$T = R_1 r^{n_+} + R_2 r^{n_-} + \frac{1}{\beta}, \tag{3.30}$$

where

$$n_{\pm} = \frac{q}{4\pi L}\left[\frac{\rho C_p}{K_T} \pm \sqrt{\left(\frac{\rho C_p}{K_T}\right)^2 + \frac{4\mu\beta}{kK_T}}\right]. \tag{3.31}$$

R_1 and R_2 are integration constants. The boundary conditions are as follow:
At the external reservoir boundary, temperature is known (geothermal temperature)

$$T\big|_{y=\frac{Y}{2}} = T_o. \tag{3.32}$$

Temperature and heat flux is continuous at the boundary between radial and linear elements

$$T\big|_{r=\frac{h}{2}} = T\big|_{y=\frac{h}{2}}, \tag{3.33}$$

and

$$\left.\frac{dT}{dr}\right|_{r=\frac{h}{2}} = \left.\frac{dT}{dy}\right|_{y=\frac{h}{2}}. \tag{3.34}$$

Heat flux is continuous at the wellbore.

$$K_T \frac{dT}{dr}\bigg|_{r=r_w} = \alpha\left(T\big|_{r=r_w} - T_w\right). \tag{3.35}$$

where α is the overall heat transfer coefficient between the wellbore and the formation (see Appendix B). The last boundary condition makes the inflow temperature dependent on the wellbore temperature and the overall heat transfer coefficient between reservoir and wellbore. From the boundary conditions, finally we have

$$L_1 = \frac{l_1 + l_2}{\psi_+ + \psi_-}, \tag{3.36}$$

$$L_2 = \frac{l_3 + l_4}{\psi_+ + \psi_-}, \tag{3.37}$$

$$R_1 = \frac{\theta_1 + \theta_2}{\psi_+ + \psi_-}, \tag{3.38}$$

and

$$R_2 = \frac{\theta_3 + \theta_4}{\psi_+ + \psi_-}. \tag{3.39}$$

where

$$l_1 = r_w^{\;n_-} e^{\frac{h}{2}m_-} \left(-K_T n_- + \alpha r_w\right)\left(\beta T_o - 1\right)\left(\frac{h}{2}\right)^{n_+} \left(\frac{h}{2}m_- - n_+\right), \tag{3.40}$$

$$\begin{aligned} l_2 = \left(\frac{h}{2}\right)^{n_-} \Bigg[& e^{\frac{h}{2}m_-} r_w^{\;n_+} \left(-\frac{h}{2}m_- + n_-\right)\left(-K_T n_+ + \alpha r_w\right)\left(\beta T_o - 1\right) \\ & + e^{\frac{Y}{2}m_-} \alpha r_w \left(\frac{h}{2}\right)^{n_+} \left(\beta T_w - 1\right)\left(n_+ - n_-\right) \Bigg], \end{aligned} \tag{3.41}$$

$$l_3 = r_w^{\;n_+} e^{\frac{h}{2}m_-} \left(K_T n_- - \alpha r_w\right)\left(\beta T_o - 1\right)\left(\frac{h}{2}\right)^{n_+} \left(\frac{h}{2}m_+ + n_+\right), \tag{3.42}$$

$$\begin{aligned} l_4 = \left(\frac{h}{2}\right)^{n_-} \Bigg[& e^{\frac{h}{2}m_+} r_w^{\;n_+} \left(\frac{h}{2}m_+ - n_-\right)\left(-K_T n_+ + \alpha r_w\right)\left(\beta T_o - 1\right) \\ & - e^{\frac{Y}{2}m_+} \alpha r_w \left(\frac{h}{2}\right)^{n_+} \left(\beta T_w - 1\right)\left(n_+ - n_-\right) \Bigg], \end{aligned} \tag{3.43}$$

$$\theta_1 = e^{\frac{h}{2}(m_+ + m_-)} \frac{h}{2} r_w^{\,n_-} (m_+ - m_-)(K_T n_- - \alpha r_w)(\beta T_o - 1), \tag{3.44}$$

$$\theta_2 = \left(\frac{h}{2}\right)^{n_-} (\beta T_w - 1)\alpha r_w \left[e^{\frac{h}{2}m_+ + \frac{Y}{2}m_-} \left(\frac{h}{2}m_+ - n_-\right) + e^{\frac{Y}{2}m_+ + \frac{h}{2}m_-} \left(-\frac{h}{2}m_- + n_-\right)\right], \tag{3.45}$$

$$\theta_3 = e^{\frac{h}{2}(m_+ + m_-)} \frac{h}{2} r_w^{\,n_+} (m_+ - m_-)(-K_T n_+ + \alpha r_w)(\beta T_o - 1), \tag{3.46}$$

$$\theta_4 = \left(\frac{h}{2}\right)^{n_+} (\beta T_w - 1)\alpha r_w \left[e^{\frac{h}{2}m_- + \frac{Y}{2}m_+} \left(\frac{h}{2}m_- - n_+\right) + e^{\frac{Y}{2}m_- + \frac{h}{2}m_+} \left(-\frac{h}{2}m_+ + n_+\right)\right], \tag{3.47}$$

and

$$\psi_\pm = \beta r_w^{\,n_\pm} \left(\frac{h}{2}\right)^{n_\mp} (K_{Tt} n_\pm - \alpha r_w) \left[e^{\frac{Y}{2}m_\pm + \frac{h}{2}m_\mp} \left(\frac{h}{2}m_\mp - n_\mp\right) + e^{\frac{h}{2}m_\pm + \frac{Y}{2}m_\mp} \left(-\frac{h}{2}m_\pm + n_\mp\right)\right]. \tag{3.48}$$

The solution of the reservoir temperature mainly depends on Joule-Thomson effect in the reservoir and the conduction of heat to or from the wellbore. **Fig. 3.3** shows the reservoir temperature profiles (perpendicular to the wellbore) comparison for various reservoir pressure drawdowns (100 psi, 300 psi, and 500 psi) neglecting the wellbore temperature effect (zero heat transfer with the wellbore) for single-phase oil flow. Unless stated, the default properties listed in **Table 3.1** are used in the examples through in this chapter.

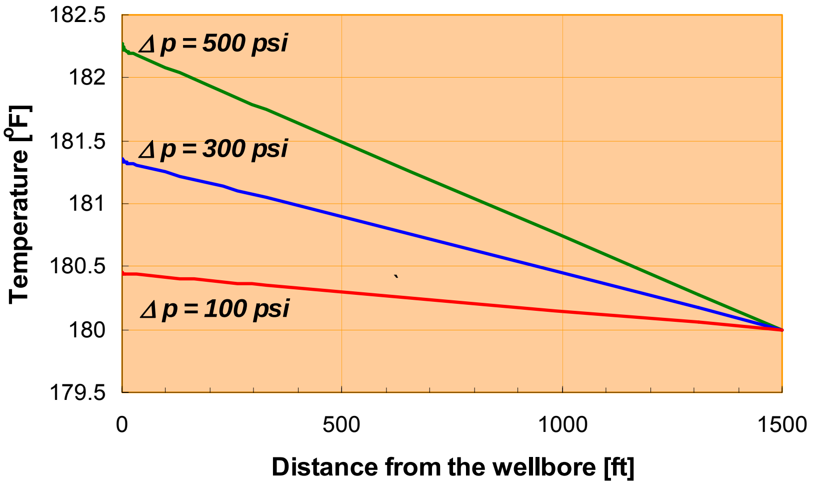

Fig. 3.3 Reservoir temperature profiles (Joule-Thomson effect).

Table 3.1 Properties used in the examples.

Reservoir length [ft]	2000
Reservoir width [ft]	3150
Reservoir height [ft]	55
Pressure drawdown [psi]	300
T at outer boundary [°F]	180

	Oil	*Water*	*Gas*
Density [lb/ft^3]	41	63	14
Viscosity [cp]	0.49	0.48	0.03
K_{Tt} [Btu/hr ft °F]	2	2.5	1.3

The Joule-Thomson effect is proportional to the pressure drop in the system. Therefore, the higher the pressure drawdown, the more significant the Joule-Thomson effect can be observed and the higher the inflow temperature of the fluid. When a different type of fluid is produced than the one flowing in the wellbore, there is often a temperature difference between the inflowing fluid from the reservoir and the fluid flowing inside the wellbore. In this case, the wellbore temperature effect becomes important. In Fig. **3.4**, the reservoir temperature profiles near the wellbore vicinity (- 1.5 ft) for different wellbore temperatures with a fixed heat transfer coefficient (88 Btu/hr-ft^2-^{o}F) are shown. As can be seen in Fig. **3.4**, inflow temperature is affected by the wellbore temperature. Because of the high non-linearity between reservoir and wellbore temperature, the equations have to be solved iteratively. The details about the coupling model are discussed in Chapter 5.

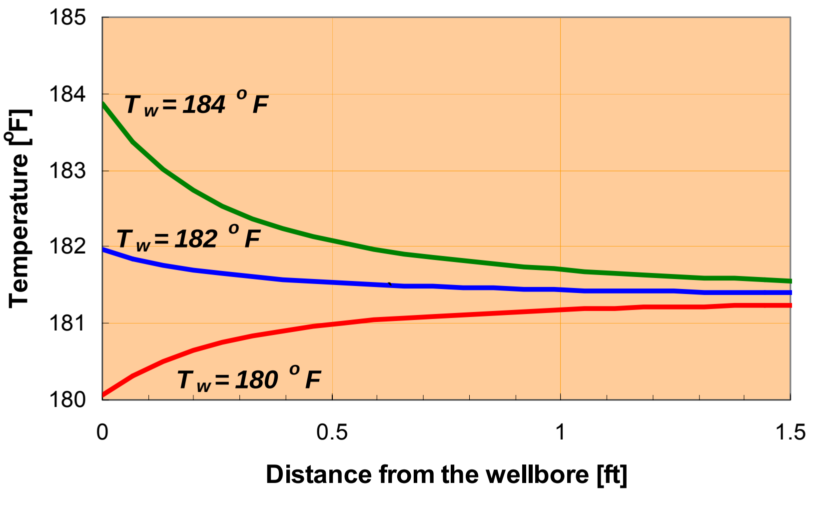

Fig. 3.4 Wellbore temperature effect.

Reservoir temperature profile also varies if the types of fluid differ. The example calculations of temperature profiles of various types of fluid (oil, gas, and water) flowing into a wellbore are shown in **Fig. 3.5.** If the pressure drawdowns (300 psi) and the boundary temperatures (180 °F) are same for all the types of fluid, the temperature difference is essentially governed by the Joule-Thomson coefficient, K_{JT}, of the fluid.

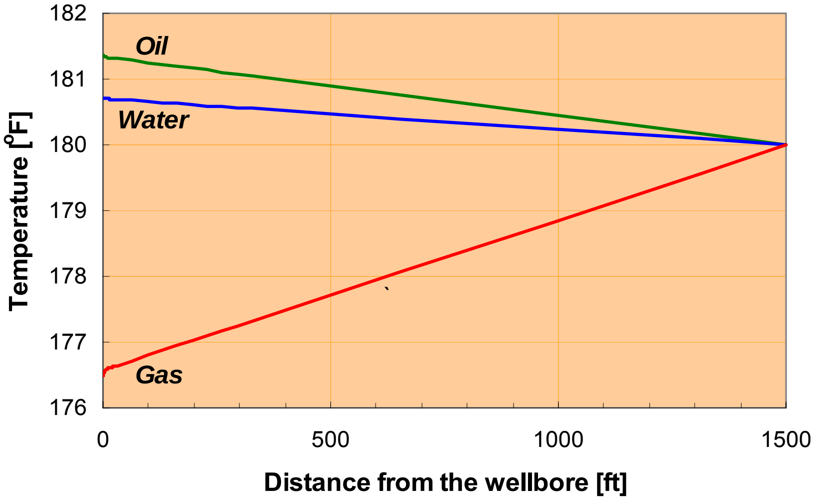

Fig. 3.5 Reservoir temperature profiles (different fluid types).

3.3.2 Studies from reservoir model

We have derived the rigorous temperature solution to the reservoir energy balance equation, and demonstrated some key behaviors of the reservoir temperature behavior. From the above examples, we can see that the temperature profiles follow straight lines except for the radial flow region near the wellbore. This implies that we can neglect the second derivative (conductive heat flux) of the temperature in the linear flow region.

Neglecting the heat conduction term, $K_T \dfrac{d^2T}{dy^2}$, and dividing both sides by u_y, Eq. 3.23 becomes

$$\rho C_p \frac{dT}{dy} - (\beta T - 1)\frac{dp}{dy} = 0 . \tag{3.49}$$

Solving for $\dfrac{dT}{dy}$ yields

$$\begin{aligned}\frac{dT}{dy} &= \frac{\beta T - 1}{\rho C_p}\frac{dp}{dy} \\ &= K_{JT}\frac{dp}{dy}\end{aligned} \quad . \tag{3.50}$$

Assuming the Joule-Thomson coefficient, K_{JT}, is invariant over the domain of interest ($y = W \rightarrow y = h/2$), we can integrate Eq. 3.50 as

$$\int_{y=h/2}^{W} \frac{dT}{dy} dy = \int_{h/2}^{W} K_{JT} \frac{dp}{dy} dy, \tag{3.51}$$

$$\therefore \int_{y=h/2}^{W} dT = K_{JT} \int_{h/2}^{W} dp, \tag{3.52}$$

$$\therefore T\big|_{y=h/2} - T_e = -K_{JT}\left(p_e - p\big|_{y=h/2}\right). \tag{3.53}$$

Then we have the reservoir temperature at $y = h/2$

$$T\big|_{y=h/2} = T_e - K_{JT}\left(p_e - p\big|_{y=h/2}\right) \equiv T_L. \tag{3.54}$$

The solution to the radial region (Eq. 3.30) is now obtained with the new coefficients

$$T = R_1' r^{n_+} + R_2' r^{n_-} + \frac{1}{\beta}. \tag{3.55}$$

The new coefficients are to be estimated by the following two boundary conditions:

$$T\big|_{r=\frac{h}{2}} = T\big|_{y=\frac{h}{2}} = T_L, \tag{3.56}$$

and

$$K_T \frac{dT}{dr}\bigg|_{r=r_w} = \alpha\left(T\big|_{r=r_w} - T_w\right). \tag{3.35}$$

Thus, we obtain

$$R_1' = \frac{1}{D}\left[\beta r_w^{n_-}\left(K_T n_- - \alpha r_w\right)T_L - r_w^{n_-}\left(K_T n_- - \alpha r_w\right) + \left(\frac{h}{2}\right)^{n_-} \alpha r_w\left(\beta T_w - 1\right)\right], \tag{3.57}$$

and

$$R_2' = \frac{1}{D}\left[\beta r_w^{n_+}\left(\alpha r_w - K_T n_+\right)T_L - r_w^{n_+}\left(\alpha r_w - K_T n_+\right) - \left(\frac{h}{2}\right)^{n_+} \alpha r_w\left(\beta T_w - 1\right)\right], \tag{3.58}$$

where

$$D = \beta\left[r_w^{\,n_-}\left(\frac{h}{2}\right)^{n_+}\left(K_T n_- - \alpha r_w\right) - r_w^{\,n_+}\left(\frac{h}{2}\right)^{n_-}\left(K_T n_+ - \alpha r_w\right)\right]. \tag{3.59}$$

The comparisons with the rigorous solution are shown in **Figs. 3.6** and **3.7**. A small discrepancy can be observed in a fine scale near the wellbore (**Fig. 3.7**). However, the results are almost identical. From the results above, we conclude that the approximate model is a fair alternative to the rigorous solution.

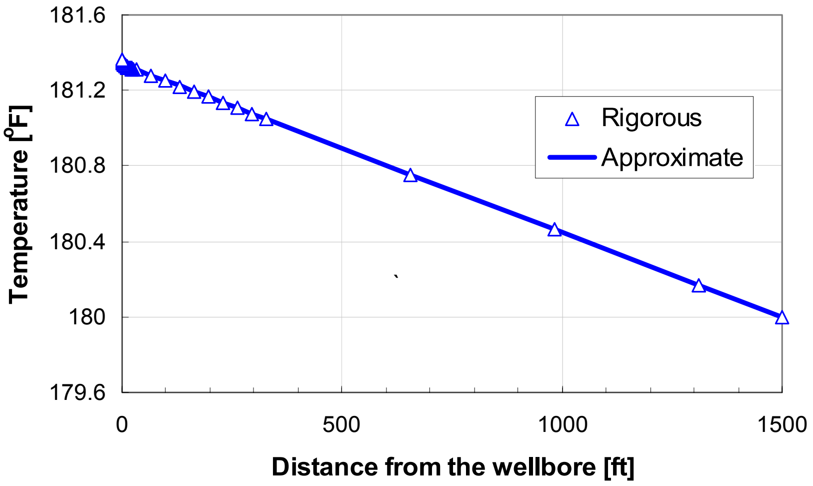

Fig. 3.6 Comparison between rigorous and approximate solution.

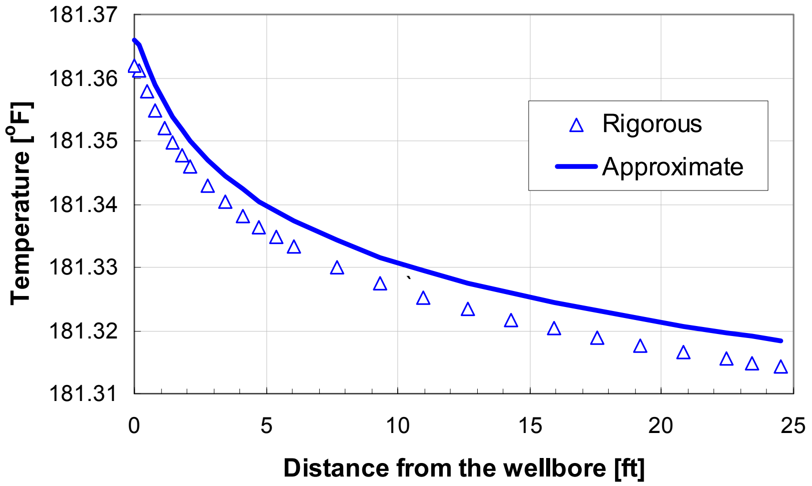

Fig. 3.7 Comparison with rigorous solution in the radial flow region.

3.3.1 Effect of damage skin on reservoir temperature

Damaged skin factor is created by formation damage during drilling or other well operations. If the damaged formation affects the reservoir inflow temperature enough to detect, we would be able to estimate skin distribution along the well from DTS data. The inferences can be performed easily by adding another radial flow region that has a reduced permeability. In this section, we revisit the inflow temperature model to include the damaged zone and show how much temperature changes could occur under various conditions.

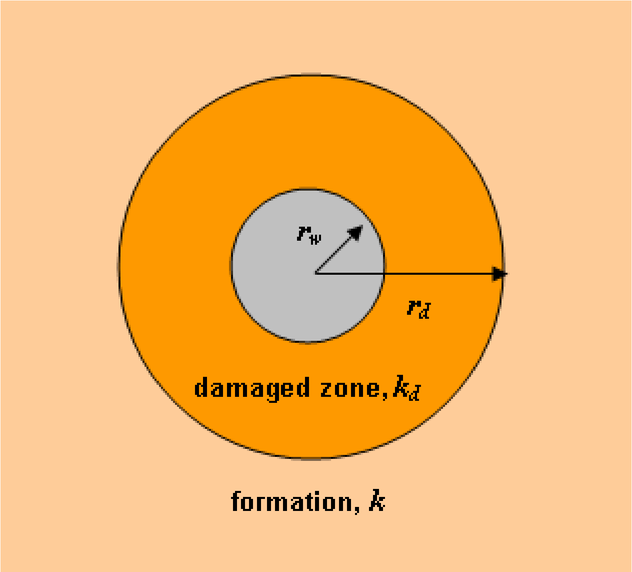

Fig. 3.8 Schematic of a well with formation damage.

The damaged region usually extends a few feet from the wellbore radially if permeability field is isotropic and homogeneous (**Fig. 3.8**). According to the streamline geometry depicted in **Fig. 3.2**, the potential profile $\Phi(y,z)$ in the reservoir can be simply estimated by the following.

For the radial region:

$$\Phi(y,z)=\frac{\mu}{2\pi k}\left(\frac{q}{L}\right)\ln\left(\frac{\sqrt{y^2+z^2}}{r_w}\right), \qquad \text{for } r_w \le \sqrt{y^2+z^2} \le h/2 . \qquad (3.60)$$

For the linear region:

$$\Phi(y,z)=\frac{\mu}{2\pi k}\left(\frac{q}{L}\right)\ln\left(\frac{h/2}{r_w}\right)+\frac{\mu}{kh}\left(\frac{q/2}{L}\right)\left(y-\frac{h}{2}\right), \qquad \text{for } h/2 \le \sqrt{y^2+z^2} \le W . \qquad (3.61)$$

Considering a small region of formation damage, we assume the geometry of a streamline does not change. Then, for the pressure field,

For the damaged region:

$$\Phi(y,z) = \frac{\mu}{2\pi k_d}\left(\frac{q}{L}\right)\ln\left(\frac{\sqrt{y^2+z^2}}{r_w}\right), \qquad \text{for } r_w \le \sqrt{y^2+z^2} \le r_d \,. \tag{3.62}$$

For the radial region:

$$\Phi(y,z) = \frac{\mu}{2\pi k_d}\left(\frac{q}{L}\right)\ln\left(\frac{r_d}{r_w}\right) + \frac{\mu}{2\pi k}\left(\frac{q}{L}\right)\ln\left(\frac{\sqrt{y^2+z^2}}{r_d}\right), \qquad \text{for } r_d \le \sqrt{y^2+z^2} \le h/2 \,. \tag{3.63}$$

For the linear region:

$$\begin{aligned}\Phi(y,z) = \frac{\mu}{2\pi k_d}\left(\frac{q}{L}\right)\ln\left(\frac{r_d}{r_w}\right) + \frac{\mu}{2\pi k}\left(\frac{q}{L}\right)\ln\left(\frac{h/2}{r_d}\right) \\ + \frac{\mu}{kh}\left(\frac{q/2}{L}\right)\left(y-\frac{h}{2}\right)\end{aligned}, \qquad \text{for } h/2 \le \sqrt{y^2+z^2} \le W \,. \tag{3.64}$$

From Eqs. 3.62 - 3.64, the total pressure drop with fixed flow rate is obtained as

$$\Delta p_t = \frac{q\mu}{2\pi kL}\left[\ln\left(\frac{h\sqrt{2}}{2r_w}\right) + \pi(W/h - 1/2) + s\right], \tag{3.65}$$

where

$$s = \left(\frac{k}{k_d} - 1\right)\ln\left(\frac{r_d}{r_w}\right). \tag{3.66}$$

where k_d is a damaged permeability and r_d is a damaged radius. As an example, we consider $k_d = 0.1k$ and $r_d = 3\,\text{ft}$ ($s = 20.7$). The pressure profiles of an undamaged reservoir and a damaged reservoir for 500 psi pressure drawdown with fixed flow rate are plotted on a log-log plot in **Fig. 3.9**.

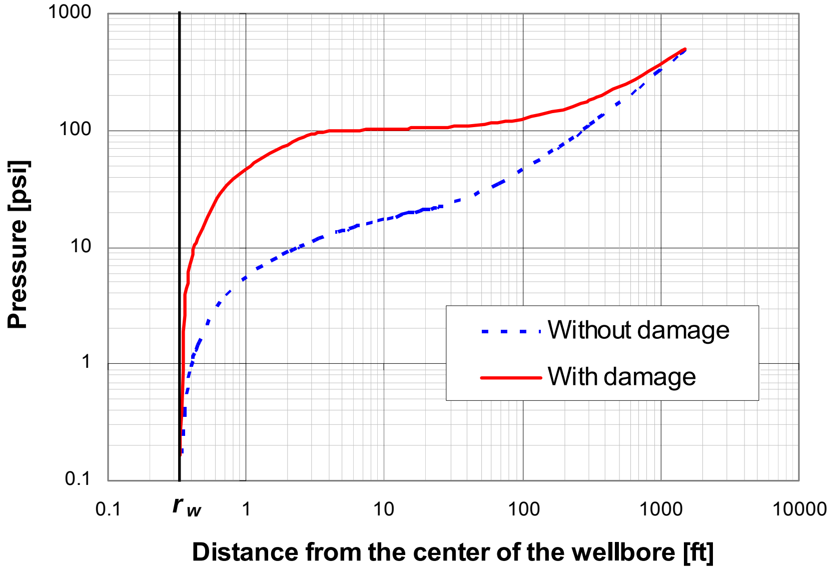

Fig. 3.9 Pressure profile comparison between undamaged and damaged reservoir.

From **Fig. 3.9**, we can observe the higher pressure drawdown in the radial flow region if the damage zone, which creates additional pressure drop, exists. Since the temperature profile is very sensitive to the reservoir pressure drawdown, the temperature profile should be affected by the existence of skin as well. The solutions to the temperature profile are given by

$$T = C_1 r^{n_+} + C_2 r^{n_-} + \frac{1}{\beta}, \quad \text{for } r_d \le r \le h/2, \tag{3.67}$$

and,

$$T = C_3 r^{d_+} + C_4 r^{d_-} + \frac{1}{\beta}, \quad \text{for } r_w \le r \le r_d, \tag{3.68}$$

where

$$d_{\pm} = \frac{q}{4\pi L}\left[\frac{\rho C_p}{K_T} \pm \sqrt{\left(\frac{\rho C_p}{K_T}\right)^2 + \frac{4\mu\beta}{k_d K_T}}\right]. \tag{3.69}$$

We estimate these coefficients, C_1, C_2, C_3, and C_4 with the following boundary conditions in addition to Eqs. 3.35 and 3.56:

The temperatures at the damaged and undamaged boundary are same,

$$C_1 r_d^{\,n_+} + C_2 r_d^{\,m_-} + \frac{1}{\beta} = C_3 r_d^{\,d_+} + C_4 r_d^{\,d_-} + \frac{1}{\beta}, \tag{3.70}$$

and first derivatives of Eqs. 3.67 and 3.68 are equal since the temperatures should be continuous

$$C_1 n_+ {r_d}^{n_+ -1} + C_2 n_+ {r_d}^{n_+ -1} = C_3 d_+ {r_d}^{d_+ -1} + C_2 d_- {r_d}^{d_- -1} \quad . \tag{3.71}$$

Then the coefficients are:

$$\begin{aligned} C_1 = \frac{\alpha}{D'} \Big[& (T_w - 1/\beta)(h/2)^{n_-} r_w r_d^{d_+ + d_-} (-d_+ + d_-) \\ & + (T_L - 1/\beta)\left\{ {r_w}^{d_- +1} r_d^{n_- + d_+} (d_+ - n_-) + {r_w}^{d_+ +1} r_d^{n_- + d_-} (n_- - d_-) \right\} \\ & + \frac{K_T}{\alpha} (T_L - 1/\beta)\left\{ {r_w}^{d_-} r_d^{n_- + d_+} d_- (-d_+ + n_-) - {r_w}^{d_+} r_d^{n_- + d_-} d_+ (n_- - d_+) \right\} \Big] \end{aligned} \quad , \tag{3.72}$$

$$\begin{aligned} C_2 = \frac{\alpha}{D'} \Big[& (T_w - 1/\beta)(h/2)^{n_+} r_w r_d^{d_+ + d_-} (d_+ - d_-) \\ & + (T_l - 1/\beta)\left\{ {r_w}^{d_- +1} r_d^{n_+ + d_+} (n_+ - d_+) + {r_w}^{d_+ +1} r_d^{n_+ + d_-} (-n_+ + d_-) \right\} \\ & + \frac{K_T}{\alpha} (T_l - 1/\beta)\left\{ {r_w}^{d_-} r_d^{n_+ + d_+} d_- (d_+ - n_+) + {r_w}^{d_+} r_d^{n_+ + d_-} d_+ (n_+ - d_-) \right\} \Big] \end{aligned} \quad , \tag{3.73}$$

$$\begin{aligned} C_3 = \frac{1}{D'} \Big[& (T_l - 1/\beta)(K_T d_- - \alpha r_w) {r_w}^{d_-} {r_d}^{n_+ + d_-} (-n_+ + n_-) \\ & + \alpha r_w (T_w - 1/\beta)\left\{ (h/2)^{n_-} r_d^{n_+ + d_-} (-n_+ + d_-) + (h/2)^{n_+} r_d^{n_- + d_-} (n_- - d_-) \right\} \Big] \end{aligned} , \tag{3.74}$$

and,

$$\begin{aligned} C_4 = \frac{1}{D'} \Big[& (T_l - 1/\beta)(K_T d_+ - \alpha r_w) {r_w}^{d_+} {r_d}^{n_+ + n_-} (n_+ - n_-) \\ & + \alpha r_w (T_w - 1/\beta)\left\{ (h/2)^{n_-} r_d^{n_+ + d_-} (n_+ - d_+) + (h/2)^{n_+} r_d^{n_- + d_+} (-n_- + d_-) \right\} \Big] \end{aligned} , \tag{3.75}$$

where

$$\begin{aligned} D' = & (K_T d_- - \alpha R) {r_w}^{d_-} \Big[(h/2)^{d_-} r_d^{n_+ + d_-} (-n_+ + d_+) + (h/2)^{n_+} r_d^{n_- + d_+} (n_- - d_+) \Big| \\ & - (K_T d_+ - \alpha r_w) {r_w}^{d_+} \Big[(h/2)^{n_-} r_d^{n_+ + d_-} (-n_+ + d_-) + (h/2)^{n_+} r_d^{n_- + d_-} (n_- - d_-) \Big] \end{aligned} . \tag{3.76}$$

Using the solution derived above, we can calculate the temperature profile. The temperature profiles corresponding to the pressure profiles in **Fig. 3.9** are plotted on a semi-log plot in **Fig. 3.10**. Reservoir temperature is warmed up linearly in the linear flow region, while it follows the radial pressure change in the radial flow region. For both cases, as fluid approaches to the wellbore, the temperature change is accelerated. The well with damage has more pressure drawdown near the wellbore, and the fluid arrives at the wellbore with a higher temperature, 0.4 ^{o}F higher for this example.

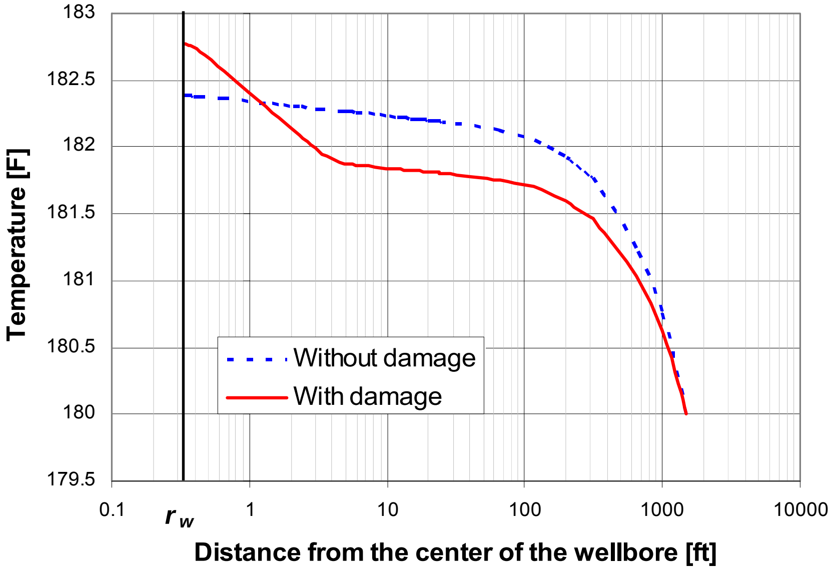

Fig. 3.10 Temperature profile comparison between undamaged and damaged reservoir.

Fig 3.11 shows the variation of the inflowing temperature varying damaged permeability ratio from 0.05 to 1 and damaged radii of 1, 3, and 5 ft. The more damaged, the higher the inflow temperature observed. **Fig. 3.12** shows the same inflow temperature example plotted with the skin factor values calculated from Eq. 3.66 in **Fig. 3.7**. From the figure, we can see the almost proportional change of inflow temperature to the skin.

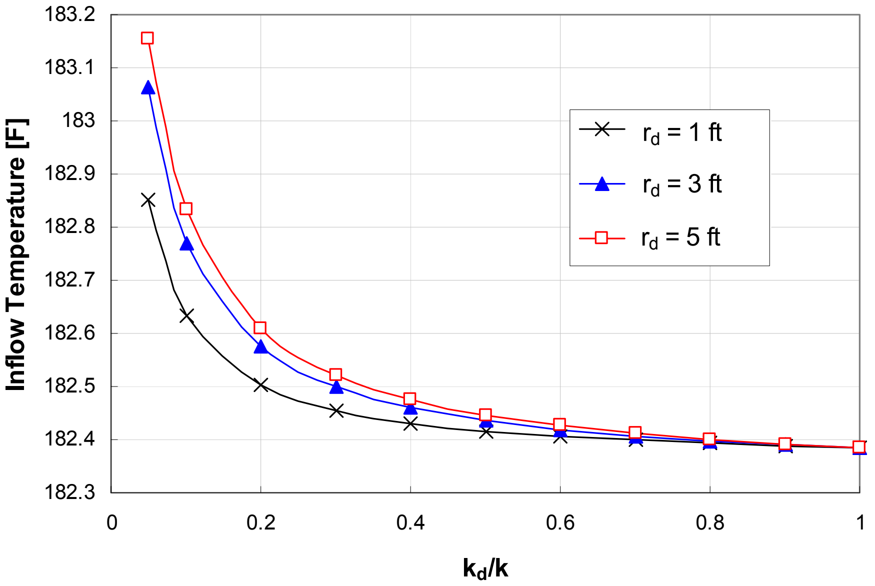

Fig. 3.11 Inflow temperature vs k_d/k.

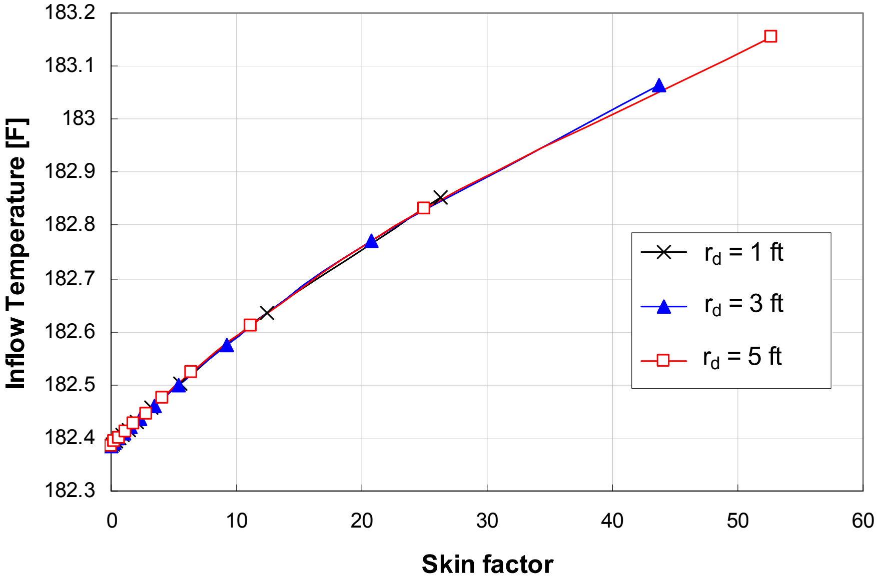

Fig. 3.12 Inflow temperature vs skin factor.

CHAPTER 4

WELLBORE MODEL

4.1 INTRODUCTION TO WELLBORE MODEL

Because of the long exposed length of a horizontal wellbore to the reservoir, fluid may enter the wellbore continuously throughout the producing zone. Therefore, we must account for two streams that are in the axial direction (along the wellbore) and the radial direction (from the reservoir) in deriving equations. Also, the extensive length of the well that is exploiting the reservoir makes the downhole pressure and temperature inside the wellbore vary with the positions.

The mass or heat transferred between the wellbore and the reservoir will be determined by both the wellbore and the reservoir conditions. For instance, as a result of fluid flow in a horizontal well, the wellbore pressure of near the heel tends to be lower than that of the toe, which creates more pressure difference from the reservoir pressure, resulting in higher inflow rate near the heel. In development of a wellbore model, these dependences on the reservoir have to be considered.

4.2 WORKING EQUATIONS FOR SINGLE-PHASE FLOW

In this section, we derive the steady-state conservation equations for the wellbore region averaging any variation in temperature or pressure in the radial direction over a differential volume element shown in **Fig. 4.1**. Then we account for the net input and output of intensive properties such as mass, momentum and total energy using the shell balance.

The completion types may be open hole, perforated liner, etc. We introduce the open pipe ratio defined as

$$\gamma = \frac{\text{Open area of pipe}}{\text{Surface area of pipe}}. \tag{4.1}$$

The open pipe ratio is a function of position considered over a given length of the wellbore. It will be the perforation density over a segment for a perforated well and is the reservoir porosity of a section for an openhole completed well. Using γ, the surface area of a differential volume element can be expressed as $2\pi R\gamma\Delta x$, and convective properties from the formation, for instance, transferred mass can be written as $2\pi R\gamma\Delta xM$.

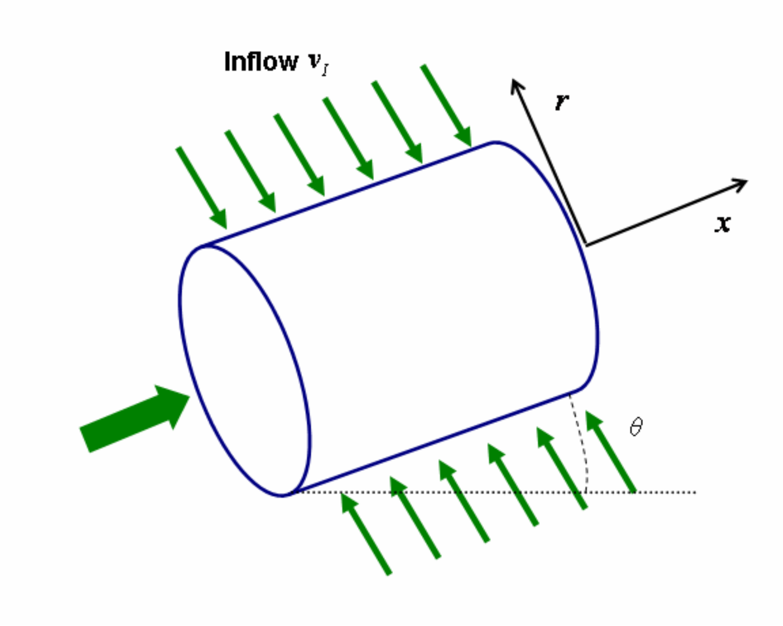

Fig. 4.1 Volume element of a wellbore.

As depicted in **Fig. 4.1**, the main streams of the fluid flow are in two directions that are axial (x-direction) and radial (r-direction). We assume the velocity vector as

$$\mathbf{v} = \begin{pmatrix} v_x \\ v_r \end{pmatrix} = \begin{cases} \begin{pmatrix} 0 \\ v \end{pmatrix} & \text{otherwise} \\ \begin{pmatrix} 0 \\ v_I \end{pmatrix} & \text{at } r = R \end{cases}, \tag{4.2}$$

where the subscript *I* means inflow properties. Equation Figure 4.2 indicates that there is no slip ($v_x = 0$) at the wall, and the radial velocity only exists at the wall ($v_r = v_I$) which is reasonable because in most part of the well, radial velocity is much smaller than the axial velocity. As stated previously, inflow velocity v_I is a function of the reservoir and the wellbore condition. Using the productivity index of the well, J, the inflow rate for a certain distance (Δx) of the well can be written as

$$\int_{\Delta x} 2\pi R\gamma v dx = J\left(p_R - p\right), \tag{4.3}$$

where p_R is the reservoir pressure.

4.2.1 Mass balance

Conservation of mass can be equated by observing the incoming mass flux and outgoing mass flux as

$$\begin{Bmatrix}\text{rate of}\\ \text{increase}\\ \text{of mass}\end{Bmatrix}=\begin{Bmatrix}\text{rate of}\\ \text{mass}\\ \text{in}\end{Bmatrix}-\begin{Bmatrix}\text{rate of}\\ \text{mass}\\ \text{out}\end{Bmatrix}. \tag{4.4}$$

The rate of increase of mass within the differential volume element is

$$\begin{Bmatrix}\text{rate of}\\ \text{increase}\\ \text{of mass}\end{Bmatrix}=\pi R^2\Delta x\frac{\partial\rho}{\partial t}, \tag{4.5}$$

The rates of mass in and out of the differential volume are given as follows.

$$\begin{Bmatrix}\text{rate of}\\ \text{mass}\\ \text{in}\end{Bmatrix}=2\pi R\gamma\Delta x(\rho v_r)_R+\pi R^2(\rho v_x)_x, \tag{4.6}$$

and,

$$\begin{Bmatrix}\text{rate of}\\ \text{mass}\\ \text{out}\end{Bmatrix}=\pi R^2(\rho v_x)_{x+\Delta x}. \tag{4.7}$$

Substituting Eqs. 4.5 - 4.7 into Eq. 4.4 gives

$$\begin{aligned}\pi R^2\Delta x\frac{\partial\rho}{\partial t}&=2\pi R\gamma\Delta x(\rho v_r)_R+\pi R^2(\rho v_x)_x-\pi R^2(\rho v_x)_{x+\Delta x}\\ &=2\pi R\gamma\Delta x\rho v_I+\pi R^2\left[(\rho v_x)_x-(\rho v_x)_{x+\Delta x}\right]\end{aligned}. \tag{4.8}$$

Dividing by $\pi R^2\Delta x$, Eq. 4.8 becomes

$$\frac{\partial\rho}{\partial t}=\frac{2}{R}\gamma\rho v_I+\frac{(\rho v_x)_x-(\rho v_x)_{x+\Delta x}}{\Delta x}. \tag{4.9}$$

Taking $\Delta x\to 0$, we have

$$\frac{\partial\rho}{\partial t}=\frac{2\gamma}{R}\rho_I v_I-\frac{\partial(\rho v)}{\partial x}. \tag{4.10}$$

Finally, for steady-state, we obtain

$$\frac{d(\rho v)}{dx}=\frac{2\gamma}{R}\rho_I v_I. \tag{4.11}$$

4.2.2 Momentum balance

To derive the equation for momentum, we write a momentum balance over the differential volume as

$$\left\{\begin{matrix}\text{rate of}\\ \text{increase}\\ \text{of momentum}\end{matrix}\right\}=\left\{\begin{matrix}\text{rate of}\\ \text{momentum}\\ \text{in}\end{matrix}\right\}-\left\{\begin{matrix}\text{rate of}\\ \text{momentum}\\ \text{out}\end{matrix}\right\}+\left\{\begin{matrix}\text{external}\\ \text{force on}\\ \text{the fluid}\end{matrix}\right\}. \qquad (4.12)$$

The rate of increase of momentum in the x-direction is given as

$$\left\{\begin{matrix}\text{rate of}\\ \text{increase}\\ \text{of momentum}\end{matrix}\right\}=\pi R^2\Delta x\frac{\partial(\rho v_x)}{\partial t}. \qquad (4.13)$$

Let $\mathbf{\Phi}$ be the combined convective and molecular momentum tensor that is defined as

$$\mathbf{\Phi}=\rho\mathbf{vv}+p\boldsymbol{\delta}-\boldsymbol{\tau}, \qquad (4.14)$$

where $\boldsymbol{\delta}$ is the Kronecker delta. Then the rate of momentum in and out are written as

$$\begin{aligned}\left\{\begin{matrix}\text{rate of}\\ \text{momentum}\\ \text{in}\end{matrix}\right\}&=2\pi R\Delta x(\Phi_{rx})_R+\pi R^2(\Phi_{xx})_x\\ &=2\pi R\Delta x(\rho v_r v_x-\tau_{rx})_R+\pi R^2(\rho v_x v_x+p-\tau_{xx})_x\end{aligned}. \qquad (4.15)$$

For Newtonian fluid, the shear stress is given by

$$\begin{aligned}\tau_{xx}&=2\mu\frac{\partial v_x}{\partial x}-\frac{2}{3}\mu\left[\frac{1}{r}\frac{\partial(rv_r)}{\partial r}+\frac{\partial v_x}{\partial x}\right]\\ &=\frac{4}{3}\mu\frac{\partial v_x}{\partial x}\end{aligned}. \qquad (4.16)$$

There is no slip at the wall ($(v_x)_R=0$) and Eq. 4.15 becomes

$$\left\{\begin{matrix}\text{rate of}\\ \text{momentum}\\ \text{in}\end{matrix}\right\}=-2\pi R\Delta x(\tau_{rx})_R+\pi R^2\left(\rho v_x v_x+p-\frac{4}{3}\mu\frac{\partial v_x}{\partial x}\right)_x. \qquad (4.17)$$

The rate of momentum out is

$$\begin{Bmatrix}\text{rate of}\\ \text{momentum}\\ \text{out}\end{Bmatrix} = \pi R^2\left(\rho v_x v_x + p - \frac{4}{3}\mu\frac{\partial v_x}{\partial x}\right)_{x+\Delta x}. \tag{4.18}$$

The external force on the fluid is

$$\begin{Bmatrix}\text{external}\\ \text{force on}\\ \text{the fluid}\end{Bmatrix} = -\pi R^2 \Delta x \rho g \sin\theta\,. \tag{4.19}$$

Substituting into Eq. 4.12 and dividing by $\pi R^2 \Delta x$, we obtain

$$\begin{aligned}\frac{\partial(\rho v_x)}{\partial t} = -\frac{2}{R}(\tau_{rx})_R + \frac{1}{\Delta x}\Bigg[&\left(\rho v_x v_x + p - \frac{4}{3}\mu\frac{\partial v_x}{\partial x}\right)_x \\ &-\left(\rho v_x v_x + p - \frac{4}{3}\mu\frac{\partial v_x}{\partial x}\right)_{x+\Delta x}\Bigg] - \rho g\sin\theta\end{aligned}. \tag{4.20}$$

Taking $\Delta x \to 0$, Eq. 4.20 becomes

$$\frac{\partial(\rho v)}{\partial t} = -\frac{2}{R}(\tau_{rx})_R - \frac{\partial}{\partial x}\left(\rho v\cdot v + p - \frac{4}{3}\mu\frac{\partial v_x}{\partial x}\right) - \rho g\sin\theta\,. \tag{4.21}$$

We neglect the second derivative of the velocity and for steady-state, Eq.4.21 can be written as

$$0 = -\frac{2}{R}(\tau_{rx})_R - \frac{d}{dx}\left(\rho v^2 + p\right) - \rho g\sin\theta\,. \tag{4.22}$$

The wall shear stress, τ_{rx}, is given by introducing a fanning friction factor as

$$\tau_{rx} = \frac{\rho f v_x^2}{2}. \tag{4.23}$$

The friction factor for porous pipe was estimated as a function of the friction factor without radial flux and wall Reynolds number by Ouyang (1998). For laminar flow, it is independent of completion type and is given as

$$f = f_o\left(1 + 0.04304\left(N_{\mathrm{Re},w}\right)^{0.6142}\right). \tag{4.24}$$

For turbulence flow, friction factor for openhole completion is given as

$$f = f_o\left(1 - 29.03\left(\frac{N_{\mathrm{Re},w}}{N_{\mathrm{Re}}}\right)^{0.8003}\right), \tag{4.25}$$

and for perforated well, it is

$$f = f_o\left(1 - 0.0153\left(N_{\mathrm{Re},w}\right)^{0.3978}\right). \tag{4.26}$$

where N_{Re} and $N_{\mathrm{Re},w}$ are the Reynolds number and the wall Reynolds number that are given by

$$N_{\mathrm{Re}} = \frac{2R\rho v}{\mu}, \tag{4.27}$$

and

$$N_{\mathrm{Re},w} = \frac{2R\rho_I v_I}{\mu_I}, \tag{4.28}$$

f_o is the friction factor without radial influx and is estimated from the Moody's diagram or from Chen's correlation

$$f_0 = \left[-4\log\left\{\frac{\varepsilon}{3.7065} - \frac{5.0452}{N_{\mathrm{Re}}}\log\left[\frac{\varepsilon^{1.1098}}{2.8257} + \left(\frac{7.149}{N_{\mathrm{Re}}}\right)^{0.8981}\right]\right\}\right]^{-2}. \tag{4.29}$$

where ε is the relative pipe roughness.

Finally, solving for pressure gradient yields

$$\frac{dp}{dx} = -\frac{\rho v^2 f}{R} - \frac{d\left(\rho v^2\right)}{dx} - \rho g \sin\theta. \tag{4.30}$$

4.2.3 Energy balance

Total energy flux is a combination of convective energy flux, rate of work done by molecular mechanisms, and rate of transporting heat by molecular mechanisms, which is written as

$$\mathbf{e} = \left(\frac{1}{2}\rho v^2 + \rho U\right)\mathbf{v} + [\boldsymbol{\pi}\cdot\mathbf{v}] + \mathbf{q}, \tag{4.31}$$

or

$$\mathbf{e} = \left(\frac{1}{2}\rho v^2 + \rho H\right)\mathbf{v} + [\boldsymbol{\tau}\cdot\mathbf{v}] + \mathbf{q}, \tag{4.32}$$

where $\boldsymbol{\pi}$ denotes the total molecular stress tensor which is defined as

$$\boldsymbol{\pi} = p\boldsymbol{\delta} + \boldsymbol{\tau}. \tag{4.33}$$

An energy balance can be written as

$$\left\{\begin{matrix}\text{rate of kinetic}\\ \text{and internal}\\ \text{energy increase}\end{matrix}\right\} = \left\{\begin{matrix}\text{rate of}\\ \text{total energy}\\ \text{in}\end{matrix}\right\} - \left\{\begin{matrix}\text{rate of}\\ \text{total energy}\\ \text{out}\end{matrix}\right\} + \left\{\begin{matrix}\text{rate of work}\\ \text{done on system}\\ \text{by external forces}\end{matrix}\right\} + \left\{\begin{matrix}\text{rate of}\\ \text{energy}\\ \text{production}\end{matrix}\right\}. \tag{4.34}$$

The rate of kinetic and internal energy increase is

$$\left\{\begin{matrix}\text{rate of kinetic}\\ \text{and internal}\\ \text{energy increase}\end{matrix}\right\} = \pi R^2 \Delta x \frac{\partial}{\partial t}\left(\frac{1}{2}\rho v^2 + \rho U\right). \tag{4.35}$$

The rates of total energy in and out are

$$\left\{\begin{matrix}\text{rate of}\\ \text{total energy}\\ \text{in}\end{matrix}\right\} = 2\pi R \Delta x \left(e_r\right)_R + \pi R^2 \left(e_x\right)_x, \tag{4.36}$$

and

$$\left\{\begin{matrix}\text{rate of}\\ \text{total energy}\\ \text{out}\end{matrix}\right\} = \pi R^2 \left(e_x\right)_{x+\Delta x}, \tag{4.37}$$

The rate of work is done by gravity force and is given as

$$\left\{\begin{matrix}\text{rate of work}\\ \text{done on system}\\ \text{by external forces}\end{matrix}\right\} = -\pi R^2 \Delta x \rho v g \sin\theta . \tag{4.38}$$

The energy production in the system is zero. Therefore, Eq. 4.34 becomes

$$\pi R^2 \Delta x \frac{\partial}{\partial t}\left(\frac{1}{2}\rho v^2 + \rho U\right) = 2\pi R \Delta x \left(e_r\right)_R + \pi R^2 \left(e_x\right)_x - \pi R^2 \left(e_x\right)_{x+\Delta x} - \pi R^2 \Delta x \rho v g \sin\theta . \tag{4.39}$$

The total energy in at $r=R$ is obtained from Eq. 4.32 as

$$\begin{aligned}\left(e_r\right)_R &= \left[\left(\frac{1}{2}\rho v^2 + \rho H\right)v_r\right]_R + \left(q_r\right)_R - \left(\tau_{rx} v_x\right)_R - \left(\tau_{rr} v_r\right)_R \\ &= \left(\frac{1}{2}\rho_I {v_I}^2 + \rho_I H_I\right)v_I + q_I + \frac{2}{3}\mu \frac{{v_I}^2}{R}\end{aligned}. \tag{4.40}$$

We can split the energy in into two parts as

$$
\begin{aligned}
2\pi R\Delta x\left(e_r\right)_R = 2\pi R\gamma\Delta x&\left[\left(\frac{1}{2}\rho_I v_I{}^2+\frac{2}{3}\mu\frac{v_I}{R}+\rho_I H_I\right)v_I+q_I\right] \\
&+2\pi R(1-\gamma)\Delta x\left[\left(\frac{1}{2}\rho_I v_I{}^2+\frac{2}{3}\mu\frac{v_I}{R}+\rho_I H_I\right)v_I+q_I\right].
\end{aligned}
\tag{4.41}
$$

The first term on the right side of Eq. 4.41 is the energy in through the pipe material and the second one is through the open area. Since the covered area of the pipe is impermeable, fluid velocity is zero. Also, we neglect the heat conductions between fluids. Therefore, the heat flux in the pipe open area consists of only convection as depicted in **Fig. 4.2**.

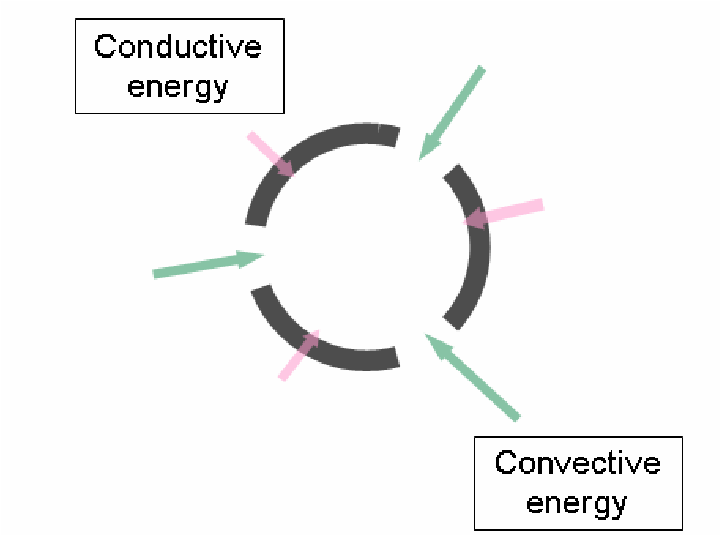

Fig. 4.2 Energy transport through a perforated/slotted pipe.

Therefore, Eq. 4.41 becomes

$$
2\pi R\Delta x\left(e_r\right)_R = 2\pi R\Delta x\gamma\left(\frac{1}{2}\rho_I v_I{}^2+\frac{2}{3}\mu\frac{v_I}{R}+\rho_I H_I\right)v_I+2\pi R\Delta x(1-\gamma)q_I\,. \tag{4.42}
$$

Substituting Eq. 4.42 into Eq. 4.38 and dividing by $\pi R^2\Delta x$ yield

$$
\begin{aligned}
\frac{\partial}{\partial t}\left(\frac{1}{2}\rho v^2+\rho U\right)=\frac{2\gamma}{R}&\left(\frac{1}{2}\rho_I v_I{}^2+\frac{2}{3}\mu\frac{v_I}{R}+\rho_I H_I\right)v_I+\frac{2(1-\gamma)}{R}q_I \\
&+\frac{\left(e_x\right)_x-\left(e_x\right)_{x+\Delta x}}{\Delta x}-\rho v g\sin\theta
\end{aligned}
.\tag{4.43}
$$

Taking $\Delta x\to 0$, Eq. 4.43 becomes

$$\frac{\partial}{\partial t}\left(\frac{1}{2}\rho v^2+\rho U\right)=\frac{2\gamma}{R}\left(\frac{1}{2}\rho_I v_I{}^2+\frac{2}{3}\mu\frac{v_I}{R}+\rho_I H_I\right)v_I+\frac{2(1-\gamma)}{R}q_I \\ -\frac{\partial e_x}{\partial x}-\rho v g\sin\theta \quad . \tag{4.44}$$

Also, the energy flux in the *x*-direction is

$$e_x=\left(\frac{1}{2}\rho v^2+\rho H\right)v_x-\tau_{xx}v_x-\tau_{xr}v_r+q_x\,. \tag{4.45}$$

Since we neglect the heat conduction between fluids, the heat flux in the *x*-direction is dropped ($q_x=0$). Using average velocity for an entire region of the cross section area, the energy flux can be written as

$$e_x=\left(\frac{1}{2}\rho v^2+\rho H\right)v-\frac{4}{3}\mu\frac{\partial v}{\partial x}v\,. \tag{4.46}$$

Substituting Eq. 4.46 into Eq. 4.43, we obtain

$$\frac{\partial}{\partial t}\left(\frac{1}{2}\rho v^2+\rho U\right)=\frac{2\gamma}{R}\left(\frac{1}{2}\rho_I v_I{}^2+\frac{2}{3}\mu\frac{v_I}{R}+\rho_I H_I\right)v_I+\frac{2(1-\gamma)}{R}q_I \\ -\frac{\partial}{\partial x}\left[\left(\frac{1}{2}\rho v^2+\rho H\right)v-\frac{4}{3}\mu\frac{\partial v}{\partial x}v\right]-\rho v g\sin\theta \quad . \tag{4.47}$$

We denote the kinetic energy terms as

$$\frac{2\gamma}{R}\left(\frac{1}{2}\rho_I v_I{}^2\right)v_I-\frac{\partial}{\partial x}\left[\left(\frac{1}{2}\rho v^2\right)v\right]=E_{KE}\,, \tag{4.48}$$

and the viscous shear terms as

$$\frac{4}{3}\frac{\gamma}{R}\left(\mu\frac{v_I}{R}\right)v_I+\frac{4}{3}\frac{\partial}{\partial x}\left(\mu\frac{\partial v}{\partial x}v\right)=E_{VS}\,. \tag{4.49}$$

For steady-state, Eq. 4.47 becomes

$$0=\frac{2\gamma}{R}\rho_I v_I H_I+\frac{2(1-\gamma)}{R}q_I-\frac{\partial(\rho H v)}{\partial x}+E_{KE}+E_{VS}-\rho v g\sin\theta\,. \tag{4.50}$$

Expanding the third term on the right side of Eq. 4.50, we have

$$\frac{d(\rho H v)}{dx}=\rho v\frac{dH}{dx}+H\frac{d(\rho v)}{dx}\,. \tag{4.51}$$

From mass balance (Eq.4.11), we obtain

$$\frac{d(\rho H v)}{dx}=\rho v\frac{dH}{dx}+H\frac{2}{R}\gamma\rho_I v_I\,. \tag{4.52}$$

Substituting Eq. 4.52 into Eq. 4.50 gives

$$0=\frac{2\gamma}{R}\rho_I v_I\left(H_I-H\right)+\frac{2(1-\gamma)}{R}q_I-\rho v\frac{dH}{dx}+E_{KE}+E_{VS}-\rho vg\sin\theta\,. \tag{4.53}$$

Let the pressure at the boundary, p_I, be the same as the pressure of wellbore p. Then, the enthalpy difference term between inflow and wellbore becomes

$$\begin{aligned}H_I-H&=C_p\left(T_I-T\right)+\frac{1}{\rho}\left(1-\beta T_I\right)\left(p_I-p\right)\\&=C_p\left(T_I-T\right)\end{aligned}\,. \tag{4.54}$$

From Eq. 4.54 and the relationship between enthalpy and pressure and temperature (Eq. 3.16), we obtain

$$\begin{aligned}0=\frac{2\gamma}{R}\rho_I v_I C_p\left(T_I-T\right)+\frac{2(1-\gamma)}{R}q_I-\rho vC_p\frac{dT}{dx}\\-v\left(1-\beta T\right)\frac{dp}{dx}+E_{KE}+E_{VS}-\rho vg\sin\theta\end{aligned}\,. \tag{4.55}$$

Solving for temperature gradient, we have

$$\frac{dT}{dx}=\frac{2\gamma}{R\rho v}\rho_I v_I\left(T_I-T\right)+\frac{2(1-\gamma)}{R\rho vC_p}q_I-\frac{1-\beta T}{\rho C_p}\frac{dp}{dx}+\frac{1}{\rho vC_p}\left(E_{KE}+E_{VS}\right)-\frac{g\sin\theta}{C_p}\,. \tag{4.56}$$

Joule – Thomson coefficient is defined as

$$K_{JT}=\frac{\beta T-1}{\rho C_P}\,. \tag{4.57}$$

The heat flux can be estimated in terms of the temperature difference by solving the heat conduction equation in steady-state, which is given as

$$q_I=\alpha\left(T_I-T\right). \tag{4.58}$$

Substituting Eqs. 4.57 and 4.58 into Eq. 4.55 yields

$$\frac{dT}{dx}=K_{JT}\frac{dp}{dx}+\frac{2}{R\rho v}\left(\gamma\rho_I v_I+\frac{1-\gamma}{C_P}\alpha\right)\left(T_I-T\right)+\frac{1}{\rho vC_p}\left(E_{KE}+E_{VS}\right)-\frac{g\sin\theta}{C_P}\,. \tag{4.59}$$

4.2.4 Studies from a single-phase model

In the above derivations, we made as few assumptions as possible. Before extending the temperature equation to multi-phase flow, we have performed sensitivity studies to determine the impact of each term in Eq. 4.59 on the wellbore temperature profile by numerically solving the equation under various conditions. From these evaluations, we have determined that the kinetic energy, E_{KE}, and viscous shear, E_{VS}, are less important to the temperature profile. Example temperature profiles are shown below. The procedure of the numerical solution is addressed explicitly in next chapter.

Fig. 4.3 shows example temperature profiles obtained from the original temperature equation, Eq. 4.59 and the one without the kinetic energy term. This example was generated with the wellbore that has an inner diameter of 4.6 in and is producing about 6,000 b/d oil. **Fig. 4.4** shows a comparison of the temperature profiles with and without the viscous shear terms.

From these examinations, we can conclude that neither kinetic energy nor viscous shear affect the computed temperature very much. We neglect kinetic energy and viscous shear terms in further discussions. Dropping these terms, the energy balance equation becomes

$$\frac{dT}{dx} = K_{JT}\frac{dp}{dx} + \frac{2}{R\rho v}\left(\gamma\rho_I v_I + \frac{1-\gamma}{C_P}\alpha\right)(T_I - T) - \frac{g\sin\theta}{C_P}, \quad \text{..........................} \quad (4.60)$$

or

$$\frac{dT}{dx} = K_{JT}\frac{dp}{dx} + \frac{2}{R\rho v C_P}\alpha_I (T_I - T) - \frac{g\sin\theta}{C_P}, \quad \text{..} \quad (4.61)$$

where

$$\alpha_I = \gamma\rho_I v_I C_P + (1-\gamma)\alpha \,. \quad \text{..} \quad (4.62)$$

We call α_I a combined overall heat transfer coefficient in this research. It combines both conductive and convective heat transfer for porous wall pipe that has an additional convective term added to the conventional overall conductive heat transfer.

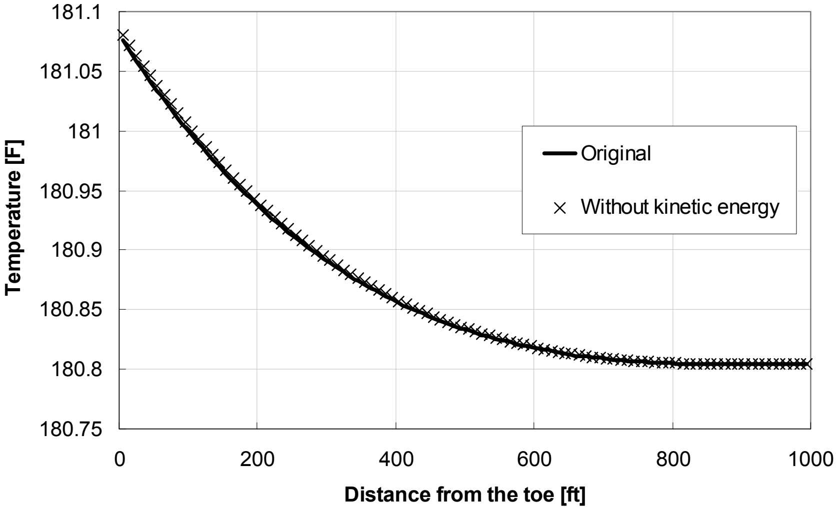

Fig. 4.3 Temperature profiles with and without kinetic energy.

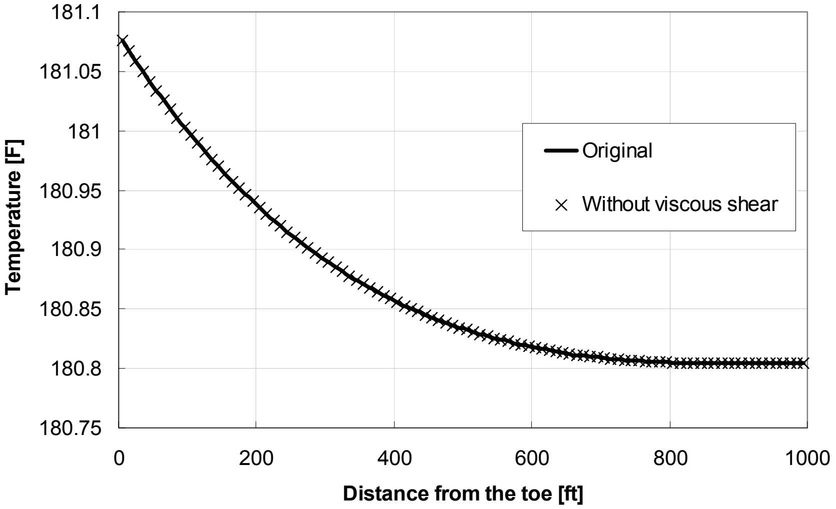

Fig. 4.4 Temperature profiles with and without viscous shear.

4.3 WORKING EQUATIONS FOR MULTI-PHASE FLOW

Using a similar shell balance method to the single-phase flow derivations, the mass and energy balance equations for multi-phase flow can be developed. The main difference from the single-phase flow is that the conserved properties are weighted by their volume fraction (holdup) in the system. As for the momentum balance of multi-phase flow, it needs a special treatment and a number of models have been developed for wellbore pressure and holdup calculations (Hasan and Kabir, 1998; Flores *et al.*, 1998; Taitel and Dukler, 1976). We apply a homogeneous model for oil-water flow and a homogeneous with drift-flux model for gas-liquid flow (Ouyang and Aziz, 2000).

4.3.1 Mass and energy balance

The mass balance for phase i (= oil, water, or gas) is given as

$$\frac{d\left(\rho_i v_i y_i\right)}{dx} = \frac{2\gamma y_{i,I}}{R}\rho_i v_{i,I}\,. \tag{4.63}$$

where y_i is a volume fraction of phase i.

Neglecting kinetic energy and viscous shear terms, the energy balance for phase i is

$$\rho_i v_i y_i C_{p,i} \frac{dT_i}{dx} = \rho_i v_i y_i C_{p,i} K_{JT,i} \frac{dp_i}{dx} + \frac{2}{R} \gamma \rho_{i,I} v_{i,I} y_{i,I} C_{p,i} \left(T_{i,I} - T_i \right) + \frac{2}{R} q_{i,I} (1-\gamma) - \rho_i y_i v_i g \sin\theta . \tag{4.64}$$

Summation of the equation for the three phases gives

$$\sum_i \rho_i v_i y_i C_{p,i} \frac{dT_i}{dx} = \sum_i \rho_i v_i y_i C_{p,i} K_{JT,i} \frac{dp_i}{dx} + \frac{2}{R} \gamma \sum_i \rho_{i,I} v_{i,I} y_{i,I} C_{p,i} \left(T_{i,I} - T_i \right) + \frac{2}{R} (1-\gamma) \sum_i q_{i,I} - \sum_i \rho_i y_i v_i g \sin\theta . \tag{4.65}$$

Assuming that the pressures and temperatures are the same in each phase, we have

$$\frac{dT}{dx} \sum_i \rho_i v_i y_i C_{p,i} = \frac{dp}{dx} \sum_i \rho_i v_i y_i C_{p,i} K_{JT,i} + \frac{2}{R} \gamma (T_I - T) \sum_i \rho_{i,I} v_{i,I} y_{i,I} C_{p,i} + \frac{2(1-\gamma)}{R} \alpha_T (T_I - T) - \sum_i \rho_i y_i v_i g \sin\theta . \tag{4.66}$$

where α_T is an overall heat transfer coefficient for multi-phase flow. The details are discussed in Appendix B. Solving for temperature gradient, we obtain

$$\frac{dT}{dx} = \frac{dp}{dx} \frac{\sum_i \rho_i v_i y_i C_{p,i} K_{JT,i}}{\sum_i \rho_i v_i y_i C_{p,i}} + \frac{2}{R} (T_I - T) \left[\frac{\gamma \sum_i \rho_{i,I} v_{i,I} y_{i,I} C_{p,i} + (1-\gamma) \alpha_T}{\sum_i \rho_i v_i y_i C_{p,i}} \right] - \frac{\sum_i \rho_i v_i y_i}{\sum_i \rho_i v_i y_i C_{p,i}} g \sin\theta . \tag{4.67}$$

Total (mixing) properties can be factorized as

$$(\rho v)_T = \sum_i \rho_i v_i y_i \ , \tag{4.68}$$

$$\left(\rho v C_p \right)_T = \sum_i \rho_i v_i y_i C_{p,i} \ , \tag{4.69}$$

and

$$\left(\rho v C_p K_{JT} \right)_T = \sum_i \rho_i v_i y_i C_{p,i} K_{JT,i} \ . \tag{4.70}$$

Finally, we have

$$\frac{dT}{dx} = \frac{\left(\rho v C_p K_{JT} \right)_T}{\left(\rho v C_p \right)_T} \frac{dp}{dx} + \frac{2}{R} \left[\frac{\gamma \left(\rho v C_p \right)_{T,I} + (1-\gamma) \alpha_T}{\left(\rho v C_p \right)_T} \right] (T_I - T) - \frac{(\rho v)_T}{\left(\rho v C_p \right)_T} g \sin\theta , \tag{4.71}$$

or

$$\frac{dT}{dx} = \frac{(\rho v C_p K_{JT})_T}{(\rho v C_p)_T}\frac{dp}{dx} + \frac{2}{R}\frac{\alpha_{T,I}}{(\rho v C_p)_T}(T_I - T) - \frac{(\rho v)_T}{(\rho v C_p)_T} g \sin\theta , \tag{4.72}$$

where

$$\alpha_{T,I} = \gamma(\rho v C_p)_{T,I} + (1-\gamma)\alpha_T . \tag{4.73}$$

4.3.2 Momentum balance

When estimating the pressure profile and holdup along the well, we can apply a homogeneous, a drift flux, or a mechanistic model to the problem. The simplest model is a homogeneous model which regards flow as homogenized single-phase flow. A mechanistic model is the most realistic and complicated model. However, it sometimes encounters problems in convergence between flow regime transitions. A drift flux model relaxes the assumptions of homogeneous model and considers a slip velocity between phases. Because of the ease and continuities in the parameters of drift flux model, it has been widely accepted in a variety of petroleum engineering applications.

Oil-water two-phase flow

For oil-water two-phase flow, a homogeneous model is applied and the momentum balance equation is given with mixture properties as

$$\frac{dp}{dx} = -\frac{\rho_m v_m^{\ 2} f_m}{R} - \frac{d(\rho_m v_m^{\ 2})}{dx} - \rho_m g \sin\theta , \tag{4.74}$$

Where the mixture density, ρ_m is given by

$$\begin{aligned} \rho_m &= \frac{M_o + M_w}{V_T} \\ &= \frac{M_o}{V_o}\frac{V_o}{V_T} + \frac{M_w}{V_w}\frac{V_w}{V_T} . \\ &= \rho_o y_o + \rho_w y_w \end{aligned} \tag{4.75}$$

Since no slip velocity between phases is considered, the holdup is

$$y_w = \frac{v_{sw}}{v_{sw} + v_{so}} . \tag{4.76}$$

where v_{sw} and v_{so} represent superficial velocities of water and oil. Mass flux can be written as

$$\rho_m v_{TP} = \rho_o v_{so} + \rho_w v_{sw} . \tag{4.77}$$

Therefore, the two-phase velocity is

$$v_{TP} = \frac{\rho_o}{\rho_m} v_{so} + \frac{\rho_w}{\rho_m} v_{sw}\,. \tag{4.78}$$

The oil-water mixture viscosity is estimated by the model that takes into account the phase inversion point (Jayawardena *et al.*, 2001). It is given by

$$\mu_m = \mu_c \left(1 - y_d\right)^{-2.5}. \tag{4.79}$$

The inversion point is

$$y_{inv} = \left[1 + \left(\frac{\mu_c}{\mu_d}\right)^{1/6} \left(\frac{\rho_c}{\rho_d}\right)^{5/6}\right]^{-1}. \tag{4.80}$$

where the subscript c means continuous phase and d means dispersed phase. The dimensionless numbers to be used for friction factor estimation will be calculated based on the mixture properties as

$$N_{\mathrm{Re}} = \frac{\rho_m v_{TP} D}{\mu_m}, \tag{4.81}$$

and

$$N_{\mathrm{Re},w} = \frac{\rho_{m,I} v_{TP,I} D}{\mu_{m,I}}. \tag{4.82}$$

Liquid-gas two-phase flow

When the flow is liquid-gas multi-phase flow, the homogenized pressure gradient model by Ouyang and Aziz (2000) is used. It consists of frictional, gravitational, and accelerational pressure drops and is given as

$$\frac{dp}{dx} = \frac{1}{1 - \left(\rho_l v_{sl} + \rho_g v_{sg}\right)\frac{v_{sg}}{p}} \left[-\frac{f \rho_m v_{TP}{}^2}{R} - \rho_m g \sin\theta + \left(\frac{dp}{dx}\right)_{aW}\right], \tag{4.83}$$

where v_{sl} and v_{sg} are superficial velocities of liquid and gas respectively. $\left(\frac{dp}{dx}\right)_{aW}$ is an accelerational pressure drop caused by wall friction and is given as

$$\left(\frac{dp}{dx}\right)_{aW} = \varpi \left(\frac{dp}{dx}\right)_{aW1} + \left(1 - \varpi\right)\left(\frac{dp}{dx}\right)_{aW2}, \tag{4.84}$$

where

$$\left(\frac{dp}{dx}\right)_{aW1} = -\frac{1}{\pi R^2}\left[\left(v_{sl} + v_{sg}\right)\left(\rho_l w_{l,I} + \rho_g w_{g,I}\right) + \left(\rho_l v_l + \rho_g v_g\right)\left(w_{l,I} + w_{g,I}\right)\right], \tag{4.85}$$

and

$$\left(\frac{dp}{dx}\right)_{aW2} = -\frac{2}{\rho_m \pi R^2}\left(\rho_l v_{sl} + \rho_g v_{sg}\right)\left(\rho_l w_{l,I} + \rho_g w_{g,I}\right), \tag{4.86}$$

where w is the mass flow rate. Subscription l and g denote liquid and gas respectively. The value for ϖ is proposed as 0.8.

The mixture properties are given by

$$\rho_m = \rho_l y_l + \rho_g y_g\ , \tag{4.87}$$

$$\mu_m = \mu_l y_l + \mu_g y_g\ , \tag{4.88}$$

and

$$v_{TP} = \frac{\rho_l}{\rho_m} v_{sl} + \frac{\rho_g}{\rho_m} v_{sg}\ . \tag{4.89}$$

The in-situ velocity of gas is estimated from drift-flux model as

$$v_g = C_0 (v_{sl} + v_{sg}) + v_d\ , \tag{4.90}$$

where v_d is the drift velocity and C_0 is the profile parameter. They are determined experimentally (Franca and Lahey, 1992; Shi *et al.*, 2005).

CHAPTER 5

COUPLED MODEL

5.1 INTRODUCTION TO COUPLED MODEL.

In the last two chapters, we have derived the wellbore and reservoir equations. Our objective in this chapter is to develop a pressure and temperature prediction model that provides the flow rate, the pressure, and the temperature profiles along the horizontal or near horizontal wellbore. The three unknowns have to be determined from the mass, the momentum, and the energy balance equations of the wellbore along with the reservoir equations.

As Eq. 4.11 indicates, inflow rate profile is obtained from wellbore pressure profile. Simultaneously, estimating wellbore pressure profile requires flow rate profile. Similarly, the wellbore temperature is estimated from the wellbore pressure and the reservoir temperature which is a function of the inflow rate and the wellbore temperature. Since the working equations of the wellbore and the reservoir are highly dependent each other, they must be solved iteratively at the same time.

We consider a horizontal well fully penetrated through a box-shaped homogeneous reservoir as described in **Fig. 3.1** and divide the reservoir into a number of segments (**Fig. 5.1**). With no-flow lateral boundaries, flow in the reservoir is only in the *y* and *z* directions; flow in the horizontal wellbore is in the *x*-direction. The assumptions for this coupled model are the followings:

1) Steady-state flow: For continuous well flow, changes in the well rate are much slower than the response time of any sensor. We use the steady-state equations derived in Chapter 3 for the reservoir and Chapter 4 for the wellbore.

2) Isolated reservoir segments: Each segment of the reservoir is idealized to be isolated from each other. There is no flow in the *x*-direction within the reservoir.

3) Single-phase reservoir flow: Each reservoir segment produces a single-phase fluid. Multi-phase flow occurs only in the wellbore as a result of the combination of single-phase flows of different phases from the reservoir segments.

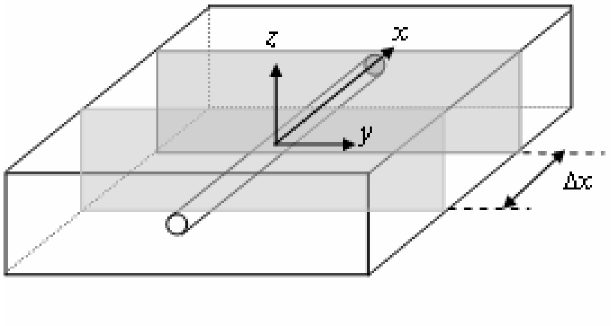

Fig. 5.1 Geometry of the forward model.

5.2 SOLUTION PROCEDURE

These highly non-linear equations are solved numerically. We first discretize the equations with a finite difference scheme and solve the matrices for each equation as many times as necessary until the variables meet the convergence by the successive substitution.

The mass balance equation (Eq. 4.63) can be discretized as

$$\left(v_i\right)_j + \left(A_i\right)_j \left(v_i\right)_{j-1} = \left(B_i\right)_j , \tag{5.1}$$

where i denotes phase and j denotes position index. $\left(A_i\right)_j$ and $\left(B_i\right)_j$ are given respectively as

$$\left(A_i\right)_j = -\frac{\left(\rho_i y_i\right)_{j-1}}{\left(\rho_i y_i\right)_j} , \tag{5.2}$$

and

$$\left(B_i\right)_j = \frac{\left(\rho_{i,I}\right)_j}{\left(\rho_i y_i\right)_j} \frac{\left(J_i\right)_j \left(p_R - p_j\right)}{\pi R^2} , \tag{5.3}$$

In matrix form, the equations are given by

$$\mathbf{A}\left(p,T\right) \cdot \mathbf{V} = \mathbf{B}\left(p,T\right). \tag{5.4}$$

Since fluid properties are also pressure and temperature dependent, both coefficients are a function of pressure and temperature.

If the flow is oil-water two-phase, we can discretize the momentum equation (Eq. 4.74) as

$$p_j - p_{j-1} = D_j , \tag{5.5}$$

where

$$D_j = \Delta x \left[-\frac{\left(\rho_m\right)_j \left(v_m\right)_j^2 f_j}{R} - \left(\rho_m\right)_j g \sin\theta_j \right] - \left[\left(\rho_m v_m\right)_i^2 - \left(\rho_m v_m\right)_{i-1}^2 \right]. \tag{5.6}$$

In matrix form the equation becomes

$$\mathbf{C} \cdot \mathbf{P} = \mathbf{D}\left(v,T\right). \tag{5.7}$$

In discretized form, the temperature equation (Eq. 2.72) can be written as

$$E_j T_j - T_{j-1} = F_j , \tag{5.8}$$

where

$$E_j = 1 + \frac{2\Delta x}{R} \left[\frac{\alpha_{T,I}}{\left(\rho v C_p\right)_T} \right]_j , \tag{5.9}$$

and

$$F_j = \Delta x\left(\left[\frac{(\rho v C_p K_{JT})_T}{(\rho v C_p)_T}\right]_j \left(\frac{dp}{dx}\right)_j + \frac{2}{R}\left[\frac{\alpha_{T,I}}{(\rho v C_p)_T}\right]_j (T_I)_j - \left[\frac{(\rho v)_T}{(\rho v C_p)_T}\right]_j g\sin\theta_j\right). \tag{5.10}$$

Then we have

$$\mathbf{E}(v,p)\cdot\mathbf{T} = \mathbf{F}(v,p,T_I). \tag{5.11}$$

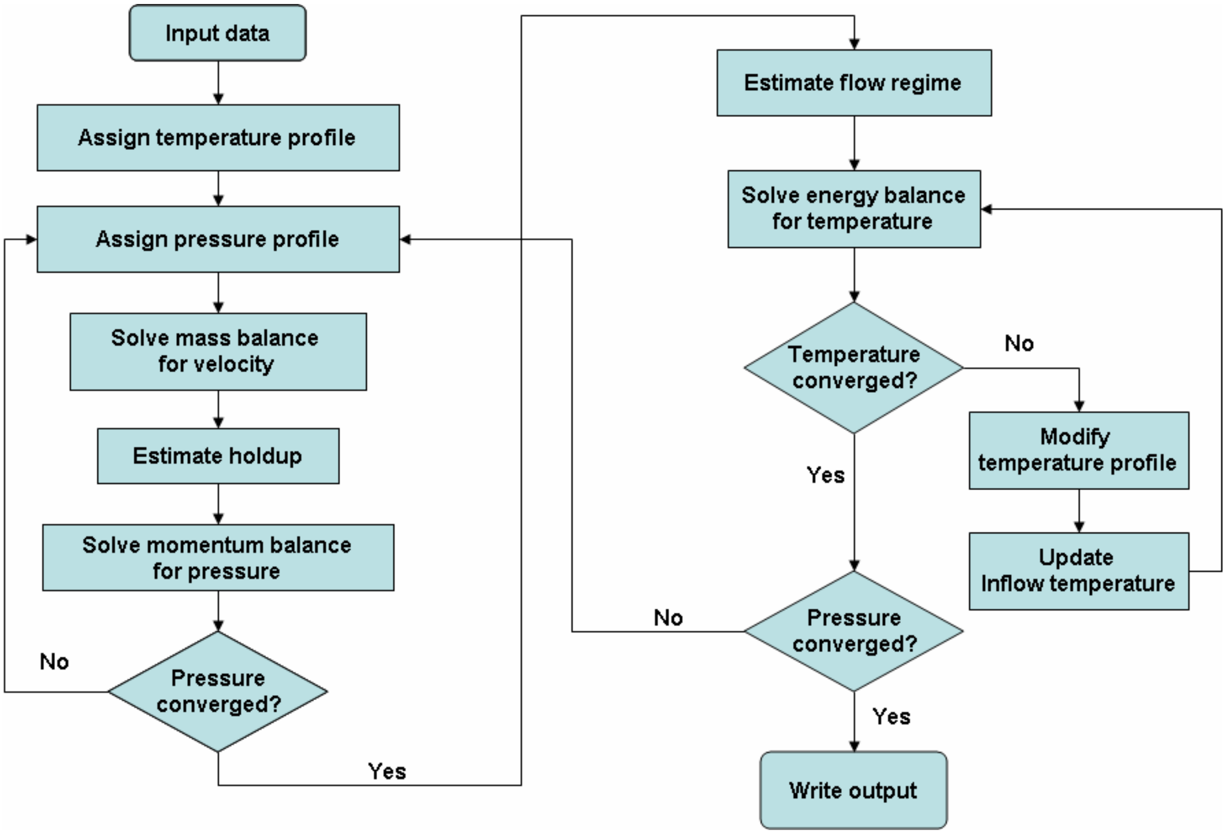

Fig. 5.2 Schematic of the solution procedure.

The solution can be found iteratively. For instance, when velocity and pressure profiles are known as ($\mathbf{v}^n, \mathbf{p}^n$), then the temperature profile can be obtained as follows:
Solve

$$\mathbf{E}(\mathbf{v}^n, \mathbf{p}^n, \mathbf{T}^l)\cdot\mathbf{T} = \mathbf{F}(\mathbf{v}^n, \mathbf{p}^n, \mathbf{T}^l), \tag{5.12}$$

for $\mathbf{T}$. Then $\mathbf{T}$ will be updated as

$$\mathbf{T}^{l+1} = \kappa(\mathbf{T} - \mathbf{T}^l) + \mathbf{T}^l, \tag{5.13}$$

where superscript *n* means the known variable and *l* means the current status of the unknown variable, and κ is a relaxation factor that takes value between 0 and 1. This process will be repeated until we have

$$\frac{(\mathbf{T}^l - \mathbf{T})^T (\mathbf{T}^l - \mathbf{T})}{(\mathbf{T}^l)^T (\mathbf{T}^l)} < \varepsilon_{tol}{}^2, \tag{5.14}$$

where ε_{tol} is a pre-assigned tolerance. A schematic of the solution procedure is shown in **Fig. 5.2**.

5.3 RESULTS AND DISCUSSIONS

With the recent fiber optic technology, a temperature can be measured with a resolution on the order of 0.0045 ^{o}F at some spatial and temporal resolutions (Sensornet Limited, 2007). The changes in the horizontal wellbore are normally very limited. Hypothetically, we set up the measurable temperature resolution as 0.01 ^{o}F. However, if the estimated total temperature change of the wellbore is on the order of 0.01 ^{o}F, it may not benefit us to install the equipment and measure the profile. Therefore, it is important to infer the possible temperature changes under various synthetic production cases.

Other than the quantity of temperature change, we can also learn from the quality of temperature changes by taking a spatial derivative of temperature (Hill, 1990). When the different types of fluid are produced or well trajectory is changed at some position of the horizontal well, the slope of the temperature profile show some anomalies (Yoshioka *et al.*, 2006; Yoshioka, 2007).

We consider two kinds of wells: one with a small diameter and the other large, and both are completed as cased and perforated wells. The details of the well properties are shown in **Table 5.1**. Oil, gas and water are the produced fluids. The reservoir and fluid properties are listed in **Table 5.2**. The physical fluid properties are estimated based on pressure and temperature along the wellbore, and **Table 5.2**, using accepted correlations (McCain, 1990).

Table 5.1 Well properties.

	Small	***Large***
ID [in]	**2.602**	**4**
OD [in]	**3.5**	**4.5**
Diameter with cement [in]	**5**	**6**
K_{casing} [Btu/hr ft ^{o}F]	**6.933**	
K_{cement} [Btu/hr ft ^{o}F]	**4.021**	
Relative roughness	**0.01**	
Total Length [ft]	**2000**	
Pipe opened ratio [%]	**2**	

Table 5.2 Reservoir and fluid properties.

Reservoir length [ft]		2000	
Reservoir width [ft]		3150	
Reservoir height [ft]		55	
Pressure drawdown [psi]		300	
T at outer boundary [^{o}F]		180	
Specific gravity of gas		0.75	
Salinity of water [%]		5	
Oil API		45.176	
Disolved GOR [SCF/STB]		800	
Surface tenstion [dyne/cm]		10	
	Oil	*Water*	*Gas*
K_{Tt} [Btu/hr ft °F]	2	2.5	1.3
K [Btu/hr ft ^{o}F]	0.0797	0.3886	0.0116

5.3.1 Possible temperature changes

To evaluate the possible temperature changes along the horizontal wellbore in a single-phase production system, we studied two extreme cases: small and large production scenarios with small or large well diameter. These examples should bracket the possible temperature changes in actual single-phase producers.

Fig. 5.3 displays the pressure change from the toe pressure for flow through a well with small diameter. With a total flow rate of about 5,000 b/d, the total pressure drop in the 2,000 ft long well is about 30 psi; at a very high rate of about 20,000 b/d, the wellbore pressure drop is over 300 psi. The corresponding temperature change profiles, the temperature at any location along the well minus the temperature at the toe, are shown in **Fig. 5.4**. For the small flow rate case, the temperature changes less than 0.2 ^{o}F throughout the well while the temperature changes 1.4 ^{o}F for the large flow rate case. Since the pressure drop for this case, a high flow rate in a small diameter well, is quite large, this order of change would be the largest temperature change caused by wellbore flow effects that can be expected in a horizontal single-phase oil production well.

Table 5.3 summarizes results from several other cases. The profiles for each are similar to those shown in **Figs. 5.3** and **5.4**. In these calculations, the temperature changes for low production rates with the larger diameter wellbore for both oil (maximum change of 0.02 ^{o}F) and gas production (0.01 ^{o}F) cases were small. However, if the production rate is large, the temperature change would be measurable. Even though the pressure change along a well producing gas is small, the temperature change of gas is more sensitive to the production rate.

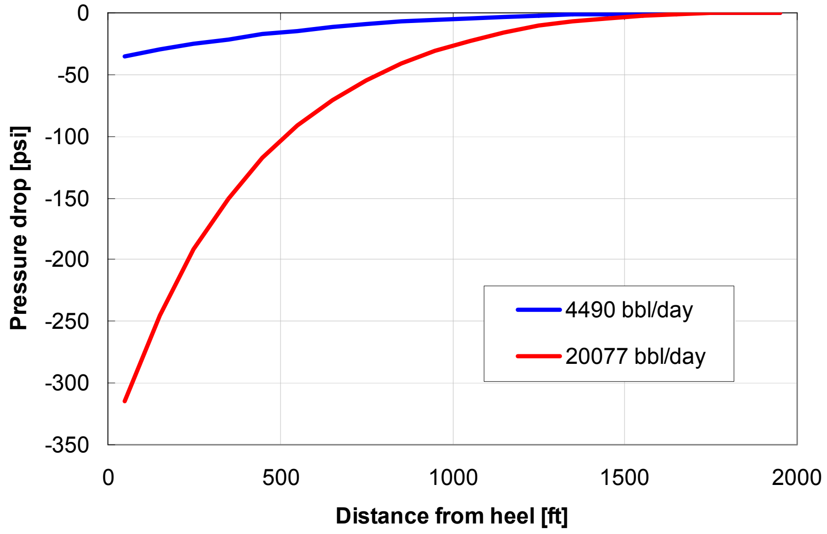

Fig. 5.3 Pressure deviation profiles (oil production with small well diameter).

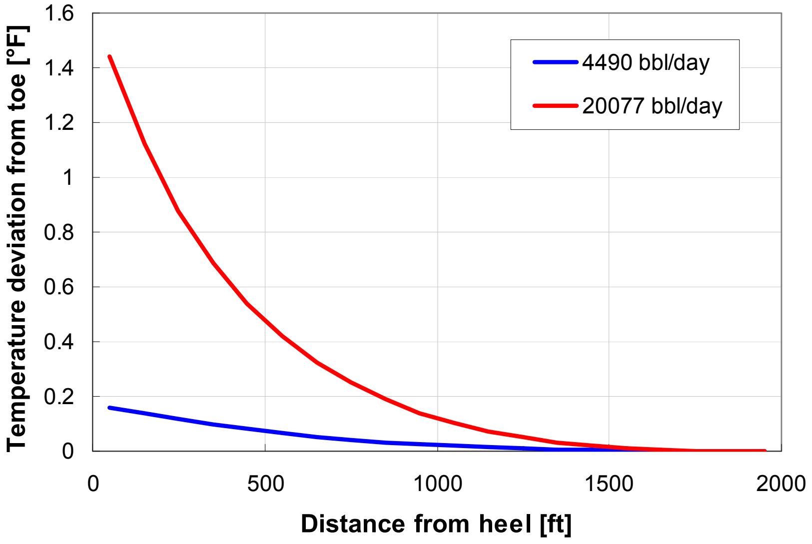

Fig. 5.4 Temperature deviation profiles (oil production with small well diameter).

Table 5.3 Summary of possible temperature changes.

Fluid	Rate	Diameter	ΔP_{Total}, psi	ΔT_{Total}, ^oF
oil	Low (4990 bbl/day)	*Small*	35.2	0.16
oil	High (20077 bbl/day)	*Large*	314.9	1.44
oil	Low (5064 bbl/day)	*Small*	4.4	0.02
oil	High (20053 bbl/day)	*Large*	63.4	0.29
gas	Low (5046 MSCF/day)	*Small*	6	0.08
gas	High (20039 MSCF/day)	*Large*	63.9	0.79
gas	Low (5097 MSCF/day)	*Small*	0.73	0.01
gas	High (20039 MSCF/day)	*Large*	10.5	0.13

5.3.2 Pressure and temperature profiles with well inclination

Horizontal wells are rarely perfectly horizontal, with the inclination angle varying along the trajectory. Deviations of the well trajectory may alter the temperature and pressure profiles along the wellbore from that of a perfectly horizontal wellbore.

The geothermal temperature of the formation monotonically increases with depth so that in upward flow, the wellbore fluids will encounter cooler formation temperatures as they move up the wellbore, and will encounter warmer surroundings with a downward trajectory. For this example, the geothermal gradient is taken to be 0.01 ^oF/ft. Inclinations of 2^o and -2^o from horizontal were examined. These results were compared with the horizontal small-diameter case that has uniform inflow (5b/day/ft for oil and 25 MCF/day/ft for gas).

Fig. 5.5 shows the comparisons of pressure changes from the toe pressure (wellbore Δp) for upward and downward trajectories. For oil flow, the pressure loss will be larger in upward flow compared to horizontal flow and less in downward flow as depicted in **Fig. 5.5** because of the decreasing hydrostatic pressure drop. **Fig. 5.6** plots the temperature deviations from the toe temperature. In downward flow, the wellbore encounters warmer formation temperature and, as expected, temperature deviation of downward flow is more than the horizontal case. Upward flow temperature behavior is more profound. The fluid temperature decreases first because of a cooler environment, and then increases because of Joule-Thomson warming. Although this results in the minimum temperature deviation among cases, its shape is remarkable since temperature should not decrease in a perfectly horizontal wellbore producing liquid. This downward concave shape could be an identification of the upward trajectory of the well and illustrates that an accurate measurement of well trajectory is needed to interpret temperature and pressure profiles in nominally horizontal wells.

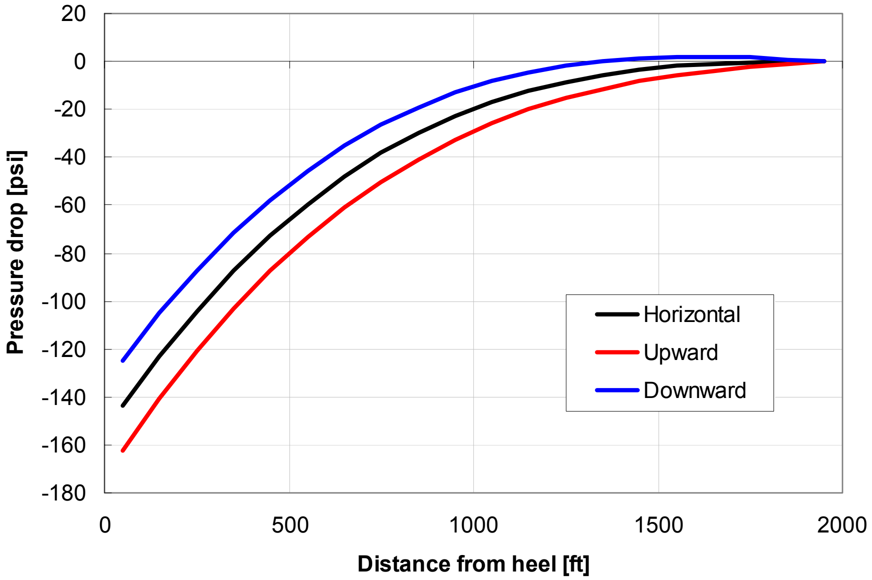

Fig. 5.5 Wellbore pressure changes (single-phase oil).

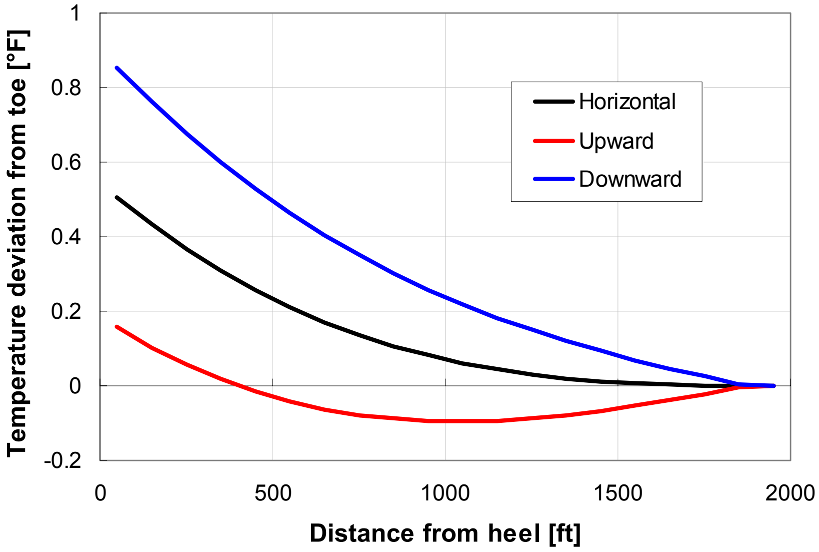

Fig. 5.6 Wellbore temperature changes (single-phase oil).

Next, we present the gas production cases. Comparisons with the horizontal case are displayed in **Figs. 5.7** and **5.8**. Similarly, the pressure drop is smaller in downward flow and larger in upward flow. And, the temperature deviation profiles show distinct differences for the two inclinations. Because of Joule-Thomson cooling, the usual temperature profile shows a monotonically decreasing curve in gas production. But in downward flow, the wellbore is exposed to the warmer surrounding and ends up with a higher temperature at the heel than at the toe. This does not usually occur in a flowing horizontal gas well.

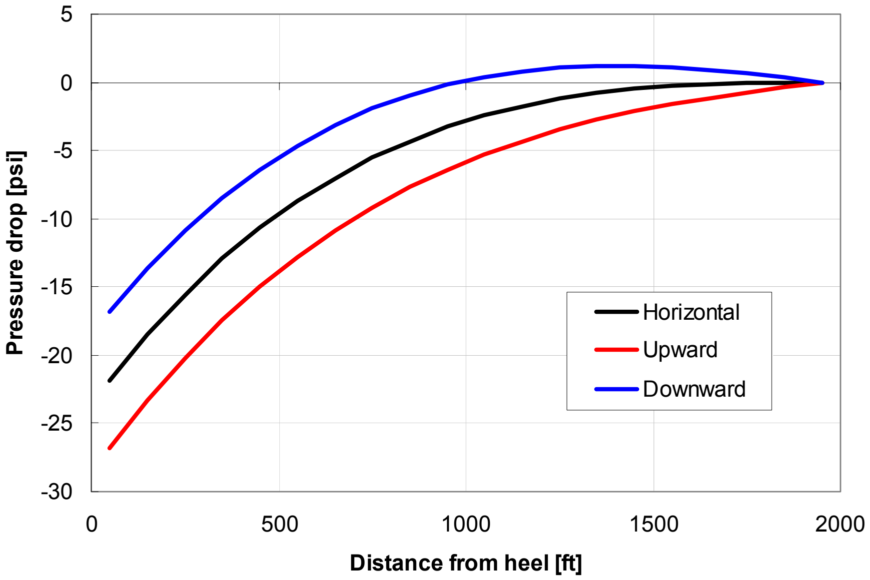

Fig. 5.7 Wellbore pressure changes (single-phase gas).

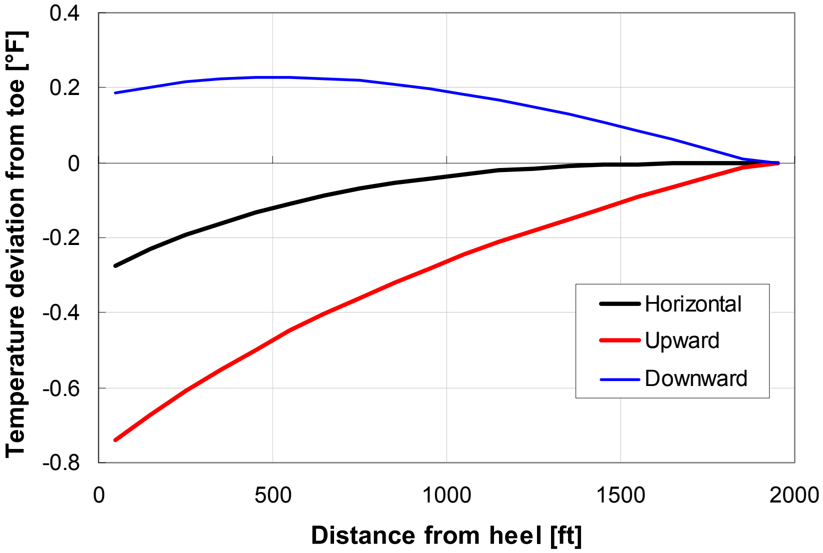

Fig. 5.8 Wellbore temperature changes (single-phase gas).

5.3.3 Water entry effects

When water is produced from the same elevation as the oil zone, the water producing zone can be actually cooler than oil-producing zones because of the difference in Joule-Thomson coefficients as shown in **Fig. 3.5**. We have observed in Chapter 3, that oil, gas, and water would have different inflow temperatures and difference in inflow temperature is dominated mostly by Joule-Thomson effects in the formation and the reservoir boundary temperature. A case for which the boundary temperatures are different is when water entry is caused by water coning. Since water is produced from the deeper zone, water entry tends to cause warming of the wellbore (Dawkrajai et al., 2006). In this study, we consider the boundary temperatures are the same for all the fluid types. Therefore, the Joule-Thomson effect of the reservoir, which is a product of pressure drawdown and the Joule-Thomson coefficient, is the dominant term.

Fig. 5.9 shows an example of temperature profiles for water entry near the middle with different water cut values and **Fig. 5.10** shows the corresponding pressure curve. In this example water is entering the wellbore from 1,200 to 1,400 ft from the heel of the well. This water entry is identified by the cool anomaly along the well. Beginning from the toe of the well, the water producing zone is clearly indicated by the cool temperature anomaly, with the beginning of the water zone corresponding to the sudden drop in temperature and the end of the water zone marked by the increase in temperature. For the higher water cut, this difference is more pronounced. While temperature profiles indicate where the water entry starts and ends, the pressure profiles (**Fig. 5.10**) do not clearly show the location of the water entry. We can see that the overall pressure drop of the higher water cut case is higher. Since the density of water is higher than that of oil, the mixture density of the flowing fluid in the wellbore for the higher water cut case is higher. Therefore, the frictional pressure, which is proportional to the density, ends up with being larger for the higher water cut case. The slope of the pressure curve with a water cut of 0.3 was changed where the water entry began. However, the pressure profiles did not exhibit distinct anomalies.

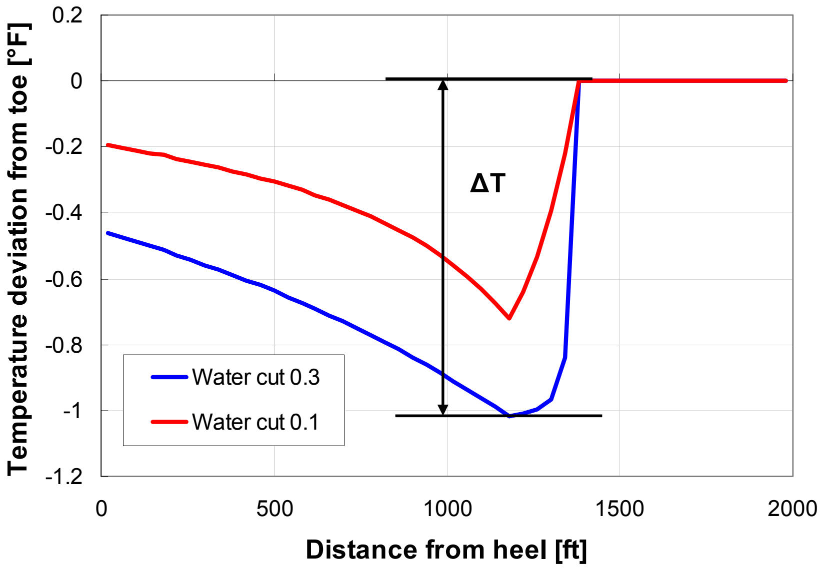

Fig. 5.9 Temperature deviation profiles for different water cuts.

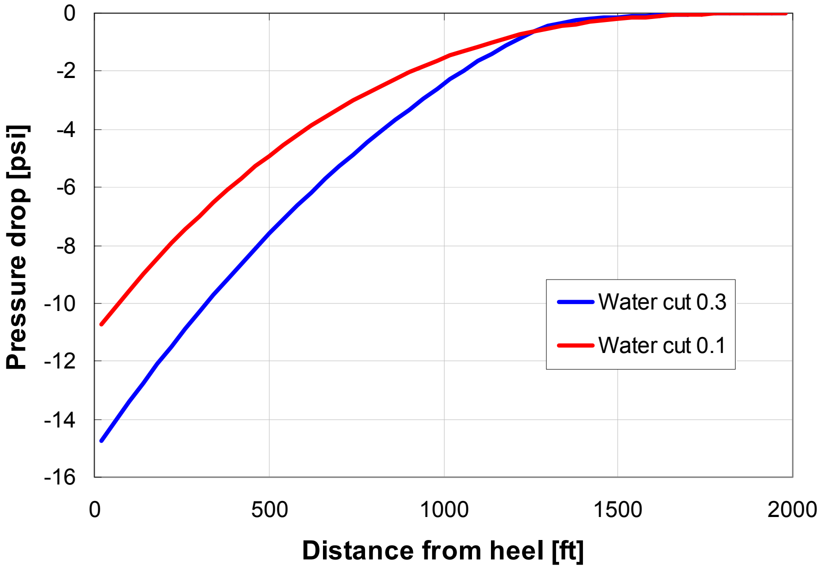

Fig. 5.10 Pressure drop profiles for different water cuts.

The temperature drops observed on the profiles also vary with the water entry locations. **Fig. 5.11** depicts the temperature profiles with different water entry locations with a water cut of 0.3. Water entry near the heel has limited effects on the wellbore temperature profile compared to the water entry near the toe because the relative amount of water production will be smaller. For instance, supposing that a well is producing 5b/d/ft uniformly, the maximum water holdup along a horizontal well can be as high as 0.5 if water is entering over 1600-1800 ft from the heel. However, if water is entering over 0-200 ft from the heel, water holdup can only be 0.1. Therefore, as water entry occurs closer to the toe, fluid in the wellbore is more affected. The pressure drop profiles are also plotted in **Fig. 5.12**. Again, we can observe the slope change where water entry starts. Compared with temperature profiles, pressure profiles would be less informative to identify amount and location of water entry.

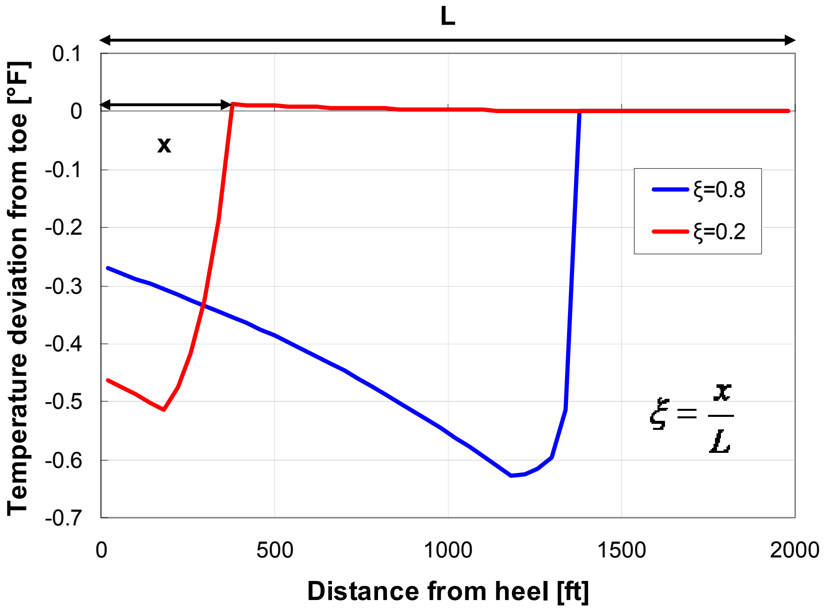

Fig. 5.11 Temperature deviation profiles for different water entry locations.

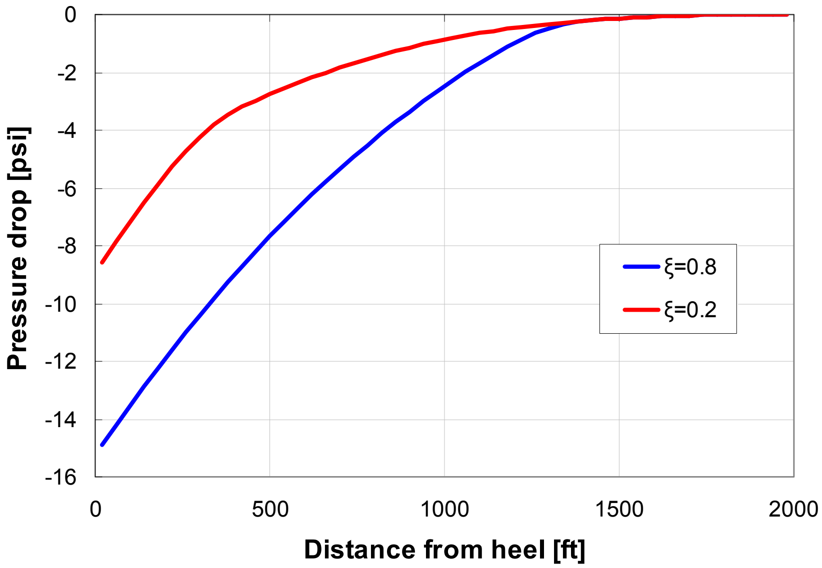

Fig. 5.12 Pressure drop profiles for different water entry locations.

To examine the use of a temperature log as a means to locate water entry location, we define the temperature difference (ΔT) cause by water inflow into an oil as shown in **Fig. 5.9** as the difference between the wellbore temperature upstream of the entry and the minimum temperature caused by the water entry. Also, the dimensionless water entry location is defined as the fraction of the water entry start distance from the heel divided by the total well length as shown in **Fig. 5.11**. To develop guidelines for what conditions lead to identifiable temperature anomalies, we varied the water cut (0.05 – 0.3) and the water entry location while fixing total flow rate (10,000 b/d), the pressure drawdown in the reservoir (300 psi), and the length of the water entry zone (10% of total well length). The temperature differences from these simulations are summarized in **Fig. 5.13**, which shows broad conditions of detectable temperature changes except for conditions of low water cut and water entry locations close to the heel. As the water cut increases, and the location goes away from the heel, the temperature changes become larger.

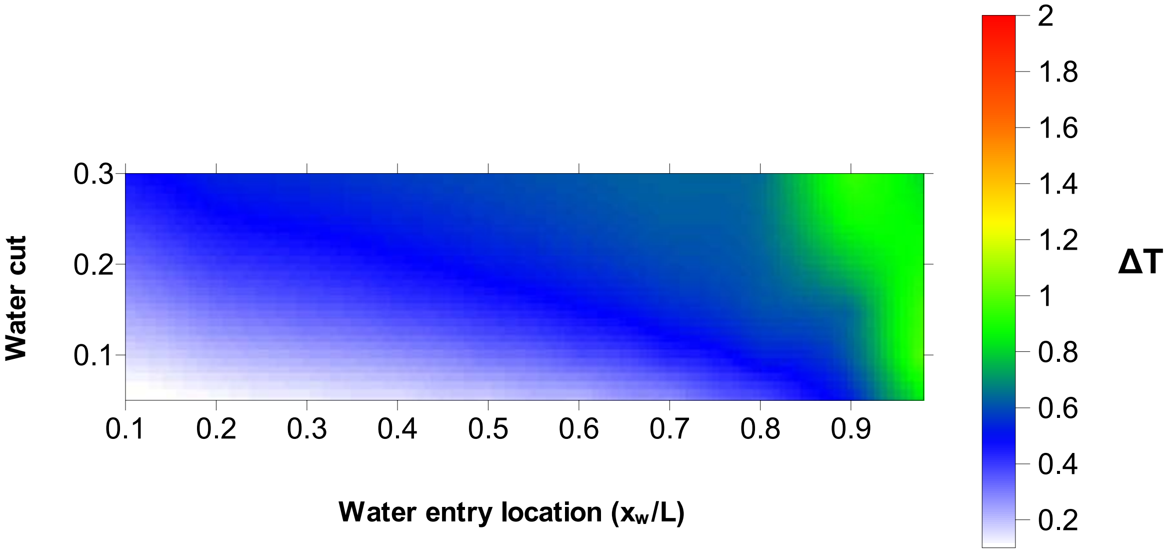

Fig. 5.13 Temperature difference contour (water).

5.3.4 Gas entry effects

When gas is produced, the wellbore will usually experience a temperature cooling. The temperature deviation profiles for different amounts for gas production and the pressure drop profiles are shown in **Figs. 5.14** and **5.15** respectively. The sensitivity of the temperature behavior to the amount of gas production is clearer than those of water entry cases. But for the pressure profiles, the profiles with different amount of gas production cases are almost identical. The temperature deviation profiles of gas entry with different entry locations are shown in **Fig. 5.16** and the pressure drop profiles are plotted in **Fig. 5.17**. While the temperature behaves sensitively to the gas entry locations, the pressure profiles only change the slopes. Similarly to the water entry example, the temperature change caused by a gas entry increases as the amount of gas production becomes higher and the gas entry occurs farther away from the heel.

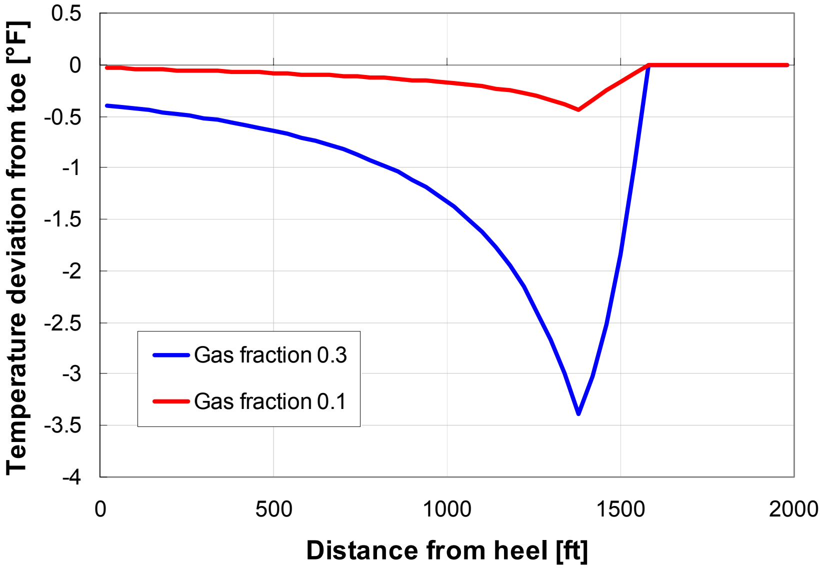

Fig. 5.14 Temperature deviation profiles for different gas fractions.

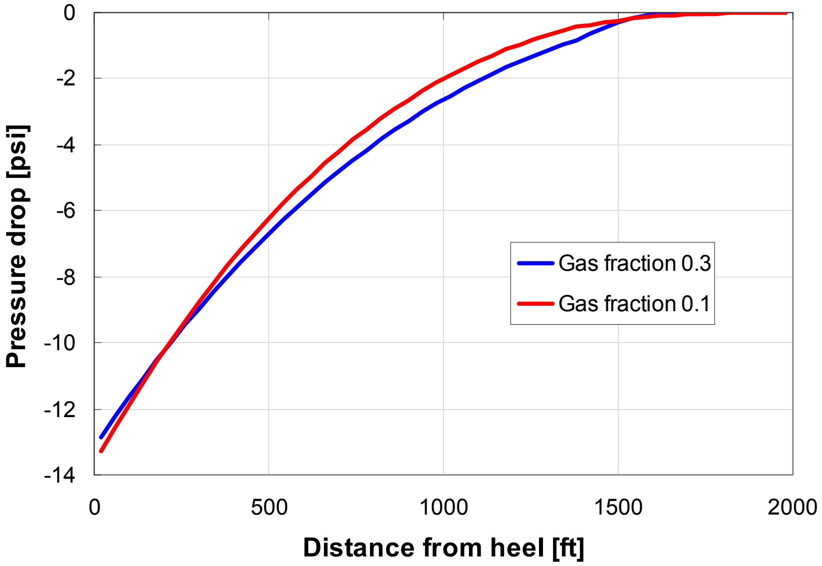

Fig. 5.15 Pressure drop profiles for different gas fractions.

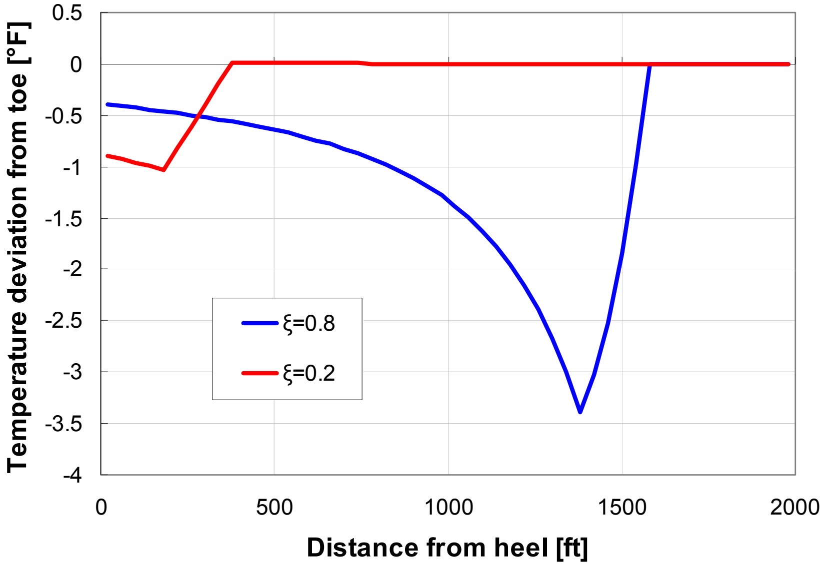

Fig. 5.16 Temperature deviation profiles for different gas entry locations.

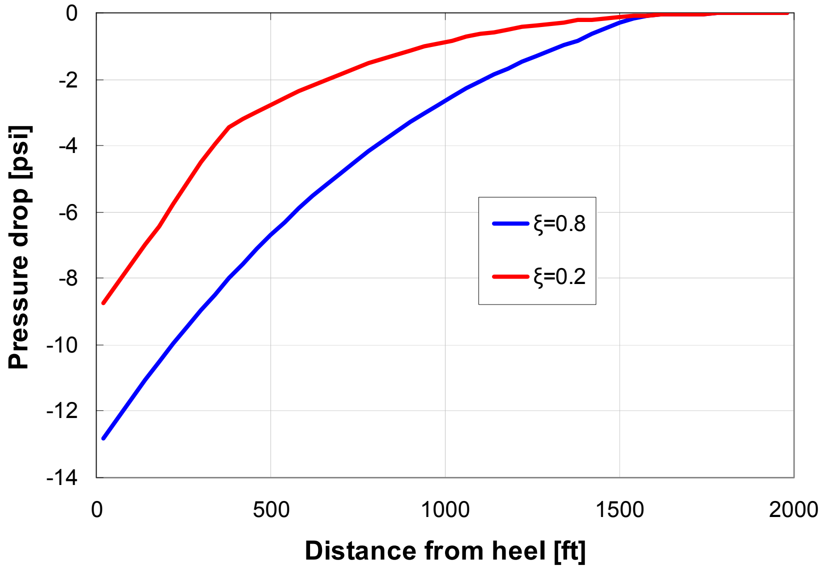

Fig. 5.17 Pressure drop profiles for different gas entry locations.

As with the water entry case, we varied the volume fraction of gas production (0.05 – 0.3) and the gas entry location, and fixed total flow rate (10,000 b/d or 56,146 CF/d), the length of the gas entry zone (10% of total well length), and the reservoir pressure drawdown (300 psi) to determine the conditions which gas entries can be identified from the temperature profile. The gas flow rates for these calculations are the downhole volumetric flow rate, so a gas cut of 0.3 means that at the bottomhole pressure and temperature, 30% of the total volumetric flow rate is gas. The results from these simulations are summarized in Fig**. 5.18**. Similar features to the water entry scenario can be observed from the figure. When gas production rate is small and entry occurs near the heel, the temperature changes are not significant enough to detect. As gas production rate increases or gas enters farther away from the heel, the temperature changes become large. Considering the fact that the inflow temperature of a gas is cooler than geothermal temperature, it is clear that we see more pronounced effects of the gas entry on the temperature profile than those of the water entry.

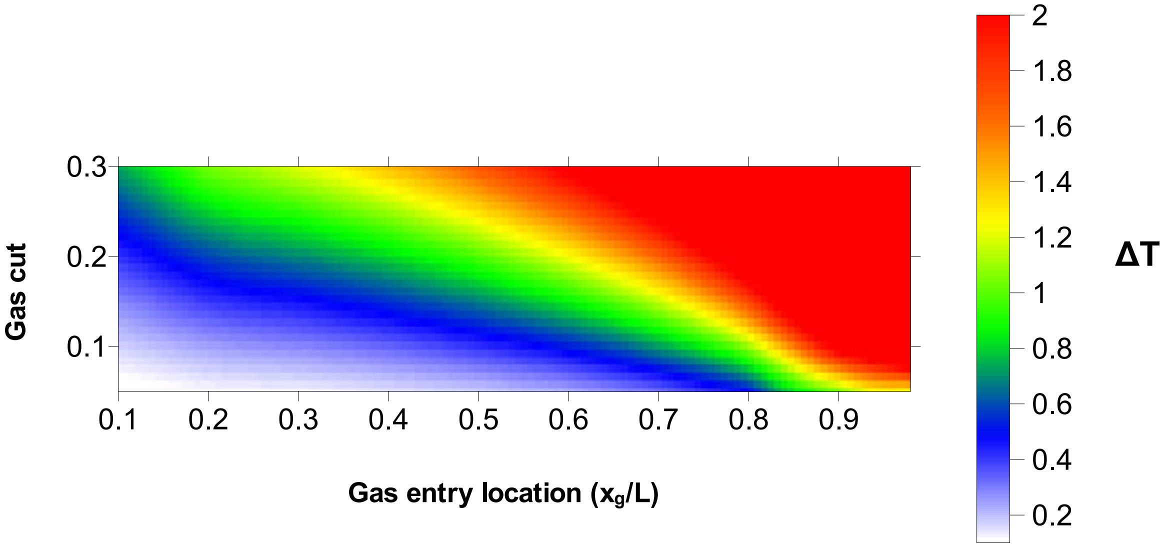

Fig. 5.18 Temperature difference contour (gas)

5.3.5 Damaged skin effect

With the existence of formation damage, the pressure profile in the reservoir changes. As a result, the inflow temperature increases proportional to the damage skin factor were shown in **Fig. 3.13**. Inflow temperature changes caused by a near well damaged region are not as significant as the ones caused by water or gas entry. However, while the occurrence of water or gas entry can be noticed at the surface once they have been produced, the distributions of formation damage are hard to profile.

If formation damage is evenly distributed in the entire producing zone, there would be little chance to observe skin effects on temperature log since it would not leave any anomalies on the profiles. In the following examples, we show the cases that formation being damaged in a particular zone, namely toe, middle, and heel. We consider a single-phase oil production with uniform inflow (5 b/d/ft) while the pressure drawdown in the reservoir (300 psi) being fixed by adjusting the undamaged permeabilities. We also assume that the damaged zone is extended radially into the formation for distance of 3 ft. The reduced permeability ratios, k_d/k, of 0.1 ($s = 24.6$), 0.3 ($s = 6.4$), and 0.5 ($s = 2.7$) are considered.

Fig. 5.19 shows the case of damage existing near the toe for 500 ft. For small k_d/k of 0.1 and 0.3, the temperature changes are measurable. We can also observe the temperature slope change where the damage zone exists. **Fig. 5.20** displays a similar example but with the damage zone lying in the middle. The inflow temperature effects are less observable because the difference in inflow temperature is smoothed by the wellbore temperature as have been seen in the water or gas entry examples. Finally, the profiles of the damage zone at the heel are shown in Fig**. 5.21**. The changes are not distinct for this case.

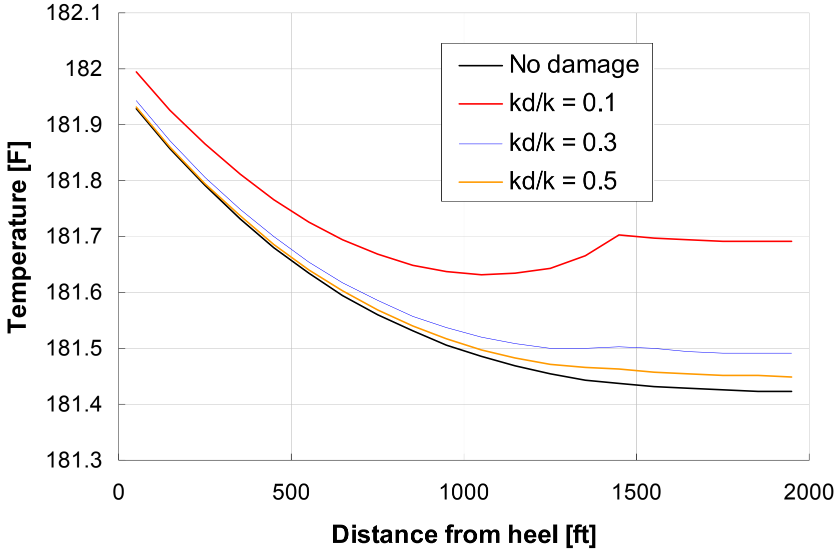

Fig. 5.19 Temperature profiles with damaged zone (toe).

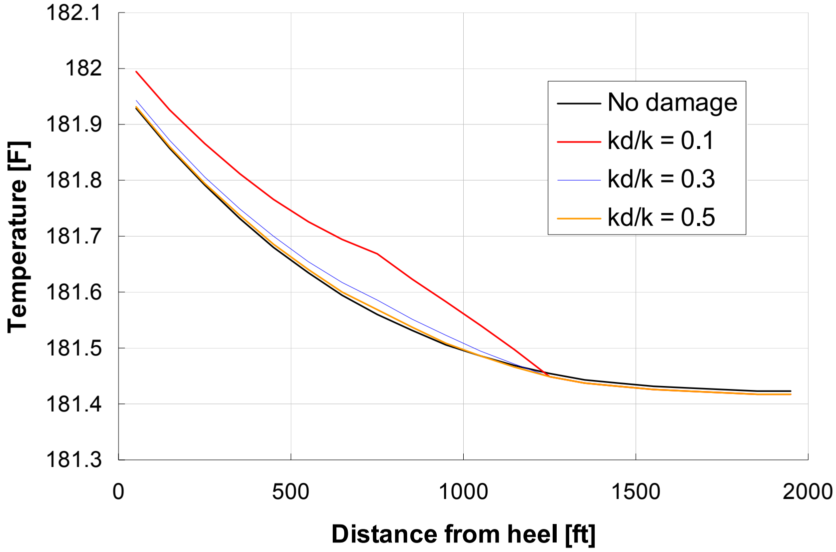

Fig. 5.20 Temperature profiles with damaged zone (middle).

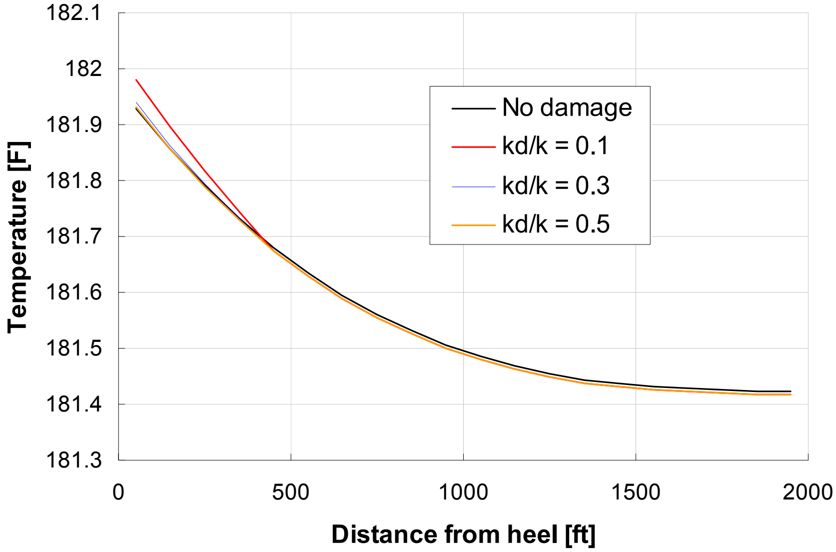

Fig. 5.21 Temperature profiles with damaged zone (heel).

CHAPTER 6

INVERSION METHOD

6.1 INTRODUCTION TO INVERSION METHOD

In this chapter, we develop an inversion method to analyze distributed pressure and temperature data. The coupled model described in the previous chapters will be used as a forward model to calculate pressure and temperature profiles. With the steady-state model, we perform production profile matching along a horizontal well.

We also present the study of the effects by adding temperature data to flow rate and pressure data in reservoir property estimation. Having more data as observations simply increases restrictions in parameter estimation and should decrease the uncertainty but possibly over-determines the problem. Even though pressure data are commonly used as observation to be matched, the temperature change is often neglected in normal production system. As discussed previously, that is a fair assumption especially for horizontal wells. However, with the advanced technology to accurately measure temperature, it is important to give some insights into the effect of having temperature data additionally on the reservoir property estimation.

6.2 INVERSION METHOD

We regard the total flow rate, the pressure and temperature profiles as observation data, and productivity (inflow) distribution as parameters to be estimated. In synthetic examples, we generate observations from a forward model and invert them to obtain the productivity distribution along the horizontal well. The discrepancy between observation and calculation is the error (objective) function to be minimized.

The relationships between productivity (or inflow rate) profile and observations (total flow rate, pressure, and temperature) are highly nonlinear. Let the relationship between parameter vector $\mathbf{w}$ and model-generated observations be represented by $f(\mathbf{x};\mathbf{w})$. $f(\mathbf{x};\mathbf{w})$ is a function of both observation space $\mathbf{x}$ and parameter $\mathbf{w}$, and maps *N*-dimensional parameter space into *M*-dimensional observation space. The Levenberg-Marquardt Algorithm (1963) is a blending method of a least-squares estimation and a steepest descent method, and it outperforms both methods. In what follows, we briefly show the derivations of both methods and of the Levenberg-Marquardt algorithm.

6.2.1 Least-Square Estimation

We assume that the model-generated observation $f(\mathbf{x};\mathbf{w})$ corresponding to a vector $\mathbf{w}$ that differs slightly from $\mathbf{w}_0$ is a linear function of $\mathbf{w}$. A linear approximation of $f(\mathbf{x};\mathbf{w})$ in the neighborhood of $\mathbf{w}_0$ is given by a truncated Taylor series as

$$f(\mathbf{x};\mathbf{w}) = f(\mathbf{x};\mathbf{w}_0) + \mathbf{J}(\mathbf{w} - \mathbf{w}_0), \tag{6.1}$$

where $\mathbf{J}$ is a Jacobian matrix given by

$$\mathbf{J} = \nabla f(\mathbf{x};\mathbf{w}_0). \tag{6.2}$$

Now we define an objective function as a squared error of the model-generated observation $f(\mathbf{x};\mathbf{w})$ from the observations $\mathbf{y}$. It is given as

$$E(\mathbf{w}) = \left\| \left(f(\mathbf{x};\mathbf{w}) - \mathbf{y} \right) \right\|^2. \tag{6.3}$$

Taking a derivative of the objective function with respect to the parameter vector $\mathbf{w}$, we have

$$\nabla E(\mathbf{w}) = 2\nabla f(\mathbf{x};\mathbf{w})^T \left(f(\mathbf{x};\mathbf{w}) - \mathbf{y} \right). \tag{6.4}$$

Substituting Eq. 6.1 into Eq. 6.4 gives

$$\nabla E(\mathbf{w}) = 2\nabla f(\mathbf{x};\mathbf{w})^T \left(f(\mathbf{x};\mathbf{w}_0) + \mathbf{J}(\mathbf{w} - \mathbf{w}_0) - \mathbf{y} \right). \tag{6.5}$$

Since we have assumed a linear approximation of f 's dependence on $\mathbf{w}$, we have

$$\begin{aligned} \nabla f(\mathbf{x};\mathbf{w}) &= \nabla f(\mathbf{x};\mathbf{w}_0) \\ &= \mathbf{J} \end{aligned}. \tag{6.6}$$

We denote

$$\mathbf{d} = \mathbf{J}^T \left(f(\mathbf{x};\mathbf{w}_0) - \mathbf{y} \right), \tag{6.7}$$

and

$$\mathbf{H} = \mathbf{J}^T \mathbf{J}. \tag{6.8}$$

The letters $\mathbf{d}$ and $\mathbf{H}$ stand for the derivative and the Hessian respectively. While $\mathbf{d}$ is the actual derivative of $E(\mathbf{w})$, $\mathbf{H}$ is the approximate Hessian obtained by neglecting the second order derivative. The rigorous Hessian is estimated as (Duijndam, 1988)

$$\mathbf{H} = \mathbf{J}^T \mathbf{J} + \sum_{i=1}^{M} \left(f(x_i;\mathbf{w}) - y_i \right) \mathbf{T}_i, \tag{6.9}$$

where $\mathbf{T}_i$ is the Hessian matrix of the residual $\left(f(x_i;\mathbf{w}) - y_i \right)$ at this observation point and is neglected here because of the linear assumption of *f*. With Eqs. 6.7 and 6.8, Eq. 6.5 becomes

$$\nabla E(\mathbf{w}) = 2\mathbf{H}(\mathbf{w} - \mathbf{w}_0) + 2\mathbf{d}. \tag{6.10}$$

With the optimal parameter vector $\mathbf{w}_{opt}$, the gradient of the objective function $\nabla E(\mathbf{w})$ should be zero. Therefore, we have

$$\mathbf{0} = 2\mathbf{H}(\mathbf{w}_{opt} - \mathbf{w}_0) + 2\mathbf{d}. \tag{6.11}$$

Solving for $\mathbf{w}_{opt}$ yields

$$\mathbf{w}_{opt} = -\mathbf{H}^{-1}\mathbf{d} + \mathbf{w}_0. \tag{6.12}$$

Because of the linear approximation of f, Eq. 6.12 is approximately correct. That is $\mathbf{w}_{opt}$, defined by adding the upgrade vector to the vector set $\mathbf{w}_0$, is not guaranteed to be the minimum of the objective function $E(\mathbf{w})$. Therefore, the new set of parameters contained in $\mathbf{w}_{opt}$ is then to be used as a starting point to determine new upgrade vector given by Eq. 6.12. By repeating this procedure, we can supposedly reach the global minimum of $E(\mathbf{w})$. The process of iteratively arriving at the minimum is depicted for a two-parameter problem in **Fig. 6.1**.

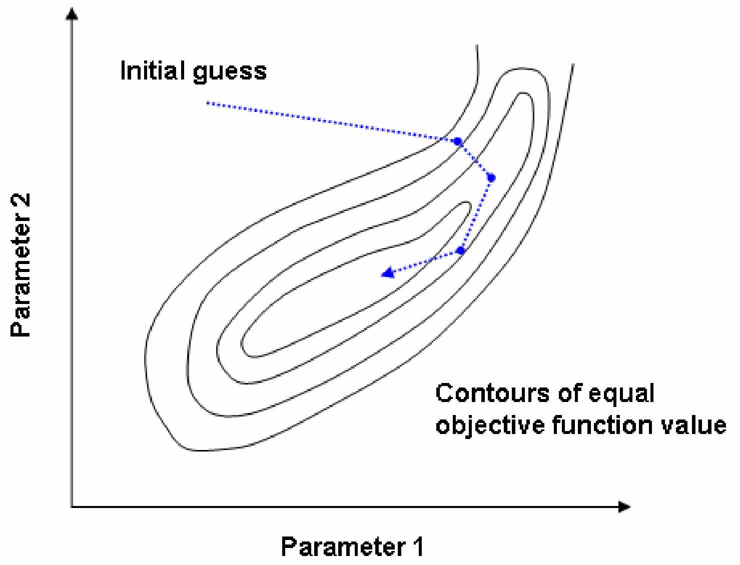

Fig. 6.1 Image of least-square method's iterative behavior.

6.2.2 Steepest Descent Method

The gradient vector of $E(\mathbf{w})$ can be written as

$$\begin{aligned}\mathbf{g} &= \nabla E(\mathbf{w}) \\ &= 2\mathbf{J}^T\left(f(\mathbf{x};\mathbf{w}_0)-\mathbf{y}\right). \\ &= 2\mathbf{d}\end{aligned} \tag{6.13}$$

In the steepest descent method, the upgrade vector follows the direction of that the objective function decreases from the current parameter set $\mathbf{w}_0$. Therefore, the upgrade vector will be computed from

$$\mathbf{w} = \mathbf{w}_0 - \eta\mathbf{g}, \tag{6.14}$$

where the constant η is the upgrading parameter. The negative gradient vector $-\mathbf{g}$ is in the descend direction of the error function $E(\mathbf{w})$ in which the current parameter set is supposed to move. The upgrade vector, however, has to be damped by multiplying η so as not to overshoot the downhill direction.

6.2.3 Levenberg-Marquardt Method

The upgrade vector derived from the local linear assumption (Least-Square Estimation) should not allow the error function $E(\mathbf{w})$ to increase from the current state. Therefore, the angle between the upgrade vector derived from local linear assumption, $-\mathbf{H}^{-1}\mathbf{d}$, and the negative gradient vector, $-\mathbf{g}$, cannot be greater than 90 degrees. If the angle is greater than 90 degrees, the upgrade vector leads $E(\mathbf{w})$ to increase. However, the upgrade vector, $-\mathbf{H}^{-1}\mathbf{d}$, can normally speed up the convergence toward the global minimum especially when the parameters are highly correlated even though $-\mathbf{g}$ defines the direction of steepest descent of $E(\mathbf{w})$. In such situations, since the descend direction becomes too sensitive to the parameters, we tend to wander between the valleys of the objective function near the minimum and the convergence speed becomes enormously slow. This behavior is diagrammatically shown in **Fig. 6.2**.

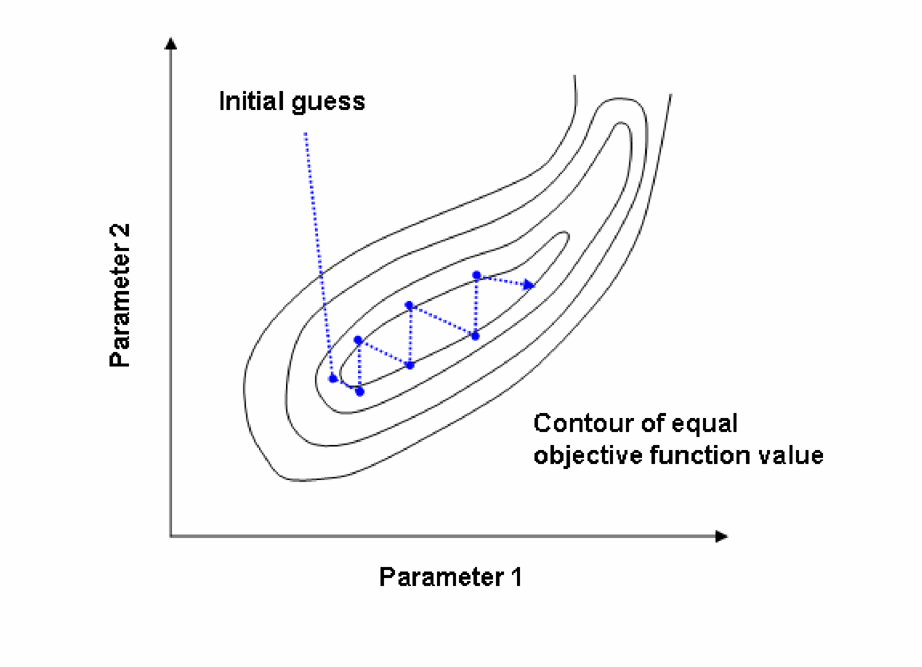

Fig. 6.2 Image of steepest descent method's iterative behavior.

The upgrade vector Eq. 6.12 is not always better because it assumes a local linearity of $f(\mathbf{x};\mathbf{w})$ and that is only valid near a minimum. Marquardt (1963) invented a technique that involves 'blending' between least-square (Eq. 6.12) and steepest descent (Eq. 6.14) methods. We take full advantage of steepest descent until we reach near the minimum and gradually shift the upgrading method into the least-square method. Introducing a blending factor λ, the upgrade vector is given as

$$\mathbf{w} = \mathbf{w}_0 - (\mathbf{H} + \lambda\mathbf{I})^{-1}\mathbf{d}\,. \tag{6.15}$$

where **I** is the identity matrix. If a small value for λ is taken, Eq. 6.15 becomes identical to the least-square method. And, as λ gets large, Eq. 6.15 approaches to

$$\mathbf{w} = \mathbf{w}_0 - \frac{1}{\lambda}\mathbf{d}\,, \tag{6.16}$$

which is a steepest descent method.

6.3 APPLICATION

We now apply a Levenberg-Marquardt method to our problem, which has flow rate, temperature, and pressure data as observations. Supposing downhole pressure and temperature profiles are measured at N points, we will obtain N points of pressure and temperature, respectively, in addition to the total flow rates of each phase. In the following, we define the corresponding variables for the Levenberg-Marquardt method.

6.3.1 Variable definitions

We denote the measured pressure data as

$$\mathbf{p}_m = \left[p_{m1}, p_{m2}, \cdots, p_{mN}\right]^{\mathrm{T}}, \tag{6.17}$$

And the temperature measurements as

$$\mathbf{T}_m = \left[T_{m1}, T_{m2}, \cdots, T_{mN}\right]^{\mathrm{T}}. \tag{6.18}$$

The flow rates of each phase (1 = oil, 2 = water, and 3 = gas) are

$$\mathbf{q}_m = \left[q_{m1}, q_{m2}, q_{m3}\right]^{\mathrm{T}}. \tag{6.19}$$

The parameters we wish to estimate from these data are the productivity profile along the well. The productivity index J is defined as

$$J = \frac{q}{\Delta p}. \tag{6.20}$$

From Eq. 3.63, we can solve for the productivity index of horizontal well. Then we obtain

$$J = \frac{2\pi kL}{\mu\left[\ln\left(\frac{h}{R}\right) + \pi\frac{W}{h} - 1.917 + s\right]}. \tag{6.21}$$

From Eq. 6.21, the productivity index is proportional to permeability if other parameters stay the same. Therefore, the permeability profile along the well is chosen as the parameters to be estimated from production data. To match the pressure and temperature data measured at N points, the forward model must divide the reservoir into N segments. Following the notation of the previous section, the parameters can be written as

$$\begin{aligned}\mathbf{w} &= \left[k(x_1), k(x_2), \cdots, k(x_N)\right]^{\mathrm{T}} \\ &= \left[k_1, k_2, \cdots, k_N\right]^{\mathrm{T}}\end{aligned}. \tag{6.22}$$

From the forward model with N segments, we can calculate N pressures and N temperatures respectively. The calculated pressure profile from the model is

$$\mathbf{p}_c(\mathbf{w}) = \left[p_{c1}, p_{c2}, \cdots, p_{cN}\right]^{\mathrm{T}}, \tag{6.23}$$

and temperature profile is

$$\mathbf{T}_c(\mathbf{w}) = \left[T_{c1}, T_{c2}, \cdots, T_{cN}\right]^{\mathrm{T}}. \tag{6.24}$$

Additionally we have production of each phase

$$\mathbf{q}_c(\mathbf{w}) = \left[q_{c1}, q_{c2}, q_{c3}\right]^{\mathrm{T}}, \tag{6.25}$$

where subscript c stands for calculated.

Now we define the objective function as a squared difference of the model-calculated values and measurements. However, we cannot treat temperature, pressure, and flow rate equally because they have different impacts on the permeability profile and have even different unit (temperature in $^{\mathrm{o}}$F, pressure in psi, and flow rate in b/d or MCF/d). For this purpose we must weight each measurement in defining the error term. Hence, we define the error components as follows

$$\mathbf{e}_p = \mathbf{D}_p^{1/2}(\mathbf{p}_c - \mathbf{p}_m), \tag{6.26}$$

$$\mathbf{e}_T = \mathbf{D}_T^{1/2}(\mathbf{T}_c - \mathbf{T}_m), \tag{6.27}$$

and

$$\mathbf{e}_q = \mathbf{D}_q^{1/2}(\mathbf{q}_c - \mathbf{q}_m). \tag{6.28}$$

where $\mathbf{D}_p$, $\mathbf{D}_T$, and $\mathbf{D}_Q$ are weights for each error element and are diagonal matrices. Then we can define the objective function as

$$\begin{aligned} E(\mathbf{w}) &= \mathbf{e}_p^{\mathrm{T}}\mathbf{e}_p + \mathbf{e}_T^{\mathrm{T}}\mathbf{e}_T + \mathbf{e}_q^{\mathrm{T}}\mathbf{e}_q \\ &= \sum_{j=1}^{N}\left[(\mathbf{D}_p)_{jj}(p_{cj} - p_{mj})^2 + (\mathbf{D}_T)_{jj}(T_{cj} - T_{mj})^2\right] + \sum_{i=1}^{3}(\mathbf{D}_q)_{ii}(q_{ci} - q_{mi})^2 \end{aligned}. \tag{6.29}$$

Using the error components vector, the gradient vector $\mathbf{d}$ is given by

$$\mathbf{d} = \mathbf{J}_p^{\mathrm{T}}\mathbf{e}_p + \mathbf{J}_T^{\mathrm{T}}\mathbf{e}_T + \mathbf{J}_q^{\mathrm{T}}\mathbf{e}_q, \tag{6.30}$$

where Jacobian matrices $\mathbf{J}_p$, $\mathbf{J}_T$, and $\mathbf{J}_Q$ are given by

$$(\mathbf{J}_p)_{jk} = \frac{\partial e_{pj}}{\partial k_k} = \left(\mathbf{D}_p^{1/2}\right)_{jj}\frac{\partial p_{cj}}{\partial k_k}, \tag{6.31}$$

$$(\mathbf{J}_T)_{jk} = \frac{\partial e_{Tj}}{\partial k_k} = \left(\mathbf{D}_T^{1/2}\right)_{jj}\frac{\partial T_{cj}}{\partial k_k}, \tag{6.32}$$

and

$$(\mathbf{J}_q)_{ik} = \frac{\partial e_{qi}}{\partial k_k} = \left(\mathbf{D}_p^{1/2}\right)_{ii}\frac{\partial q_{ci}}{\partial k_k}. \tag{6.33}$$

Therefore, the k^{th} component of the derivative vector $\mathbf{d}$ is given as

$$
\begin{aligned}
d_k &= \left(\mathbf{J}_p{}^{\mathrm{T}}\mathbf{e}_p\right)_k + \left(\mathbf{J}_T{}^{\mathrm{T}}\mathbf{e}_T\right)_k + \left(\mathbf{J}_q{}^{\mathrm{T}}\mathbf{e}_q\right)_k \\
&= \sum_{j=1}^{N}\left[\left(\mathbf{D}_p\right)_{jj}\left(p_{cj}-p_{mj}\right)\frac{\partial p_{cj}}{\partial k_k}\right] + \sum_{j=1}^{N}\left[\left(\mathbf{D}_T\right)_{jj}\left(T_{cj}-T_{mj}\right)\frac{\partial T_{cj}}{\partial k_k}\right] \\
&\qquad + \sum_{i=1}^{3}\left[\left(\mathbf{D}_q\right)_{ii}\left(q_{ci}-q_{mi}\right)\frac{\partial q_{ci}}{\partial k_k}\right]
\end{aligned}
\quad . \tag{6.34}
$$

Similarly, the Hessian matrix **H** is

$$\mathbf{H} = \mathbf{J}_p{}^{\mathrm{T}}\mathbf{J}_p + \mathbf{J}_T{}^{\mathrm{T}}\mathbf{J}_T + \mathbf{J}_q{}^{\mathrm{T}}\mathbf{J}_q\,. \tag{6.35}$$

The component of the matrix is estimated as

$$\left(\mathbf{H}\right)_{jk} = \sum_{l=1}^{N}\left[\left(\mathbf{D}_p\right)_{ll}\frac{\partial p_{cl}}{\partial k_j}\frac{\partial p_{cl}}{\partial k_k} + \left(\mathbf{D}_T\right)_{ll}\frac{\partial T_{cl}}{\partial k_j}\frac{\partial T_{cl}}{\partial k_k}\right] + \sum_{i=1}^{3}\left[\left(\mathbf{D}_q\right)_{ii}\frac{\partial q_{ci}}{\partial k_j}\frac{\partial q_{ci}}{\partial k_k}\right]. \tag{6.36}$$

Each component of Jacobian matrices can be obtained numerically. For instance, $\frac{\partial p_{cj}}{\partial k_k}$, can be computed by perturbing k_k while keeping other parameters constant. The sensitivity of k_k to p_{cj} is approximated to

$$\frac{\partial p_{cj}}{\partial k_k} \cong \frac{p_{cj}\left(k_1,\cdots,k_k+\delta k,\cdots k_N\right) - p_{cj}\left(k_1,\cdots,k_k,\cdots k_N\right)}{\delta k}\,. \tag{6.37}$$

As obvious from Eq. 6.37, calculating a sensitivity of one parameter k_k requires at least one forward model run. Therefore, to compute the whole Jacobian matrix, we must generate a number of parameters (*N*) forward runs.

Starting from an initial guess of the parameters, $\mathbf{w}_0$, the update rule follows the Levenberg-Marquardt method that is given as

$$\mathbf{w} = \mathbf{w}_0 - \left(\mathbf{H} + \lambda\mathbf{I}\right)^{-1}\mathbf{d}\,. \tag{6.38}$$

The schematic of the inversion process is shown in **Fig. 6.3**.

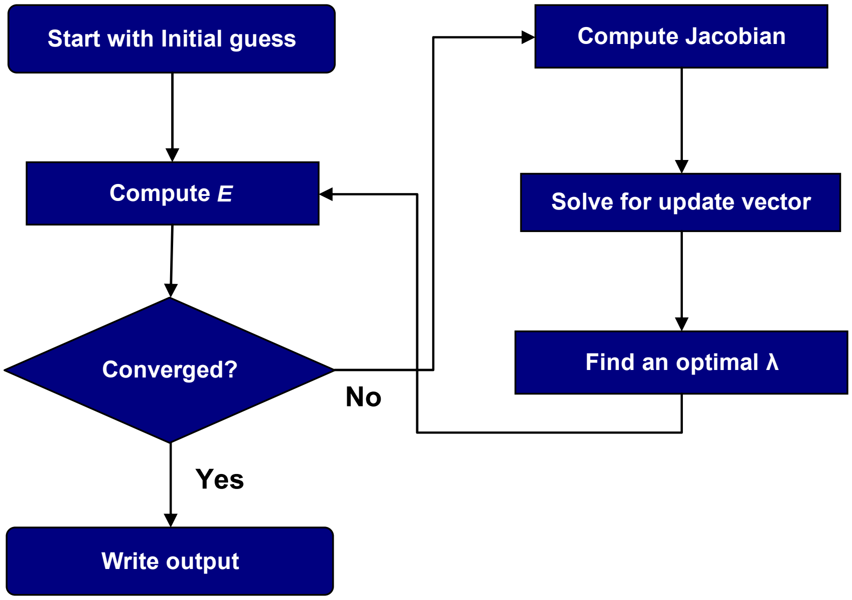

Fig. 6.3 Schematic of the inversion procedure.

6.3.2 Observation weights

In 6.3.1, we supposed that the production data measured were pressure and temperature profiles in addition to total flow rate of each phase. Giving many types of input data to the objective function, however, might result in the problem being over-determined and the objective function losing the right path without making any improvements. Therefore, in this example, we go through a variety of numerical experiments with different input data combinations to evaluate the effects of each input data on the permeability inversion. As observations we possibly obtain, we consider pressure and temperature profiles, and flow rates of each phase. Plus, we consider the spatial derivative of pressure and temperature profiles (dp/dx and dT/dx) because we have observed the slope of these curves sometimes indicating additional information.

In Eqs. 6.26 – 28, we introduced the weights for each observation. As stated, each observation has different physical properties and units. Therefore, they should have different contributions to the objective function. For instance, if the weight of flow rate is improperly high compared to the other inputs, the inversion problem becomes identical to the problem of simply matching the flow rate data only. Although knowing the relative importance of different types of input data is essential, there is no explicit way to quantitatively calculate the weights.

In this study, we approximately equalize the sensitivities of the input data to the permeability estimation with observation weights to quantify the relative importance. Also, we treat the input data of the same kind equally in further discussion. Therefore, for instance, the component of weight matrices $(\mathbf{D}_p)_{jj}$ can be replaced with simply D_p for all pressure observations. Since each observation has different units, we introduce dimensionless observation as follows.

$$q_{D,i} = \frac{q_i \mu}{k p_R \Delta x}, \tag{6.39}$$

$$p_{D,j} = \frac{p_j}{p_R}, \tag{6.40}$$

$$T_{D,j} = \frac{T_j}{\rho C_p p_R}, \tag{6.41}$$

$$x_D = \frac{x}{R}. \tag{6.42}$$

where Δx is the length of the segment.

The sensitivity of the dimensionless observation $p_{D,j}$ to the permeability of the k^{th} segment k_k can be written as $\partial k_k / \partial p_{D,j}$. To obtain similar contributions from different observations, we equate the sensitivities with the weights. Then we have

$$\begin{aligned} \frac{1}{D_p^{1/2}} \frac{\partial k_k}{\partial p_{D,j}} &= \frac{1}{D_T^{1/2}} \frac{\partial k_k}{\partial T_{D,j}} = \frac{1}{D_q^{1/2}} \frac{\partial k_k}{\partial q_{D,j}} \\ &= \frac{1}{D_{dp}^{1/2}} \frac{\partial k_k}{\partial (dp_D / dx_D)_j} = \frac{1}{D_{dT}^{1/2}} \frac{\partial k_k}{\partial (dT_D / dx_D)_j}, \end{aligned} \tag{6.43}$$

where D_{dp} and D_{dT} are the weights for dp/dx and dT/dx.

From Eq. 6.43, the relative sensitivity of the dimensionless pressure observation to the flow rate can be written as

$$\begin{aligned} \frac{D_q^{1/2}}{D_p^{1/2}} &= \frac{\partial k_k / \partial q_{D,i}}{\partial k_k / \partial p_{D,j}} \\ &= \frac{\partial p_{D,j}}{\partial q_{D,j}} \end{aligned}. \tag{6.44}$$

Therefore, the relationship between D_p and D_q is given by

$$D_q = \left(\frac{\partial p_{D,j}}{\partial q_{D,i}} \right)^2 D_p. \tag{6.45}$$

$\partial p_{D,j} / \partial q_{D,i}$ is the sensitivity of $q_{D,i}$ to $p_{D,j}$. Flow rate of the phase *i* is given by

$$\sum_{k=1}^{N} J_k \left(p_R - p_k \right) = q_i \,. \tag{6.46}$$

To estimate the sensitivity, we consider small perturbations of pressure and flow rate caused by, say, permeability and the resulting changes can be written as

$$p_j = p_j^{\;0} + \delta p_j \,, \tag{6.47}$$

$$q_i = q_i^{\;0} + \delta q_i \,, \tag{6.48}$$

where $p_j^{\;0}$ and $q_i^{\;0}$ are the initial pressure and flow rate before perturbations. The change in the flow rate is

$$\begin{aligned} \delta q_i &= q_i - q_i^{\;0} \\ &= \sum_{k=1}^{N} J_k \left(p_R - p_k \right) - J_j \delta p_j - \sum_{k=1}^{N} J_k \left(p_R - p_k \right), \\ &= -J_j \delta p_j \end{aligned} \tag{6.49}$$

Therefore, we have

$$\frac{\partial p_j}{\partial q_i} = -\frac{1}{J_j} \,. \tag{6.50}$$

In dimensionless form, the sensitivity becomes

$$\begin{aligned} \frac{\partial p_{D,j}}{\partial q_{D,i}} &= \frac{k \Delta x}{\mu} \frac{\partial p_j}{\partial q_i} \\ &= -\frac{k \Delta x}{\mu} \left(\frac{1}{J_j} \right) \end{aligned} . \tag{6.51}$$

Therefore, from Eq. 6.21 and 6.45, the relative weight then becomes

$$D_q = \left[\frac{\ln\left(\frac{h}{R} \right) + \pi \frac{W}{h} - 1.917 + s}{2\pi} \right]^2 D_p \,. \tag{6.52}$$

Similarly, the weight of dimensionless temperature observation is given by

$$D_T = \left(\frac{\partial p_{D,j}}{\partial T_{D,j}} \right)^2 D_p \,. \tag{6.53}$$

From Eq. 4.61, the physical relationship between wellbore temperature and pressure can be approximated as

$$\frac{dT_j}{dx} = K_{JT} \frac{dp_j}{dx}. \tag{6.54}$$

From Eq. 6.54, we have

$$\frac{\partial p_j}{\partial T_j} = \frac{1}{K_{JT}}. \tag{6.55}$$

The dimensionless sensitivity is then

$$\begin{aligned} \frac{\partial p_{D,j}}{\partial T_{D,j}} &= \frac{1}{\rho C_p} \frac{\partial p_j}{\partial T_j} = \frac{1}{\rho C_p}\left(\frac{1}{K_{JT}}\right) \\ &= \frac{1}{\beta T_j - 1} \cong -1 \end{aligned}. \tag{6.56}$$

Therefore, the weight for the dimensionless temperature is

$$D_T = (-1)^2 D_p = D_p. \tag{6.57}$$

What remain are the weights of $(dp_D/dx_D)_j$ and $(dT_D/dx_D)_j$. From Eq. 6.43, we have

$$D_{dp} = \left(\frac{\partial p_{D,j}}{\partial (dp_D/dx_D)_j}\right)^2 D_p. \tag{6.58}$$

$(dp_D/dx_D)_j$ is actually calculated by the pressure difference across a segment divided by the length of the segment as

$$\left(\frac{dp_D}{dx_D}\right)_j = \left(\frac{\Delta p_D}{\Delta x_D}\right)_j = \frac{p_{D,j} - p_{D,j-1}}{\Delta x_D}, \tag{6.59}$$

With a small perturbation, the changes of $p_{D,j}$ and $(\Delta p_D/\Delta x_D)_j$ result in

$$p_{D,j} = p_{D,j}{}^0 + \delta p_{D,j}, \tag{6.60}$$

$$\left(\frac{\Delta p_D}{\Delta x_D}\right)_j = \left(\frac{\Delta p_D}{\Delta x_D}\right)_j^0 + \delta\left(\frac{\Delta p_D}{\Delta x_D}\right)_j. \tag{6.61}$$

Solving for the perturbed change of $(\Delta p_D/\Delta x_D)_j$ gives

$$\begin{aligned}\delta\left(\frac{\Delta p_D}{\Delta x_D}\right)_j &= \left(\frac{\Delta p_D}{\Delta x_D}\right)_j - \left(\frac{\Delta p_D}{\Delta x_D}\right)_j^0 \\ &= \frac{p_{D,\,j}{}^0 + \delta p_{D,\,j} - p_{D,\,j-1}}{\Delta x_D} - \frac{p_{D,\,j}{}^0 - p_{D,\,j-1}}{\Delta x_D}\,. \\ &= \frac{\delta p_{D,\,j}}{\Delta x_D}\end{aligned} \tag{6.62}$$

Therefore, we obtain

$$\frac{\partial p_{D,\,j}}{\partial\left(dp_D/dx_D\right)_j} = \Delta x_D\,, \tag{6.63}$$

Substituting into Eq. 6.56, the weight for D_{dp} is then given as

$$\begin{aligned}D_{dp} &= \left(\frac{\partial p_{D,i}}{\partial\left(dp_D/dx_D\right)_j}\right)^2 D_p\,. \\ &= \left(\Delta x_D\right)^2 D_p\end{aligned} \tag{6.64}$$

Similarly to $\left(\Delta p_D/\Delta x_D\right)_j$, the weight for $\left(dT_D/dx_D\right)_j$ is

$$D_{dT} = \left(\Delta x_D\right)^2 D_T\,. \tag{6.65}$$

6.4 SYNTHETIC AND FIELD EXAMPLES

With the inversion method described above, we show synthetic and field examples in this section. Synthetic examples include single-phase oil and gas examples to demonstrate the effects of each production data (pressure, temperature, etc.), and detections of water and gas entry. In the field example, we use production log data measured from a horizontal well in the North Sea which is producing oil and water.

6.4.1 Effects of Input Data Choice

The possible candidates for input data are the pressure profile, the temperature profile, the flow rate, the pressure derivative, and the temperature derivative. Total flow rate will be given as an observation for every case. Through numerical examples, we evaluate the effects of each input data on the inversion results. The experiments were conducted for single-phase oil production and single-phase gas production with a variety of permeability distributions.

Experiments for single-phase oil production. “Observations” are generated from a forward model following the “true” permeability distribution that we set up, and then inversion of the true permeability distribution is performed by matching the observations that are generated from the model.

As true permeability distributions, we consider four different distributions (cases A, B, C, and D) along the horizontal well as shown in **Fig. 6.4** for the single-phase oil production example. High permeability (500 md) zone and low permeability (50 md) zones are located alternately in different ways. To obtain larger wellbore effects on the profiles, the well with small diameter described in **Table 5.1** is used in the experiments and the bottomhole (heel) pressure is set for 3,600 psi. The reservoir whose properties are listed in **Table 5.2** is considered. The measurement resolutions of the pressure, temperature and flow rate are assumed to be the order of 0.1 psi, 0.01 ^{o}F, and 1 b/d respectively. The measurements are logged over 20 points located every 100 ft along the well. As an initial permeability distribution, a homogeneous 300 md distribution is considered assuming we have no a priori information about the permeability.

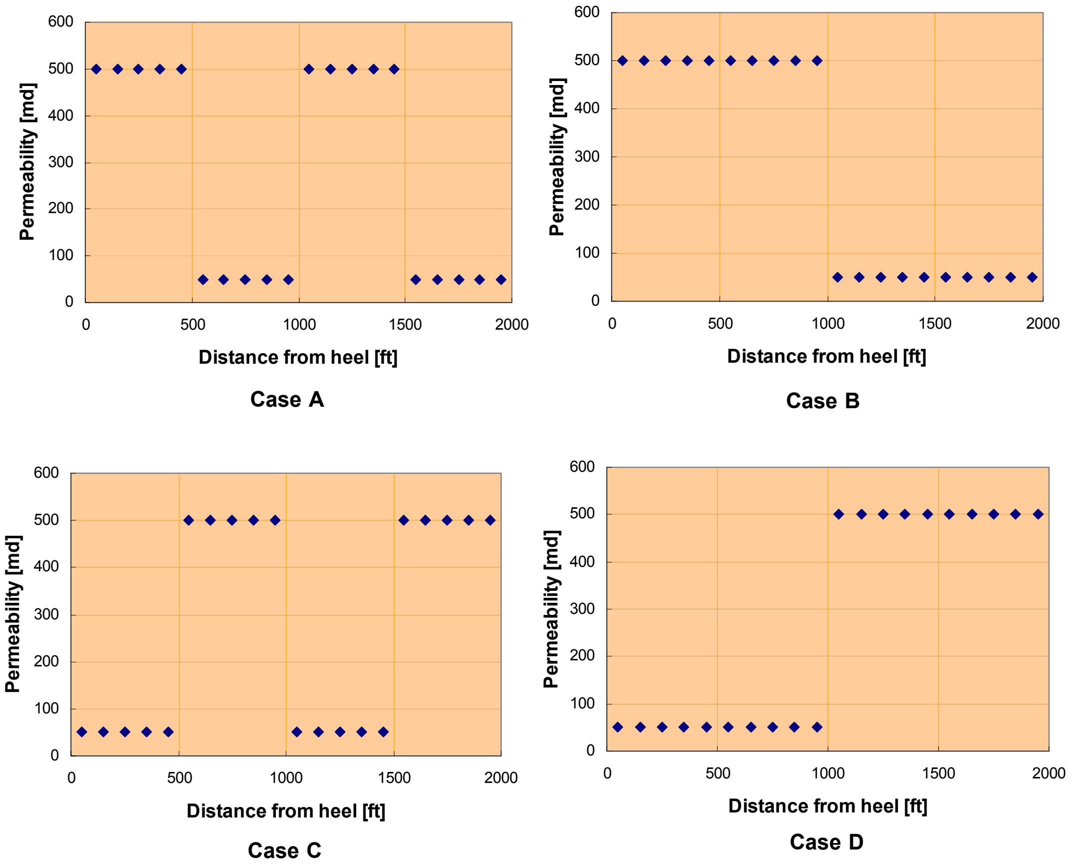

Case A

Case B

Case C

Case D

Fig. 6.4 Four different permeability distributions along a horizontal well.

For all the cases, we evaluate the effect of input data given on the inversion calculation. The combinations we give are: pressure only, temperature only, pressure and temperature, pressure and pressure derivative, temperature and temperature derivative, and all of them. We will determine the best combination among them through numerical experiments. As an example of additional input data effects, the generated observations of case A and the matched curves by using pressure only, temperature only, and all the observations are shown in **Fig. 6.5.**

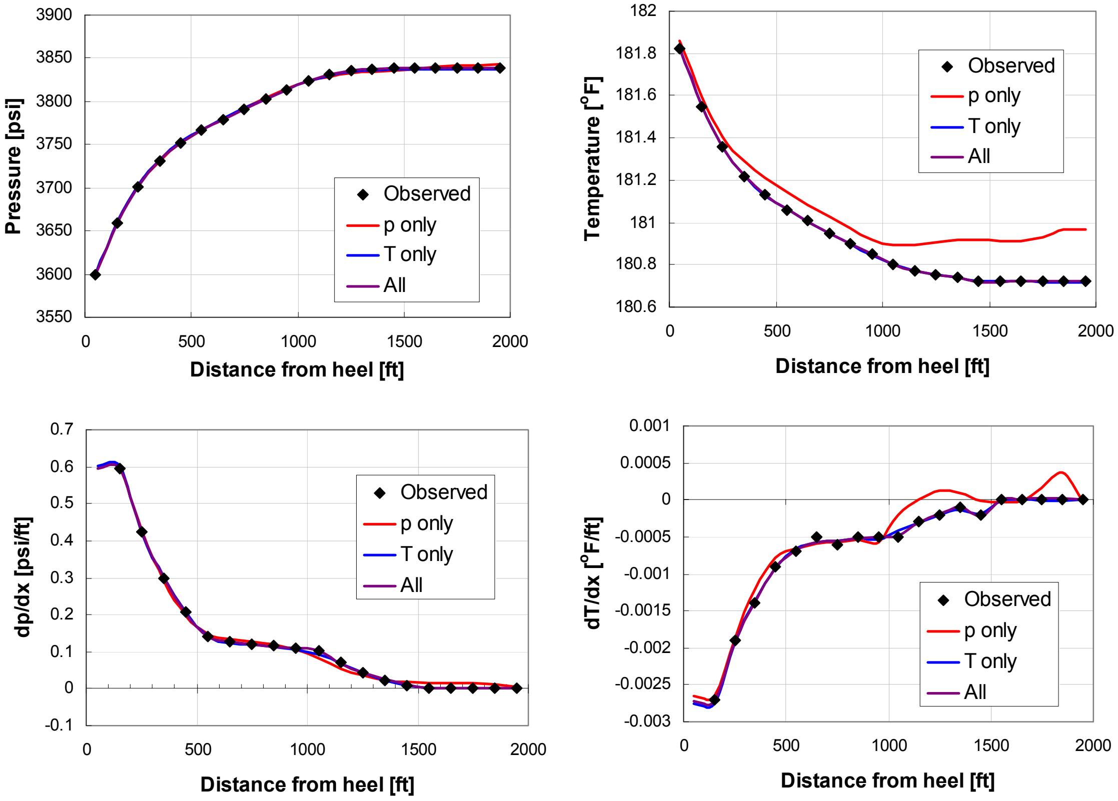

Fig.6.5 Observation and matched curves with different input data (Case A, oil).

Giving the pressure data only shows a close match with the pressure profile but the temperature curves did not match. That indicates that pressure could be matched even if its temperature profile is off from the observation. On the other hand, giving temperature only obtains a good match while the pressure profiles also match. With more input data (giving all possible input), not significant difference can be observed in this example compared with the match from temperature only.

Fig. 6.6 displays the inversion results from case A. As pressure data only did not show a good match of temperature curve in **Fig. 6.5**, it is not surprising that inversion from pressure only did not match the true permeability field well. However, other combination choices captured the features of the alternating permeability zone locations, and their inversion results show good resemblance to the true permeability distribution. Inverted flow rate profile from temperature and pressure data were compared with the observed one in **Fig. 6.6c**. They show very close match.

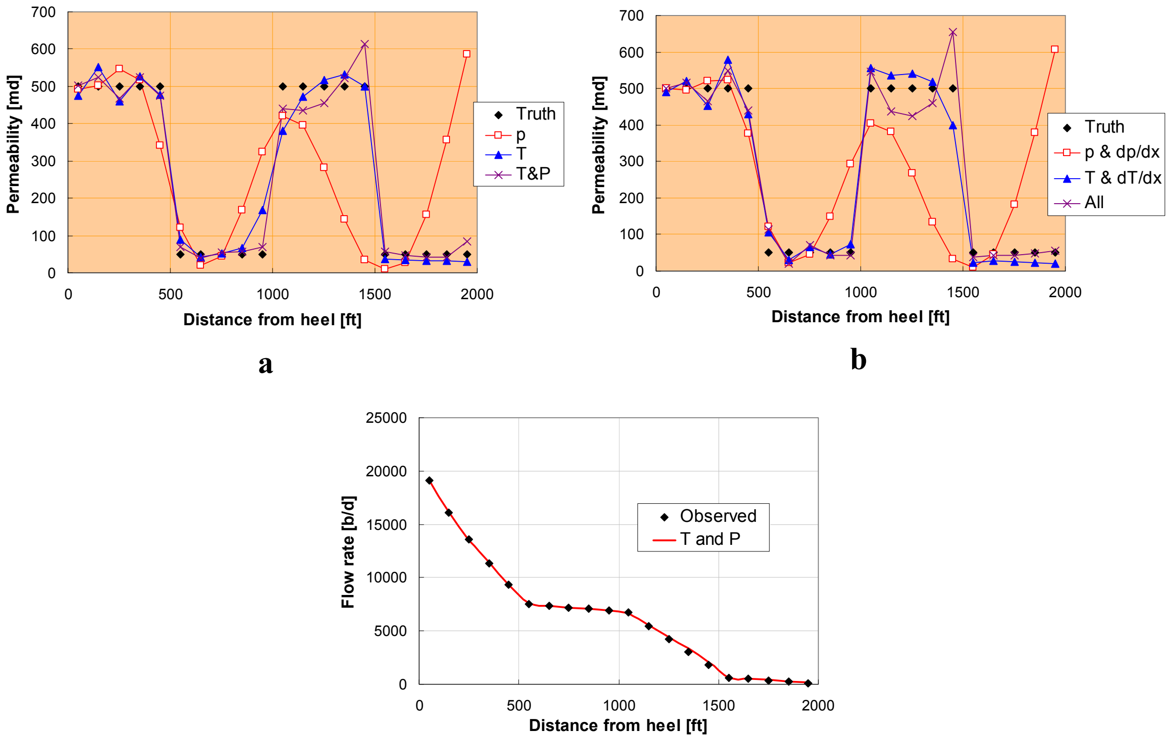

a

b

c

Fig. 6.6 Inverted results for case A, (a) permeability distributions from original data. (b) permeability distributions from derivative of the data, and (c) flow rate profile from temperature and pressure.

The inversion results of case B are shown in **Fig. 6.7**. Similarly to case A, the inversion with pressure data only or pressure and dp/dx did not produce better distributions than the ones with the other input data. Using the choice of temperature and pressure gives the very close distribution to the true permeability distribution. The inverted flow rate profile from temperature and pressure data is also shown in **Fig. 6.7**. The flow rate profiles are identically agreed.

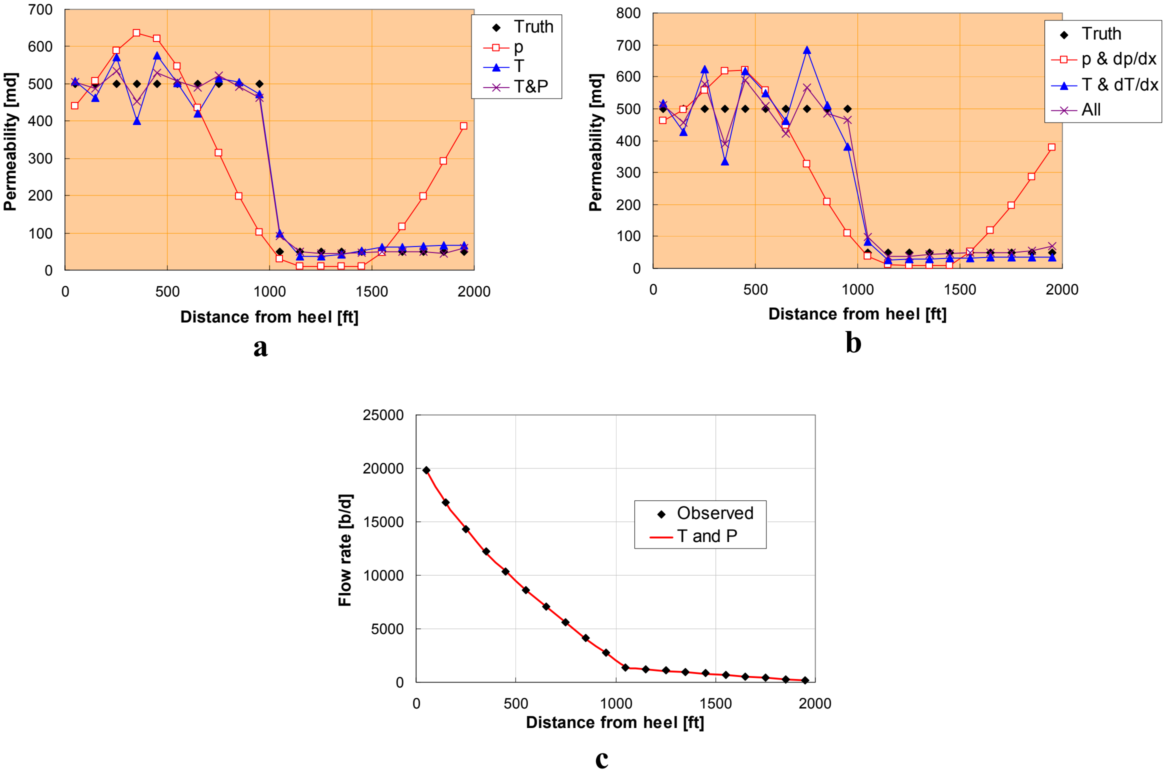

a

b

c

Fig. 6.7 Inverted results for case B, (a) permeability distributions from original data. (b) permeability distributions from derivative of the data, and (c) flow rate profile from temperature and pressure.

The inversion results for the permeability distribution case C are depicted in **Fig. 6.8**. Unlike the previous two cases, the choice of pressure data only performed well in this case. Also, the choice of all input data including the derivative of the data as shown in **Fig. 6.8b** did not succeed in inverting the permeability distribution. Considering the fact that we can obtain better permeability inversion from other input data combination, this result from all input data choice implies the error minimization process strayed away from the right direction because of too many restrictions. The inverted flow rate from pressure and its derivative is shown in **Fig. 6.8c**.

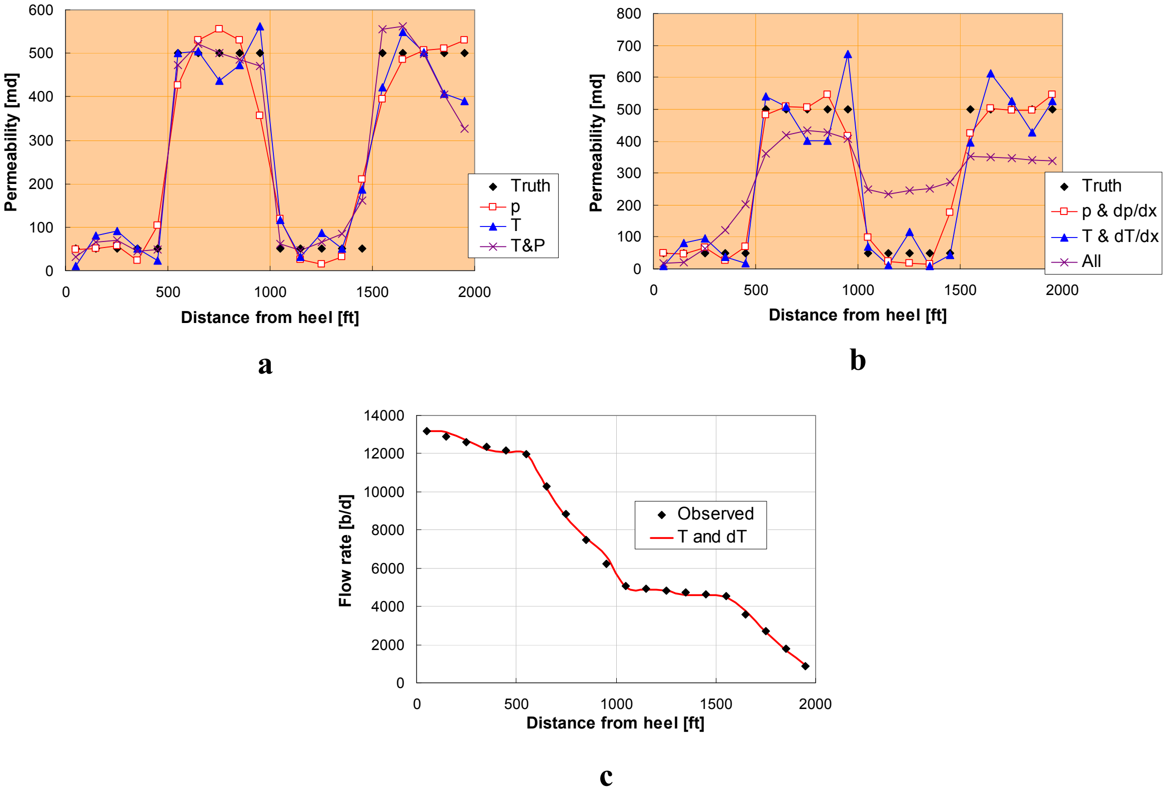

Fig. 6.8 Inverted results for case C, (a) permeability distributions from original data. (b) permeability distributions from derivative of the data, and (c) flow rate profile from temperature and its derivative.

The last example of single-phase oil production is Case D. The inverted permeability distributions and flow rate profile are shown in **Fig. 6.9**. Neither the choice of pressure only nor of temperature only show a good match with the true permeability distribution. Similar behavior can be observed in the results including the derivative of the data. However, the combination of temperature and pressure or all the data performances are improved compared with the other choices. The inverted flow rate by temperature and pressure data is compared with the observation in **Fig. 6.9c**.

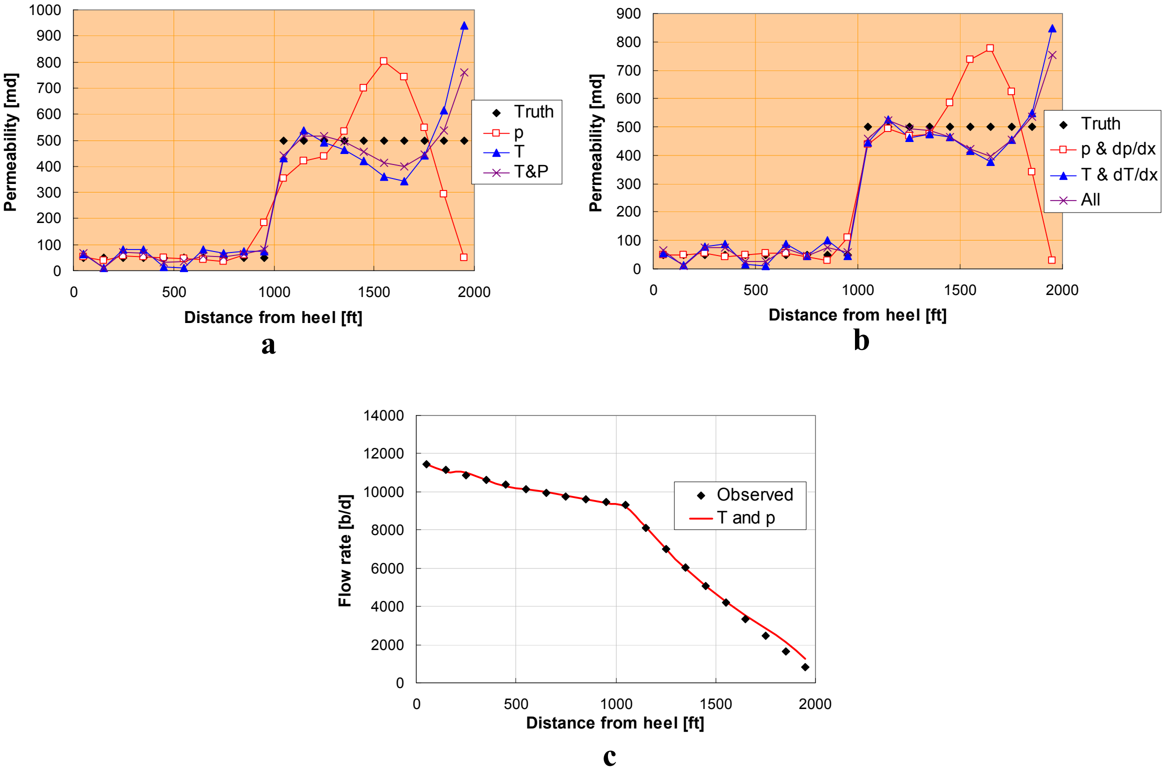

Fig. 6.9 Inverted results for case D, (a) permeability distributions from original data. (b) permeability distributions from derivative of the data, and (c) flow rate profile from temperature and pressure.

In order to evaluate the inverted results, we calculated the *l*-2 norm of the discrepancy as

$$Err = \sqrt{\sum_{j=1}^{20}\left(\frac{k_{j,true} - k_{j.inverted}}{k_{j,true}}\right)^2}, \tag{6.64}$$

where $k_{j,true}$ and $k_{j,inverted}$ are the true and the inverted permeability of the position j respectively. The obtained errors were normalized by dividing by the error of the result from pressure data for comparison reason and shown in **Fig. 6.10**. In cases A, B, and D, the combination of temperature and pressure gives the best result. While the combination of temperature and derivative of the temperature gives the best result in the case C, the result from the temperature and pressure combination is still better than the others. The combinations that provided the lowest error are highlighted in the figures.

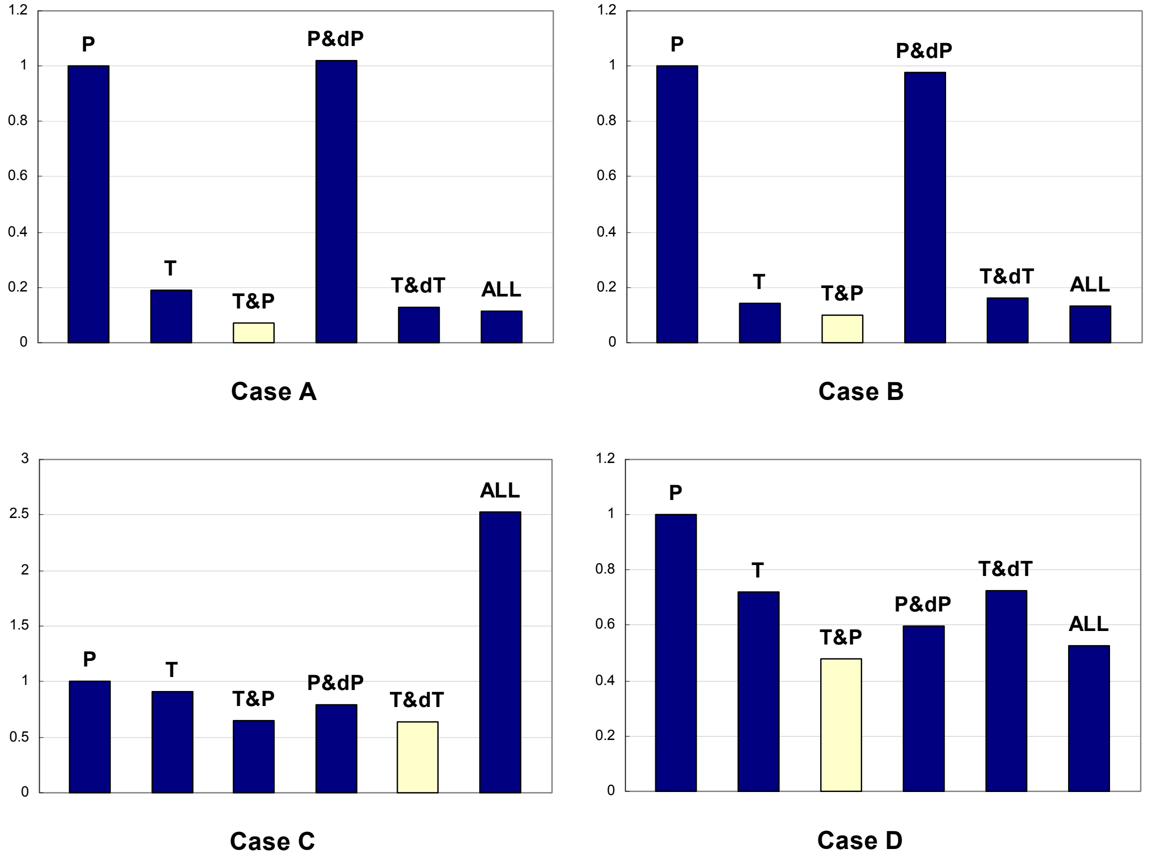

Fig. 6.10 Error comparisons (single-phase oil production).

Experiments for single-phase gas production. We perform the same experiments for single-phase gas production. The permeability distributions used as true distribution are displayed in **Fig. 6.11**. Similarly to the previous experiments, high permeability (100 md) zone and low permeability (10 md) are located alternately. Again, we examine the goodness of inversion results when using different combinations of input data while flow rate is always given. As an initial permeability distribution, homogeneous 50 md distribution is considered.

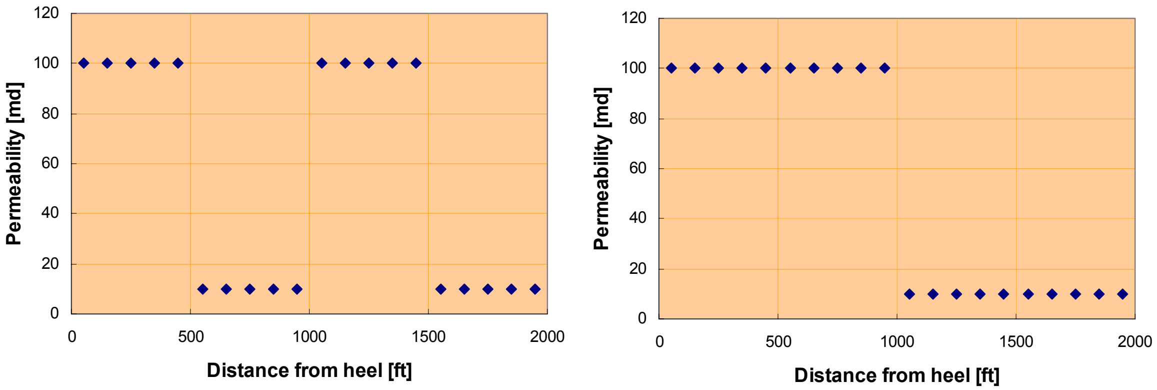

Case A

Case B

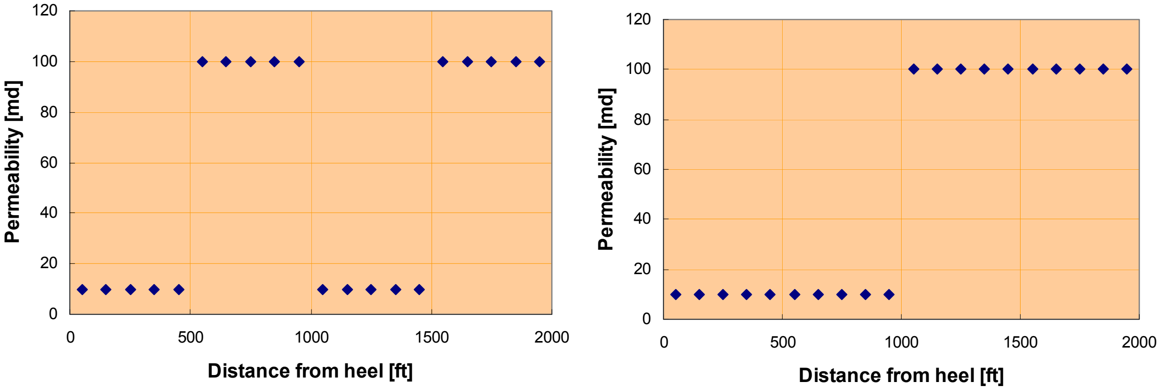

Case C

Case D

Fig. 6.11 Four different permeability distributions along a horizontal well.

We show an example of the observation and matched curves discrepancy. The observed curves of case A and the matched curves are depicted in **Fig. 6.12**. The choice of pressure data only shows a close match of the pressure curve while its temperature curve slightly deviates from the observation. On the other hand, the matched curves from temperature data only show poor matches for both pressure and temperature curves. These discrepancies can be seen more clearly in the derivative of the data. Interestingly, the choice of all input data provides better matches than these choices.

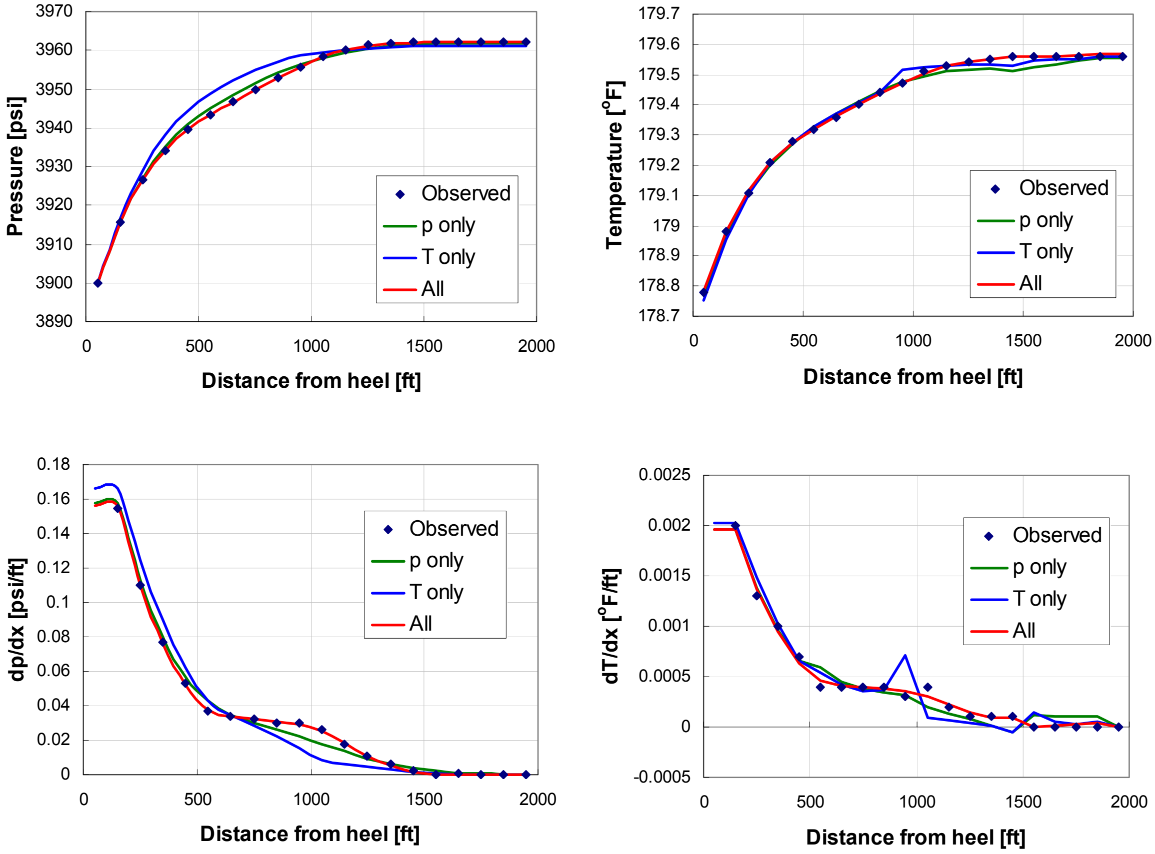

Fig.6.12 Observation and matched curves with different input data (Case A, gas).

The inversion of permeability results are shown in **Fig. 6.13**. As expected, the results from the choices of pressure data only and temperature data only did not capture the features of the permeability profile well while the combination of pressure and temperature and their derivatives gives a close match to the true permeability distribution. Obtained flow rate profile shows a very close match with the observed one.

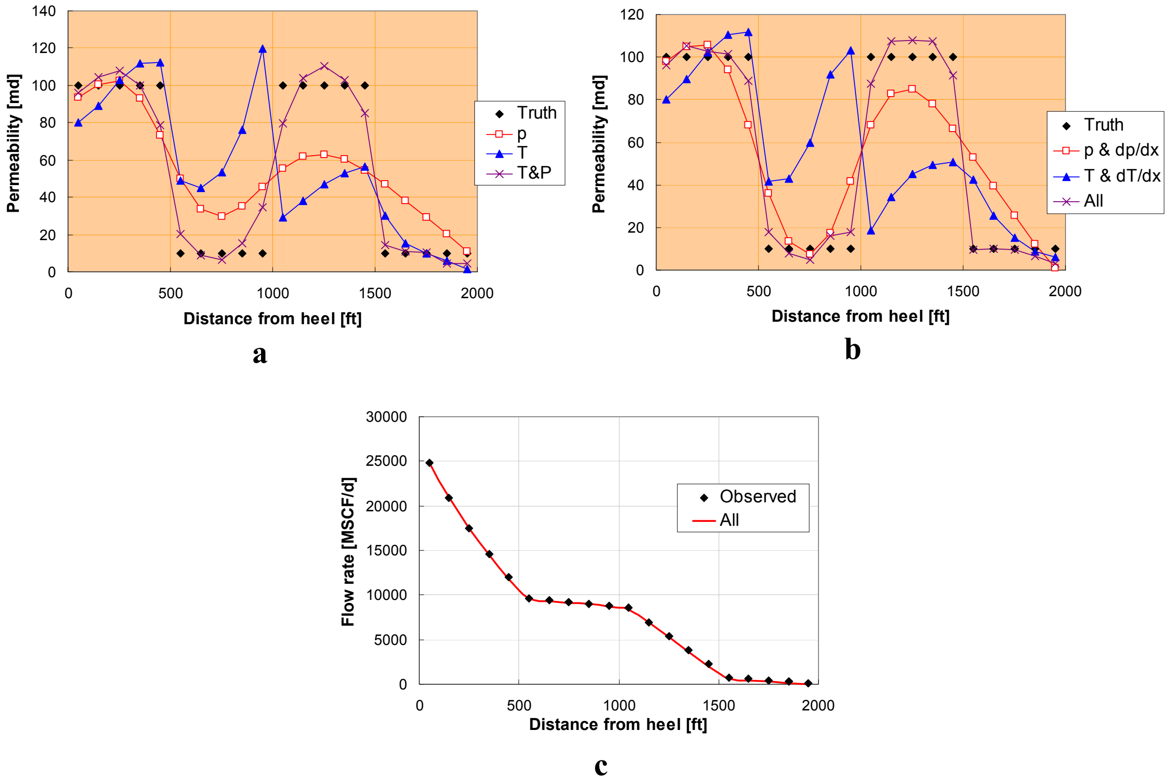

a

b

c

Fig. 6.13 Inverted results for case A, (a) permeability distributions from original data. (b) permeability distributions from derivative of the data, and (c) flow rate profile from all input data.

We performed the permeability inversions for other cases as well. As we have observed in the experiments with single-phase oil production, there is no single best choice of the input data. One combination performs better one time, and another choice performs better another time. **Fig. 6.14** summarizes the inversion results from single-phase gas production. Except for case C, including all the input data gave the best results.

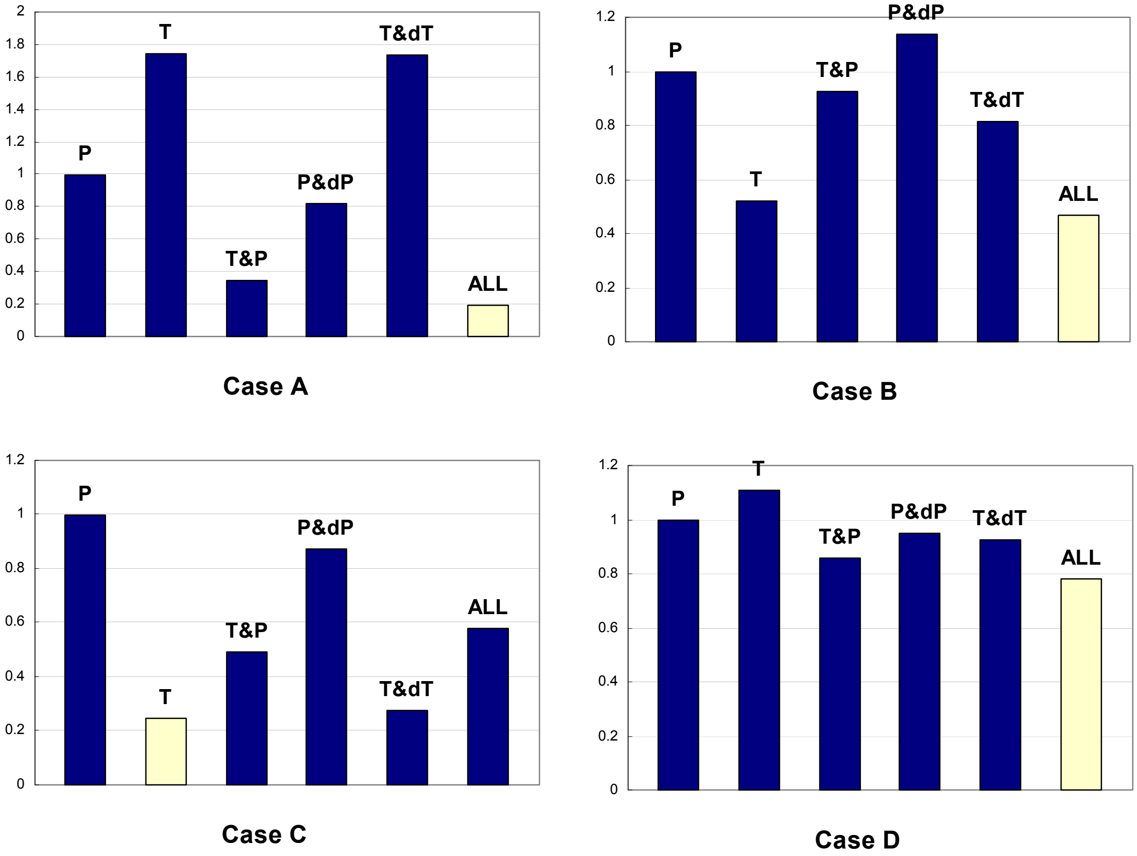

Case A

Case B

Case C

Case D

Fig. 6.14 Error comparisons (single-phase gas production).

The choice of input data. Through these experiments to determine the best choice of input data combinations for single-phase oil and gas, we have seen most of the time giving multiple input data provides better permeability inversion than the single input data. In order for us to determine the best choice, we took an average of normalized permeability distribution errors. The comparison is shown in Fig. **6.16.** The combination of temperature and pressure provides the least error above all the choices. Therefore, we select temperature and pressure profiles as input data to the inversion process in addition to flow rate in further discussion.

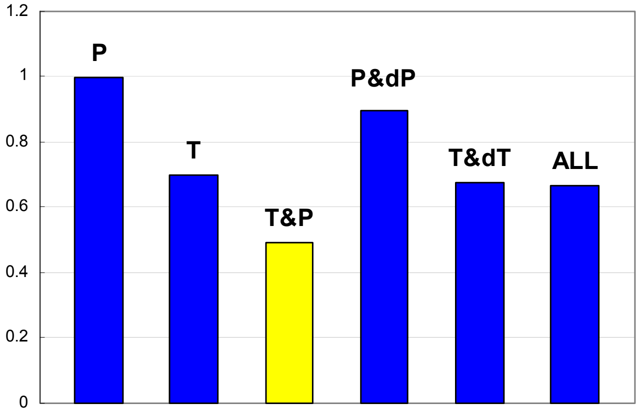

Fig. 6.15 Average of normalized errors.

6.4.2 Single-Phase Inversion

In the determination of input data choice, we considered horizontal wells producing high flow rates to obtain substantial wellbore effects. The inversions of permeability distribution were promising for those cases. In this section, we use a well with large diameter described in **Table 5.1** with larger bottomhole pressure to have small production rate (small wellbore effect) to generate "pessimistic" conditions that have small pressure drop and small temperature changes along the well. We again invert the permeability distributions of cases A and B shown in **Fig. 6.4** for single-phase oil production and in **Fig. 6.11** for single-phase gas production. For inversion of the permeability profile, we select pressure and temperature as observed data choice as determined in the last section.

Single-phase oil production. With large diameter well and bottomhole pressure 3900 psi instead of 3600 psi, the generated observations of pressure and temperature profiles are shown in **Fig. 6.16**. The total flow rate is 7767 b/d. Overall pressure drop in the well is only about 7 psi and the temperature change is 0.04 ^{o}F as shown in the figures. The matched curves are also depicted in **Fig. 6.16**. Because the resolution of temperature is restricted to 0.01 ^{o}F, temperature profile is discretized. Yet, the observed and inverted profiles closely matched. **Fig. 6.17** shows the inverted permeability distribution and flow rate profile. Despite the small changes of pressure and temperature profile, the inverted profile reproduced the feature of the true profile quite well.

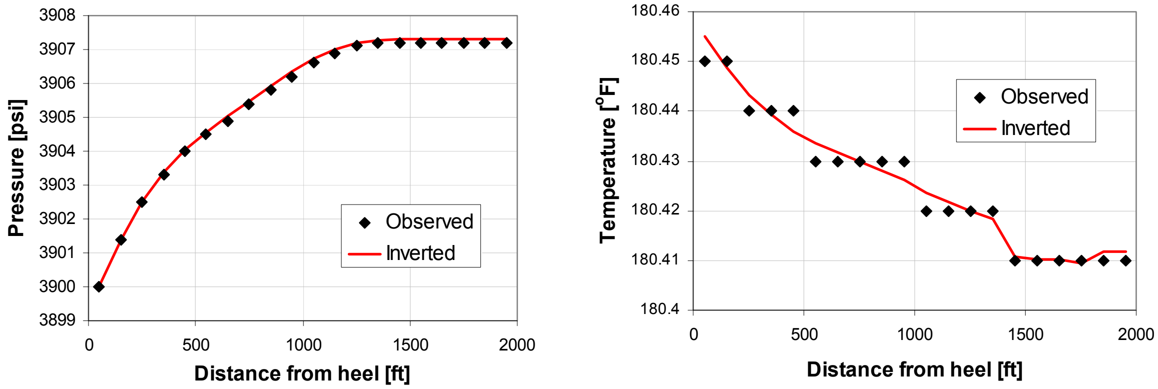

Fig. 6.16 Observed and matched curves (case A, oil).

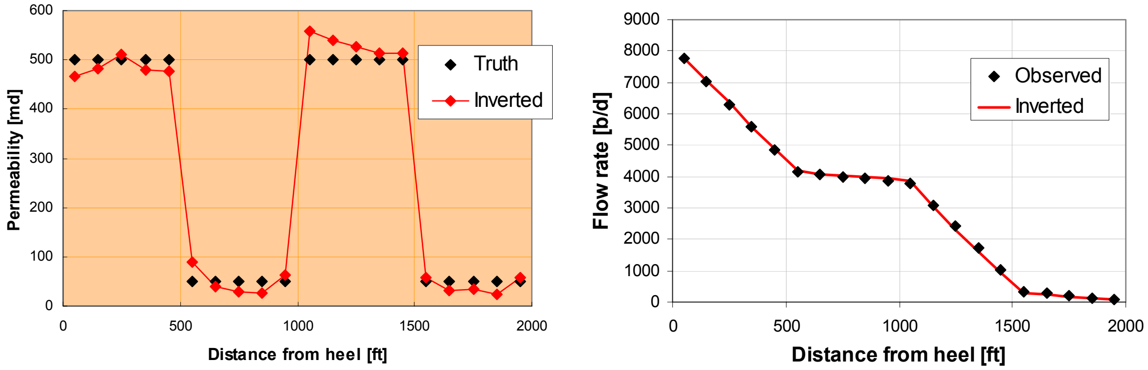

a **b**

Fig. 6.17 Inverted (a) permeability distribution and (b) flow rate profile (case A, oil).

Fig. 6.18 shows the observed profiles with the permeability distribution of the case B. The total flow rate is 7842 b/d. Also, the pressure drop (15 psi) and temperature changes (0.07 ^{o}F) are very limited. The obtained matches are very close. The inverted permeability distribution and flow rate are compared with the true distribution and shown in **Fig. 6.19**. In **Fig. 6.19a**, the low permeability zone near the toe is well represented but the inversion of the high permeability zone near the heel shows some differences. However, the overall permeability prediction is good and obtained flow rate profile (**Fig. 6.19b**) shows a close match.

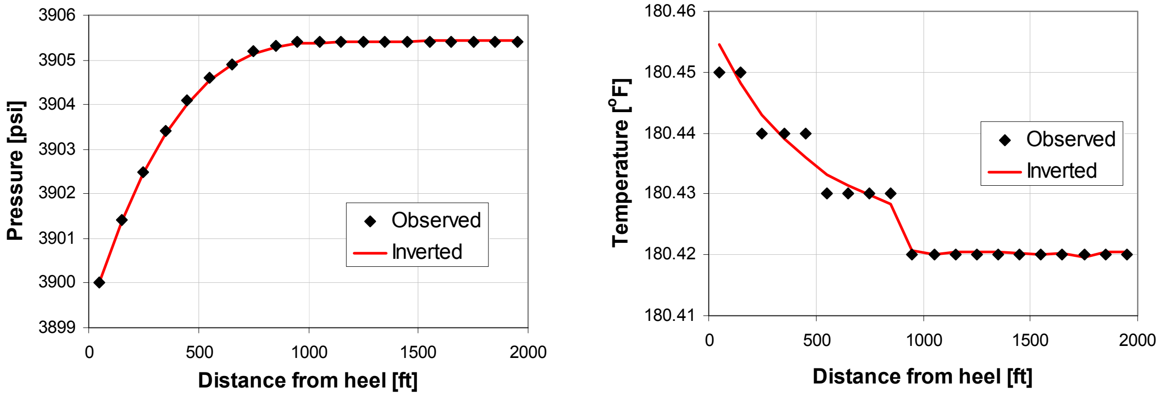

Fig. 6.18 Observed and matched curves (case B, oil).

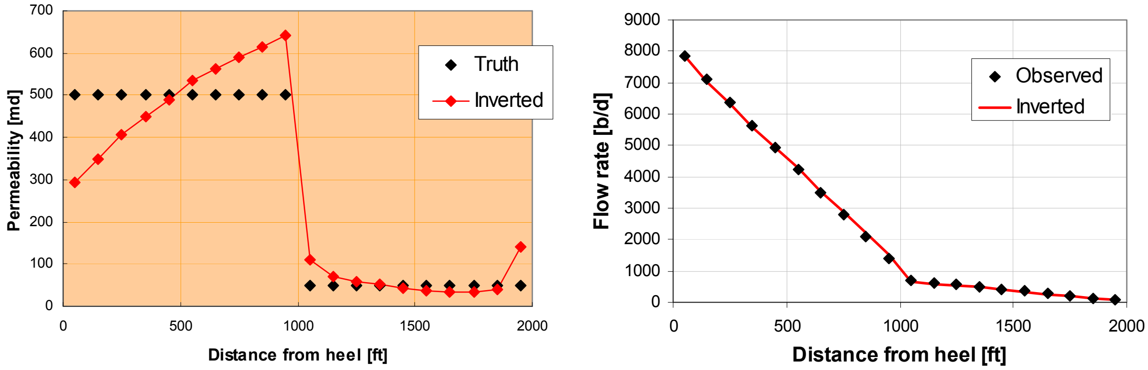

Fig. 6.19 Inverted (a) permeability distribution and (b) flow rate profile (case B, oil).

Single-phase gas production. Now we perform the permeability inversion with single-phase gas production. The well used for the calculation is the same and the bottomhole pressure is set at 3980 psi this time. **Fig. 6.20** shows the observed pressure and temperature profiles with the inverted curves for case A permeability profile. The total flow rate at the surface is 8449 MSCF/d.

The pressure drop in the horizontal well is about 1.4 psi and the overall temperature change is 0.02 ^{o}F. Both the inverted temperature and pressure curves give very close match to the observations. The inverted permeability and flow rate profiles are shown in **Fig. 6.21**. Even though the changes along the well are small, the inverted permeability and flow rate profiles capture the features of the true profiles well.

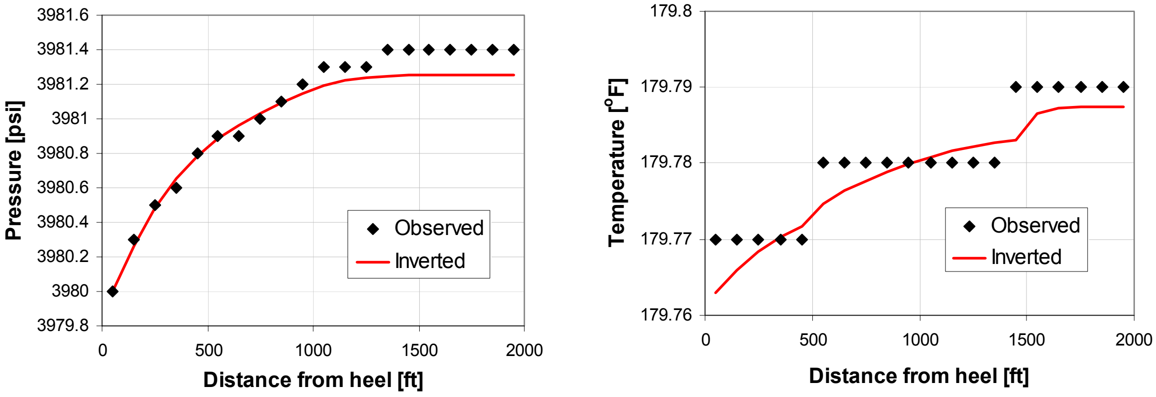

Fig. 6.20 Observed and matched curves (case A, gas).

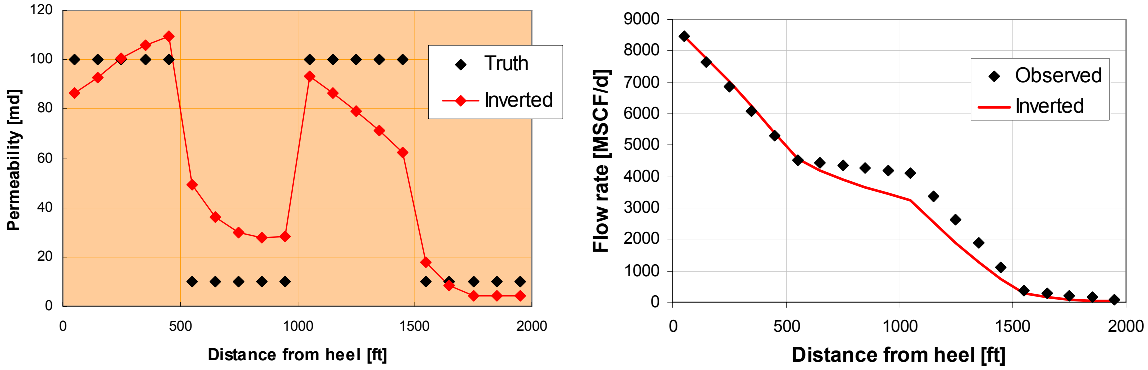

a **b**

Fig. 6.21 Inverted (a) permeability distribution and (b) flow rate (case A, gas).

With the true permeability profile of case B, the total production is 8529 MSCF/d. The total pressure drop in the well is about 1 psi and the total temperature cooling is 0.02 ^{o}F. **Fig. 6.22** shows the observed profiles and the matched curves. Both pressure and temperature profiles are closely matched. The inverted results are depicted in **Fig. 6.23**. The inverted permeability gives a profile close to the true except for the near heel region. Although the temperature profile is matched very well, the change itself is limited and is not captured by the measurement. If the measurement resolution were high, the temperature drop caused by high permeability zone near the heel would appear clearly and better permeability distribution could be inverted. However, this permeability difference near the heel does not affect much on the flow rate profile as shown in **Fig. 6.23b**.

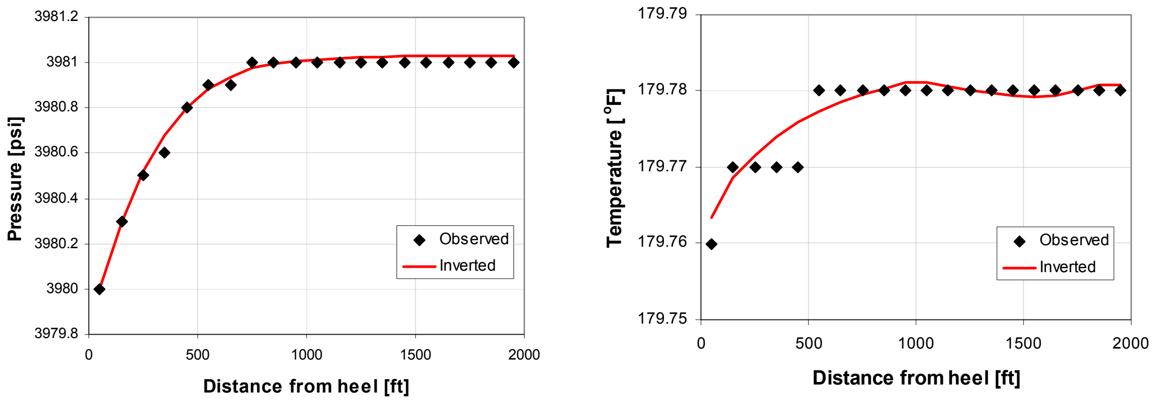

Fig. 6.22 Observed and matched curves (case B, gas).

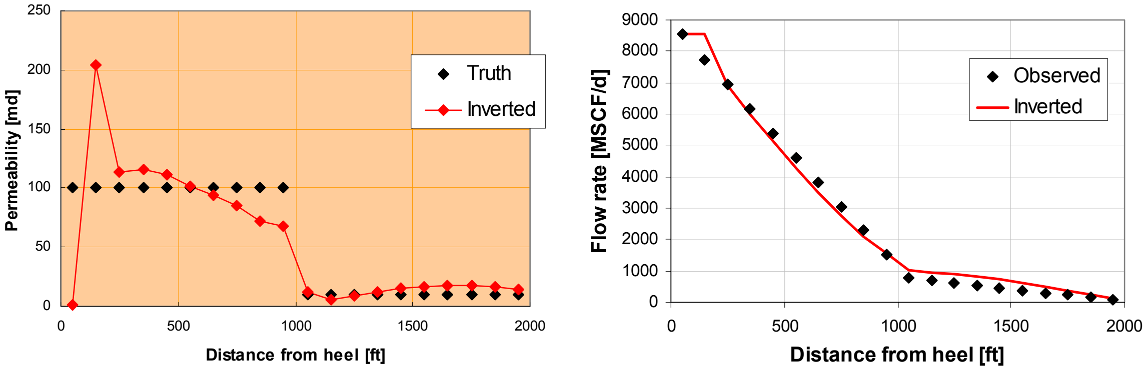

a **b**

Fig. 6.23 Inverted (a) permeability distribution and (b) flow rate profile (case B, gas).

6.4.3 Water Entry Detection

When water is produced, we can detect its entry from the wellbore temperature cooling if the water and oil are produced from the same level (same boundary temperature). We show water entry examples of water entering from two regions (900 – 1100 ft, and 1600 – 1800 ft from heel) and invert the permeabilities of these zones.

For a first example, we consider a permeability profile as shown in **Fig. 6.24**. Two water entry zones are indicated in the figure. Observations generated based on this permeability field are shown **in Fig. 6.25.** The well with large diameter described in **Table 4.1** is used and the bottomhole pressure is set as 3600 psi. As depicted in **Fig. 6.25a**, we have two water entry zones: one at the middle and the other at near the heel of the well. For each water entry zone, the wellbore temperature is cooled as shown in **Fig. 6.25c**, while the pressure profile (**Fig. 6.25b**) does not show any signs of water entries. For this case, both water entry zones have equal permeability.

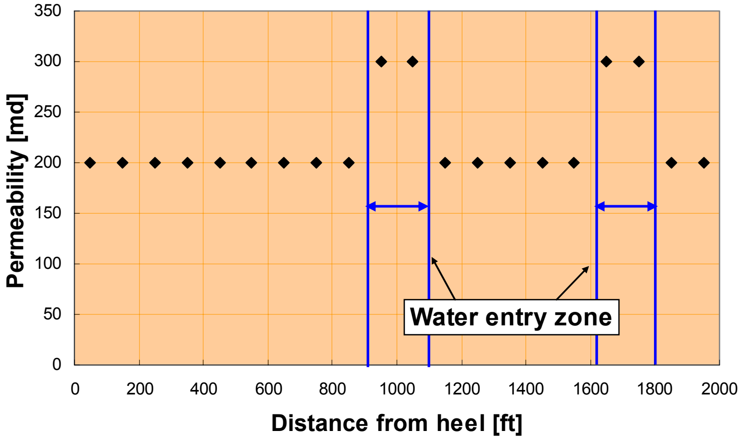

Fig. 6.24 Permeability distribution and water entry zones.

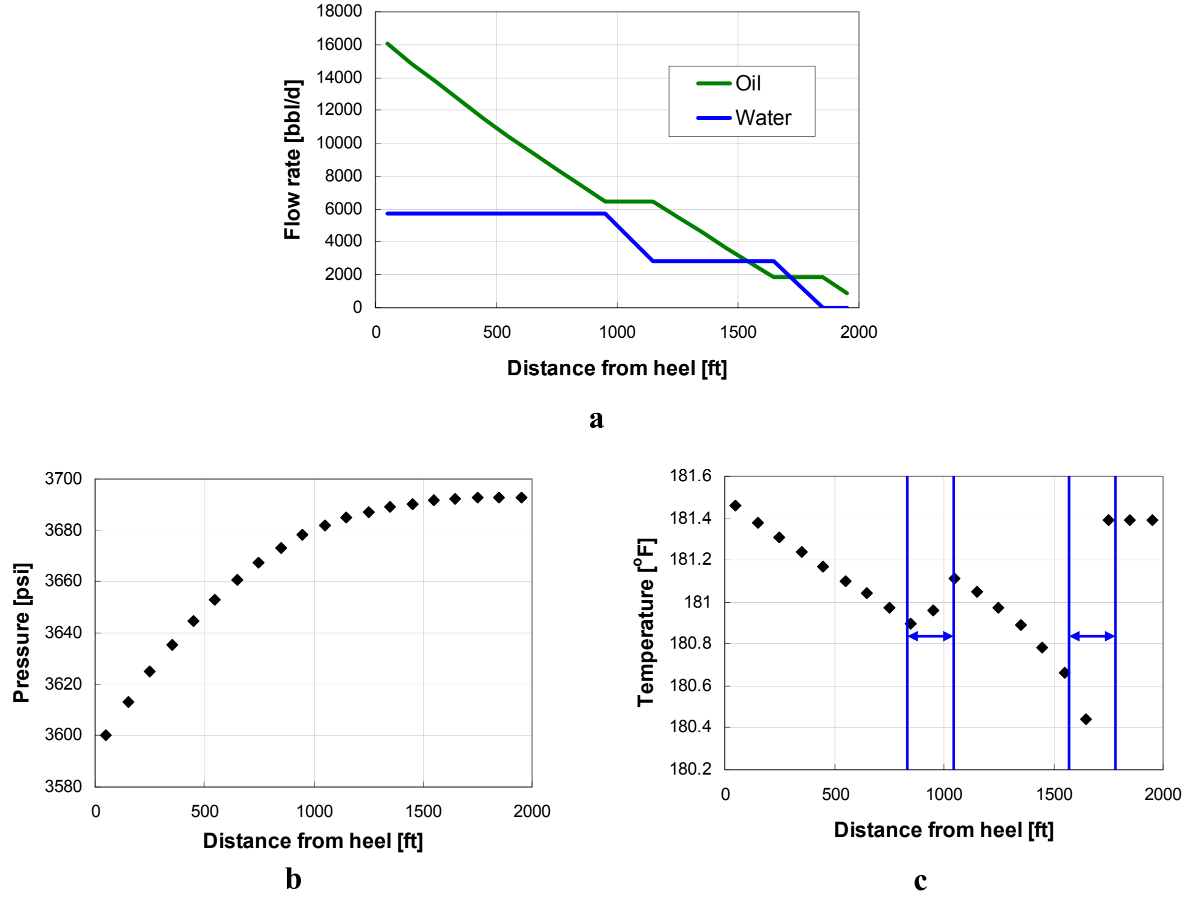

Fig. 6.25 Generated observations (a) flow rate, (b) pressure, and (c) temperature profiles.

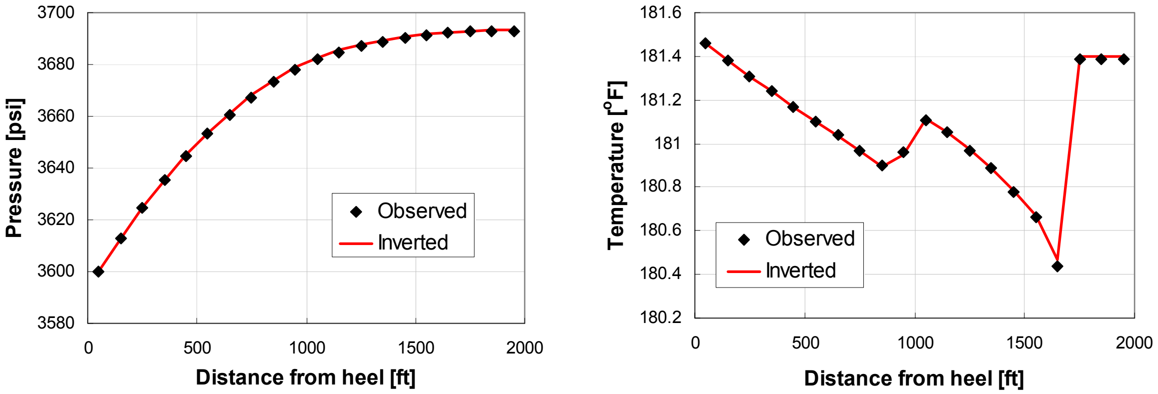

Fig. 6.26 Observations and matched curves (water entry).

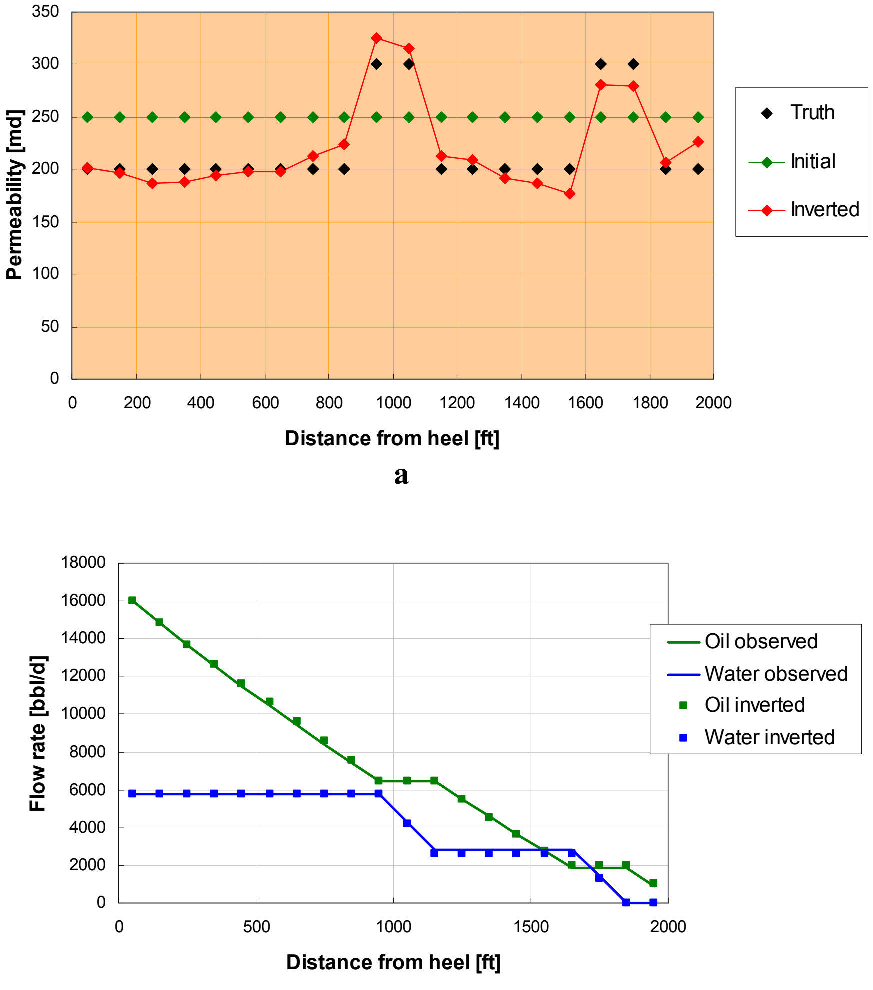

a

b

Fig. 6.27 Inverted (a) permeability distribution and (b) flow rate profiles (water entry).

We inverted the permeabilities of the water entry zones and the permeabilities of the oil producing zone by matching the pressure and temperature profiles, and the flow rates of oil and water. The matched temperature and pressure curves are displayed in **Fig. 6.26** and the inverted permeability distribution and flow rate profile are in **Fig. 6.27**. Both the temperature and pressure profiles are closely fitted by the inversion method. As a consequence, we were able to reproduce very accurate permeability and flow rate profiles for the two water entry zones.

In the next example, we consider the case in which water entry from the middle is smaller than the one from near the heel. The permeability profile shown in **Fig. 6.28** is considered as the true profile. The generated flow rate and temperature profiles according to this permeability distribution are shown in **Fig. 6.29**.

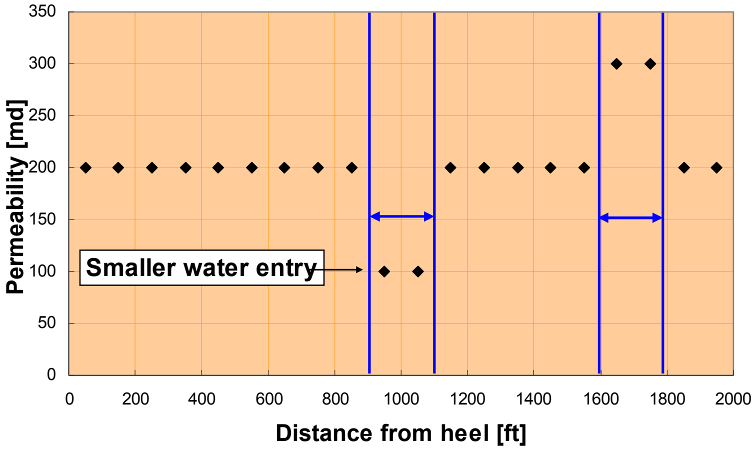

Fig. 6.28 Permeability distribution and water entry zones.

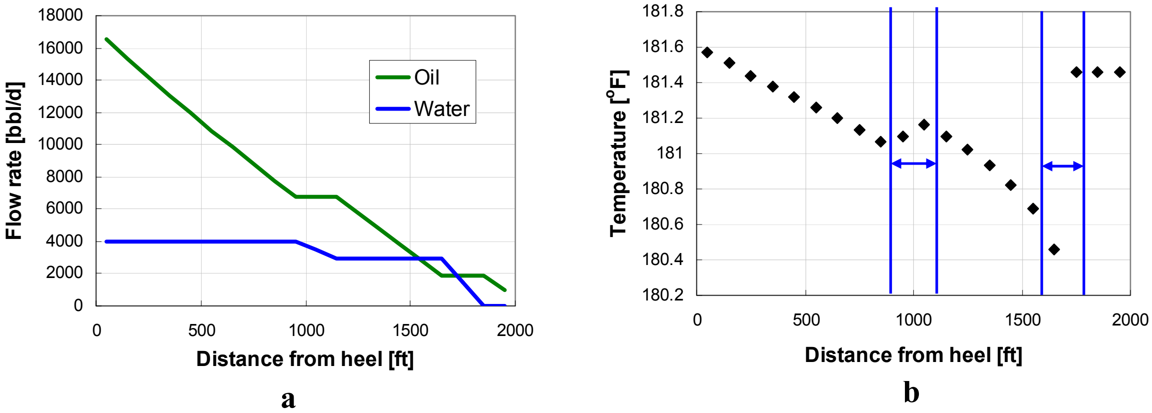

Fig. 6.29 Generated observations (a) flow rate and (b) temperature profiles.

Again, we can find the water entry zones by looking for temperature drop along the well. The true permeability distribution is inferred by matching the production data. The matched curves are depicted in **Fig. 6.30** and the obtained permeability and flow rate distributions are shown in **Fig. 6.31**.

The observations were regenerated very precisely as depicted in **Fig. 6.30**. As we have observed in Chapter 4, the wellbore temperature cooling by water entry are mainly determined by the location of the entry zone and the water production rate. The cooling effect is more emphasized as its flow rate becomes higher and as it occurs closer to the heel. Therefore, in this case, the temperature cooling at the middle is less significant than the previous water entry example. The permeability inversion still shows a good match with the true permeability distribution. Also, the flow rates in both water entry region are precisely inverted.

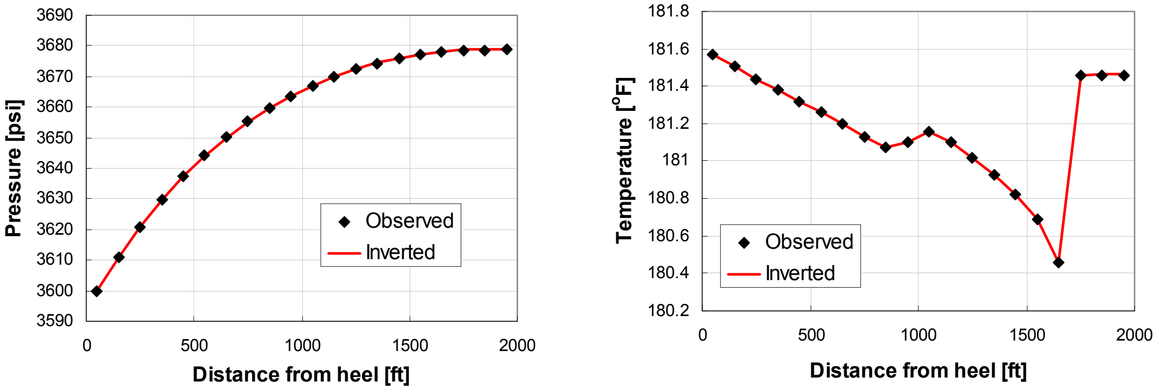

Fig. 6.30 Observations and matched curves (water entry).

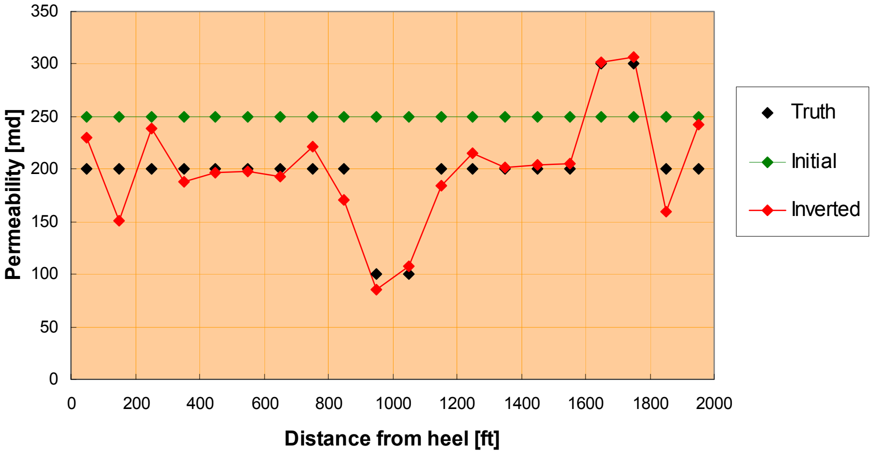

a

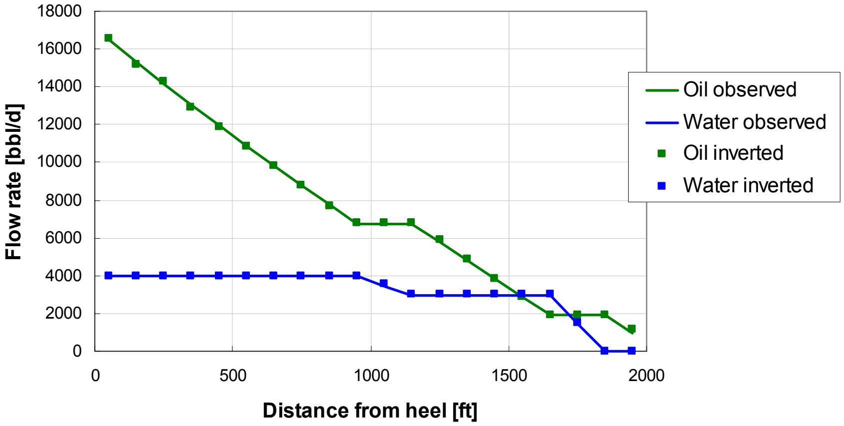

b

Fig. 6.31 Inverted (a) permeability distribution and (b) flow rate profiles (water entry).

For a last example of water entry, we consider a smaller water flow rate near the toe as shown in **Fig. 6.32**. The temperature drop near the toe, as can be expected, became less and at the middle it became more. The observed profiles and the inverted profiles are shown in **Fig. 6.33**. The inverted pressure and temperature curves are accurately matched with the observation. The inverted permeability and flow rate profiles are shown in **Fig. 6.34**. The obtained permeability distribution predicts both water entry zones' permeability very closely. The flows rates of both water and oil are closely matched as well.

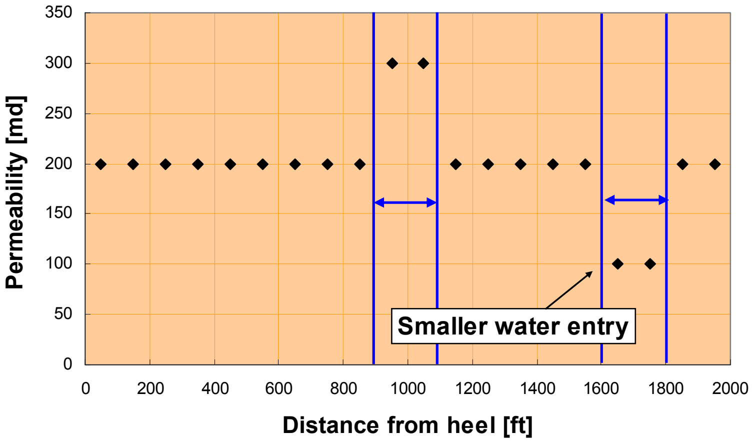

Fig. 6.32 Permeability distribution and water entry zones.

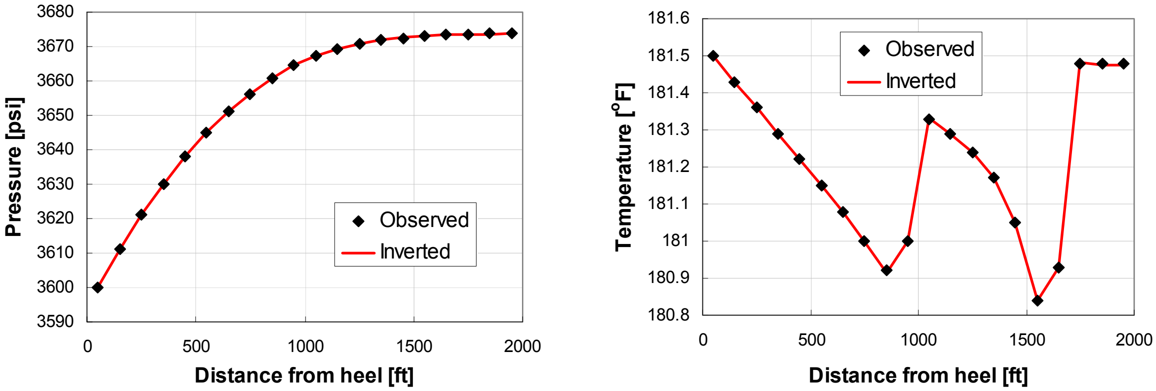

Fig. 6.33 Observations and matched curves (water entry).

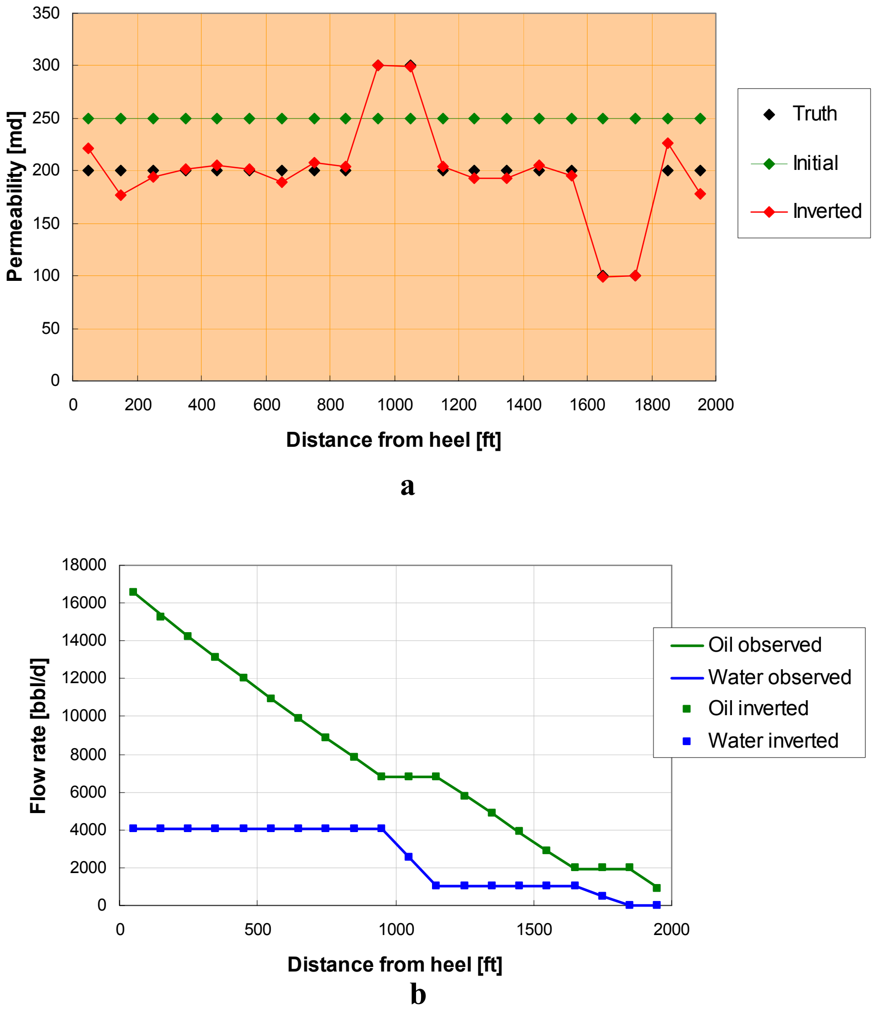

Fig. 6.34 Inverted (a) permeability distribution and (b) flow rates profiles (water entry).

6.4.4 Gas Entry Detection

Similarly to water entry, gas entry cools the wellbore. However, the cooling effect by gas is much larger than that of water because the gas temperature actually cools off below the geothermal temperature while oil and water warm up. Therefore, the detection of gas becomes relatively easy as discussed in Chapter 4. In this section, we show examples of permeability inversions when oil and gas are produced. Again, we consider two gas entry regions: one is located near the toe (1,600 – 1,800 ft from heel). The other one is at the middle (900 – 1,100 ft from heel). The well properties are the same as the water entry example except for bottomhole pressure which is set at 3900 psi.

As a first example, we consider the two gas entry zones having the same permeability (20 md) while the oil permeability is 200 md as shown in **Fig. 6.35.** The observations (flow rate, pressure, and temperature profiles) from this permeability distribution are also shown in **Fig. 6.36**. As can be found from **Fig. 6.36a**, gas entered into the well from two regions. Similarly, whereas we cannot see any indications of gas production on the pressure profile (**Fig. 6.36b**), the locations of gas entries can be found from the temperature profile by detecting the temperature drop as depicted in **Fig. 6.36c**. We give the total flow rates of each phase, and pressure and temperature profiles to the inversion process as input data in this case as well.

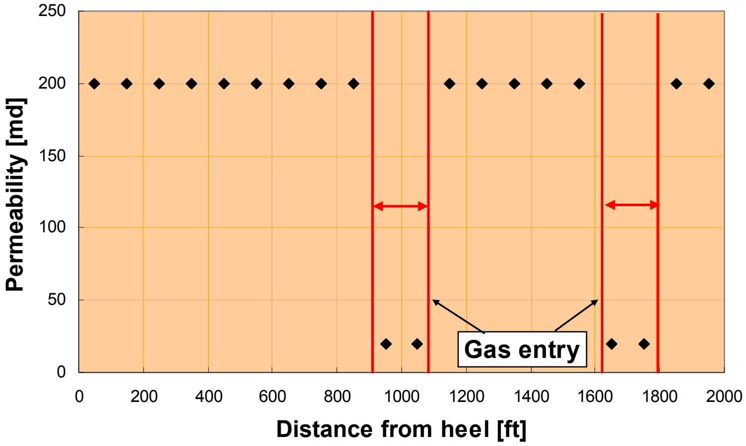

Fig. 6.35 Permeability distribution and gas entry zones.

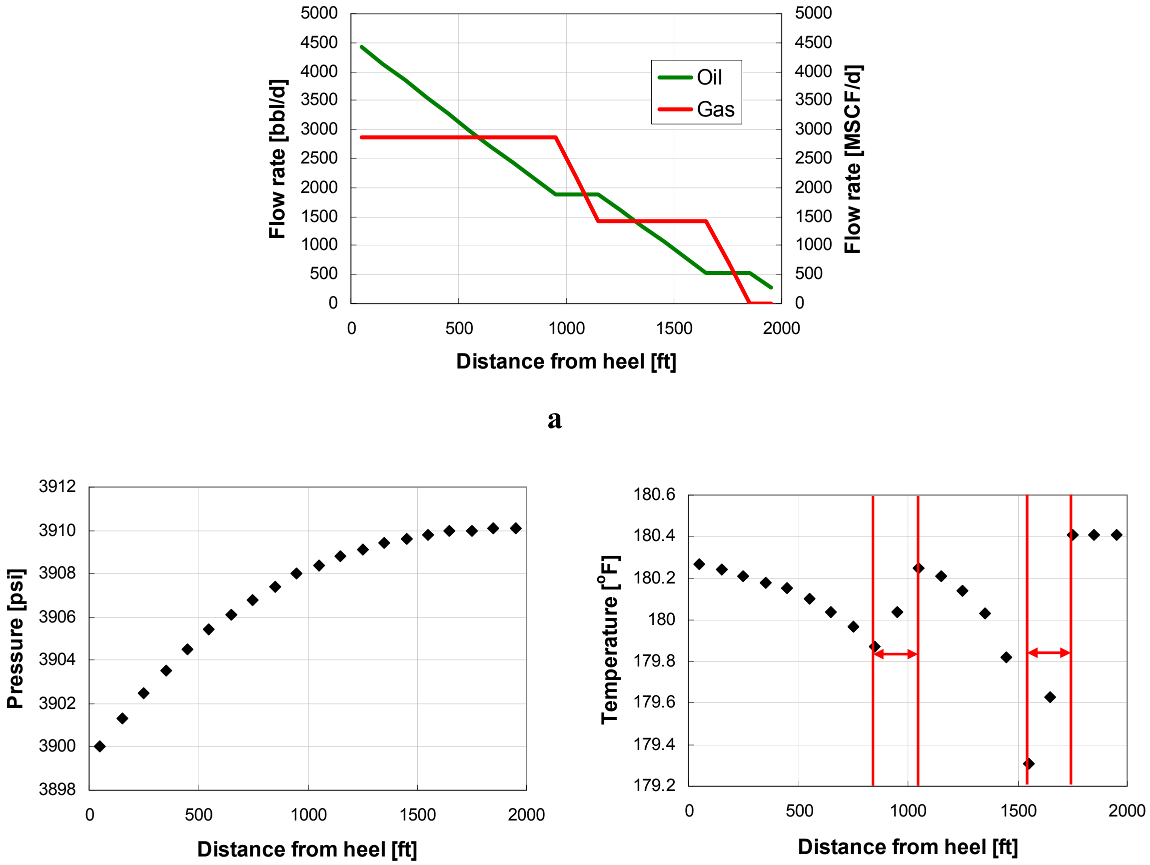

a

b

c

Fig. 6.36 Generated observations (a) flow rate, (b) pressure, and (c) temperature profiles.

The matched pressure and temperature profiles are shown in **Fig. 6.37** and the inverted permeability and flow rate distributions are shown in **Fig. 6.38** with the initial permeability distribution used to start the inversion.

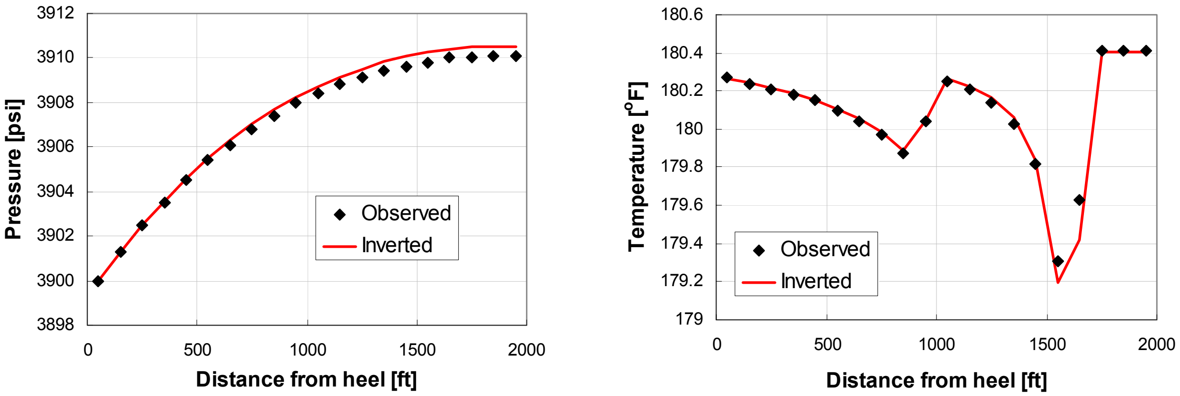

Fig. 6.37 Observations and matched curves (gas entry).

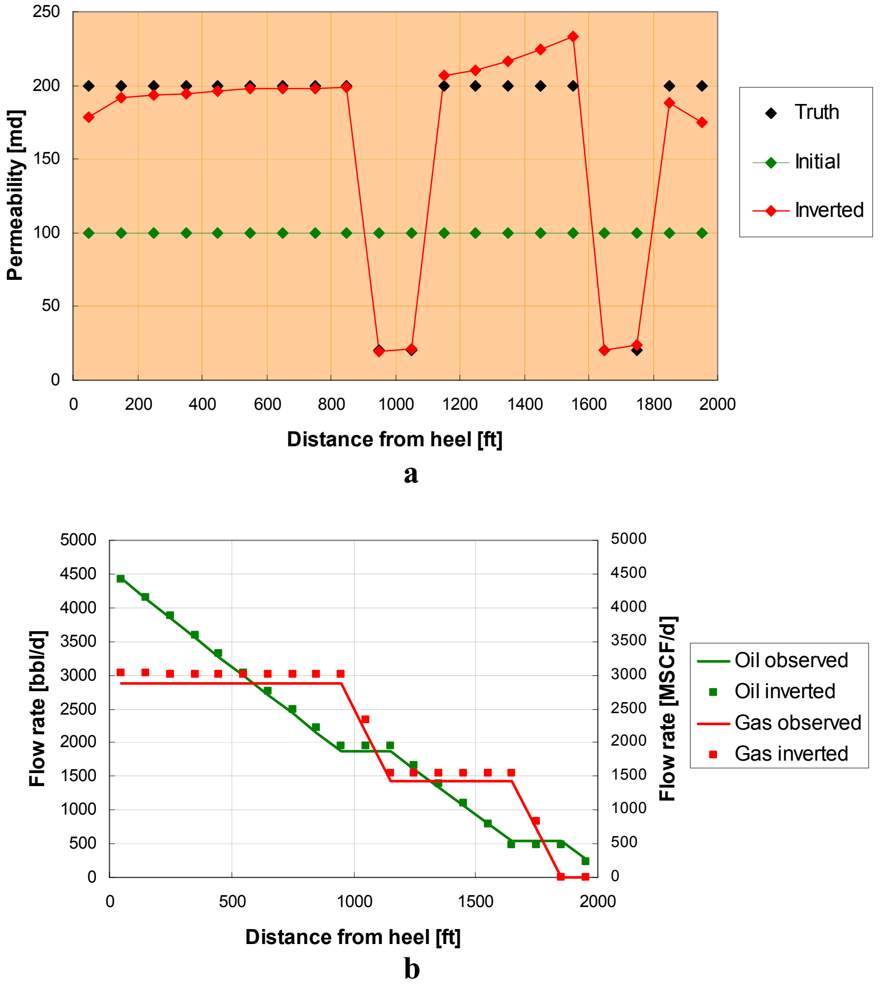

Fig. 6.38 Inverted (a) permeability distribution and (b) flow rates profile (gas entry).

We slightly missed matching the pressure profile near the toe but the other zone and entire temperature profile are very closely matched. The obtained permeability distribution is close to the true permeability distribution. While the oil flow rate profile is successfully reproduced, gas flow rate replication shows slight off from the observation. However, more importantly, the permeabilities of both gas entry zones were predicted accurately.

The next example is the same as the first one except that the middle gas entry zone's permeability is lower (10 md). The matched pressure and temperature profiles are shown in **Fig. 6.39** and the inverted permeability distribution and flow rate profile are shown in **Fig. 6.40**. The temperature and pressure profiles are almost exactly matched. Also, **Fig. 6.40a** shows a very successful permeability inversion result. High and low gas permeabilities of both gas entry zones are predicted correctly. The obtained flow rates profiles are agreed well with the observations.

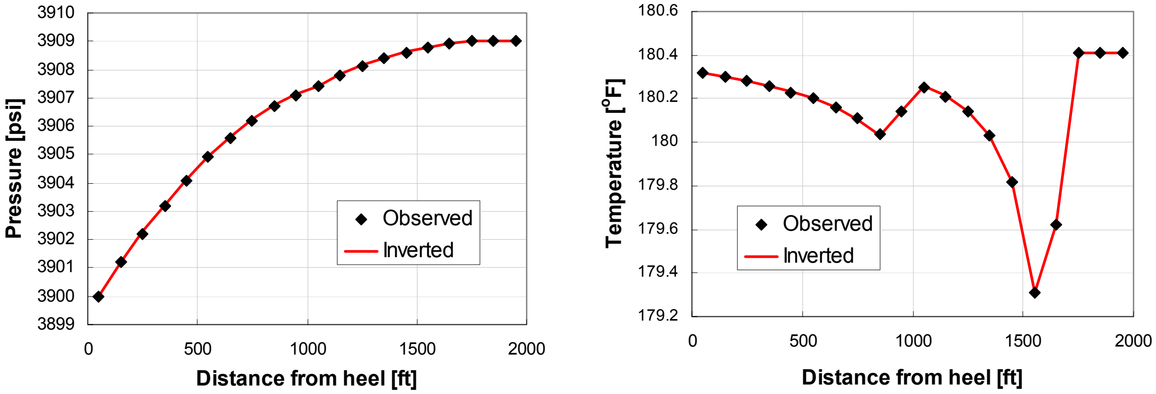

Fig. 6.39 Observations and matched curves (gas entry).

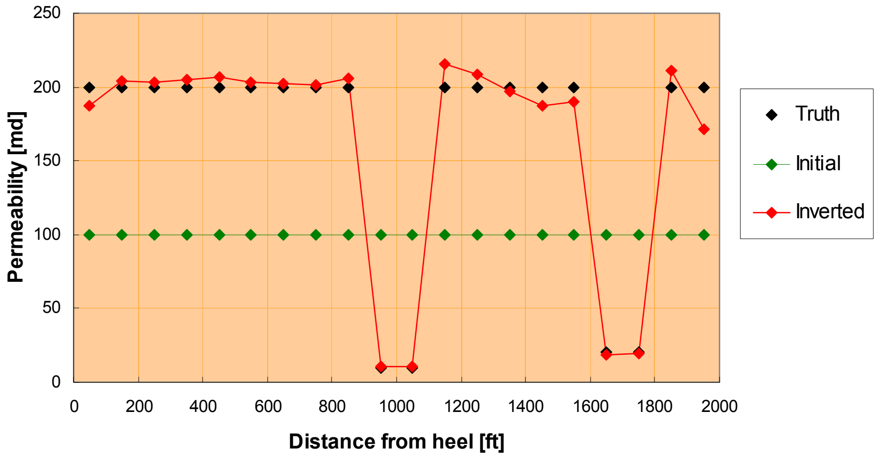

a

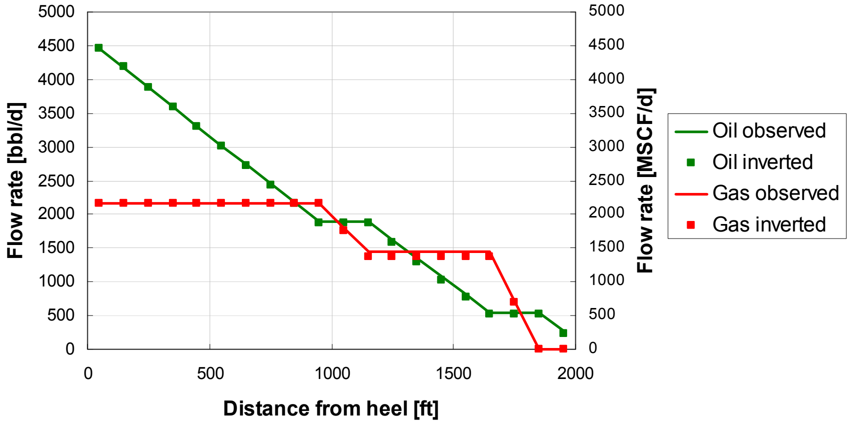

b

Fig. 6.40 Inverted (a) permeability distribution and (b) flow rate profiles (gas entry).

For a last example, we invert the permeability distribution that has low permeability (10 md) gas entry zone near the toe (1600 – 1800 ft from heel) and high permeability (20 md) at the middle (900 – 1100 ft from heel). The matched curves of pressure and temperature are shown in **Fig. 6.41**, and the inverted permeability distribution and flow rate profiles are shown in **Fig. 6.42**.

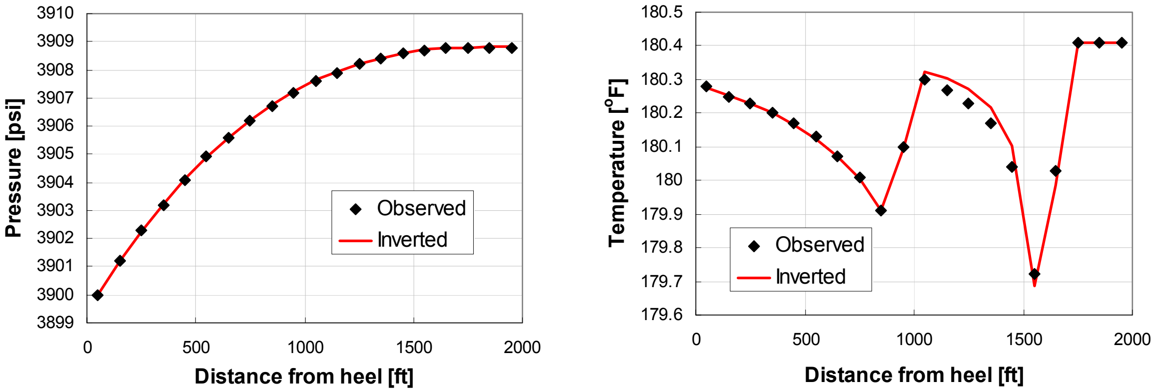

Fig. 6.41 Observations and matched curves (gas entry).

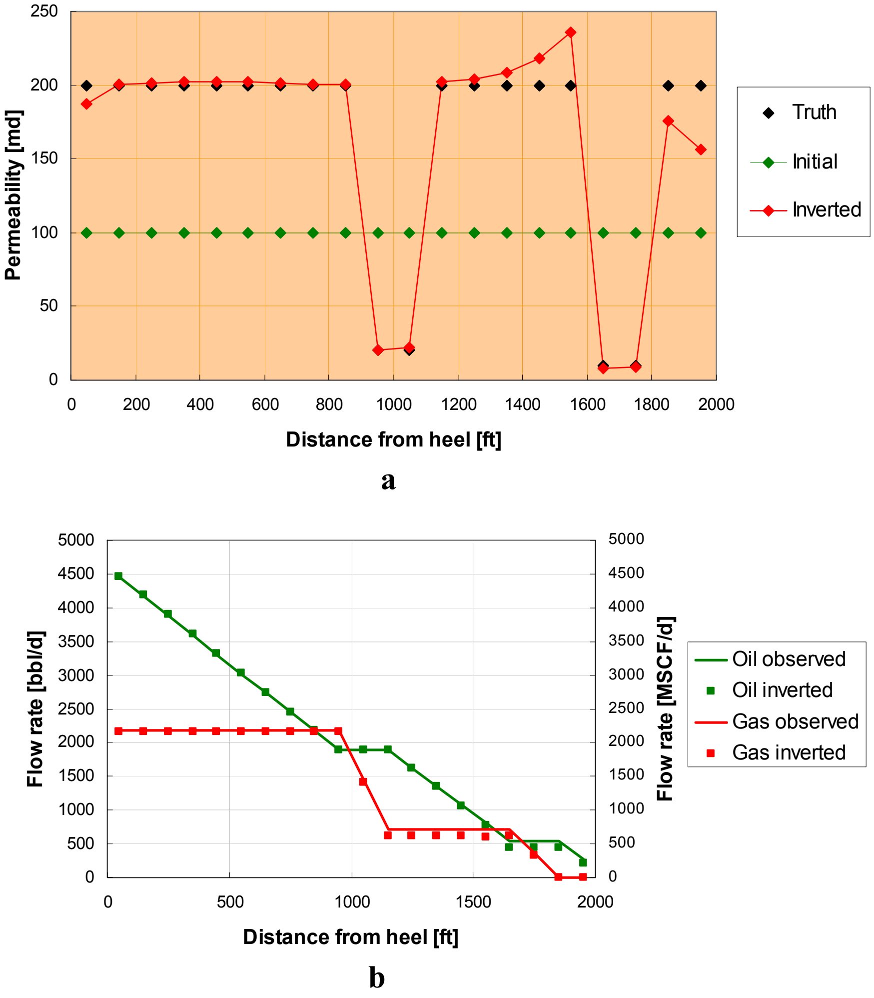

Fig. 6.42 Inverted (a) permeability distribution and (b) flow rate profiles (gas entry).

We can see in **Fig. 6.41** that the observations were almost identically reproduced. The inverted permeability distribution is also fit to the true permeability distribution including gas entry zones so are the obtained flow rate profiles. Compared with the examples of water entry, the inversion results are better. This is because a gas entry tends to create a clearer effect on the temperature profile than a water entry does. Both detection of entry locations and quantification of productivities are easier for gas entries.

6.4.5 Skin Factor Inference

Existence of formation damage changes the pressure profile of the reservoir with a fixed flow rate. This results in, as demonstrated in Chapter 3, inflow temperature increase. Temperature increases are mainly determined by the damaged formation permeability. The effects of the damage zone's radius are limited as shown in **Fig. 3.11**. We also demonstrated the wellbore temperature profile with existence of formation damages in Chapter5. **Fig. 5.18 – 5.21** showed more pronounced formation damage effects as the damage lies closer to the toe.

We apply the inversion method developed to infer the formation damage permeability. Similarly to the examples shown in Chapter 4, we consider a homogeneous reservoir having formation damage near the toe, middle, and heel with various ratios of reduced permeability. Then we study about the predictability of formation damage from temperature profile. The permeability of the reservoir is considered to be 200 md and the well with large diameter with 3600 psi bottomhole pressure is used in the calculation.

Fig. 6.43 shows the observed temperature profiles from the reservoir with formation damage extending 3 ft into the formation over the zone of 1500 – 2000 ft from the heel for 3ft from the wellbore. The ratios of reduced permeability (k_d/k) considered are 1, 0.5, 0.3, and 0.1.

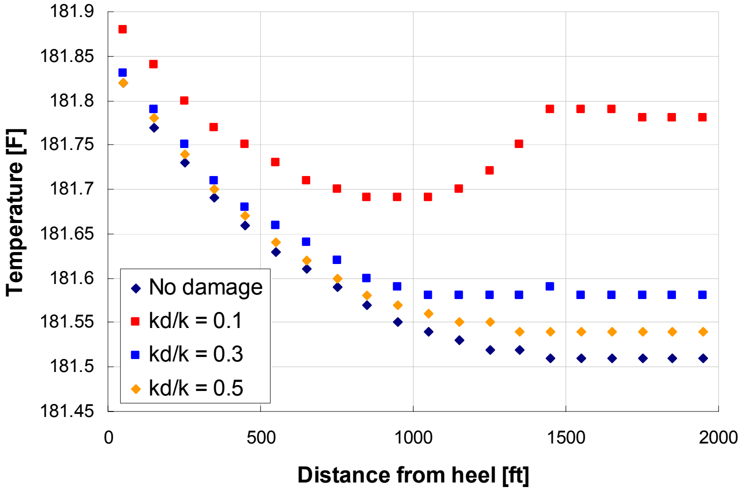

Fig. 6.43 Wellbore temperature profiles with different formation damage.

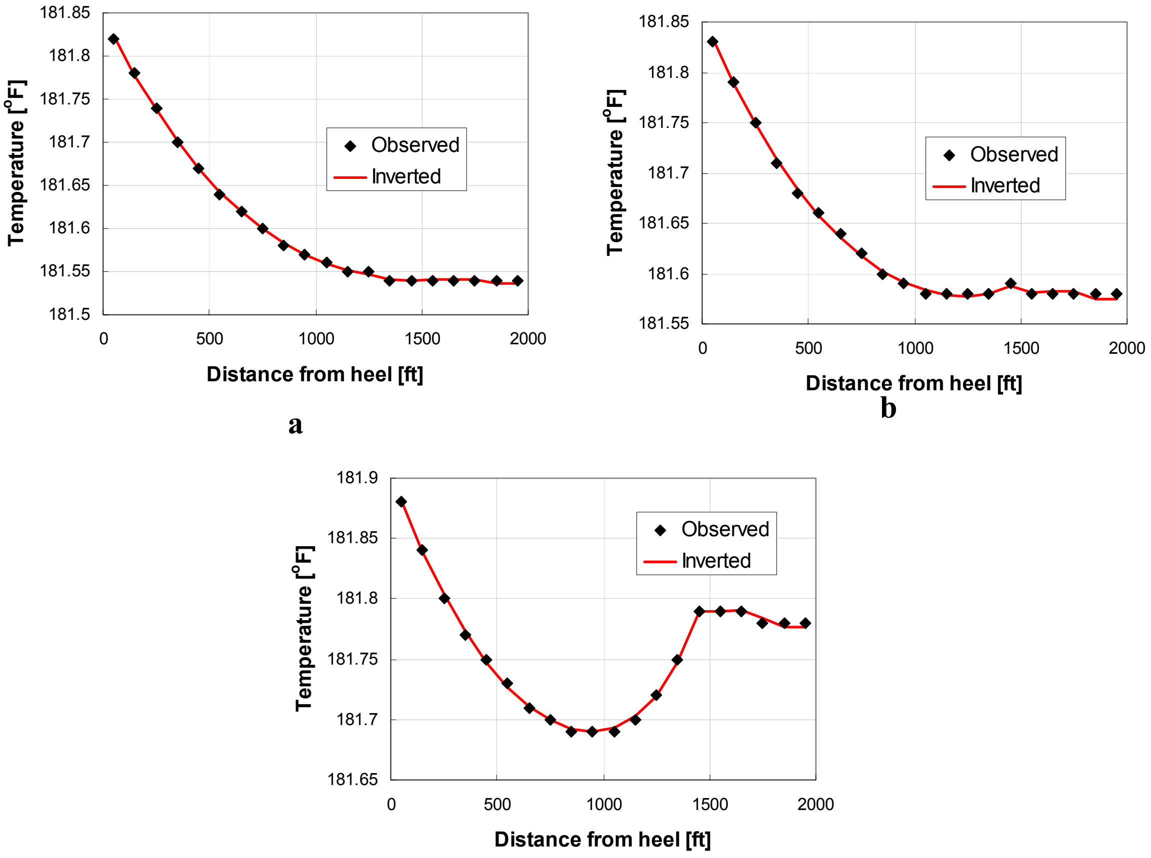

a

b

c

Fig. 6.44 Matched temperature profiles (toe) of (a) k_d/k = 0.5, (b) k_d/k = 0.3, and (c) k_d/k = 0.1

We inverted the damaged permeability by matching the temperature profiles. The matched temperature profiles are shown in **Fig. 6.44** and the inverted damage skin factors are shown in **Fig. 6.45**. We can see that the inversion result becomes better as the damage becomes more severe. The more the reservoir is damaged, the more the temperature profiles are affected and therefore, the more chance we have to infer the damage skin factor. For k_d/k = 0.5 and k_d/k = 0.3 cases, even though the temperature profiles are closely matched, we obtained different skin factor results.

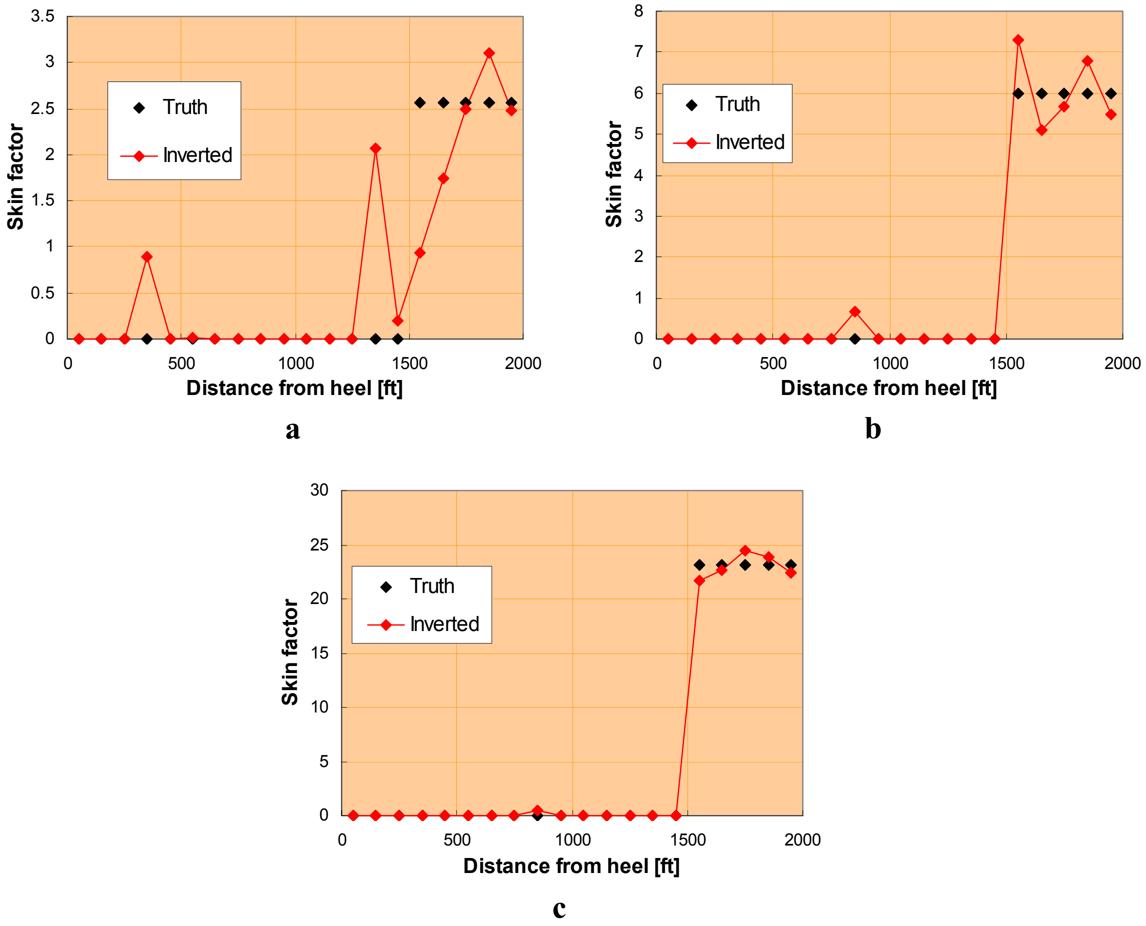

a

b

c

Fig. 6.45 True and inverted damage skin profiles (toe) of (a) k_d/k = 0.5, (b) k_d/k = 0.3, and (c) k_d/k = 0.1

If the damage zone is located closer to the heel, its effect on temperature profile becomes smaller. We next show the prediction of skin factor for the reservoir with damage zone at the middle (800 – 1300 ft from the heel). The observed and matched temperature profiles are shown together in **Fig. 6.46** and the inverted skin factor profiles are shown in **Fig. 6.47**.

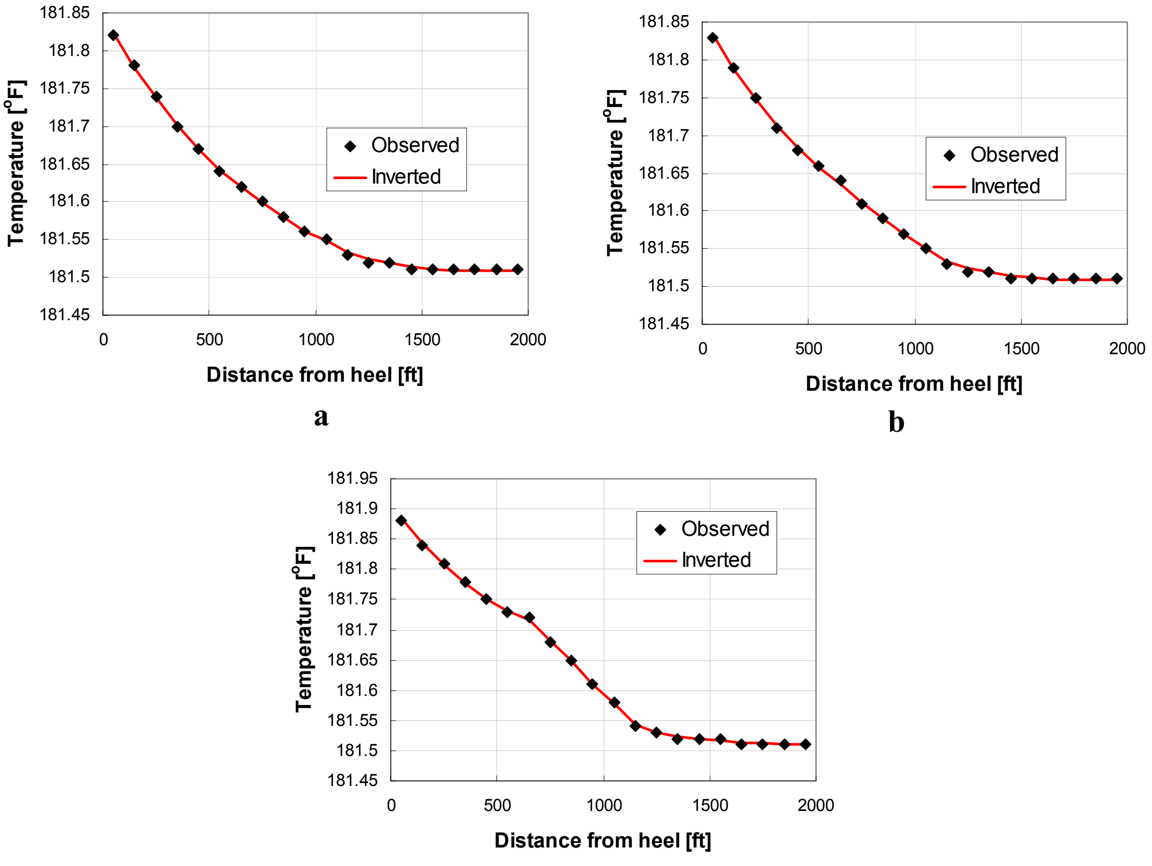

a

b

c

Fig. 6.46 Observed and matched temperature profiles (middle) of (a) k_d/k = 0.5, (b) k_d/k = 0.3, and (c) k_d/k = 0.1

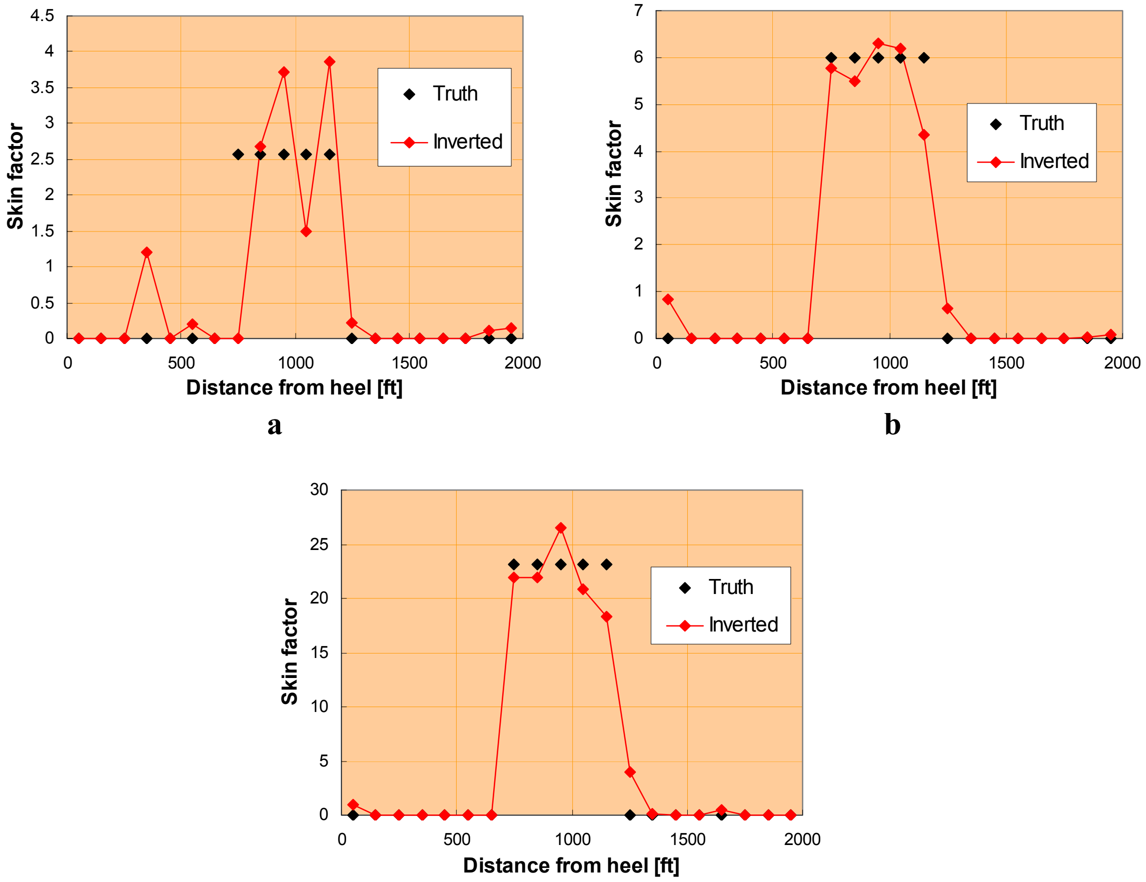

a **b**

c

Fig. 6.47 True and inverted damage skin profiles (middle) of (a) k_d/k = 0.5, (b) k_d/k = 0.3, and (c) k_d/k = 0.1

The observed temperature profiles are precisely reproduced as shown in **Fig. 6.46**. For k_d/k = 0.5 case, the profile of damage skin factor is not predicted well. However, the skin factor profiles of k_d/k = 0.3, and k_d/k = 0.1 are reasonably predicted from the temperature profile despite the small changes of temperature.

The last example contains the cases of damage zone being near the heel (0 – 500 ft from the heel). The true and inverted skin factor profiles are depicted in **Fig. 6.48**. Large skin factor can be detected by the temperature profile. However, for the temperature change caused by formation damage to distinguish, the damage cannot be uniformly distributed. In other words, if the damage is segregated and large, we can infer the damaged zone and quantify the reduced permeability.

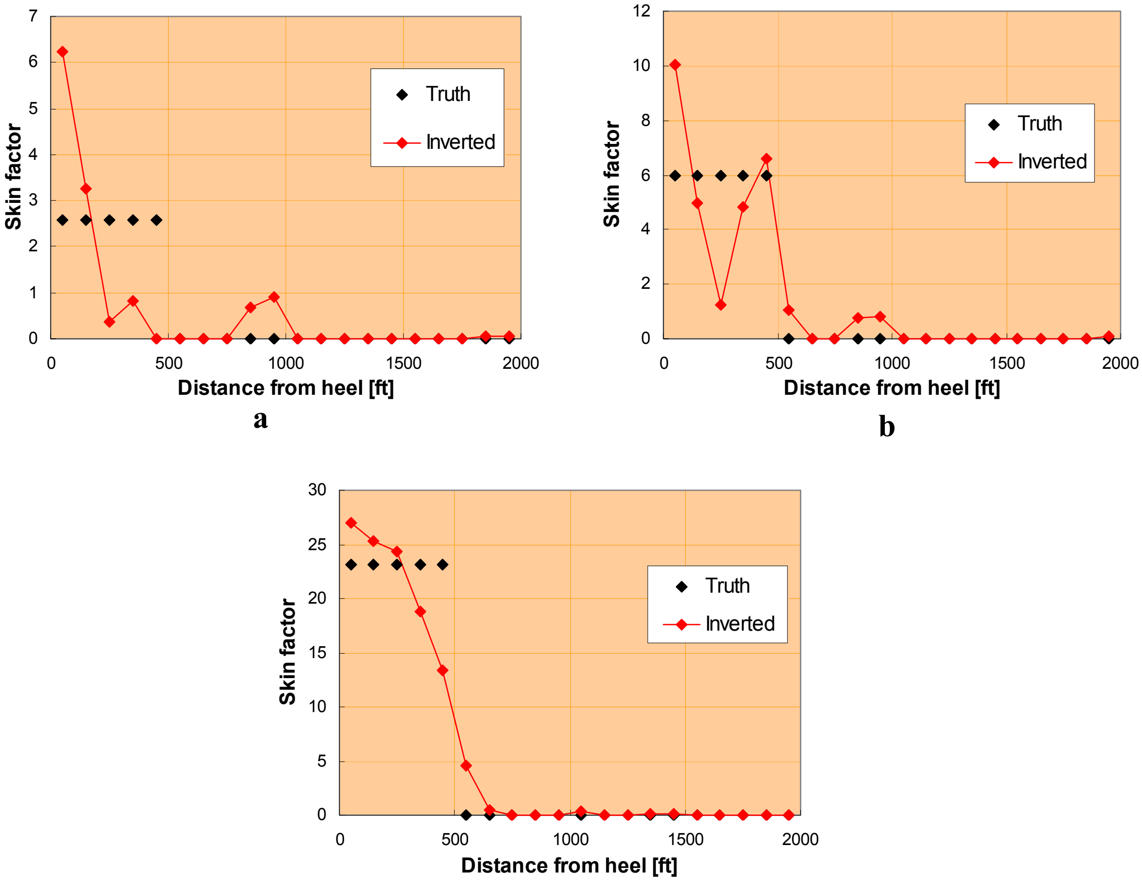

a

b

c

Fig. 6.48 True and inverted damage skin profiles (heel) of (a) k_d/k = 0.5, (b) k_d/k = 0.3, and (c) k_d/k = 0.1

6.4.6 Field Example

We use the temperature and pressure profiles measured in a horizontal well in the North Sea which is producing oil and water to test the inversion method with actual well data. While zonal production data for each phase are known, the continuous profiles of production rate have not been measured. We apply the inversion method to the field data and obtain flow rate profiles of oil and water by matching the temperature and pressure data.

The well is not perfectly horizontal and has slight deviations along its path. The trajectory of the well is shown in **Fig. 6.49**. The total oil production rate is 12,699 b/d and the water production rate is 8,554 b/d. From the measured depth 10689 ft to 9785 ft, the oil is being produced with 4,101 b/d and water with 2,201 b/d. From 9,705 ft to 8712 ft, the oil production rate is 8,598 b/d and the water production rate is 6,553 b/d.

About 65% of the total production is produced from the upper zone. The measured temperature and pressure profiles in this upper zone are shown in **Figs. 6.50** and **6.51** respectively.

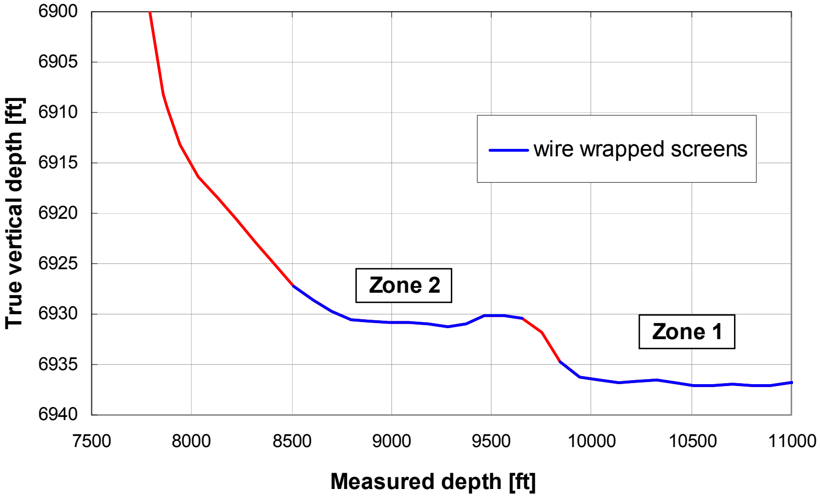

Fig. 6.49 Trajectory of the well.

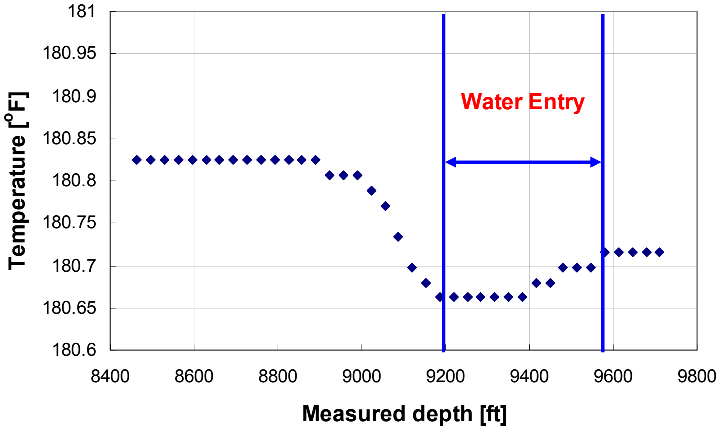

Fig. 6.50 Measured temperature profile.

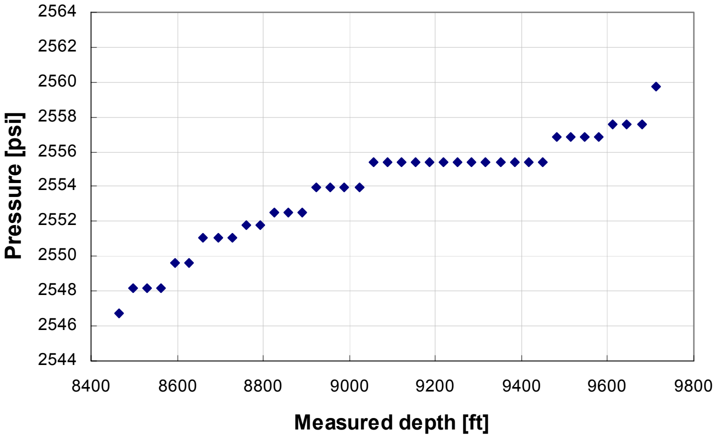

Fig 6.51 Measured pressure profile.

From the temperature profile (**Fig. 6.50**), we can detect the temperature drop. We consider this zone (about 9,200 – 9,600 ft, measured depth) as a water producing zone. Also, considering the total flow rate of oil and water (21,253 b/d), the wellbore pressure drop is very small (about 14 psi). Therefore, this well must be producing most of the fluid near the heel so that it has less frictional pressure drop inside the wellbore. The available properties given for this well are listed in **Table 6.1**. For the other properties we need for calculations, we use the values listed in **Tables 4.1 – 4.3**. The inverted temperature and pressure profiles are shown in **Figs. 6.52** and **6.53** respectively.

Table 6.1 Field properties

ID [in]	**5**
Total Length [ft]	**1250**
Reservoir height [ft]	**89**
T at outer boundary [^{o}F]	**179.6**
Specific gravity of gas	**0.85**
Oil API	**37.8**
Disolved GOR [SCF/STB]	**197**
Reservoir pressure [psi]	**2917**

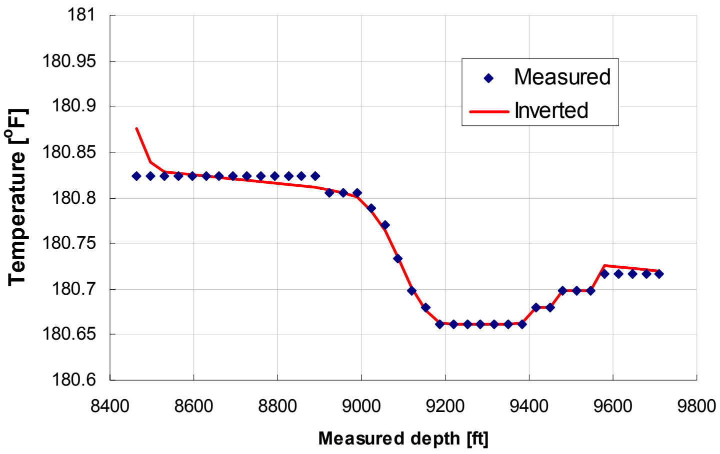

Fig. 6.52 Inverted temperature profile.

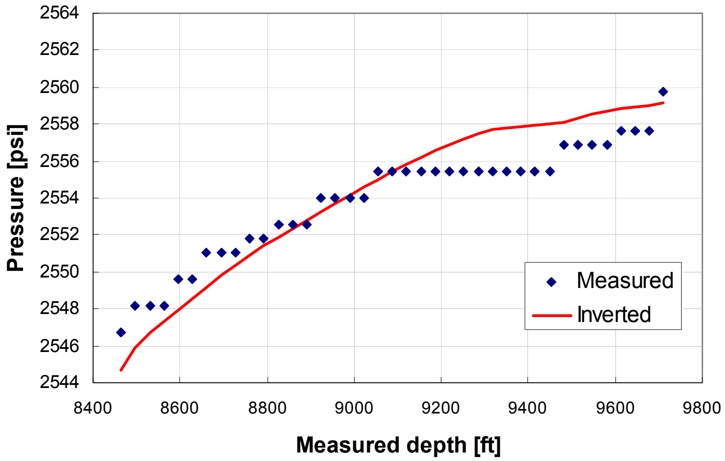

Fig. 6.53 Inverted pressure profile.

Although the inverted temperature deviated from the observation around 8500 ft of the measured depth, overall inversion is good. The pressure curves also show close agreement. Therefore, we can consider that the inverted profiles represent the actual profile. Obtained flow rates of oil and water are depicted in **Fig. 6.54**. As can be seen from the figure, oil is produced mainly from 9,000 – 9,200 ft and 8,400 – 8,500 ft. The first oil production corresponds to the temperature increase of the temperature measurement on this zone. The second oil producing zone is resulted from the fact that the wellbore pressure drop is extremely small for this high flow rate.

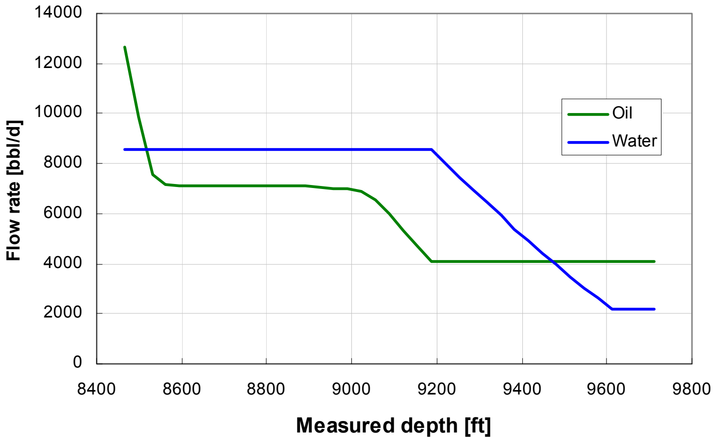

Fig. 6.54 Inverted flow rates.

CHAPTER 7

BUILD SECTION AND JUNCTION

7.1 INTRODUCTION TO BUILD SECTION AND JUNCTION

The *build* section is a section of wellbore that is closed to the formation and that connects the productive lateral to the main wellbore or to another lateral. The temperature and pressure profiles of these build sections are needed to relate the temperature and the pressure at the junction locations to the temperatures and pressures of the source laterals.

7.2 WORKING EQUATIONS FOR BUILD SECTION

To determine the temperature profile of a build section where the well inclination is changing, we apply the energy balance equation developed for the wellbore (Eq. 4.60) to a control volume of the build section as shown in **Fig. 7.1**.

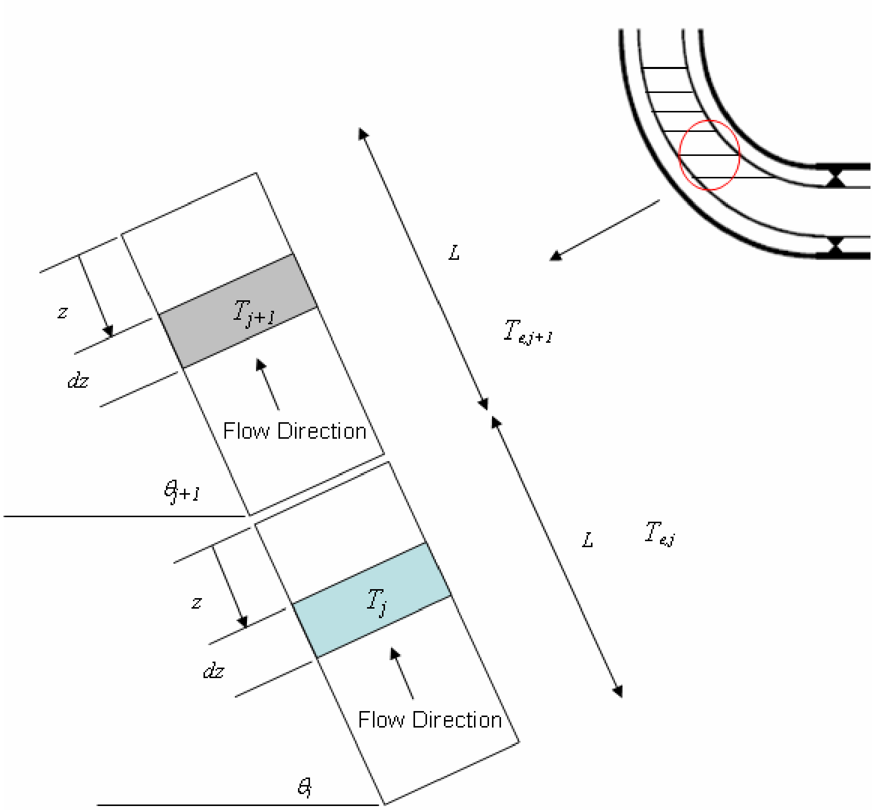

Fig. 7.1 Differential volume element of a build section.

With no production ($v_I = 0,\ \gamma = 0$), a temperature of a j$^{\text{th}}$ control volume along z-direction is given as

$$\frac{dT_j}{dz} = K_{JT}\frac{dp_j}{dz} + \frac{2}{R\rho v C_P}\alpha\left(T_{e,j} - T_j\right) - \frac{g\sin\theta}{C_P}, \tag{7.1}$$

or

$$\frac{dT_j}{dz} = K_{JT}\frac{dp_j}{dz} + \frac{\left(T_{e,j} - T_j\right)}{A} - \frac{g\sin\theta}{C_P}, \tag{7.2}$$

where A is called the relaxation parameter (Hasan and Kabir, 2002) which is defined as

$$A^{-1} = \frac{2\pi R}{wC_P}\alpha . \tag{7.3}$$

T_e is the earth (environment) temperature. With no production, formation temperature is equal to the environment temperature and is a function of depth, *z*. With the environment temperature of previous control volume, $T_{e,j}$ is given by

$$T_{e,j} = T_{e,j-1} - \left(L - z\right)g_G \sin\theta , \tag{7.4}$$

where g_G is the geothermal temperature gradient.

7.2.1 Single-Phase Liquid

The following assumptions were made to develop the equation for single-phase liquid: fluid is incompressible, and flowing friction becomes. For single-phase liquid flow, the static head loss nearly equals the total pressure gradient. Therefore, we obtain

$$\frac{dp}{dz} = \rho g \sin\theta . \tag{7.5}$$

Since we assume an incompressible fluid, the Joule-Thomson coefficient can be defined as

$$K_{JT} = \frac{1}{\rho C_p}. \tag{7.6}$$

Substituting Eqs. 7.5 and 7.6 into Eq. 7.2, we have

$$\frac{dT_j}{dz} = \frac{\left(T_{e,j} - T_j\right)}{A}. \tag{7.7}$$

With the substitution of Eq. 7.4 into Eq. 7.7, we have a first order linear differential equation as

$$\frac{dT_j}{dz} = \frac{1}{A}\left[T_j - \left\{T_{e,j-1} - (L-z) g_G \sin\theta\right\}\right]. \tag{7.8}$$

The solution of the differential equation is given by

$$T_j = T_{e,j-1} - (L-z) g_G \sin\theta + A g_G \sin\theta + C_I \exp\frac{(z-L)}{A}, \tag{7.9}$$

where C_I is the integration constant to be estimated from boundary condition. The boundary condition for this system is that the temperatures are the same at the boundary between the segments. At $z = L$, Eq. 7.9 is

$$T_j = T_{j-1} + A g_G \sin\theta + C_I, \tag{7.10}$$

Therefore, we have

$$C_I = A g_G \sin\theta, \tag{7.11}$$

Putting back into Eq. 7.9 gives

$$T_j = T_{e,j-1} - g_G \sin\theta\left[(L-z) - \left\{1 - \exp\left(\frac{(z-L)}{A}\right)\right\} A\right]. \tag{7.12}$$

7.2.1 Single-Phase Gas

For single-phase gas flow, the static head loss is not the same as the total pressure gradient but is negligible at low pressure. Therefore, the solution of Eq. 7.2 is given as

$$T_j = T_{e,j-1} + A\left(g_G \sin\theta - \frac{g\sin\theta}{C_p}\right) + C_I \exp\left(\frac{z-L}{A}\right). \tag{7.13}$$

Similarly, applying the same boundary condition at $z = L$, the integration constant is

$$C_I = -A\left(g_G \sin\theta - \frac{g\sin\theta}{C_p}\right). \tag{7.14}$$

Substituting into Eq. 7.14 yields

$$T_j = T_{e,j-1} + A\left[1 - \exp\left(\frac{z-L}{A}\right)\right]\left(g_G \sin\theta - \frac{g\sin\theta}{C_p}\right). \tag{7.15}$$

7.3 WORKING EQUATIONS FOR WELLBORE JUNCTION

For the case of modeling wellbore junctions that have commingled fluids with different properties, the mixing method is reviewed (Hill, 1990). An enthalpy balance applied to the mixing of two streams of fluid at different temperature into one combined stream is used to determine the relative flow rates of those streams.

Applying an energy balance to the wellbore junction, considering no heat loss and gain during the mixing, yields

$$w_1 C_{p1}(T_m - T_1) + w_2 C_{p2}(T_m - T_2) = 0 \tag{7.16}$$

where T_1 and T_2 are the temperatures of streams 1 and 2 respectively. T_m is the temperature of a mixture defined by

$$T_m = \frac{w_1 C_{p1} T_1 + w_2 C_{p2} T_2}{w_1 C_{p1} + w_2 C_{p2}} \tag{7.17}$$

The following equation is used to calculate the heat capacity of a mixture:

$$C_{pm} = \left(\frac{w_1}{w_1 + w_2}\right) C_{p1} + \left(\frac{w_2}{w_1 + w_2}\right) C_{p2} \tag{7.18}$$

When the two streams commingling at the junction are the same fluid, so that all heat capacities are the same, combining Eq. 7.18 with the mass balance at the junction

$$w_m = w_1 + w_2 \tag{7.19}$$

From Eq. 7.17, we have

$$T_m - T_2 = \frac{w_1 C_{p1}(T_1 - T_2)}{w_1 C_{p1} + w_2 C_{p2}} \tag{7.20}$$

Then we have

$$\frac{T_m - T_2}{T_1 - T_2} = \frac{w_1 C_{p1}}{w_1 C_{p1} + w_2 C_{p2}} \tag{7.21}$$

If a well is producing a single-phase fluid, the heat capacities are the same. Therefore, Eq. 7.21 becomes

$$\frac{T_m - T_2}{T_1 - T_2} = \frac{w_1}{w_1 + w_2} = \frac{w_1}{w_m} \tag{7.22}$$

Eq. 7.22 is very easy to use to infer the flow rates from each lateral. Thus, if there are measurable temperatures differences between T_1, T_2 and T_3, the fraction of the total flow from each lateral can be determined by measuring these temperatures. This describes the mixing method used for temperature log interpretation.

7.4 SENSITIVITY STUDIES AND RESULTS

In this chapter, results of temperature profiles along the build section with different trajectories were calculated. First, the temperature profile for the variable angle trajectory was obtained and compared to a temperature profile with a constant angle of 45^{o}. Additionally, temperature profiles for multilateral wells with two single-phase liquid laterals, and temperature profiles for multilateral wells with two single-phase gas laterals were calculated using the model for single-phase liquid and gas, as well as junction mixing, to determine whether the mixing method used in temperature log interpretation could be used to interpret the relative flow rates from different laterals.

7.4.1 Different trajectories

Temperature profiles for several constant angles (90^o, 45^o, 25^o, and 10.5^o) and variable angles along the build section were calculated for an oil flow rate of 3000 STB/d, as shown in **Fig. 7.2**, using Eq. 7.12. **Table 7.1** summarizes other important characteristics of the reservoir used. As the well deviates from the vertical, the temperature at the top of the build section decreases. This is because of the increased length of the wellbore in the build section as the deviation increases, which in turn increases the length of time for the relatively hot wellbore fluid to be cooled by the surrounding formation.

Table 7.1 Properties used for single-phase liquid examples.

Geothermal gradient [^{o}F/ft]	**0.0274**
Oil heat capacity [Btu/lb ^{o}F]	**0.485**
Wellbore diameter [in]	**7.5 in**
Outside casing diameter p [in]	**5.5 in**
Inside casing diameter [in]	**5.047 in**
Thermal conductivity of cement [Btu/hr ft ^{o}F]	**4.02**
Thermal conductivity of earth [Btu/hr ft ^{o}F]	**1.4**
^{o}API	**35**

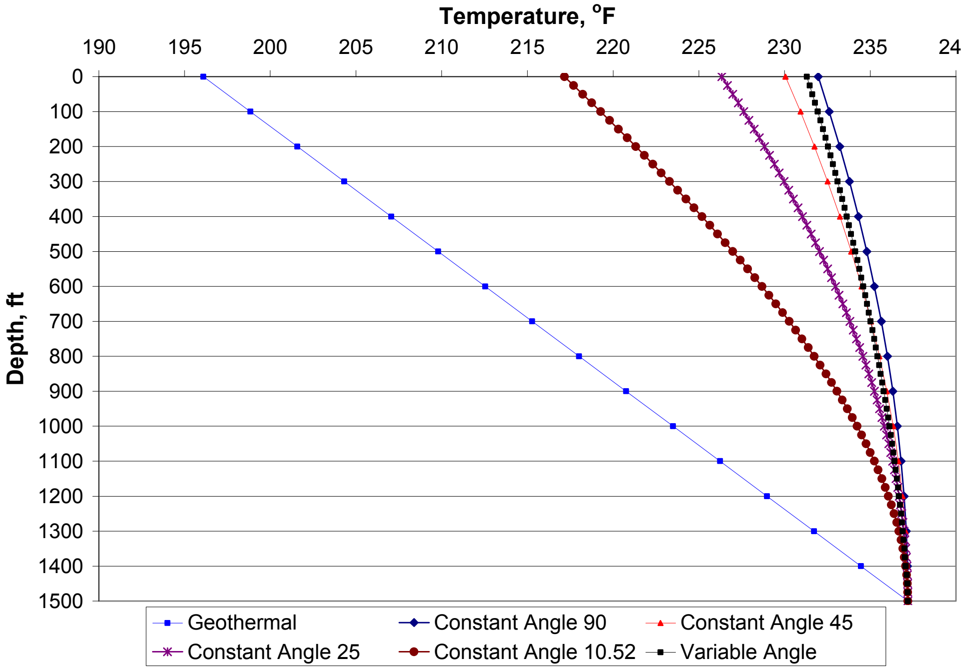

Fig. 7.2 Temperature profiles along the build section (3000 STB/d).

The temperature profile for the variable angle trajectory was surprisingly close to the profile obtained with a constant angle of 45^o. Even though these trajectories are quite different (see **Fig. 7.3**), the net heat transfer from the wellbore fluid to the formation was similar.

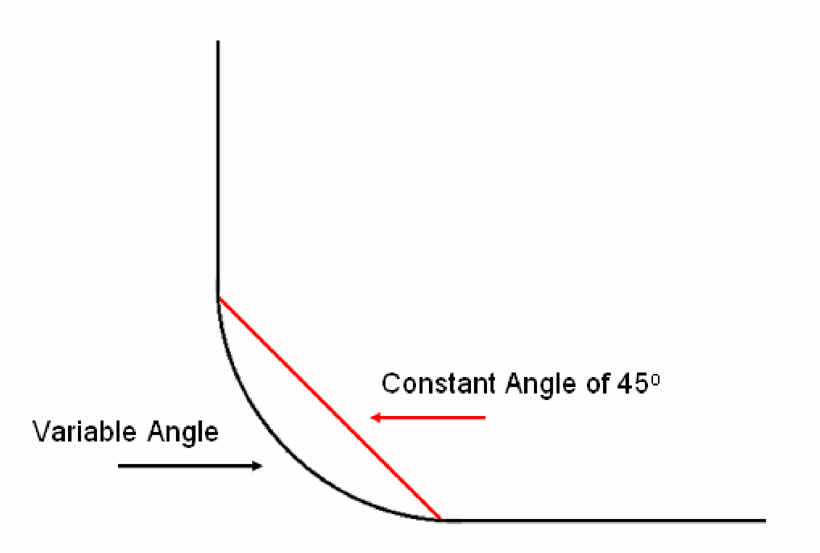

Fig. 7.3 Constant radius of curvature and constant angle trajectory.

At a much smaller flow rate (200 STB/d), the wellbore cools much more (see **Fig. 7.4**) than at a larger flow rate (3000 STB/d), as shown in **Fig. 7.2**, because of the increased length of time for the relatively hot wellbore fluid to be cooled by the surrounding formation.

For the vertical case, the temperature at the top of the build section is less than 10 ^{o}F higher than the geothermal temperature; a highly deviated (10.5 ^{o}F from the horizontal), constant angle build section has a temperature at the top of the build section that is only 2 ^{o}F different from the geothermal temperature.

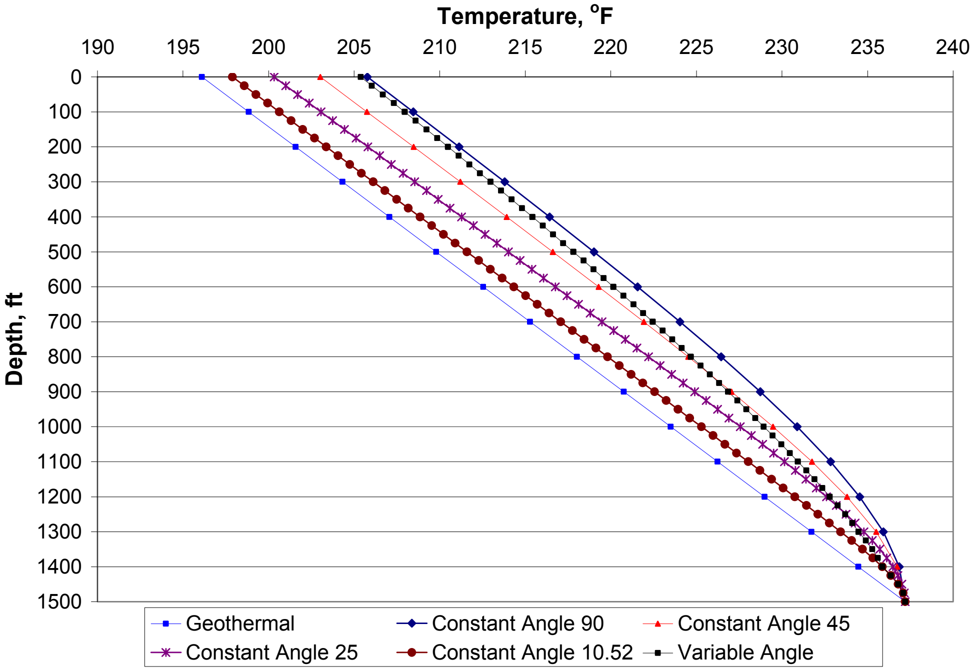

Fig. 7.4 Temperature profiles along the build section (200 STB/d).

7.4.2 Dual-lateral with single phase liquid

Data from Zuata Field in the Orinoco heavy oil belt (Ramirez *et al.*, 2004; Robles 2001) were used to calculate the temperature profiles for multilateral wells with two single-phase liquid laterals, using the model for single-phase liquid and junction mixing. In this area, dual-laterals are expected to achieve a target oil production rate per single well of approximately 3000 STB/d by increasing the contact area between the wellbore and the reservoir. Because of the depth of the reservoir (1500 ft – 2000 ft), the temperatures were moderately low. Down-hole temperature at the total vertical depth was measured to be approximately 120 ^{o}F, corresponding to an approximate temperature gradient of 0.02 ^{o}F/ft. For the three cases studied, lateral 1 produced 2000 STB/d and lateral 2 produced 3000 STB/d, with an oil gravity of 10^{o} API for both laterals. The other properties listed in **Table 7.1** were used.

To determine whether the mixing method used in the temperature log interpretation could be used to interpret the relative flow rates from different laterals, we simulated dual laterals produced from different depths as shown in **Fig.7.5**. The mixing method depends on the fact that fluids entering a well at different depths have different temperatures because of the geothermal gradient. Similarly, if fluids from two branches of a multilateral have different temperatures before commingling at a junction, the resulting intermediate temperature of the mixed stream should be proportional to the rates from each lateral.

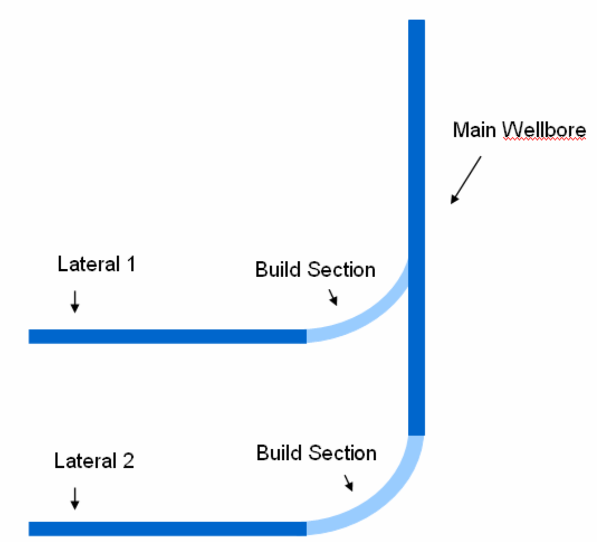

Fig. 7.5 Dual lateral geometry for the examples.

Figs. 7.6 – 7.8 show the predicted temperature profiles for laterals completed at the same depth, laterals completed 500 vertical feet apart, and laterals completed 1000 vertical feet apart. For laterals completed at the same depth (see **Fig. 6.6**), the streams from the two laterals arrive at the junction at slightly different temperatures because of the different flow rates in each lateral. However, the difference is so small (about 0.5 ^{o}F) that interpretation of the junction mixing is probably impossible. When the two laterals are spaced at a significant distance (see **Figs. 7.7 and 7.8**), the difference in the temperatures of the fluid from the two laterals is significant enough that the mixing method can be applied. The mixing temperature in these cases is different enough from the temperature of the lateral (1 ^{o}F or more) to be readily measured with current distributed temperature sensor devices.

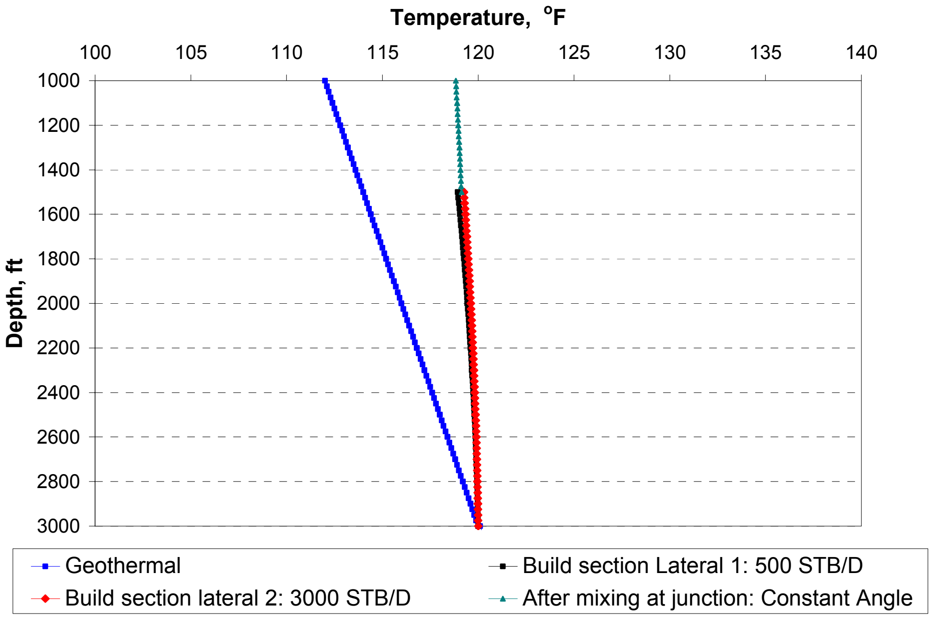

Fig. 7.6 Build section temperature profiles with liquid production at the same depth.

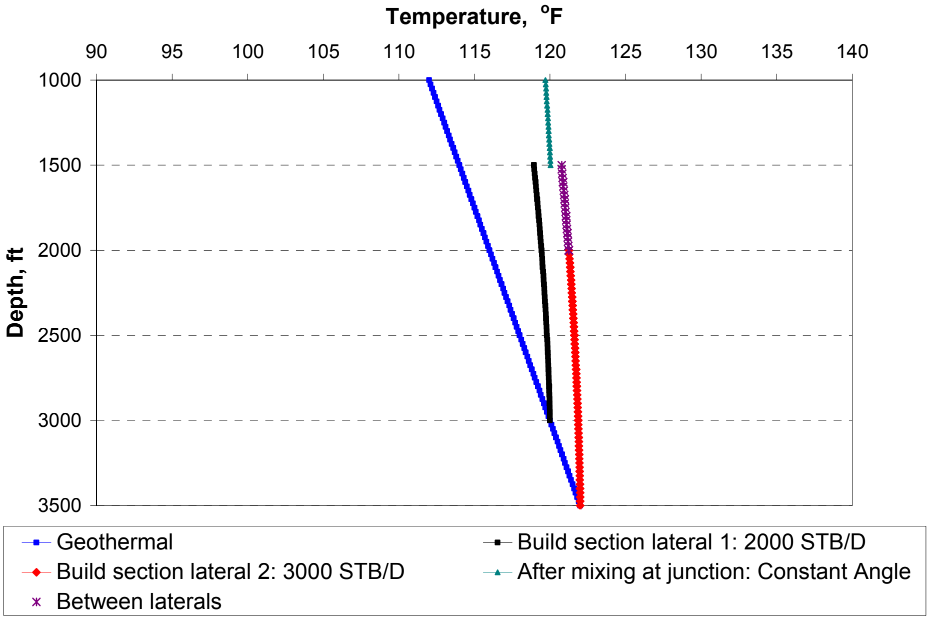

Fig. 7.7 Build section temperature profiles with liquid production at depths spaced 500 ft apart.

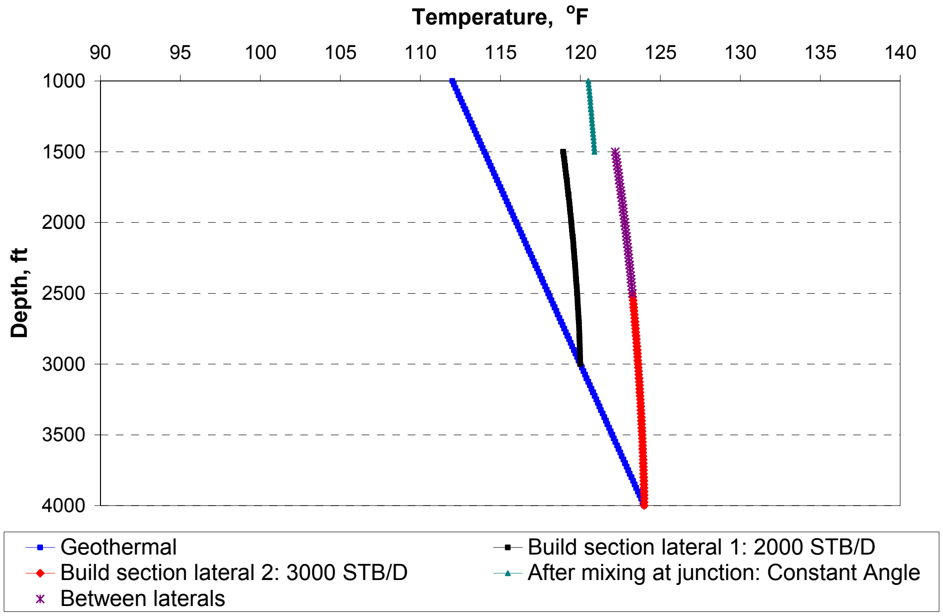

Fig. 7.8 Build section temperature profiles with liquid production at depths spaced 1000 ft apart.

When one lateral is producing at a much smaller rate than the other, a sizable temperature difference at the junction may occur during production from the same depth at both laterals. **Fig. 7.9** shows the temperature profiles for production rates of 500 STB/d for lateral 1, and 3000 STB/d for lateral 2, both produced at the same depth. The difference in the temperatures of the streams arriving at the junction is significantly greater than the case with similar rates shown in **Fig. 7.6**.

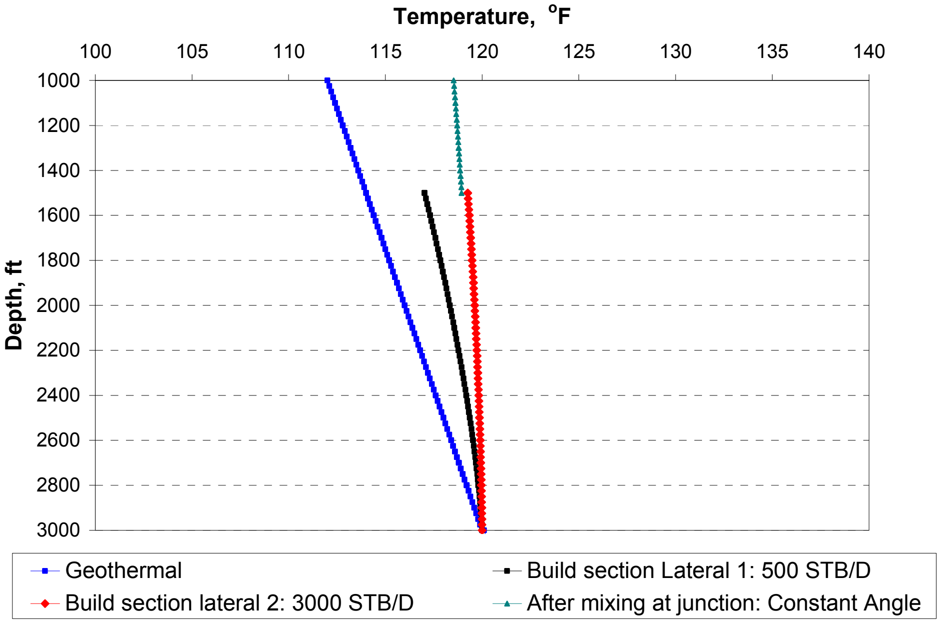

Fig. 7.9 Build section temperature profiles with different rates of 3000 STB/d and 500 STB/d.

7.4.3 Different fractions of total production

Several cases were used for calculations for different fractions of the total production from each lateral, for example if the total production of the well was 5000 STB/d, 20% - 80% means, lateral 1 is producing 1000 STB/d and lateral 2 is producing 4000 STB/d. In these examples, lateral 1 was always kept at the same level, and lateral 2 had a changing depth (0 ft, 500 ft, and 1000 ft) from lateral 1, and the difference of temperature is calculated at the junction.

The difference in temperature at the junction was calculated in the following fashion: lateral 2 minus lateral 1. Therefore, when the difference is positive it is because lateral 2 has a higher temperature than lateral 1. The total flow rate was kept constant and the fraction flow rate of each lateral changed, and calculations were made for different total flow rates.

When there is a difference in lateral production, we can see that the difference in temperature between the laterals increases as the total flow rate increases, as is illustrated in **Figs. 7.10 – 7.12**, but there is one point when this difference starts decreasing as the flow rate increases. All the differences in depth between the laterals are 0 ft, 500 ft and 1000 ft. This is because of the fact that after certain flow rates (especially high flow rates), the lateral which is producing less increases temperature in a more rapid manner than the lateral which is producing more. This effect is delayed when there is a difference in depth between the laterals. Even though lateral 1 increases rapidly temperature, lateral 2 also increases because it is deeper than lateral 1. However, eventually the difference in temperature will decrease, even for very high flow rate. For very high flow rate the difference in temperature between the laterals at the junction would have a small value, but for those cases where there is a difference in depth, the resulting effect would be delayed.

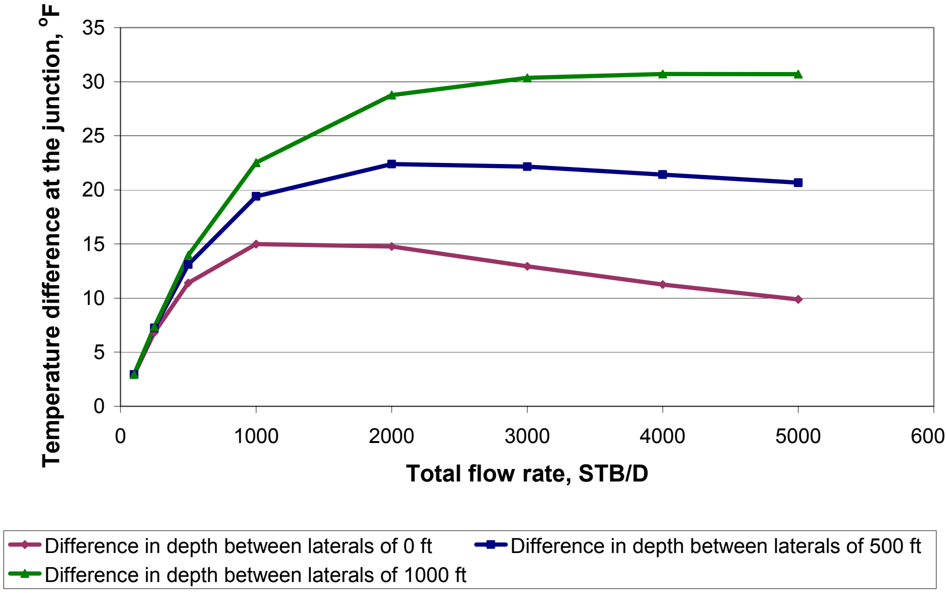

Fig. 7.10 Fraction of total production from each lateral: 20% - 80%.

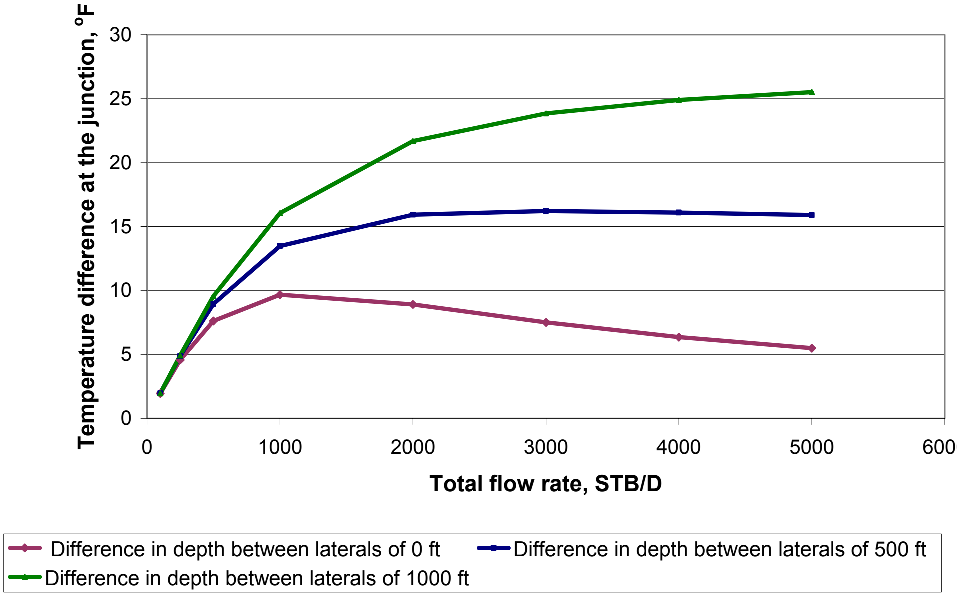

Fig. 7.11 Fraction of total production from each lateral: 30% - 70%.

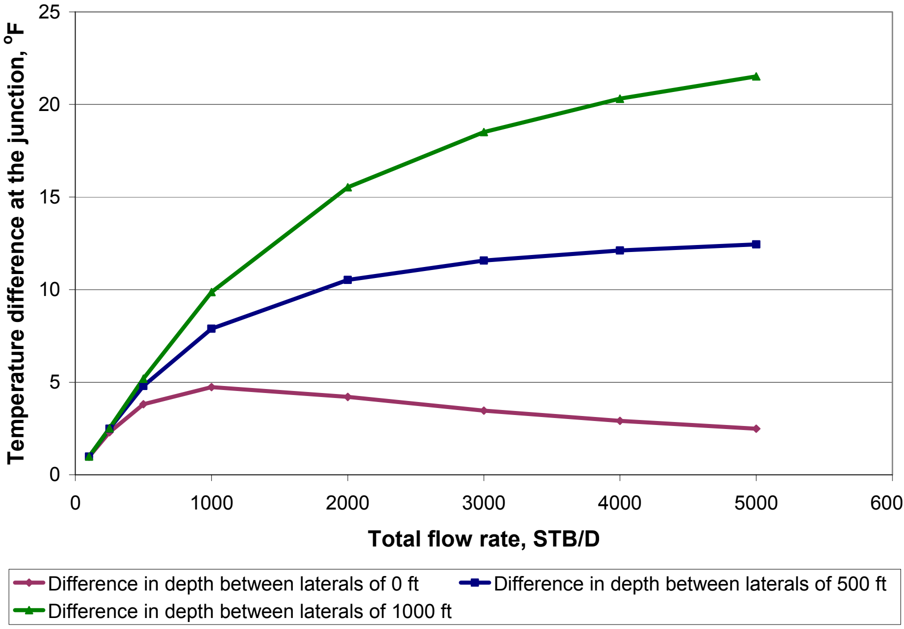

Fig. 7.12 Fraction of total production from each lateral:40% - 60%.

When the two laterals produce the same flow rate and are at the same level, there is not difference in temperatures at the junction. Therefore, the mixing method can not be applied (as can be seen in **Fig. 7.13**). The mixing method can be applied when there is a difference in depth between the laterals, and the total flow rate is large enough to have an appreciable temperature difference at the junction measurable by a sensor.

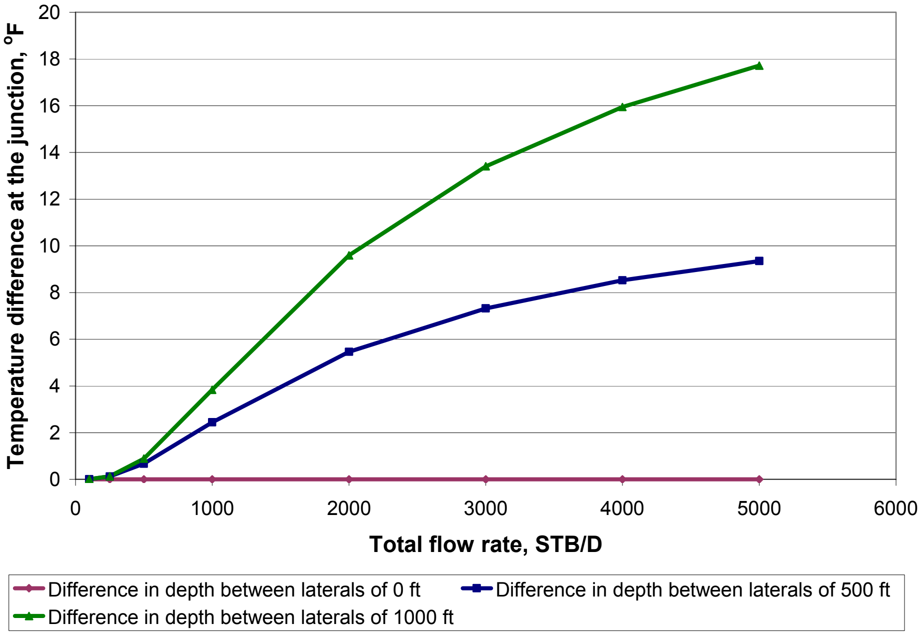

Fig. 7.13 Fraction of total production from each lateral: 50% - 50%.

When a lateral which is producing more is kept at the same level while the other lateral which is producing less is moved to changing depths, there is one instant when there is no difference in temperature at the junction (as shown in **Figs. 7.14 – 7.16**). This level is reached when the effect of having a high flow rate from lateral 1 has the same effect as having a difference in depth from lateral 2, which has a lower flow rate. If the laterals have a significant difference in flow rate, this effect will not be visible.

From **Figs 7.14 – 7.16** we see that the absolute difference in temperature at the junction for different total flow rates can be seen to be smaller for all cases, because the effect of having a higher flow rate is larger than having depth differences between the laterals. Also, in this case lateral 1 will always have a higher temperature than lateral 2, because of its higher flow rate. However, when the total flow rate increases, there is a point where lateral 2 has a higher temperature than lateral 1.

When there is a difference in the lateral's production, it can be seen that the difference in temperature between the laterals usually decreases as the total flow rate increases. However, there is one point where this difference begins to increase as the flow rate increases for all the differences in depth. These differences between the laterals are 0 feet, 500 feet and 1000 feet as shown in **Figs.7.14 – 7.16**. This is because of the fact that above certain flow rates (high flow rates), the lateral producing less increases in temperature in a more rapidly manner than the lateral producing more. When there is a difference in depth between the laterals, the lateral which has less production but a changing depth will increase in temperature even more rapidly than if the laterals are at the same level. Also, when both laterals are at the same level, the difference in temperature decreases for high flow rates. Therefore, for high flow rates and laterals at the same level, the difference in temperature at the junction has a low value.

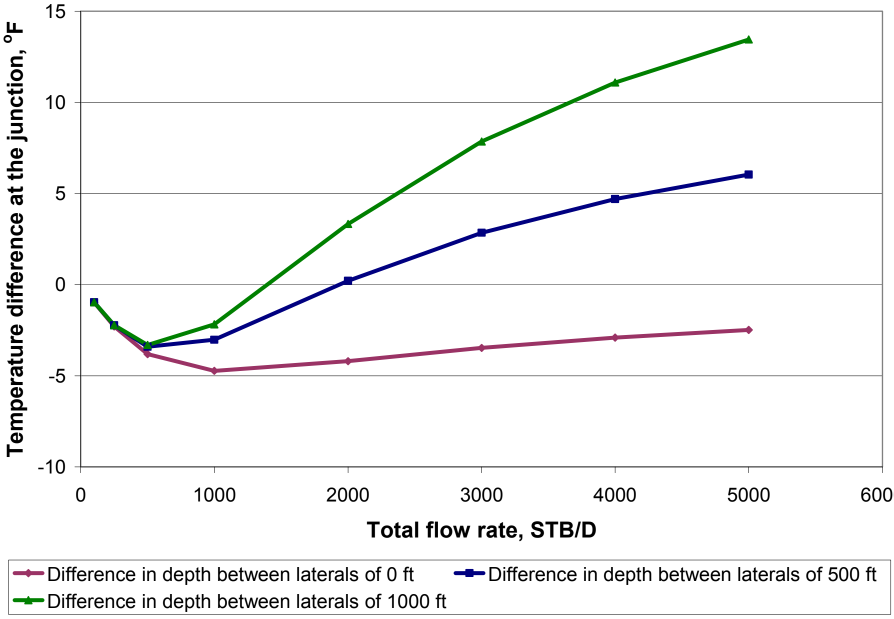

Fig. 7.14 Fraction of total production from each lateral: 60% - 40%.

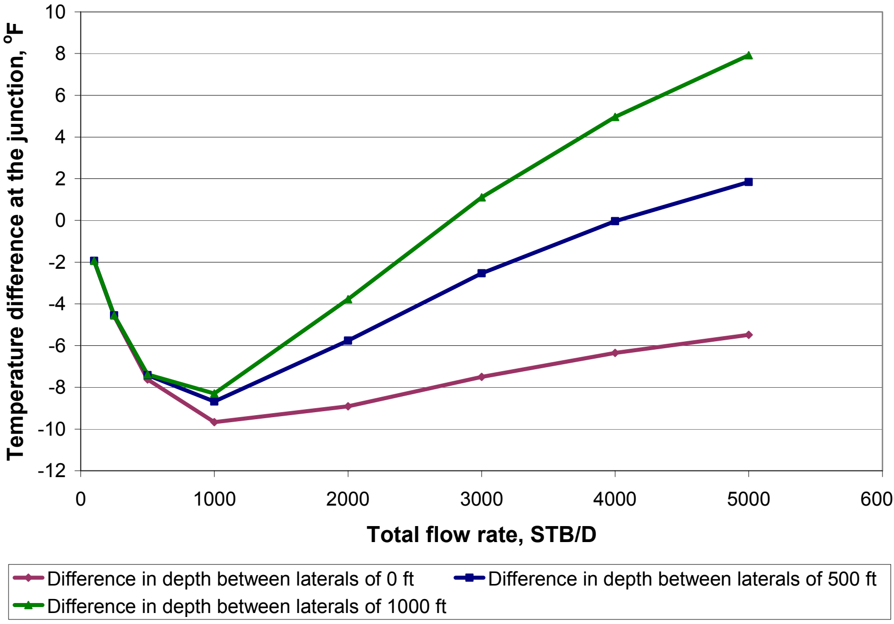

Fig. 7.15 Fraction of total production from each lateral: 70% - 30%.

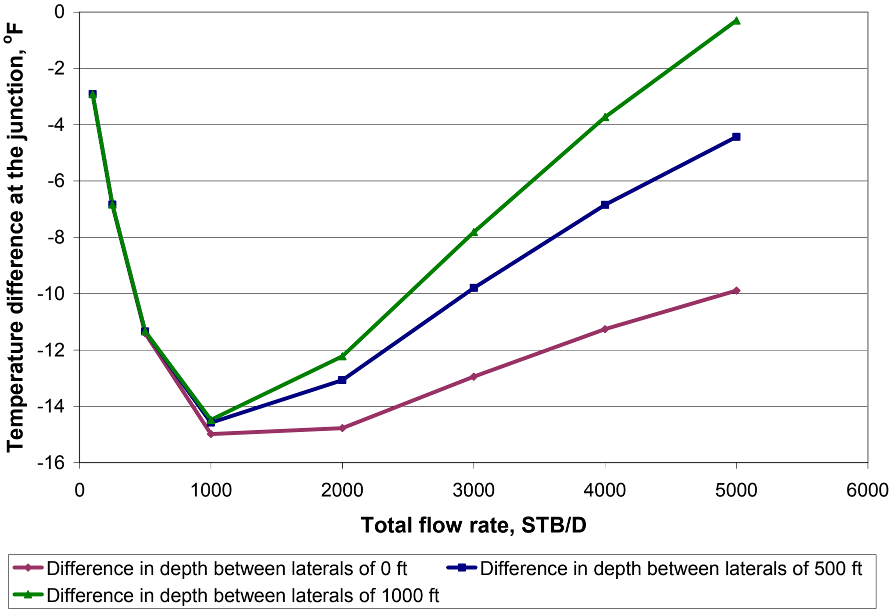

Fig. 7.16 Fraction of total production from each lateral: 80% - 20%.

7.4.4 Dual-lateral with single phase gas

Typical data from the Parks Field Unit in west Texas (Owodunni, 2003) shown in **Table 7.2** were used to calculate the temperature profiles for multilateral wells with two single-phase gas laterals, using the model for single-phase gas in the build section and mixing at the junction. Wells are design to produce gas from the upper and lower porosity lenses of geologically constrained Devonian limestone. The results from temperature profiles for this case are shown in **Figs. 7.17 – 7.19**, where lateral 1 produces 700 MSCF/d and lateral 2 produces 1.7 MMSCF/d. The geothermal temperature gradient used was 0.016°F/ ft.

Table 7.2 Properties used for single-phase gas examples.	
Geothermal gradient [°F/ft]	**0.016**
Oil heat capacity [Btu/lb °F]	**0.3**
Wellbore diameter [in]	**7.5 in**
Outside casing diameter p [in]	**5.5 in**
Inside casing diameter [in]	**5.047 in**
Thermal conductivity of cement [Btu/hr ft °F]	**4.02**
Thermal conductivity of earth [Btu/hr ft °F]	**1.4**
Specific gravity of gas	**1.04**

The results for these gas production cases are similar to those for an oil producing dual lateral. The larger the vertical separation between the laterals, the bigger the temperature difference between the produced streams arriving at the junction. For a vertical spacing of 500 or 1000 feet, the temperature difference between the streams is easily discernible, allowing the application of the mixing method to interpret the relative flow rates from the laterals.

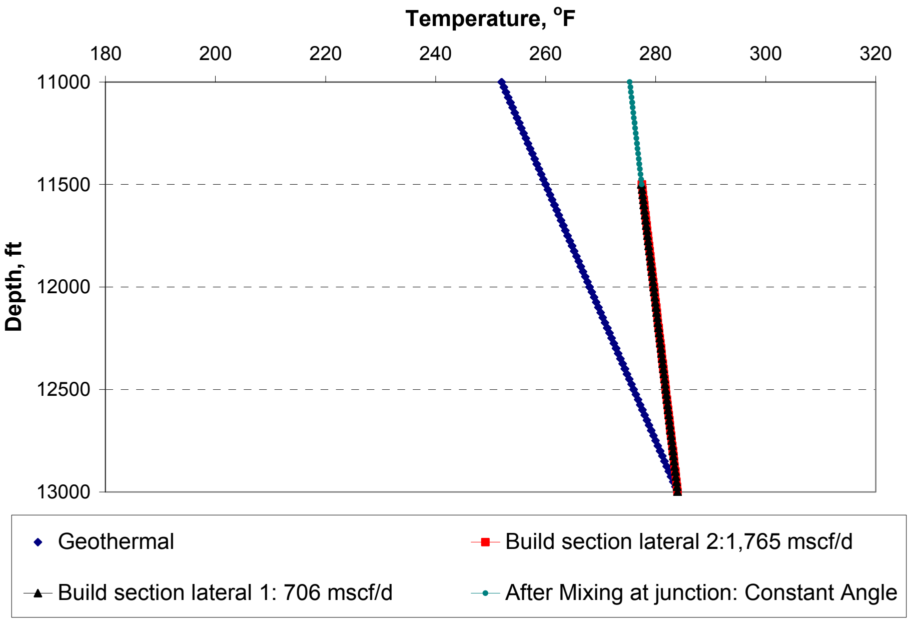

Fig. 7.17 Build section temperature profiles with gas production at the same depth.

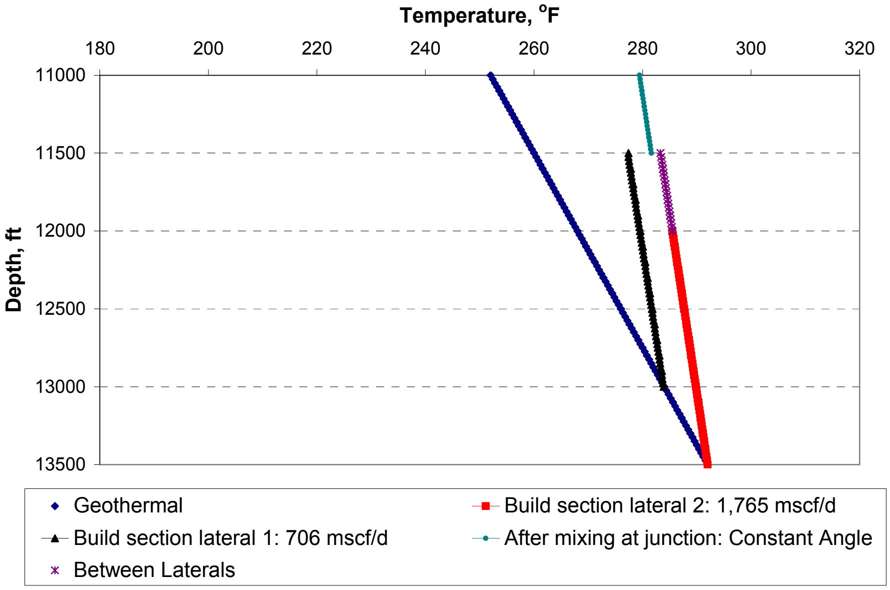

Fig. 7.18 Build section temperature profiles with gas production at depths spaced 500 ft apart.

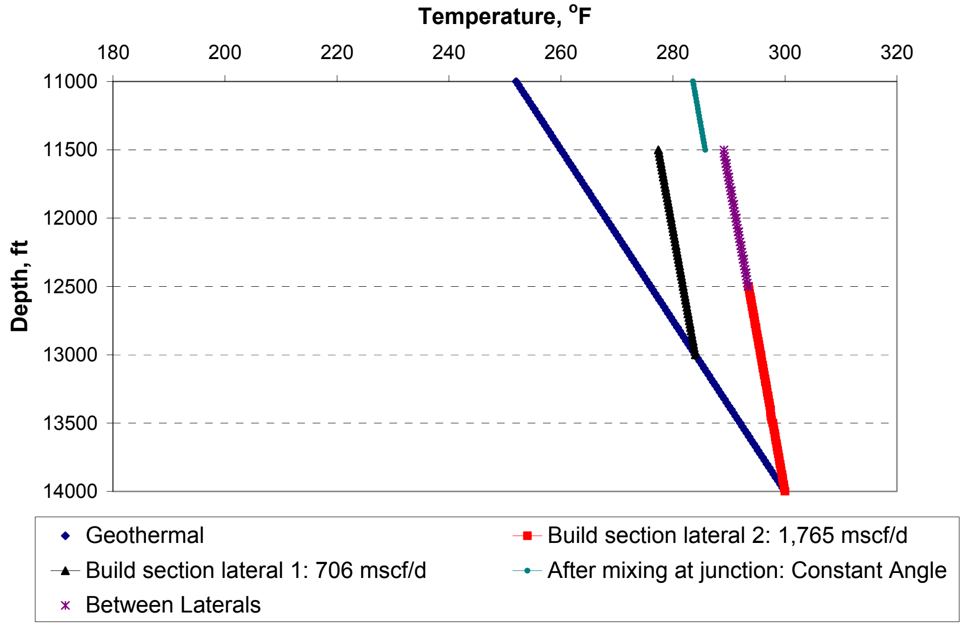

Fig.7.19 Build section temperature profiles with gas production at depths spaced 1000 ft apart.

CHAPTER 8

Numerical Temperature Model of Two-Phase Flow

8.1 INTRODUCTION TO NUMERICAL TEMPERATURE MODEL OF TWO-PHASE FLOW.

Chapter 4 presented an inflow temperature model that resulted from analytically solving the mass and energy balances of single-phase flow in a box-shaped isotropic reservoir with no-flow lateral boundaries. The model predicts wellbore temperature under the assumption that gas, oil, and water are flowing at the same geothermal temperature or from the same depth. Based on this assumption, the model predicts that water enters at a lower temperature than oil because of its larger heat capacity. The prediction seems to be in conflict with field observation where we commonly see water entering at the higher temperature than oil (Foucault *et al.*, 2004).

This chapter further studies the temperature behavior in a horizontal well subjected to bottom water drive. Water in this case is initially located in a deeper and warmer zone below a horizontal well.

Unlike the previous analytical temperature model, this model numerically solves mass and energy balances for two-phase flow both in the reservoir and wellbore. The fluid properties also vary with temperature and pressure while flowing. The key difference from typical thermal oil recovery simulators is that the model includes a temperature change caused by pressure drops, which is usually neglected by those simulators. Since the temperature change in the context of monitoring a production well is expected to be small, all of the subtle energy changes in the reservoir must be included. Neglecting the Joule-Thomson effect for liquid flow will result in an underestimation of the size of the temperature change.

We will focus our study only on a bottom water drive reservoir, in which water coning is prone to occur. Although there are pressure-based models that can predict water breakthrough time for water coning toward horizontal wells, what we are seeking here is an alternative way to detect water breakthrough by assuming that the DTS are permanently installed in a horizontal well. We will develop a basis to detect water entry and breakthrough time based on temporal changes of the temperature profiles. A similar basis could also detect gas entry in a gas-cap drive reservoir because gas properties are much different from oil. The size of the temperature decrease for gas flowing into the well should be larger and the gas inflow easier to locate than for oil-water flow.

8.2 PHYSICAL DESCRIPTION OF THE MODEL

Fig. 8.1 shows a schematic of the reservoir and well geometry. We consider a horizontal well fully penetrated through a box-shaped reservoir with no-flow boundaries at the top and the sides of the reservoir. Initial pressures are at static equilibrium at which the water pressures are function of the elevation only. For convenience, water in the reservoir is initialized at irreducible water saturation. Temperature of the five boundaries is fixed at its initial geothermal temperature. We assume that an active aquifer at the bottom of the reservoir gives a constant pressure and temperature boundary (4,000 psi, 180 ^{o}F) located at the original water-oil contact. A straight horizontal well is placed in the center of the oil reservoir having horizontal to vertical permeability ratio of five ($k_h/k_z = 5$). The horizontal well is modeled as an open hole over its entire length.

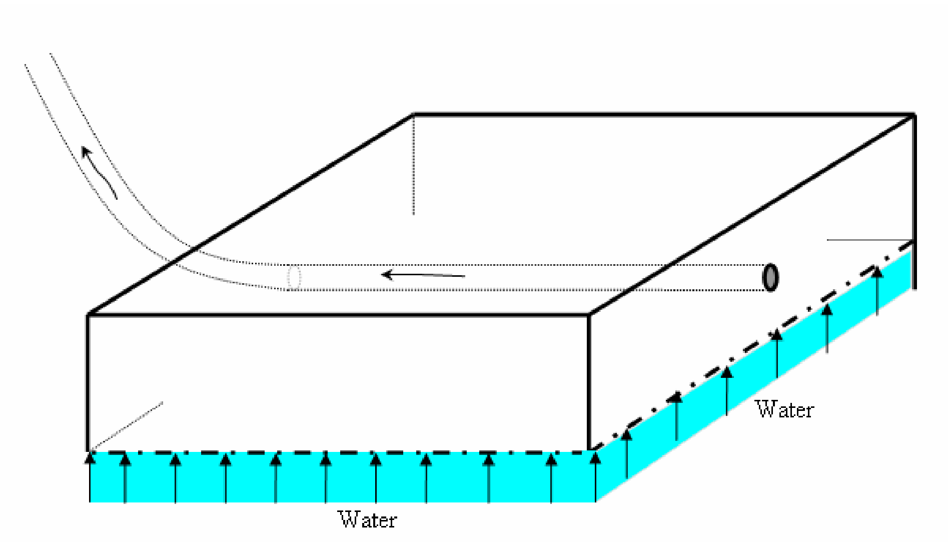

Fig. 8.1 Schematic of bottom water drive reservoir and well at the initial condition.

For two-phase flow in a reservoir, we are required to have a capillary pressure model and a relative permeability model. Although these models are not the main causes of temperature changes, they are commonly used to describe two-phase flow in reservoir simulation. In this study, we have chosen a model and consistently used it throughout example cases.

Capillary pressure is expressed as a function of interfacial tension, permeability, porosity and saturation. For water and oil flow, the capillary pressure curve is modeled as

$$p_{cow} = C\sigma\sqrt{\frac{\phi}{k}}(1-S_w)^E , \tag{8.1}$$

where k is the geometric mean of permeability in the x, y, z directions. The parameters C and E are usually determined from matching a water/oil experimental capillary pressure curve. Here we choose $C = 10$ and $E = 3$. σ is the interfacial tension between water and oil.

Relative permeability for the water and oil flow is calculated from Corey's model (Corey, 1986).

$$k_{rw} = k_{rw}^{o}\left(\frac{S_w - S_{wr}}{1 - S_{wr} - S_{or}}\right)^{ew}, \tag{8.2}$$

$$k_{ro} = k_{ro}^{o}\left(\frac{1 - S_w - S_{or}}{1 - S_{wr} - S_{or}}\right)^{eo}, \tag{8.3}$$

where k_{rw}^{o} and k_{rw}^{o} are the end point relative permeabilities of water and oil respectively. Subscripts ew and eo are the relative permeability exponents.

8.3. FINITE DIFFERENCE FORMULATIONS AND CALCULATION PROCEDURE

Mathematical formulations of mass and energy balances for oil and water flow in the reservoir and the wellbore are developed in this section. Although the formulation of mass balance is not new and commonly appears in reservoir simulation literature, it is presented here for showing the steps taken in obtaining results (temperature, pressure, and inflow rate profiles). The formulation of the energy balance is relatively new because it includes the heat resulting from fluid expansion, viscous dissipation, convection, and conduction.

8.3.1 Mass balance

Reservoir flow. For two-phase flow in a reservoir, the differential form (strong form) of the mass balance can be written as follows.

$$-\nabla \cdot (\rho_o \mathbf{u}_o) = \frac{\partial}{\partial t}(\phi \rho_o S_o), \tag{8.4}$$

$$-\nabla \cdot (\rho_w \mathbf{u}_w) = \frac{\partial}{\partial t}(\phi \rho_w S_w), \tag{8.5}$$

The divergence operator on the left side of the above equations could be expanded into any coordinate system. ϕ is the porosity of the reservoir and assumed constant in this study. $\mathbf{u}$ is the Darcy velocity that is extended to describe the two-phase flow by relative permeability. The subscripts w and o denote the water and oil phases, respectively. The right side of above equations can be rearranged and expressed in term of phase pressure and fluid compressibility.

For oil:

$$-\frac{1}{\rho_o}\nabla \cdot (\rho_o \mathbf{u}_o) = \phi \frac{\partial S_o}{\partial t} + \phi S_o c_o \frac{\partial p_o}{\partial t}, \tag{8.6}$$

For water:

$$-\frac{1}{\rho_w}\nabla\cdot\left(\rho_w\mathbf{u}_w\right)=\phi\frac{\partial S_w}{\partial t}+\phi S_w c_w\frac{\partial p_w}{\partial t}, \tag{8.7}$$

Eqs. 8.6 and 8.7 are added to eliminate the time derivative term of the saturations so that the IMPES (implicit pressure explicit saturation) formulation can be used.

$$-\frac{1}{\rho_o}\nabla\cdot\left(\rho_o\mathbf{u}_o\right)-\frac{1}{\rho_w}\nabla\cdot\left(\rho_w\mathbf{u}_w\right)=\phi S_o c_o\frac{\partial p_o}{\partial t}+\phi S_w c_w\frac{\partial p_w}{\partial t}, \tag{8.8}$$

For three-dimension flow in a Cartesian coordinate system, Eq. 8.8 can be integrated over a box-shaped control volume ($\Delta x\Delta y\Delta z$). This leads to the mass balance before taking the limit as $\Delta x, \Delta y, \Delta z$ approach zero. Then we have

$$\begin{aligned}
&-\frac{\Delta y\Delta z}{\rho_o}\Delta_x\left(\rho_o u_o\right)-\frac{\Delta x\Delta z}{\rho_o}\Delta_y\left(\rho_o u_o\right)-\frac{\Delta x\Delta y}{\rho_o}\Delta_z\left(\rho_o u_o\right)\\
&-\frac{\Delta y\Delta z}{\rho_w}\Delta_x\left(\rho_w u_w\right)-\frac{\Delta x\Delta z}{\rho_w}\Delta_y\left(\rho_w u_w\right)-\frac{\Delta x\Delta y}{\rho_w}\Delta_z\left(\rho_w u_w\right).\\
&=\phi S_o c_o\left(\frac{\Delta x\Delta y\Delta z}{\Delta t}\right)\Delta_t p_o+\phi S_w c_w\left(\frac{\Delta x\Delta y\Delta z}{\Delta t}\right)\Delta_t p_w
\end{aligned} \tag{8.9}$$

Eq. 8.9 is approximated by finite differencing. Details are given in Appendix C. With the auxiliary relations of capillary pressure ($p_c = p_o - p_w$) and saturation ($S_o + S_w = 1$), the finite-difference form of Eq. 8.9 is

$$\begin{aligned}
&A_{ijk}\,p_{wi+1jk}^{n+1}+B_{ijk}\,p_{wi-1jk}^{n+1}+C_{ijk}\,p_{wij+1k}^{n+1}+D_{ijk}\,p_{wij-1k}^{n+1}\\
&\qquad+E_{ijk}\,p_{wijk+1}^{n+1}+F_{ijk}\,p_{wijk-1}^{n+1}+G_{ijk}\,p_{wijk}^{n+1}=RHS_{ijk}
\end{aligned}. \tag{8.10}$$

where the subscripts i, j, and k refer to spatial coordinates. The coefficients (A, B, C, D, E, F, G, RHS) resulting from doing a typical finite difference are presented in Appendix C.

Well grid blocks. For grid blocks containing a wellbore, Eq. 8.10 has to include the source/sink terms on the left side as written below.

$$\begin{aligned}
&A_{ijk}\,p_{wi+1jk}^{n+1}+B_{ijk}\,p_{wi-1jk}^{n+1}+C_{ijk}\,p_{wij+1k}^{n+1}+D_{ijk}\,p_{wij-1k}^{n+1}\\
&\quad+E_{ijk}\,p_{wijk+1}^{n+1}+F_{ijk}\,p_{wijk-1}^{n+1}+G_{ijk}\,p_{wijk}^{n+1}+q_{oiJK}+q_{wiJK}=RHS_{ijk}
\end{aligned}. \tag{8.11}$$

where the subscripts J and K denote the well grid blocks. The production term, q, represents volume produced at reservoir condition, per unit time. The relationship between volumetric flow rate, grid block pressure, and wellbore pressure is expressed as

$$q_{oiJK}=-J_o\left(p_{wiJK}^{n+1}+p_{ciJK}-p_{well,i}^{n+1}\right), \tag{8.12}$$

$$q_{wiJK} = -J_w\left(p_{wiJK}^{n+1} - p_{well,i}^{n+1}\right), \tag{8.13}$$

where PI_l is the phase productivity index. We use an expression developed by Peaceman (1983), which is

$$J_l = \frac{2\pi\sqrt{k_y k_z}\,\Delta x k_{rl}}{\mu \ln\left(\dfrac{r_e}{r_w}\right)} \tag{8.14}$$

where $l = o, w$, and r_e is given by

$$r_e = 0.28\frac{\left[\left(\dfrac{k_z}{k_y}\right)^{\frac{1}{2}}\Delta y^2 + \left(\dfrac{k_y}{k_z}\right)^{\frac{1}{2}}\Delta z^2\right]^{\frac{1}{2}}}{\left(\dfrac{k_z}{k_y}\right)^{\frac{1}{4}} + \left(\dfrac{k_y}{k_z}\right)^{\frac{1}{4}}}. \tag{8.15}$$

Once we substitute Eqs. 8.12 and 8.13 into Eq. 8.11, the unknowns are the pressure in the grid blocks and the wellbore pressure. Thus, the wellbore flow is required to describe the pressure in the wellbore.

Wellbore flow. For wellbore flow, we use the equation derived in Chapter 4 given as

$$\frac{dp_{well}}{dx} = -\frac{\rho_m v_m{}^2 f_m}{R} - \frac{d\left(\rho_m v_m{}^2\right)}{dx} - \rho_m g \sin\theta\,, \tag{8.16}$$

The right side of Eq. 8.16 is evaluated from a previous iteration. The finite-difference form of Eq. 8.16 is

$$p_{well,i+1}^{n+1} - p_{well,i}^{n+1} = R_i^n\,. \tag{8.17}$$

Eq. 8.17 only describes the difference between pressure at two points, so we need another equation, which is a well constraint. In a total rate-constrained well, we have an additional equation written as

$$q_{total} = \sum_{i=1}^{I_{\max}} q_{oiJK} + \sum_{i=1}^{I_{\max}} q_{wiJK}\,, \tag{8.18}$$

where $I_{\max}$ is the maximum number of grid blocks in x-direction (along the well). $J_{\max}$ is the maximum number of grid blocks in y-direction (perpendicular to the well). $K_{\max}$ is the maximum number of grid blocks in z-direction (vertical depth).

Set of linear equations. In solving a set of linear equations, the total number of unknowns must be the same as the total number of equations. In this set, the unknowns are water pressure of each grid block and wellbore pressure. Below is the summary of equations and unknowns.

Unknowns:

1. Water pressure in grid blocks = $I_{\max} \times J_{\max} \times K_{\max}$ unknowns
2. Wellbore pressure = $I_{\max}$ unknowns

Total number of unknowns = $I_{\max} \times J_{\max} \times K_{\max} + I_{\max}$

Equations:

1. Reservoir flow in all grid blocks = $I_{\max} \times J_{\max} \times K_{\max}$ equations
   [from Eqs. 8.10 and 8.11]

2. Wellbore flow = $I_{\max} - 1$ equations
   [from Eq. 8.17]

3. Well constraint = 1 equation
   [from Eq. 8.18]

Total number of equations = $I_{\max} \times J_{\max} \times K_{\max} + I_{\max}$

Once grid block and wellbore pressure are known, water saturations are determined explicitly from the water mass balance equation (Eq. 8.7). This solution method is also known as Implicit Pressure Explicit Saturation (IMPES).

8.3.2 Energy balance

Reservoir flow. For non-isothermal flow in a reservoir, the general energy balance that describes multi-phase flow is given in the literature (Lake, 1989). We begin with this general energy balance, and rearrange the equation to express it in terms of temperature and pressure. The general energy balance without kinetic energy is written as below.

$$\nabla \cdot \left[\sum_{l=1}^{N_p} \rho_l \mathbf{u}_l \left(H_l + gD \right) \right] - \nabla \cdot \left(K_T \cdot \nabla T \right) = -\frac{\partial}{\partial t} \left[\phi \sum_{l=1}^{N_p} \rho_l S_l U_l + (1-\phi) \rho_s U_s + \rho g D \right], \tag{8.19}$$

where N_p is the number of phase.

To avoid writing unnecessarily long equations, we first simplify the Eq. 8.19 to single-phase flow and then present a derivation. Eq.8.16 for N_p =1 is

$$\nabla \cdot \left[\rho \mathbf{u} H + \rho \mathbf{u} g D \right] - \nabla \cdot \left(K_T \cdot \nabla T \right) = -\frac{\partial}{\partial t} \left[\phi \rho U + (1-\phi) \rho_s U_s + \rho g D \right], \tag{8.20}$$

On the right side of Eq. 8.20, we can replace the internal energy by enthalpy from the relation, $\rho U = \rho H - p$. The equation becomes

$$\rho\mathbf{u}\cdot\nabla H + H\nabla\cdot(\rho\mathbf{u}) + \nabla\cdot\rho\mathbf{u}gD - \nabla\cdot(K_{Tt}\nabla T) = -\frac{\partial}{\partial t}\left[\phi(\rho H - p) + (1-\phi)\rho_s U_s + \rho gD\right]. \tag{8.21}$$

Substituting the mass balance , $-\nabla\cdot(\rho\mathbf{u}) = \phi\frac{\partial\rho}{\partial t}$, into the second term, Eq. 8.21 becomes

$$\begin{aligned}&\rho\mathbf{u}\cdot\nabla H + H\left(-\frac{\partial}{\partial t}\phi\rho\right) + \nabla\cdot\rho\mathbf{u}gD - \nabla\cdot(K_{Tt}\nabla T)\\ &= -\phi\rho\frac{\partial H}{\partial t} - H\frac{\partial}{\partial t}\phi\rho + \frac{\partial}{\partial t}\phi p - (1-\phi)\rho_s\frac{\partial U_s}{\partial t} - \frac{\partial}{\partial t}\rho gD\end{aligned} \tag{8.22}$$

We assume that the temperature of the flowing fluid is the same as the temperature of the rock ($T = T_s$).r The internal energy of the rock can be expressed in terms of the temperature as $\Delta U_s \cong \Delta H_s = C_{ps}\Delta T$. The fluid enthalpy is also replaced by the definition of C_p and Maxwell's relation of thermodynamics. Eq. 8.22 becomes

$$\begin{aligned}&\rho\mathbf{u}C_p\cdot\nabla T - \beta T\mathbf{u}\cdot\nabla p + \mathbf{u}\cdot\nabla p - \nabla\cdot(K_{Tt}\nabla T) + \nabla\cdot\rho\mathbf{u}gD\\ &= -\left[(1-\phi)\rho_s C_{ps} + \phi\rho C_p\right]\frac{\partial T}{\partial t} + \phi\beta T\frac{\partial}{\partial t}p - \frac{\partial}{\partial t}\rho gD\end{aligned} \tag{8.23}$$

For oil-water flow, the final equation to be discretized is

$$\begin{aligned}&(\rho_o\mathbf{u}_o C_{po} + \rho_w\mathbf{u}_w C_{pw})\cdot\nabla T - (\beta_o\mathbf{u}_o\cdot\nabla p_o + \beta_w\mathbf{u}_w\cdot\nabla p_w)T + \mathbf{u}_o\cdot\nabla p_o + \mathbf{u}_w\cdot\nabla p_w\\ &- \nabla\cdot(K_{Tt}\nabla T) + \nabla\cdot(\rho_o\mathbf{u}_o gD + \rho_w\mathbf{u}_w gD) = -\left[(1-\phi)\rho_s C_{ps} + \phi(S_o\rho_o C_{po} + S_w\rho_w C_{pw})\right]\frac{\partial T}{\partial t}\\ &+ T\left(S_o\beta_o\phi\frac{\partial p_o}{\partial t} + S_w\beta_w\phi\frac{\partial p_w}{\partial t}\right) - \frac{\partial}{\partial t}(S_o\rho_o gD + S_w\rho_w gD)\end{aligned} \tag{8.24}$$

Eq. 8.24 will be approximated using finite difference. Details are given in Appendix D. The finite-difference form of the Eq. 8.24 is

$$\begin{aligned}&A_{ijk}T^{n+1}_{wi+1jk} + B_{ijk}T^{n+1}_{wi-1jk} + C_{ijk}T^{n+1}_{wij+1k} + D_{ijk}T^{n+1}_{wij-1k}\\ &\qquad + E_{ijk}T^{n+1}_{wijk+1} + F_{ijk}T^{n+1}_{wijk-1} + G_{ijk}T^{n+1}_{wijk} = RHS_{ijk}\end{aligned}. \tag{8.25}$$

where the subscript i, j, and k refer to spatial coordinates. The coefficients (A, B, C, D, E, F, G, RHS) resulting from doing a typical finite difference presents in Appendix D.

Well grid blocks. For grid blocks containing a wellbore, Eq. 8.25 must include source/sink terms on the left side as written below.

$$A_{ijk}T_{wi+1jk}^{n+1} + B_{ijk}T_{wi-1jk}^{n+1} + C_{ijk}T_{wij+1k}^{n+1} + D_{ijk}T_{wij-1k}^{n+1} + E_{ijk}T_{wijk+1}^{n+1} + F_{ijk}T_{wijk-1}^{n+1} + G_{ijk}T_{wijk}^{n+1} + q_{iJK}^{energy} = RHS_{ijk} \quad (8.26)$$

where

$$q_{iJK}^{energy} = -\left[K_T\left(\frac{2\pi\Delta x}{\ln(r_e/r_w)}\right) - \left(q\rho C_p\right)_T\right]\left(T_{iJK} - T_{well,i}\right), \quad (8.27)$$

$$\left(q\rho C_p\right)_T = q_{oiJK}\rho_o C_{po} + q_{wiJK}\rho_w C_{pw}. \quad (8.28)$$

Once we substitute Eq. 8.27 into Eq. 8.26, the only unknowns are the temperature in the grid blocks and the wellbore temperature. Thus, a non-isothermal wellbore flow model is required to describe the temperature in the wellbore.

Wellbore flow. For non-isothermal wellbore flow, the steady-state energy balance is derived in Chapter 4 that is

$$\frac{dT_{well}}{dx} = \frac{\left(\rho v C_p K_{JT}\right)_T}{\left(\rho v C_p\right)_T}\frac{dp}{dx} + \frac{2}{r_w}\frac{\alpha_{T,I}}{\left(\rho v C_p\right)_T}\left(T_{iJK} - T_{wekk}\right) - \frac{\left(\rho v\right)_T}{\left(\rho v C_p\right)_T}g\sin\theta \quad (8.29)$$

An additional equation comes from the fact that inflow temperature is equal to wellbore temperature at the toe end ($i = 1$) of the horizontal well.

$$T_{well,1} = T_{1,JK}. \quad (8.30)$$

Set of linear equations. In solving a set of linear equations, the total number of unknowns must be the same as the total number of equations. In this set, the unknowns are temperature of each grid block and wellbore temperature. Below is the summary of equations and unknowns.

Unknowns:

1. Temperature in all grid blocks = $I_{\max} \times J_{\max} \times K_{\max}$ unknowns
2. Wellbore temperature = $I_{\max}$ unknowns

Total number of unknowns = $I_{\max} \times J_{\max} \times K_{\max} + I_{\max}$

Equations:

1. Reservoir flow in all grid blocks = $I_{\max} \times J_{\max} \times K_{\max}$ equations
   [from Eqs. 8.25 and 8.26]

2. Wellbore flow = $I_{\max} - 1$ equations
   [from Eq. 8.28]

3. A constraint = 1 equation

[from Eq. 8.30]

$$\text{Total number of equations} = I_{\max} \times J_{\max} \times K_{\max} + I_{\max}$$

Note that $I_{\max}$ is the maximum number of grid blocks in the x-direction (along the well). $J_{\max}$ is the maximum number of grid blocks in the y-direction (perpendicular to the well). $K_{\max}$ is the maximum number of grid blocks in the z-direction (vertical depth).

8.3.3 Calculation procedure

The calculation procedure is presented in **Fig. 8.2**. We first initialize water pressure at static equilibrium at which the water pressures are functions of the elevation only. Water in the reservoir is initialized at irreducible water saturation. Initial temperature is at geothermal temperature with a gradient of 0.01 ^{o}F/ft, (dT/dz). The initialization is for all grid blocks and inside the wellbore. Next, we calculate fluid properties, and velocity and friction factor inside the wellbore. After that, water pressure is calculated from the total (water and oil) mass balance, Eq. 8.8. After the water pressure solution is obtained, the water saturation is explicitly updated by substituting the results into the water mass balance, Eq. 8.7, and the capillary pressure is calculated according to the new water saturation. When all the pressures and saturations are known, the temperature is explicitly calculated from the energy balance, Eq. 8.24. The procedure is then repeated for the next time step.

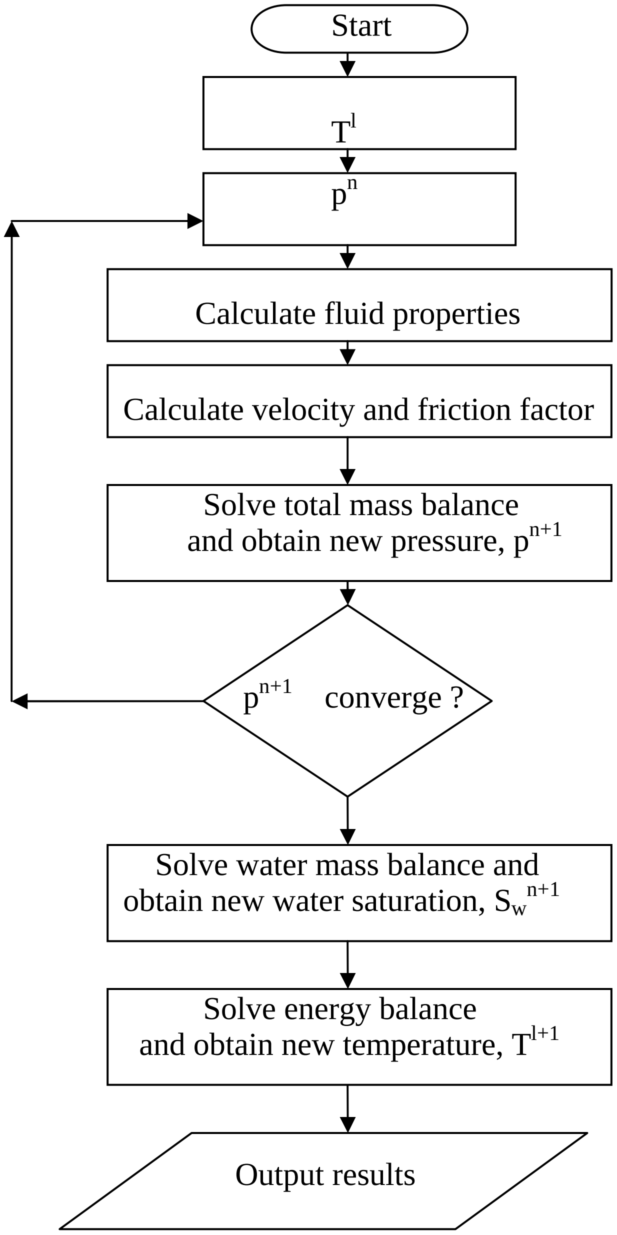

Fig. 8.2 Flow chart of the calculation procedure.

In solving the mass balance for the next iteration of pressure, we used the Newton-Raphson method. The method is discussed below.

Let $\tilde{x}$ be an unknown column matrix. We are seeking the solution, $\tilde{x}^{n+1}$. We have an equation in the following form.

$$\tilde{A}\tilde{x} = \tilde{b} \,, \qquad (8.31)$$

where

$\tilde{A}$; square matrix
$\tilde{x}$; column matrix
$\tilde{b}$; column matrix

The structure of square matrix $\tilde{A}$ in this case is the banded matrix including extra bands from wellbore flow equations as show below.

$\tilde{A} \cong$

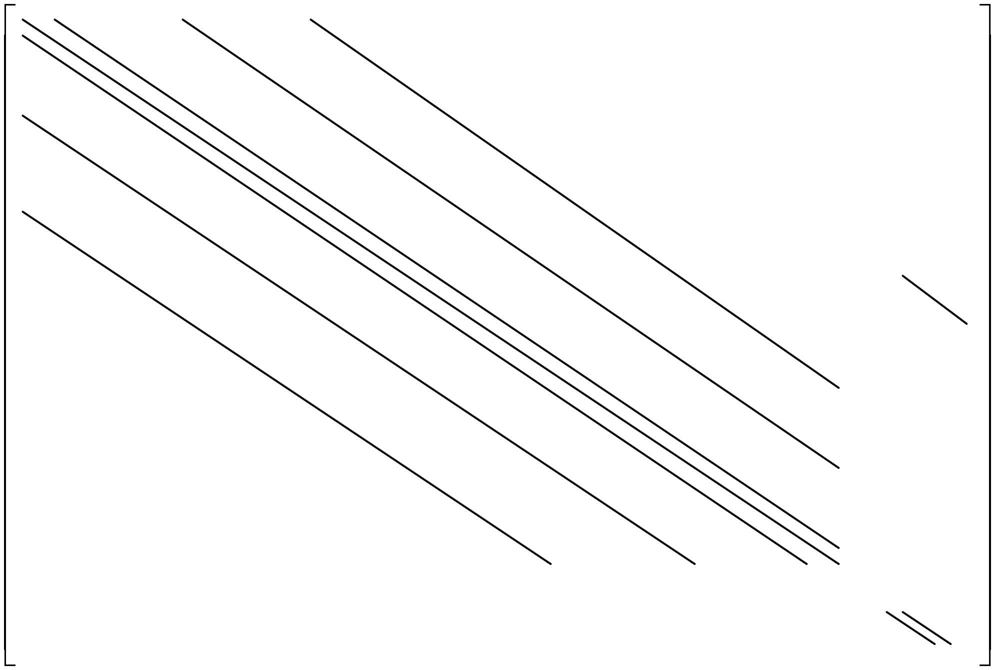

We first rearrange Eq. 8.31 and solve for the changes in $\tilde{x}$.

$$\tilde{f} = \tilde{A}\tilde{x} - \tilde{b} \,, \qquad (8.32)$$

The column matrix, $\tilde{f}$, contains f_1, f_2, …, $f_{\max}$, which are in terms of x_1, x_2, …, $x_{\max}$. The changes in $\tilde{x}$ are obtained from inverting the equation below.

$$\begin{bmatrix} \dfrac{\partial f_1}{\partial x_1} & \dfrac{\partial f_1}{\partial x_2} & \cdots & \dfrac{\partial f_1}{\partial x_{\max}} \\ \dfrac{\partial f_2}{\partial x_1} & \dfrac{\partial f_2}{\partial x_2} & \cdots & \dfrac{\partial f_2}{\partial x_{\max}} \\ \vdots & & & \vdots \\ \dfrac{\partial f_{\max}}{\partial x_1} & \dfrac{\partial f_{\max}}{\partial x_2} & \cdots & \dfrac{\partial f_{\max}}{\partial x_{\max}} \end{bmatrix} \begin{bmatrix} \delta x_1 \\ \delta x_1 \\ \vdots \\ \delta x_{\max} \end{bmatrix} = - \begin{bmatrix} f_1\left(x_1^n\right) \\ f_2\left(x_2^n\right) \\ \vdots \\ f_{\max}\left(x_{\max}^n\right) \end{bmatrix}. \tag{8.33}$$

The matrix that contains the partial derivatives is called the Jacobian matrix. Instead of taking the derivatives analytically, we numerically calculate each derivative from

$$\frac{\partial f_n}{\partial x_i} = \frac{f_n\left(x_i + \varepsilon\right) - f_n\left(x_i\right)}{\varepsilon}, \tag{8.34}$$

where ε is a small increment = 10^{-3}. Finally, we can obtain $\tilde{x}^{n+1}$ from

$$\tilde{x}^{n+1} = \tilde{x}^{n} + \delta\tilde{x}\,. \tag{8.35}$$

8.4 VALIDATION OF THE NUMERICAL MODEL DEVELOPED

A common practice in developing a numerical model is to validate the numerical result against an analytical solution. Validating the model is an important step, and can consume as much time as the program coding itself. Validation is necessary to ensure that the program coding, the mathematical formulations, and the numerical solution techniques are correct. However, we do not have a direct analytical solution for temperature and pressure profiles of a horizontal well in a bottom water drive reservoir. We will validate the numerical model developed here with the analytical model developed in Chapter 5. We simplify the numerical model to match the flow geometry of the analytical model as the followings:

1) Permeability

$$k_x = 0$$

$$k_y = k_z = 50\ md$$

2) Relative permeability

$$k_{ro} = 1$$

$$k_{rw} = 0$$

3) Capillary pressure is set to be zero ($p_c = 0$).

4) Irreducible water saturation is set to be zero ($S_{wr} = 0$).

5) No gravity effect ($g = 0$).

6) Reservoir fluid properties are evaluated at the same conditions as the analytical model, at 4,000 psi and 180 ^{o}F.

7) Boundary conditions

- No-flow for the bottom and top boundaries
- Pressure and temperature at external boundaries are 4,000 psi and 180 ^oF.

8). The accumulation terms on the right side of mass and energy balances are set to zero so that the flow is a steady-state flow.

The results from the numerical model were compared with the analytical solutions as shown in **Fig. 8.3**. The temperature, pressure, and inflow rate profiles from both analytical and numerical models agree well with each other.

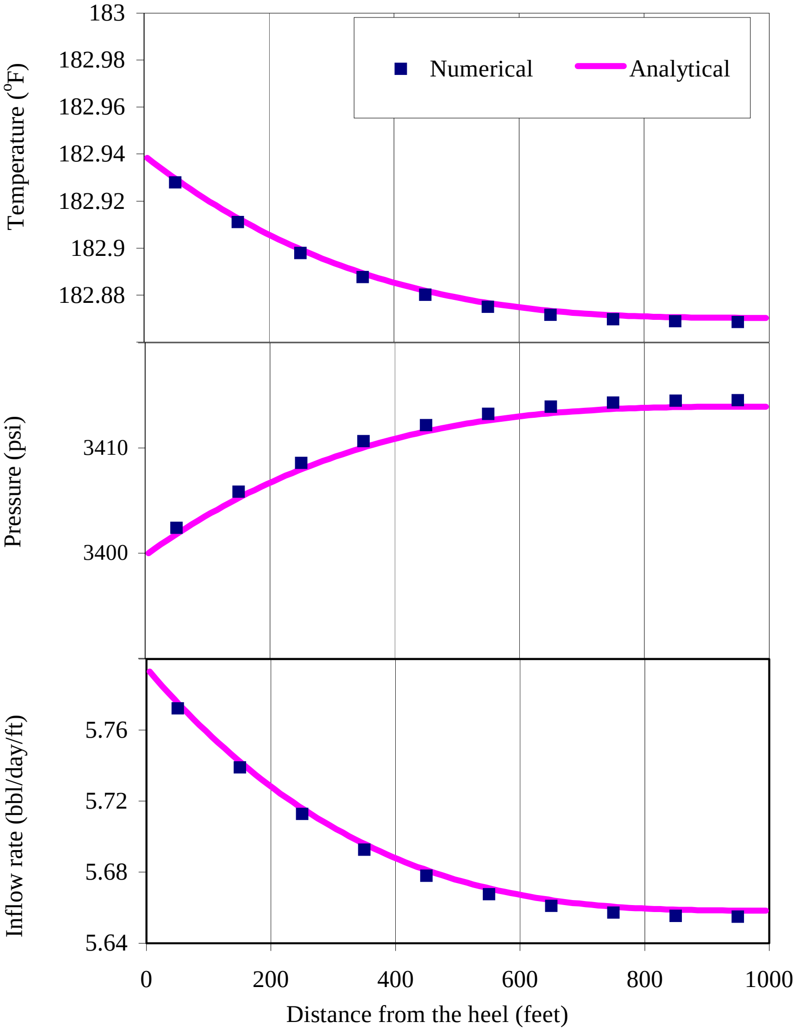

Fig. 8.3 Comparison of numerical and analytical results.

Another approach that was used to validate the numerical model under the water and oil flow in a bottom water drive reservoir sketched in Fig. 8.1 is to check the numerical model's mass balance calculation on the water component. We verify within the 5 percent of error that amount of water influx from the bottom is equal to amount of water produced and water remaining in reservoir for each time step.

8.5 RESULTS

Under the physical model described in Section 8.2, the oil reservoir is bounded with no-flow boundary except at the bottom of the boundary, which is initially in contact with water. The pressure and temperature at the bottom boundary are maintained at 4,000 psi and 180 ^{o}F. The temperature of the reservoir is initialized according to the geothermal gradient of 0.01 ^{o}F/ft. The reservoir is initially filled with oil while water is immobile at irreducible water saturation. We use fluid property correlations presented in Appendix A. Oil and water properties are correlated based on the oil gravity, the dissolved gas-oil ratio, the gas specific gravity, and the salinity of the water. The parameters of the numerical model are summarized in **Tables 8.1** and **8.2**.

Table 8.1 Reservoir and wellbore parameters

Well rate (base case) [b/d]	**5,000**
Horizontal length [ft]	**1,000**
Well inside diameter [in]	**6**
Relative pipe roughness	**0.027**
Skin factor	**0**
Pressure at WOC [psi]	**4000.00**
Temperature at WOC [^{o}F]	**180**
Reservoir thickness	**110**
Reservoir dimension [ft x ft x ft]	**1000 x 2150 x 110**
Grids [ft x ft x ft]	**100 x 10 x 10**

Table 8.2 Rock and fluid parameters	
Porosity	0
Horizontal permeability (base case), [md]	50
Vertical permeability (base case), [md]	10
Irreducible water saturation	0.25
Residual oil saturation	0.1
Capillary pressure at S_{wr} [psi]	11.00
Threshold capillary pressure [psi]	0
Total thermal conductivity [Btu/hr ft °F]	2
Rock density [lb/ft^3]	165
Rock heat capacity [Btu/lb °F]	0.22
Tempeature gradient [°F/ft]	0.01
Salinity of water [wt %]	5
Low density oil (base case)	
Oil API	45
Disolved gas-oil ration [SCF/STB]	800
Specific gravity of gas	0.75
High density oil (base case)	
Oil API	35
Disolved gas-oil ration [SCF/STB]	500
Specific gravity of gas	0.75

In the following sections, we will present example cases using the developed numerical temperature model. We focus the study on how the temperature changes along a horizontal well before and after water breakthrough from a bottom water aquifer. Since the application of the study is to use DTS for monitoring a production well, we are interested in examining the temperature changes over the span of several days, a length of time that is much greater than the response time of the DTS.

We will show three main effects on the time-varying temperature profiles. A base case is fixed at a total (oil+water) rate of 5,000 b/d, horizontal permeability of 50 md, vertical permeability of 10 md, and an oil gravity of 45 °API. We then compare the base case results with other cases, which are (1) total rate of 3,000 bbl/day, (2) a large permeability zone in the middle section of the reservoir, (3) an oil gravity of 35 °API

8.5.1 Effect of flow rates on the temperature profiles

For the base case, **Fig. 8.4** shows snapshots of temperature, pressure and inflow water rate profiles along the horizontal well at three elapsed times. The toe-to-heel pressure drop is about 12 psi, most of which occurs around the heel section (first 300 ft of horizontal wellbore). Because of this additional drawdown imposed on the reservoir, the inflow profiles of water and oil also increase toward the heel as shown in **Fig. 8.5**. Similar plots for the case of 3,000 bbl/d total rate are shown in **Figs. 8.6 and 8.7**. Here, a smaller pressure drop is observed. As a result, the size of a temperature change is smaller than for the base case. The temperature change for 5,000 b/d case is in the range of 179.4-180.6 ^{o}F while the temperature change for the 3,000 b/d case is in the range of 179.4-180.2 ^{o}F. The size of the temperature change is a strong function of flow rate. The strong sensitivity of the temperature changes to production rate demonstrates that it is possible to evaluate the amount of inflow rate from the temperature profiles if the rate is large. However, the results also show that it will be difficult to detect a temperature change in a small rate well.

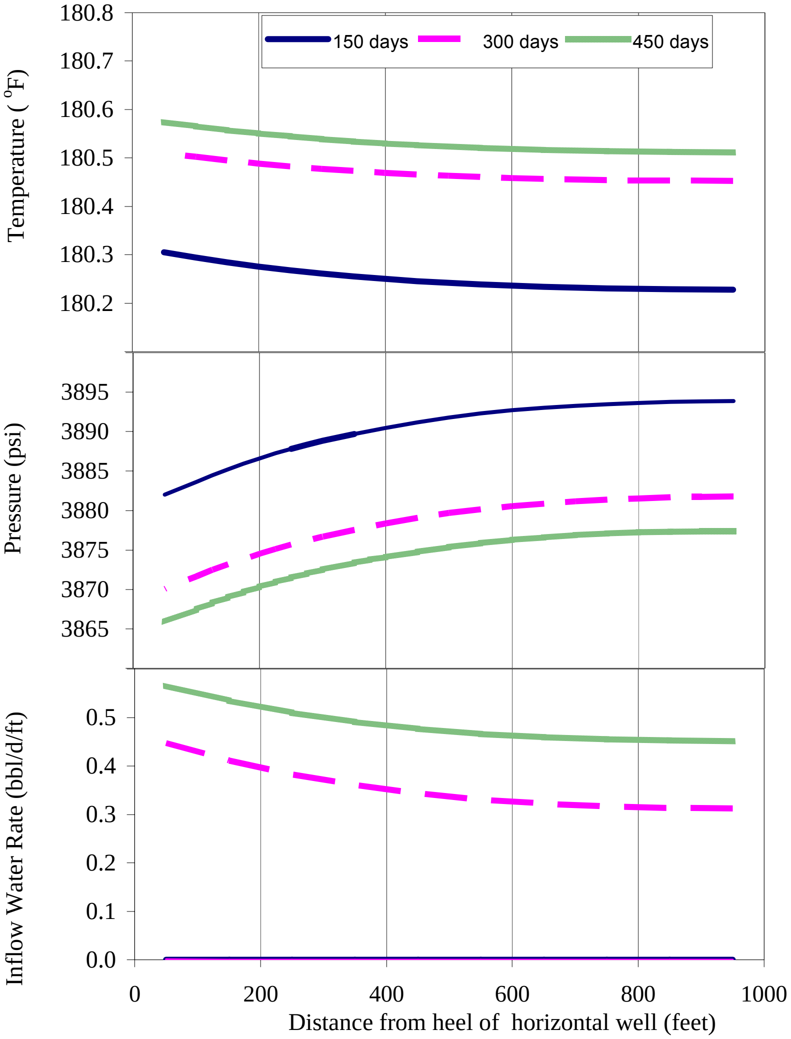

Fig. 8.4 Temperature, pressure, and inflow water rate profiles for 5,000 b/d total (oil/water) production rate.

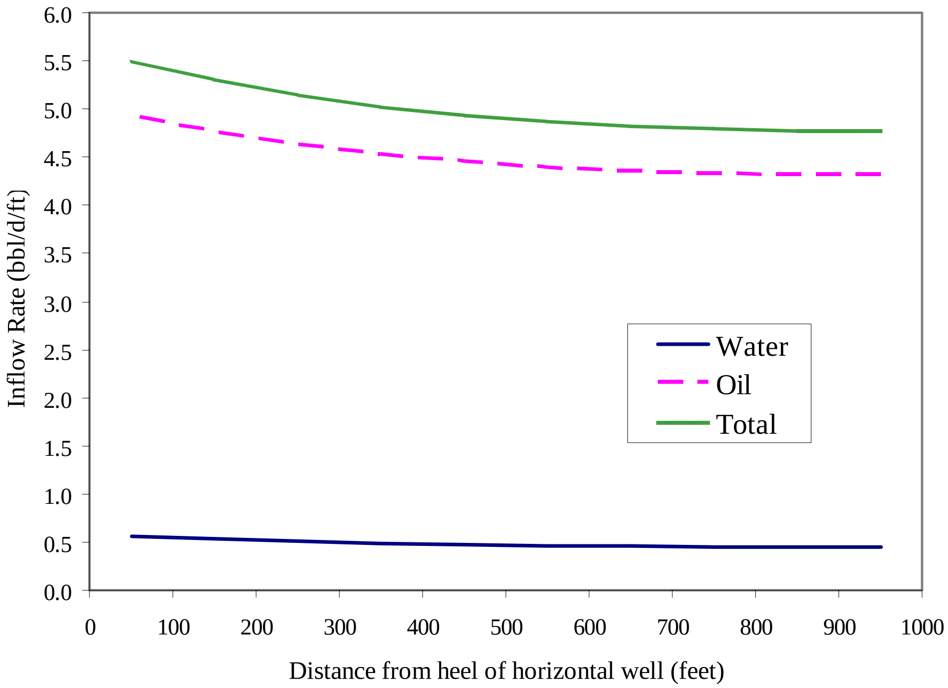

Fig. 8.5 Inflow rates along the horizontal well for 5,000 b/d total (oil/water) production rate (at 450 days).

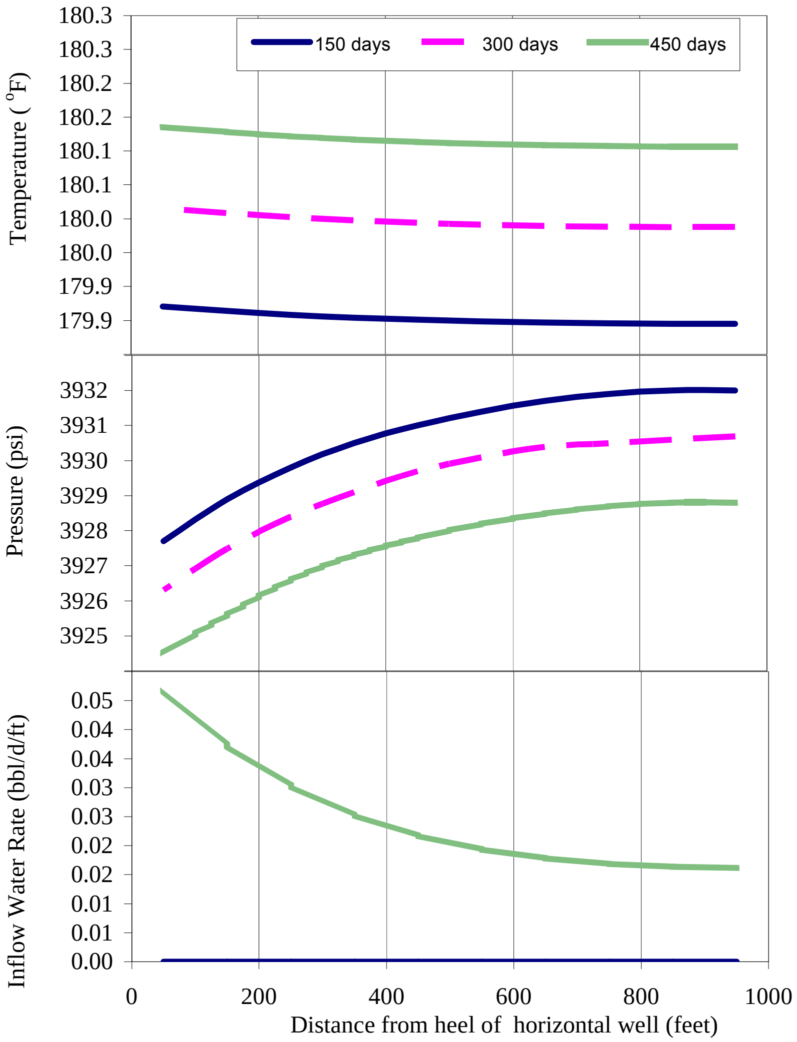

Fig. 8.6 Temperature, pressure, and inflow water rate profiles for 3,000 b/d total (oil/water) production rate

To compare the two cases in time, we plotted temperature, pressure and inflow rate at the mid point of the horizontal well in **Fig. 8.8**. After a few days of production, a relatively small pressure drop with time is observed. When the water breaks through, the reduction of total fluid mobility increases the drawdown to maintain a constant total rate of production. The distinguishing feature is the temperature versus time plot that shows different slopes before and after water breakthrough time. The slope of the temperature after breakthrough is less than the one before breakthrough. This is because water has a greater density and heat capacity than oil, causing the Joule-Thomson coefficient of water to be less than oil. The water-oil mixing property has caused the slope to decrease, at least for this type of fluid. This feature can be used to tell when water breakthrough occurs. Next, we reduced the total production rate to 4,000 b/d and

3,000 b/d. For the 3,000 b/d case we do not see the change in temperature slope because water production is not large enough to cause a significant change. The temperature gradually increases with time because friction (viscous dissipative heating) is always created when there is flow. This is similar to entropy generation in thermodynamics.

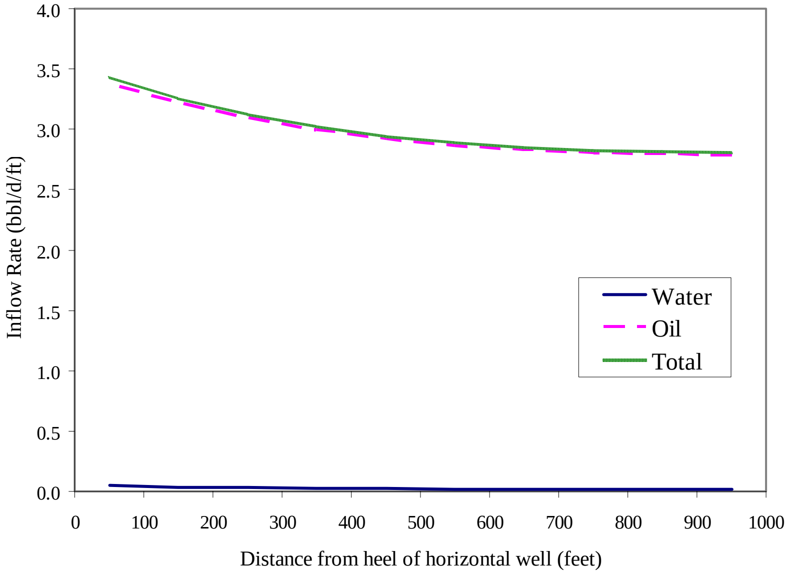

Figure 8.7 Inflow rates along the horizontal well for 3,000 b/d total (oil/water) production rate (at 450 days).

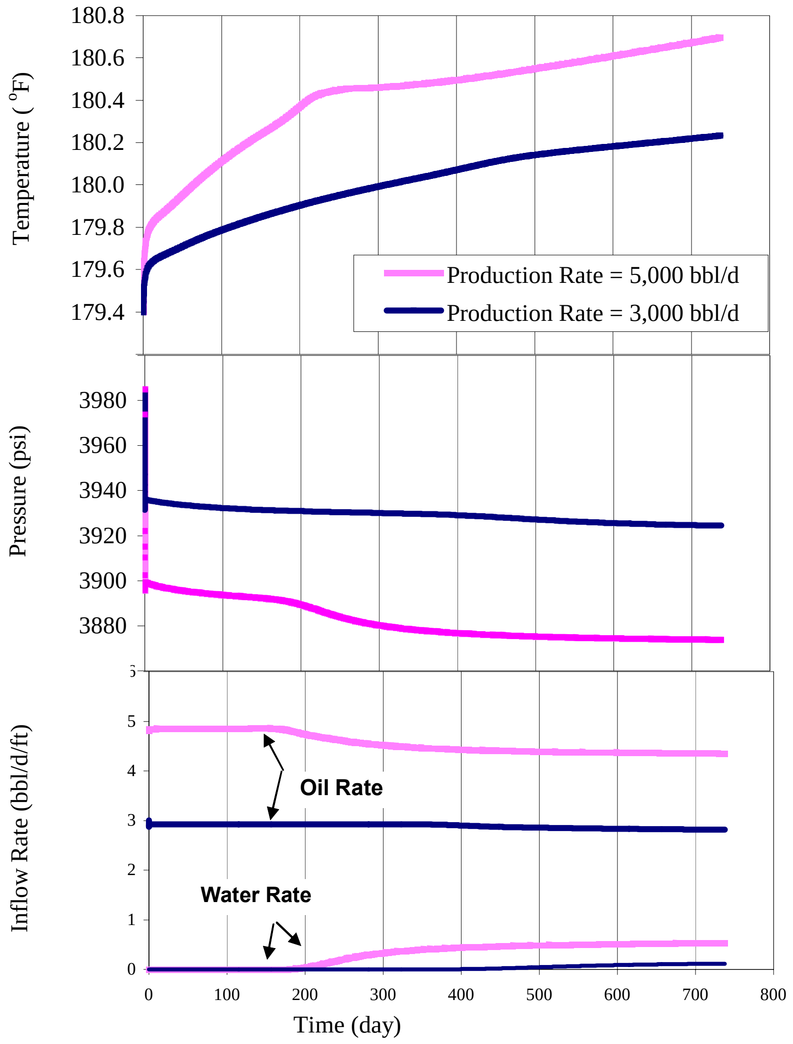

Fig. 8.8 Wellbore temperature, wellbore pressure and inflow rate changes with time for different production rates. (at center of horizontal well)

8.5.2 Effect of large permeability zone on the temperature profiles

In this section, we will examine the wellbore temperature behavior where a large permeability compartment is in the middle 300 ft of the reservoir (k_h=100 md, k_z=20 md), from the interval from 400 to 700 feet from the heel of the well. The rest of the reservoir is the same as the base case (k_h=50 md, k_z=10 md). **Fig. 8.9** illustrates this case by showing the water saturation distribution in the reservoir at 170 days of production when the warm water from the bottom of reservoir reaches the middle intervals of the well, but water has not arrived in the rest of the intervals. **Fig. 8.10** shows snapshots of temperature, pressure, and inflow water rate profiles along the horizontal well at three elapsed times. **Fig. 8.11** shows the details of water, oil, and total inflow profiles at 450 days. As time progresses, the pressure profiles do not show an abrupt change along the well, which suggests that the snapshots of pressure profiles alone for this case cannot identify the high permeability zone.

On the other hand, the temperature profiles show a noticeable change in slope. For this example case, we therefore can conclude that the location of a high permeability zone (also the large flow rate) is certainly identified as the zone over which the slope of the temperature profiles is greater than the rest of the horizontal intervals that are producing at smaller inflow rates. This implies that locations of fractures (i.e. large permeability zone) can also be detected by the temporal change of the temperature profiles.

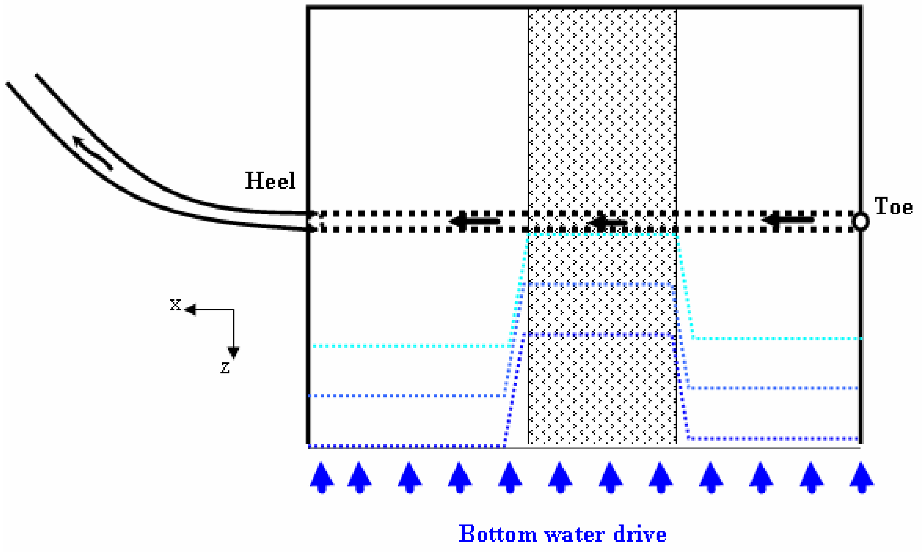

Fig. 8.9 Water saturation distribution around a well at 170 days of production. Middle interval (400-700 ft shaded) k_h = 100 md/ k_z = 20 md; end intervals k_h = 50 md/ k_z = 10 md

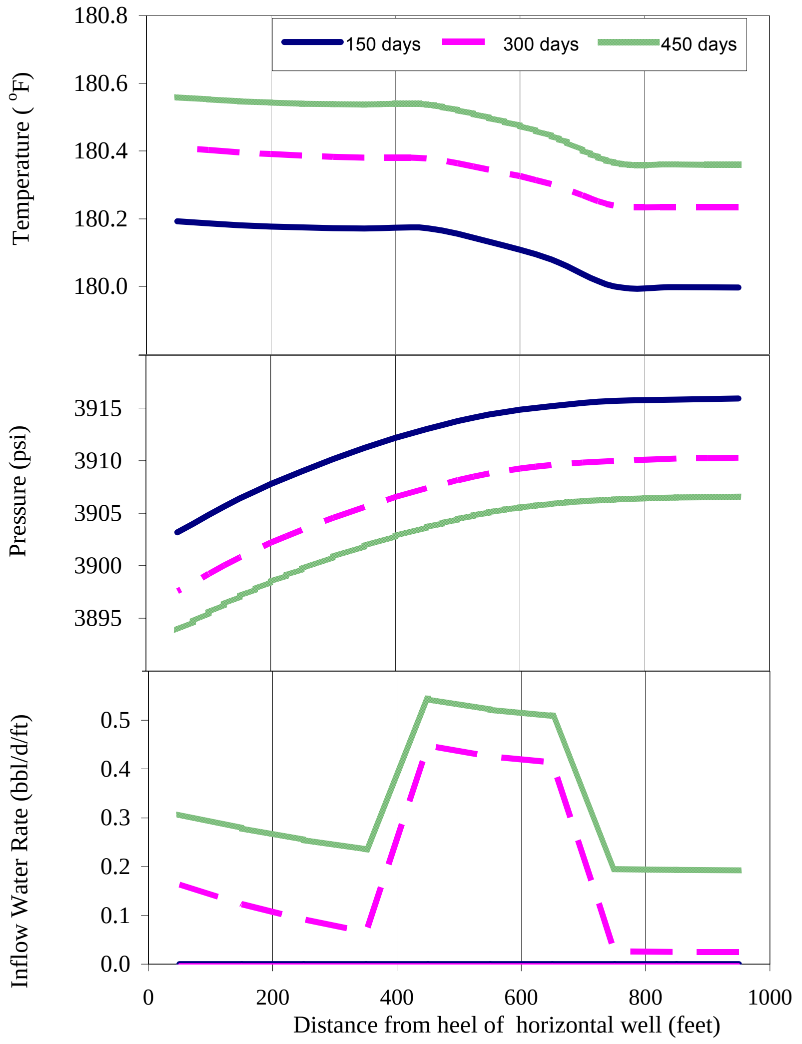

Fig. 8.10 Temperature, pressure, and inflow water rate profiles for large permeability in middle section (400 -700 ft) of well. Middle interval k_h=100 md/ k_z=20 md, end intervals k_h=50 md/ k_z=10 md.

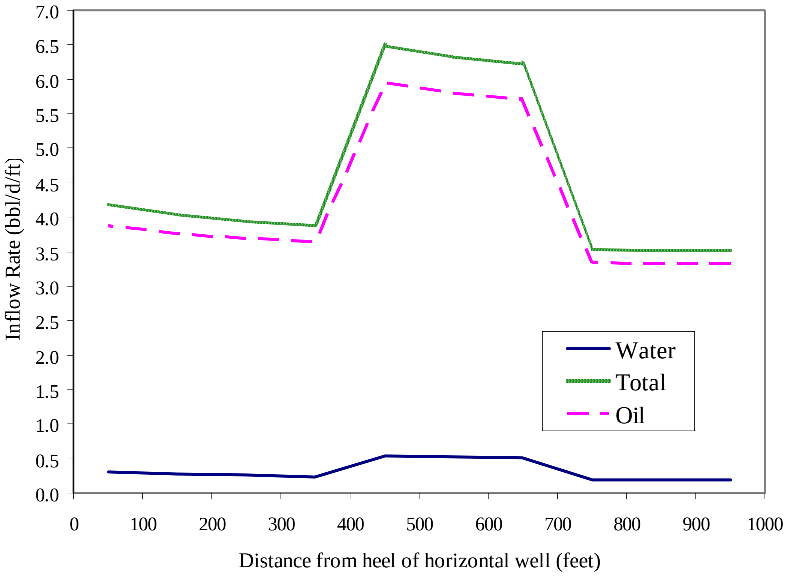

Fig. 8.11 Inflow rates along horizontal well for large permeability in middle section (400-700 ft) of well (at 450 days). Middle interval k_h=100 md/ k_z=20 md, end intervals k_h=50 md/ k_z=10 md.

Fig. 8.12 shows the plots of wellbore temperature, wellbore pressure and inflow water rate versus time at different locations along the well. We can see different slopes (dT/dt) before and after water breakthrough time in the near toe curve, but the slope differences are difficult to see in the middle and near heel curves. This is because the wellbore temperature contains the combined information both from inflow and from the upstream wellbore flow. The upstream wellbore flow tends to be dominant when moving toward the heel of the horizontal well.

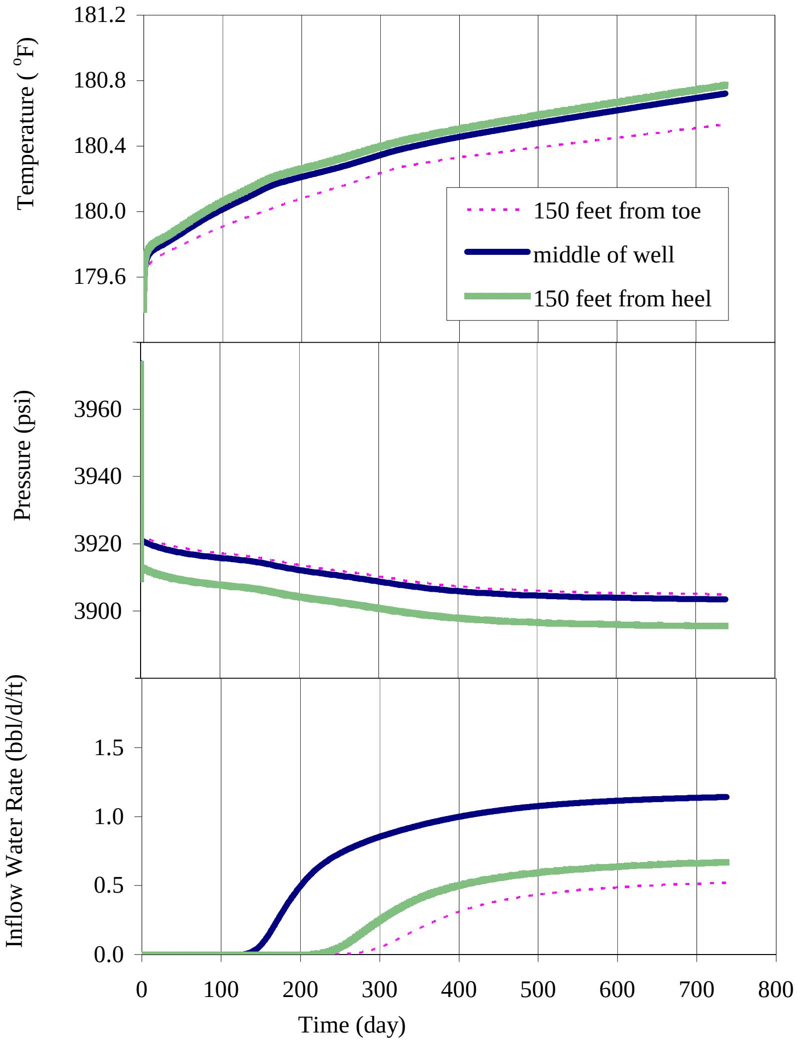

Fig. 8.12 Wellbore temperature, wellbore pressure and inflow rate changes with time for different locations.
Middle interval k_h=100 md/ k_z=20 md, end intervals k_h=50 md/ k_z=10 md.

8.5.3 Effect of oil type on the profiles

The purpose here is to assess the size of the temperature change resulting from different types of oil. We model the oil properties by using commonly known correlations based on the oil gravity (^{o}API), dissolved gas-oil ratio, and gas specific gravity. Two oils of different densities are chosen for this purpose. **Table 8.2** provides the fluid properties. **Fig. 8.13** shows profiles for an oil gravity of 35^{o}API. Compared to the base case (**Fig. 8.4**), the shapes of the profiles are similar, but the magnitude of changes is larger by a factor of two.

Fig. 8.14 is a comparison of the base case (45 °API) and the denser-oil case (35 °API) with time. As production time progresses, wellbore pressure for the 35 °API oil case drops about 120 psi more than for the base case. The reduction of mobility caused by the larger viscosity oil results in greater drawdown to maintain a constant well rate. Temperature gradually increases with time, and the temperature increase reflects the pressure drop, notably where the wellbore pressure drops when water breaks through. After water breakthrough, the rate of temperature increase is smaller than before water breakthrough when only oil flows into the wellbore. The temperature difference between the two cases is quite large, which means that fluid properties have a great impact on temperature profiles. This suggests that a good description of fluid properties is required to quantitatively infer inflow rate profiles from temperature profiles.

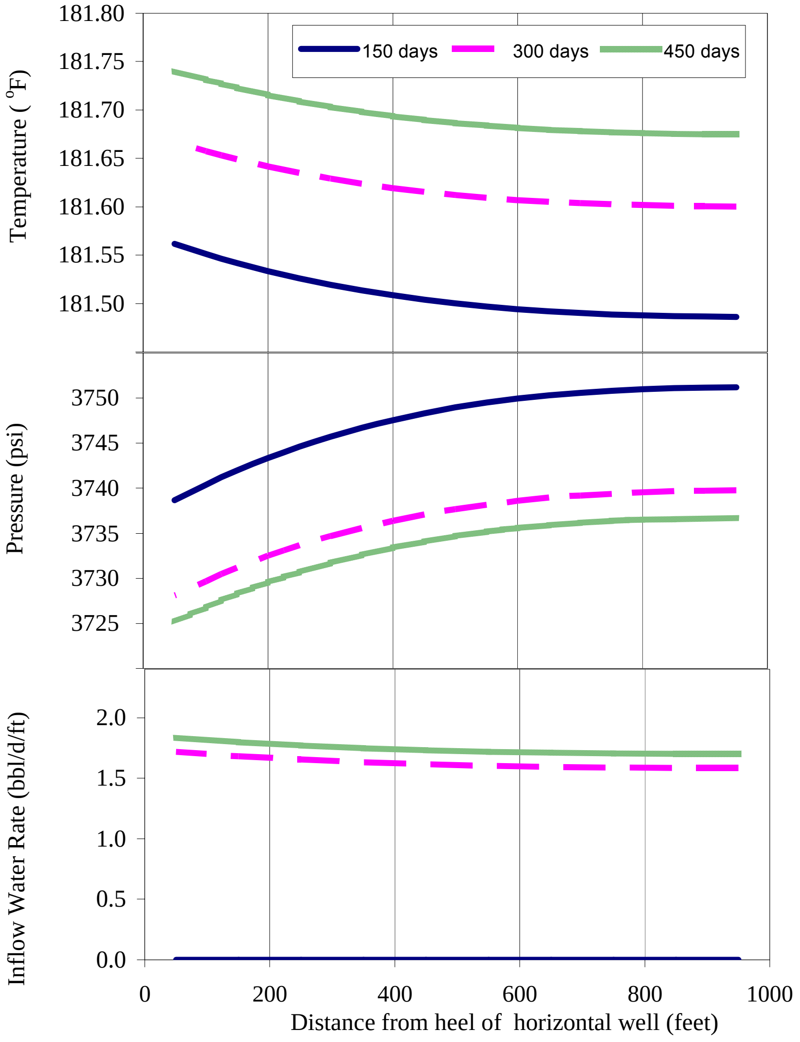

Fig. 8.13 Temperature, pressure, and inflow water rate profiles for an oil gravity of 35 °API.

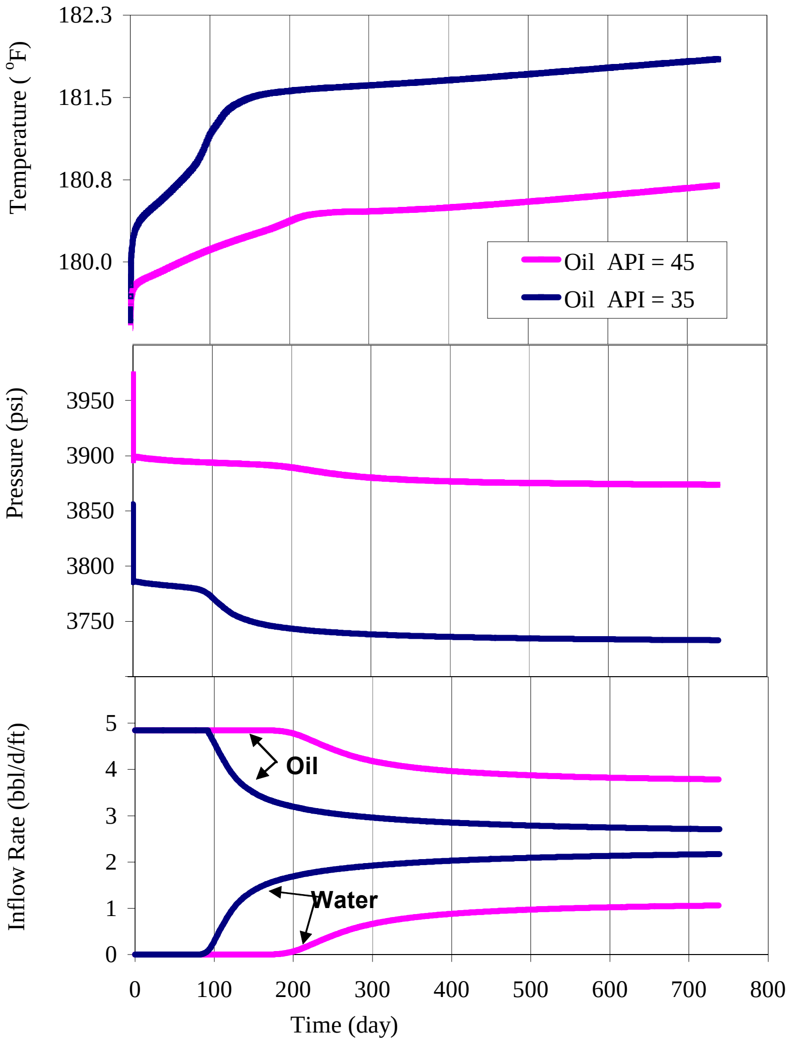

Fig. 8.14 Wellbore temperature, wellbore pressure, and inflow rate changes (at center of horizontal well) with time for different oils.

CHAPTER 9

CONCLUSIONS AND RECOMMENDATIONS

9.1 CONCLUSIONS

We have derived the equations governing the heat and mass transfer along the path of a producing wellbore. We have also derived the governing equations that describe reservoir fluid flow and heat transfer, and solved them analytically in one-dimensional (1D). Results from the 1D analytical reservoir solution indicate that the inflow temperature in a horizontal well can change from the geothermal temperature by a few degrees. The size of this change depends on the types of fluids flowing and on the pressure drawdown between the reservoir and the wellbore. Inasmuch as we must account for heat transfer from wellbore to formation, we have coupled the wellbore and reservoir equations and solved them numerically.

Based on the coupled model predictions we see little changes on the temperature profiles if the liquid flow rate is small or if the pressure drop along the well is small. We found that temperature and pressure profiles are sensitive to the well trajectories, meaning that an accurate well survey is needed to interpret temperature and pressure profiles when significant elevation changes occur. The other finding from the prediction model is that temperature decreases when water or gas enter into horizontal wells if the boundary temperatures are the same. Where the production of one fluid starts and another ends is clearly observed under certain production conditions. We also presented a sensitivity study to show the effect of flow rate and water or gas zone location on temperature behavior.

The second part of this report presented an inversion method that interprets distributed temperature and pressure data to obtain flow rate profiles along horizontal wells. We have applied the inversion method, which is based on the Levenberg-Marquardt algorithm, to minimize the differences between the measured profiles and the profiles calculated from the prediction model developed. Through numerical experiments, we inferred the relative importance of the input data and determined the best combination of input data.

We have shown synthetic and field examples to illustrate how to use the inversion model to interpret the flow profile of a horizontal well. The synthetic examples showed that even with single-phase oil production, the inflow profile can be estimated in many cases. The method is even more robust when water or gas is produced along discrete intervals in an oil production well because of the unique temperature signature of water or gas production.

We have applied the inversion method to temperature and pressure profiles measured with production logs in a horizontal North Sea producer well. With the inversion method developed, we have successfully matched the profile of temperature and pressure.

We have also developed a model to predict temperature profiles in the variable angle build sections of a multilateral well by applying the method developed by Ramey to this geometry, and a model of junction where two flow streams are commingled. In addition, we have solved the governing equations of the reservoir and wellbore numerically to simulate horizontal well water coning.

9.2 RECOMMENDATIONS

The forward (prediction) model study is intended to establish a basic understanding of temperature behavior under specific examples, and to assess the potential uses of a distributed temperature sensor (DTS) in monitoring a horizontal production well. A more advanced and detailed modeling could be further done as follows:

1. Represent the viscous dissipation ($\boldsymbol{\tau} : \nabla \mathbf{v}$) by a different model from the one used in this study.
2. Develop a model to account for the fact that horizontal wells have bends and curves, and may not be in the center of a reservoir.
3. Generalize the fluid properties by using the Peng-Robinson or Redlich-Kwong-Soave equations of state, as normally practiced in numerical reservoir simulation, and study the temperature behavior when the reservoir pressure is dropped below the bubble point pressure and gas evolves from oil.
4. Approximate a water coning model to an analytical or semi-analytical model so that we can have a fast estimate at the inflow temperature with time. Implement the model in an inversion model.

For the inversion part, we recommend following:

5. Construct or approximate Jacobian (sensitivity) matrices analytically or semi-analytically. Computation of Jacobian takes about 90% of total computation of the inversion process.
6. Study the effects of data noise on water or gas profile entry information (Deploy a Gaussian based random error.).
7. Study the effects of grids size by using finer grids for synthetic data generation and courser grids for inversion. The latter results in only a few pressure points observations.

APPENDIX A: OVERAL HEAT TRANSFER COEFFICIENT

When a fluid expands at constant enthalpy (an isenthalpic process) because of pressure drop, the temperature of the fluid changes. This phenomenon is named the Joule-Thomson effect. The temperature change per unit pressure change is called the Joule-Thomson coefficient, K_{JT}. An expression for K_{JT} can be derived as follows:

For non-flowing isenthalpic process,

$$\Delta H = 0 . \tag{A.1}$$

For a pure fluid, the fluid enthalpy is a function of pressure and temperature. The above equation can then be expanded in the following manner.

$$\left(\frac{\partial H}{\partial T}\right)_p \Delta T + \left(\frac{\partial H}{\partial p}\right)_T \Delta p = 0 . \tag{A.2}$$

Apply the definition of the heat capacity and Maxwell's relation of thermodynamics.

$$C_p \Delta T + \left\{ V - T\left(\frac{\partial V}{\partial T}\right)_p \right\}_T \Delta p = 0 . \tag{A.3}$$

Replace the specific volume with the fluid density, $V = 1/\rho$. The above equation becomes

$$C_p \Delta T + \left\{ \frac{1}{\rho} - \frac{T}{\rho}\left(-\frac{1}{\rho}\right)\left(\frac{\partial \rho}{\partial T}\right)_p \right\}_T \Delta p = 0 . \tag{A.4}$$

Substitute definition of thermal expansion coefficient into the equation.

$$C_p \Delta T + \left(\frac{1}{\rho} - \frac{\beta T}{\rho} \right)_T \Delta p = 0 . \tag{A.5}$$

Rearranging the above equation gives the expression for K_{JT}.

$$K_{JT} = \left(\frac{\partial T}{\partial p}\right)_H = \frac{\beta T - 1}{\rho C_p} . \tag{A.6}$$

For an ideal gas, $\beta = 1/T$, and the Joule-Thomson coefficient is zero, which means that when an ideal gas expands at constant enthalpy, there is no temperature change. As real fluids expand, cooling occurs if K_{JT} is positive, while warming occurs if it is negative. For natural gases up to pressures of about 5,000 psi, K_{JT} is positive in the range of 0.01 to 0.06 ^{o}F per psi (McCain, 1990). For liquids, a general rule is that K_{JT} is negative for temperatures smaller than 80-90% of the liquid's critical temperature and positive otherwise. This rule does not apply, however, for pressures below the liquid's vapor pressure. Water has a negative K_{JT} for temperature below 500 ^{o}F; and it warms up approximately 0.002-0.003 ^{o}F per psi pressure drop, as do most oils (Steffensen and Smith, 1973).

Fluid flow in a reservoir can be approximated as an isenthalpic flow (no heat nor work done on fluid). During production, the Joule-Thomson effect is a dominant factor causing the inflow temperature of the fluid to be different from the geothermal temperature at that depth.

If we were to use the energy equation in porous media (Eq. 3.20) to describe the Joule-Thomson experiment, which is a steady-state isenthalpic process with no heat conduction, we would arrive at

$$0 = \rho C_p \mathbf{u} \cdot \nabla T - \beta T \mathbf{u} \cdot \nabla p + \mathbf{u} \cdot \nabla p . \tag{A.7}$$

All of the terms are products of $\mathbf{u}$, so the equation can be rearranged as

$$0 = \mathbf{u} \cdot \left(\rho C_p \nabla T + \nabla p - \beta T \cdot \nabla p \right). \tag{A.8}$$

If $\mathbf{u}$ is not zero, we can divide both sides by $\mathbf{u}$. The equation becomes

$$\begin{aligned} \nabla T &= \left(\frac{\beta T - 1}{\rho C_p} \right) \nabla p \\ &= K_{JT} \nabla p \end{aligned} . \tag{A.9}$$

An example of this kind of process is a flow through an expansion valve illustrated in **Fig. A.1**. Thus, we can fairly conclude that the governing equation of the reservoir flow (Eq. 3.20) intrinsically includes the Joule-Thomson effect.

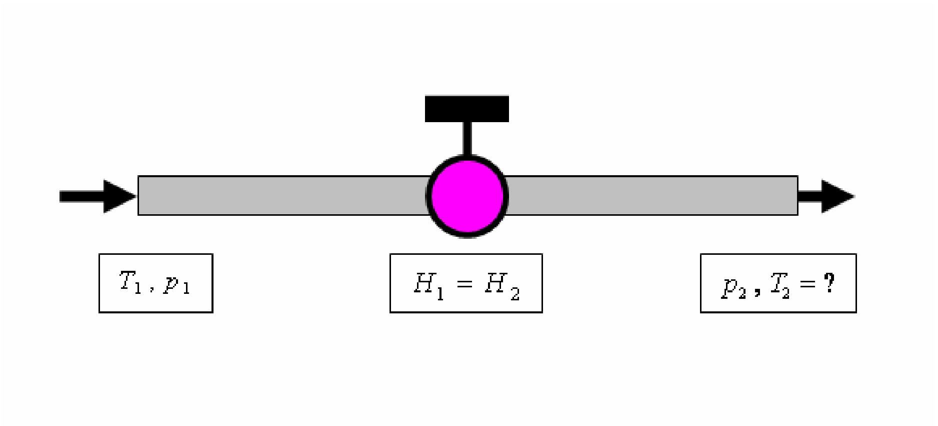

Fig. A.1 Sketch shows flow through an expansion valve.

The meaning of Eq. A.7 is that there are two main causes of thermal energy change; fluid expansion, $\beta T(-\mathbf{u} \cdot \nabla p)$, and viscous dissipation, $(-\mathbf{u} \cdot \nabla p)$. Note that the term $\left(-\mathbf{u}\cdot\nabla p\right)$ is always positive. For most gases, $\beta T\left(-\mathbf{u}\cdot\nabla p\right)$is greater than $\left(-\mathbf{u}\cdot\nabla p\right)$, and the temperature of a flowing gas decreases. On the other hand, if $\left(-\mathbf{u}\cdot\nabla p\right)$ is greater than $\beta T\left(-\mathbf{u}\cdot\nabla p\right)$, the temperature of a flowing liquid increases. If there is no change in pressure or $\beta T\left(-\mathbf{u}\cdot\nabla p\right)=\left(-\mathbf{u}\cdot\nabla p\right)$ such as a flow of ideal gas (i.e. low pressure gas) in which $\beta = 1/T$, the temperature of a fluid is constant.

It should be emphasized that the thermal energy balance can only be simplified to describe the Joule-Thomson effect if we model the viscous dissipation, $\left(-\boldsymbol{\tau}:\nabla\mathbf{u}\right)$, as $\left(-\mathbf{u}\cdot\nabla p\right)$ and $\mathbf{u}$ is not zero. For example, if we modeled that $\left(-\boldsymbol{\tau}:\nabla\mathbf{u}\right)=a\left(-\mathbf{u}\cdot\nabla p\right)$ where a is a constant, Eq. A.7 could not be simplified to the Joule-Thomson coefficient.

APPENDIX B: OVERAL HEAT TRANSFER COEFFICIENT

The object of this appendix is to derive the overall heat transfer coefficient used in this study. For a cased and cemented wellbore, the temperature profile near the wellbore will look like as shown in **Fig. B.1**. The wellbore is surrounded by casing material and cement. Fluid arrives with temperature, T_I. At the inside of the cement, the temperature is T_{cem} and the temperature is T_c at the inside of casing. The bulk average temperature inside the well is given as T_b.

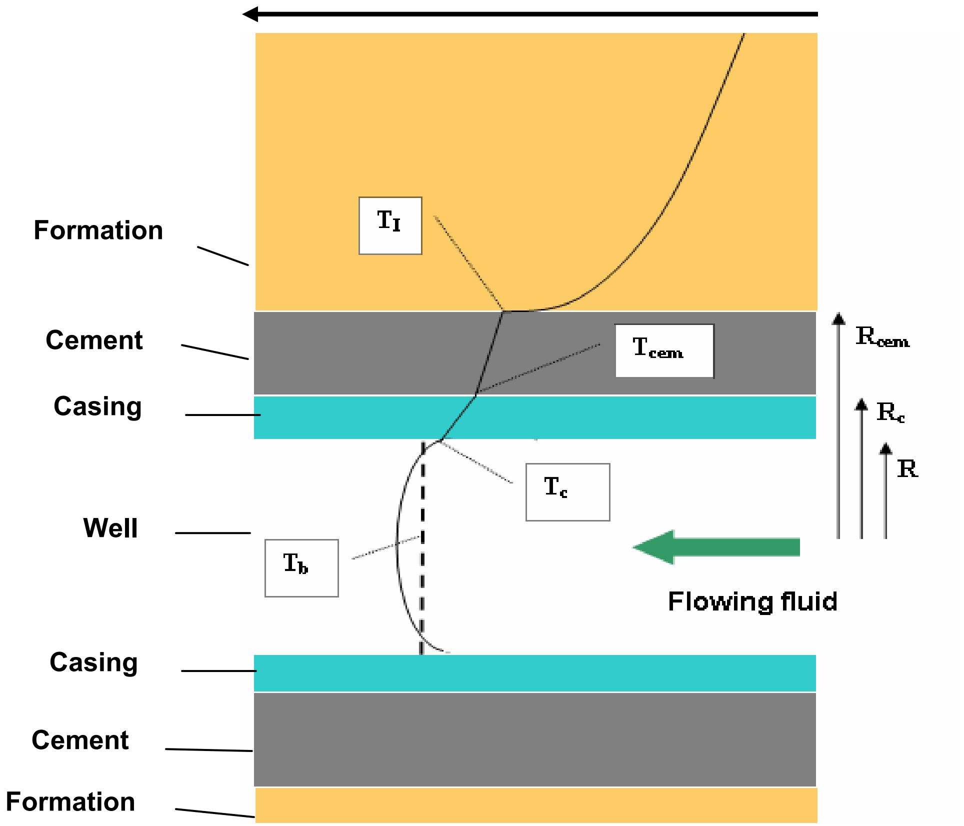

Fig. B.1 Temperature profile near a wellbore.

For steady state with constant thermal conductivity, the radial temperature distribution is given as

$$\frac{1}{r}\frac{d}{dr}\left(r\frac{dT}{dr}\right)=0\,. \tag{B.1}$$

Solving this differential equation for the casing yields

$$T = T_{cem} + \frac{T_c - T_{cem}}{\ln\left(R \middle/ R_c \right)} \ln\left(r \middle/ R_c \right). \quad \text{for } R \le r \le R_c \tag{B.2}$$

For the cement,

$$T = T_I + \frac{T_{cem} - T_I}{\ln\left(R_c \middle/ R_{cem} \right)} \ln\left(r \middle/ R_{cem} \right). \quad \text{for } R_c \le r \le R_{cem} \tag{B.3}$$

The heat flow rates are

$$\begin{aligned} Q_c &= -2\pi R(1-\gamma)K_c \left.\frac{dT}{dr}\right|_{r=R} \\ &= 2\pi(1-\gamma)K_c \frac{T_c - T_{cem}}{\ln\left(R_c \middle/ R \right)}, \end{aligned} \tag{B.4}$$

and

$$\begin{aligned} Q_{cem} &= -2\pi R_c (1-\gamma)K_{cem} \left.\frac{dT}{dr}\right|_{r=R_c} \\ &= 2\pi(1-\gamma)K_{cem} \frac{T_{cem} - T_I}{\ln\left(R_{cem} \middle/ R_c \right)}. \end{aligned} \tag{B.5}$$

The heat flow from wall to flowing fluid is given by

$$Q_{fl} = -2\pi R(1-\gamma)C_h(T_c - T_b). \tag{B.6}$$

where C_h is a heat transfer coefficient that would be determined experimentally. From boundary layer analysis with a constant wall temperature, the laminar flow heat transfer coefficient is

$$C_h = 3.656 \frac{K_{fl}}{2R}. \tag{B.7}$$

For turbulent flow, Gnielinski's formula[46] is widely used. The heat transfer coefficient is given as

$$C_h = \frac{\left(f \middle/ 2 \right)(N_{\mathrm{Re}} - 1000)N_{\mathrm{Pr}}}{1 + 12.7\left(f \middle/ 2 \right)^{0.5} \left(N_{\mathrm{Pr}}{}^{2/3} - 1\right)} \frac{K_{fl}}{2R}. \tag{B.8}$$

When liquid-gas two phase flow occurs, the heat transfer coefficient will become flow regime dependent. Kim and Ghajar[47] presented a simple flow regime dependent correlation as

$$C_{h,T} = \left(1-y_g\right)C_{h,l}\left[1+C\left(\frac{x}{1-x}\right)^m\left(\frac{y_g}{1-y_g}\right)^n\left(\frac{N_{\mathrm{Pr},g}}{N_{\mathrm{Pr},l}}\right)^s\left(\frac{\mu_g}{\mu_l}\right)^t\right], \tag{B.9}$$

where

$$x = \frac{w_g}{w_g + w_l}\,. \tag{B.10}$$

$C_{h,l}$ is the liquid heat transfer coefficient and is based on the in-situ Reynolds number. The constants are given in **TableB.1**.

Table B.1 Constant values for calculations of the heat transfer coefficient.

	C	m	n	s	t
Slug and Bubbly	2.86	0.42	0.35	0.66	-0.72
Annular	1.58	1.4	0.54	-1.93	-0.09
Stratified	27.89	3.1	-4.44	-9.65	1.56

At steady state, heat flows are equal. Then, we have

$$Q_c = Q_{cem} = Q_{fl} \equiv Q\,. \tag{B.11}$$

Summation of the relationships gives

$$T_b - T_I = \frac{Q}{2\pi(1-\gamma)}\left[\frac{\ln\left(R_c/R\right)}{K_c}+\frac{\ln\left(R_{cem}/R_c\right)}{K_{cem}}+\frac{1}{RC_h}\right]. \tag{B.12}$$

Therefore, the overall heat transfer coefficient for the wellbore is

$$\alpha = \frac{Q}{\left(T_I - T_b\right)2\pi R(1-\gamma)} = \left[\frac{R\ln\left(R_c/R\right)}{K_c}+\frac{R\ln\left(R_{cem}/R_c\right)}{K_{cem}}+\frac{1}{RC_h}\right]^{-1}. \tag{B.13}$$

Considering a partly opened well, the total energy entering the wellbore neglecting kinetic energy and viscous shear is then

$$
\begin{aligned}
-\left(e_r\right)_R 2\pi R_{cem}\Delta x &= \left(\rho_I \hat{H}_I v_I\right) 2\pi R_{cem}\gamma\Delta x - K_T \left.\frac{dT}{dr}\right|_{r=R_{cem}} 2\pi R_{cem}\left(1-\gamma\right)\Delta x \\
&= w\hat{H}_I\Big|_{r=R_{cem}} - K_T \left.\frac{dT}{dr}\right|_{r=R_{cem}} 2\pi R_{cem}\left(1-\gamma\right)\Delta x
\end{aligned}
, \qquad \text{(B.14)}
$$

Equating with the total energy from the formation is

$$
-\left(e_r\right)_R 2\pi R\Delta x = wH_I\Big|_{r=R} + 2\pi R\Delta x\left(1-\gamma\right)\alpha\left(T_I - T_b\right). \qquad \text{(B.15)}
$$

Equating Eqs. A.14 and A.15 and considering the difference of convection term $\left(wH_I\big|_{r=R} - wH_I\big|_{r=R_{cem}}\right)$ is negligible yield

$$
K_T \left.\frac{dT}{dr}\right|_{r=R_{cem}} = \frac{R}{R_{cem}}\alpha\left(T_I - T_b\right). \qquad \text{(B.16)}
$$

This is the fourth boundary condition of the reservoir solution (Eq. 3.35). For the open hole case, $R_{cem} = R$.

APPENDIX C: FINITE-DIFFERENCE FORMULATION OF MASS BALANCE

For three-dimension flow in a Cartesian coordinate system, the mass balance over a box-shaped control volume ($\Delta x \Delta y \Delta z$) can be written as below.

$$
\begin{aligned}
&-\frac{\Delta y \Delta z}{\rho_o}\Delta_x\left(\rho_o u_o\right)-\frac{\Delta x \Delta z}{\rho_o}\Delta_y\left(\rho_o u_o\right)-\frac{\Delta x \Delta y}{\rho_o}\Delta_z\left(\rho_o u_o\right)\\
&-\frac{\Delta y \Delta z}{\rho_w}\Delta_x\left(\rho_w u_w\right)-\frac{\Delta x \Delta z}{\rho_w}\Delta_y\left(\rho_w u_w\right)-\frac{\Delta x \Delta y}{\rho_w}\Delta_z\left(\rho_w u_w\right). \\
&=\phi S_o c_o\left(\frac{\Delta x \Delta y \Delta z}{\Delta t}\right)\Delta_t p_o+\phi S_w c_w\left(\frac{\Delta x \Delta y \Delta z}{\Delta t}\right)\Delta_t p_w
\end{aligned}
\qquad (8.9)
$$

An example shows how the finite differences were done. Here we show the finite difference of the third term on the left side.

$$
-\frac{\Delta y \Delta z}{\rho_o}\Delta_x\left(\rho_o u_o\right)=-\frac{\Delta y \Delta z}{\rho_o}\left[\left(\rho_o u_o\right)_{k+1/2}-\left(\rho_o u_o\right)_{k-1/2}\right]. \qquad (C.1)
$$

Substituting Darcy velocity gives

$$
\begin{aligned}
-\frac{\Delta x \Delta y}{\rho_o}\Delta_z\left(\rho_o u_o\right)=-\frac{\Delta x \Delta y}{\rho_o}\Bigg[&\left(-\rho_o\frac{kk_{ro}}{\mu_o}\left\langle\frac{\Delta p_o}{\Delta z}-\rho_o g\frac{\Delta D}{\Delta z}\right\rangle\right)_{k+1/2}\\
&-\left(-\rho_o\frac{kk_{ro}}{\mu_o}\left\langle\frac{\Delta p_o}{\Delta z}-\rho_o g\frac{\Delta D}{\Delta z}\right\rangle\right)_{k-1/2}\Bigg].
\end{aligned}
\qquad (C.2)
$$

Note that if the spatial indicators (i , j , k) are left out, the defaults are either i , j , or k .

Now, expanding Darcy velocity, we have

$$
\begin{aligned}
-\frac{\Delta x \Delta y}{\rho_o}\Delta_z\left(\rho_o u_o\right)=-\left(\frac{\Delta x \Delta y}{\rho_o}\right)_k\Bigg[&\left(-\rho_o\frac{kk_{ro}}{\mu_o}\right)_{k+1/2}\left(\frac{p_{o,k+1}^{n+1}-p_{o,k}^{n+1}}{\Delta z}-\rho_o g\frac{D_{k+1}-D_k}{\Delta z}\right)\\
&-\left(-\rho_o\frac{kk_{ro}}{\mu_o}\right)_{k-1/2}\left(\frac{p_{o,k}^{n+1}-p_{o,k-1}^{n+1}}{\Delta z}-\rho_o g\frac{D_{k+1}-D_k}{\Delta z}\right)\Bigg].
\end{aligned}
\qquad (C.3)
$$

Applying upstream weighting and rearranging the terms yield

$$\begin{aligned}
-\frac{\Delta x\Delta y}{\rho_o}\Delta_z\left(\rho_o u_o\right) = {} & p_{o,k+1}^{n+1}\left(\frac{\Delta x\Delta y}{\rho_o\Delta z}\right)_k\left(\frac{\rho_o kk_{ro}}{\mu_o}\right)_k + p_{o,k-1}^{n+1}\left(\frac{\Delta x\Delta y}{\rho_o\Delta z}\right)_k\left(\frac{\rho_o kk_{ro}}{\mu_o}\right)_{k-1} \\
& + p_{o,k}^{n+1}\left\langle -\left(\frac{\Delta x\Delta y}{\rho_o\Delta z}\right)_k\left(\frac{\rho_o kk_{ro}}{\mu_o}\right)_k - \left(\frac{\Delta x\Delta y}{\rho_o\Delta z}\right)_k\left(\frac{\rho_o kk_{ro}}{\mu_o}\right)_{k-1}\right\rangle \\
& -\left(\rho_o g\right)_k\left(D_{k+1}-D_k\right)\left(\frac{\Delta x\Delta y}{\rho_o\Delta z}\right)_k\left(\frac{\rho_o kk_{ro}}{\mu_o}\right)_k \\
& +\left(\rho_o g\right)_{k-1}\left(D_k-D_{k-1}\right)\left(\frac{\Delta x\Delta y}{\rho_o\Delta z}\right)_k\left(\frac{\rho_o kk_{ro}}{\mu_o}\right)_{k-1}
\end{aligned} \quad . \qquad \text{(C.4)}$$

Therefore, the coefficients in Eq. 8.10 are

$$A_{ijk} = \left(\frac{\Delta y\Delta z}{\rho_w\Delta x}\right)_i\left(\frac{\rho_w kk_{rw}}{\mu_w}\right)_i + \left(\frac{\Delta y\Delta z}{\rho_o\Delta x}\right)_i\left(\frac{\rho_o kk_{ro}}{\mu_o}\right)_i , \qquad \text{(C.5)}$$

$$B_{ijk} = \left(\frac{\Delta y\Delta z}{\rho_w\Delta x}\right)_i\left(\frac{\rho_w kk_{rw}}{\mu_w}\right)_{i-1} + \left(\frac{\Delta y\Delta z}{\rho_o\Delta x}\right)_i\left(\frac{\rho_o kk_{ro}}{\mu_o}\right)_{i-1} , \qquad \text{(C.6)}$$

$$C_{ijk} = \left(\frac{\Delta x\Delta z}{\rho_w\Delta y}\right)_j\left(\frac{\rho_w kk_{rw}}{\mu_w}\right)_j + \left(\frac{\Delta x\Delta z}{\rho_o\Delta y}\right)_j\left(\frac{\rho_o kk_{ro}}{\mu_o}\right)_j , \qquad \text{(C.7)}$$

$$D_{ijk} = \left(\frac{\Delta x\Delta z}{\rho_w\Delta y}\right)_j\left(\frac{\rho_w kk_{rw}}{\mu_w}\right)_{j-1} + \left(\frac{\Delta x\Delta z}{\rho_o\Delta y}\right)_j\left(\frac{\rho_o kk_{ro}}{\mu_o}\right)_{j-1} , \qquad \text{(C.8)}$$

$$E_{ijk} = \left(\frac{\Delta x\Delta y}{\rho_w\Delta z}\right)_k\left(\frac{\rho_w kk_{rw}}{\mu_w}\right)_k + \left(\frac{\Delta x\Delta z}{\rho_o\Delta y}\right)_k\left(\frac{\rho_o kk_{ro}}{\mu_o}\right)_k , \qquad \text{(C.9)}$$

$$F_{ijk} = \left(\frac{\Delta x\Delta y}{\rho_w\Delta z}\right)_k\left(\frac{\rho_w kk_{rw}}{\mu_w}\right)_{k-1} + \left(\frac{\Delta x\Delta z}{\rho_o\Delta y}\right)_k\left(\frac{\rho_o kk_{ro}}{\mu_o}\right)_{k-1} , \qquad \text{(C.10)}$$

$$\begin{aligned}
G_{ijk} = {} & -A_{ijk} - B_{ijk} - C_{ijk} - D_{ijk} - E_{ijk} - F_{ijk} \\
& -\left(\frac{\phi S_w c_w \Delta x\Delta y\Delta z}{\Delta t}\right)_{ijk}^n - \left(\frac{\phi\left(1-S_w\right)c_o \Delta x\Delta y\Delta z}{\Delta t}\right)_{ijk}^n ,
\end{aligned} \qquad \text{(C.11)}$$

$$
\begin{aligned}
RHS_{ijk} = & -p_{wijk}^{n}\left(\frac{\phi S_{w}c_{w}\Delta x\Delta y\Delta z}{\Delta t}\right)_{ijk}^{n} - p_{wijk}^{n}\left(\frac{\phi\left(1-S_{w}\right)c_{o}\Delta x\Delta y\Delta z}{\Delta t}\right)_{ijk}^{n} \\
& +\left(\rho_{w}g\right)_{k}\left(D_{k+1}-D_{k}\right)E_{ijk}^{w}-\left(\rho_{w}g\right)_{k-1}\left(D_{k}-D_{k-1}\right)F_{ijk}^{w} \\
& +\left(\rho_{o}g\right)_{k}\left(D_{k+1}-D_{k}\right)E_{ijk}^{o}-\left(\rho_{o}g\right)_{k-1}\left(D_{k}-D_{k-1}\right)F_{ijk}^{o} \\
& -p_{c,i+1}\left(\frac{\Delta y\Delta z}{\rho_{o}\Delta x}\right)_{i}\left(\frac{\rho_{o}kk_{ro}}{\mu_{o}}\right)_{i}-p_{c,i-1}\left(\frac{\Delta y\Delta z}{\rho_{o}\Delta x}\right)_{i}\left(\frac{\rho_{o}kk_{ro}}{\mu_{o}}\right)_{i-1} \\
& -p_{c,i}\left[-\left(\frac{\Delta y\Delta z}{\rho_{o}\Delta x}\right)_{i}\left(\frac{\rho_{o}kk_{ro}}{\mu_{o}}\right)_{i}-\left(\frac{\Delta y\Delta z}{\rho_{o}\Delta x}\right)_{i}\left(\frac{\rho_{o}kk_{ro}}{\mu_{o}}\right)_{i-1}\right] \\
& -p_{c,j+1}\left(\frac{\Delta x\Delta z}{\rho_{o}\Delta y}\right)_{j}\left(\frac{\rho_{o}kk_{ro}}{\mu_{o}}\right)_{j}-p_{c,j-1}\left(\frac{\Delta x\Delta z}{\rho_{o}\Delta y}\right)_{j}\left(\frac{\rho_{o}kk_{ro}}{\mu_{o}}\right)_{j-1} \\
& -p_{c,j}\left[-\left(\frac{\Delta x\Delta z}{\rho_{o}\Delta y}\right)_{j}\left(\frac{\rho_{o}kk_{ro}}{\mu_{o}}\right)_{j}-\left(\frac{\Delta x\Delta z}{\rho_{o}\Delta y}\right)_{j}\left(\frac{\rho_{o}kk_{ro}}{\mu_{o}}\right)_{j-1}\right] \\
& -p_{c,k+1}\left(\frac{\Delta x\Delta y}{\rho_{o}\Delta z}\right)_{k}\left(\frac{\rho_{o}kk_{ro}}{\mu_{o}}\right)_{k}-p_{c,k-1}\left(\frac{\Delta x\Delta y}{\rho_{o}\Delta z}\right)_{k}\left(\frac{\rho_{o}kk_{ro}}{\mu_{o}}\right)_{k-1}. \qquad \text{(C.12)} \\
& -p_{c,k}\left[-\left(\frac{\Delta x\Delta y}{\rho_{o}\Delta z}\right)_{k}\left(\frac{\rho_{o}kk_{ro}}{\mu_{o}}\right)_{k}-\left(\frac{\Delta x\Delta y}{\rho_{o}\Delta z}\right)_{k}\left(\frac{\rho_{o}kk_{ro}}{\mu_{o}}\right)_{k-1}\right]
\end{aligned}
$$

APPENDIX D: FINITE-DIFFERENCE FORMULATION OF ENERGY BALANCE

The energy balance from Eq. 8.24 is

$$\left(\rho_o \mathbf{u}_o C_{po} + \rho_w \mathbf{u}_w C_{pw}\right)\cdot \nabla T - \left(\beta_o \mathbf{u}_o \cdot \nabla p_o + \beta_w \mathbf{u}_w \cdot \nabla p_w\right) T + \mathbf{u}_o \cdot \nabla p_o + \mathbf{u}_w \cdot \nabla p_w$$
$$- \nabla \cdot \left(K_{Tt} \nabla T\right) + \nabla \cdot \left(\rho_o \mathbf{u}_o gD + \rho_w \mathbf{u}_w gD\right) = -\left[(1-\phi)\rho_s C_{ps} + \phi\left(S_o \rho_o C_{po} + S_w \rho_w C_{pw}\right)\right]\frac{\partial T}{\partial t}$$
$$+ T\left(S_o \beta_o \phi \frac{\partial p_o}{\partial t} + S_w \beta_w \phi \frac{\partial p_w}{\partial t}\right) - \frac{\partial}{\partial t}\left(S_o \rho_o gD + S_w \rho_w gD\right)$$

(8.24)

An example shows how the finite differences were done over a box-shaped control volume ($\Delta x \Delta y \Delta z$). Here we show the finite difference of the first term on the left side. Note that if the spatial indicators (i , j , k) are left out, the defaults are either i , j ,or k .

$$\left(\Delta x \Delta y \Delta z\right)\left(\rho_o \mathbf{u}_o C_{po} + \rho_w \mathbf{u}_w C_{pw}\right)\cdot \nabla T \approx \left(\Delta y \Delta z\right)\left(\rho_o \mathbf{u}_o C_{po} + \rho_w \mathbf{u}_w C_{pw}\right)_i \left(T_{i+1}^{n+1} - T_i^{n+1}\right)$$
$$+ \left(\Delta x \Delta z\right)\left(\rho_o \mathbf{u}_o C_{po} + \rho_w \mathbf{u}_w C_{pw}\right)_j \left(T_{j+1}^{n+1} - T_j^{n+1}\right)$$
$$+ \left(\Delta x \Delta y\right)\left(\rho_o \mathbf{u}_o C_{po} + \rho_w \mathbf{u}_w C_{pw}\right)_k \left(T_{k+1}^{n+1} - T_k^{n+1}\right)$$

(D.1)

Therefore, the coefficients used in Eq. 8.25 are

$$A_{ijk} = -\Delta y \Delta z P1_{ijk} + \left(\frac{\Delta y \Delta z}{\Delta x}\right) K_{T,x}\,, \qquad \text{(D.2)}$$

$$B_{ijk} = \left(\frac{\Delta y \Delta z}{\Delta x}\right) K_{T,x}\,, \qquad \text{(D.3)}$$

$$C_{ijk} = -\Delta x \Delta z P2_{ijk} + \left(\frac{\Delta x \Delta z}{\Delta y}\right) K_{T,y}\,, \qquad \text{(D.4)}$$

$$D_{ijk} = \left(\frac{\Delta x \Delta z}{\Delta y}\right) K_{T,y}\,, \qquad \text{(D.5)}$$

$$E_{ijk} = -\Delta x \Delta y P3_{ijk} + \left(\frac{\Delta x \Delta y}{\Delta z}\right) K_{T,z}\,, \qquad \text{(D.6)}$$

$$F_{ijk} = \left(\frac{\Delta x \Delta y}{\Delta z}\right) K_{T,z}\,, \qquad \text{(D.7)}$$

$$\begin{aligned} G_{ijk} &= \Delta y \Delta z P1_{ijk} + \Delta x \Delta z P2_{ijk} + \Delta x \Delta y P3_{ijk} \\ &\quad - 2\left(\frac{\Delta y \Delta z}{\Delta x}\right) K_{T,x} - 2\left(\frac{\Delta x \Delta z}{\Delta y}\right) K_{T,y} - 2\left(\frac{\Delta x \Delta y}{\Delta z}\right) K_{T,z} + P7_{ijk} + P8_{ijk} \end{aligned} , \qquad \text{(D.8)}$$

$$RHS_{ijk} = \Delta x \Delta y \Delta z P5_{ijk} + \Delta x \Delta y \Delta z P6_{ijk} + P7_{ijk} T_{ijk}^{n} + P9_{ijk} , \qquad \text{(D.9)}$$

where

$$P1_{ijk} = \left(-\rho_o \frac{kk_{ro}}{\mu_o}\right)_i \left(\frac{p_{o,i+1}^{n+1} - p_{o,i}^{n+1}}{\Delta z}\right) C_{p\,o,i} + \left(-\rho_w \frac{kk_{rw}}{\mu_o}\right)_i \left(\frac{p_{w,i+1}^{n+1} - p_{w,i}^{n+1}}{\Delta z}\right) C_{p\,w,i} , \qquad \text{(D.10)}$$

$$P2_{ijk} = \left(-\rho_o \frac{kk_{ro}}{\mu_o}\right)_j \left(\frac{p_{o,j+1}^{n+1} - p_{o,j}^{n+1}}{\Delta z}\right) C_{p\,o,j} + \left(-\rho_w \frac{kk_{rw}}{\mu_o}\right)_j \left(\frac{p_{w,j+1}^{n+1} - p_{w,j}^{n+1}}{\Delta z}\right) C_{p\,w,j} , \qquad \text{(D.11)}$$

$$\begin{aligned} P3_{ijk} &= \left(-\rho_o \frac{kk_{ro}}{\mu_o}\right)_k \left(\frac{p_{o,k+1}^{n+1} - p_{o,k}^{n+1}}{\Delta z} - \rho_{o,k}\, g \frac{D_{k+1} - D_k}{\Delta z}\right) C_{p\,o,k} \\ &\quad + \left(-\rho_w \frac{kk_{rw}}{\mu_o}\right)_k \left(\frac{p_{w,k+1}^{n+1} - p_{w,k}^{n+1}}{\Delta z} - \rho_{w,k}\, g \frac{D_{k+1} - D_k}{\Delta z}\right) C_{p\,w,k} \end{aligned} , \qquad \text{(D.12)}$$

$$\begin{aligned} P4_{ijk} &= \beta_{o,i} \left(-\frac{kk_{ro}}{\mu_o}\right)_i \left(\frac{p_{o,i+1}^{n+1} - p_{o,i}^{n+1}}{\Delta x}\right)^2 + \beta_{o,j} \left(-\frac{kk_{ro}}{\mu_o}\right)_j \left(\frac{p_{o,j+1}^{n+1} - p_{o,j}^{n+1}}{\Delta y}\right)^2 \\ &\quad + \beta_{o,k} \left(-\frac{kk_{ro}}{\mu_o}\right)_k \left(\frac{p_{o,k+1}^{n+1} - p_{o,k}^{n+1}}{\Delta z}\right) \left(\frac{p_{o,k+1}^{n+1} - p_{o,k}^{n+1}}{\Delta z} - \rho_{o,k}\, g \frac{D_{k+1} - D_k}{\Delta z}\right) \\ &\quad \beta_{w,i} \left(-\frac{kk_{rw}}{\mu_w}\right)_i \left(\frac{p_{w,i+1}^{n+1} - p_{w,i}^{n+1}}{\Delta x}\right)^2 + \beta_{w,j} \left(-\frac{kk_{rw}}{\mu_w}\right)_j \left(\frac{p_{w,j+1}^{n+1} - p_{w,j}^{n+1}}{\Delta y}\right)^2 \\ &\quad + \beta_{w,k} \left(-\frac{kk_{rw}}{\mu_w}\right)_k \left(\frac{p_{w,k+1}^{n+1} - p_{w,k}^{n+1}}{\Delta z}\right) \left(\frac{p_{w,k+1}^{n+1} - p_{w,k}^{n+1}}{\Delta z} - \rho_{w,k}\, g \frac{D_{k+1} - D_k}{\Delta z}\right) \end{aligned} , \qquad \text{(D.13)}$$

$$\begin{aligned} P5_{ijk} = & \left(-\frac{kk_{ro}}{\mu_o}\right)_i \left(\frac{p^{n+1}_{o,i+1}-p^{n+1}_{o,i}}{\Delta x}\right)^2 + \left(-\frac{kk_{ro}}{\mu_o}\right)_j \left(\frac{p^{n+1}_{o,j+1}-p^{n+1}_{o,j}}{\Delta y}\right)^2 \\ & + \left(-\frac{kk_{ro}}{\mu_o}\right)_k \left(\frac{p^{n+1}_{o,k+1}-p^{n+1}_{o,k}}{\Delta z} - \rho_{o,k}\, g\, \frac{D_{k+1}-D_k}{\Delta z}\right)^2 \\ & \left(-\frac{kk_{rw}}{\mu_w}\right)_i \left(\frac{p^{n+1}_{w,i+1}-p^{n+1}_{w,i}}{\Delta x}\right)^2 + \left(-\frac{kk_{rw}}{\mu_w}\right)_j \left(\frac{p^{n+1}_{w,j+1}-p^{n+1}_{w,j}}{\Delta y}\right)^2 , \\ & + \beta_{w,k} \left(-\frac{kk_{rw}}{\mu_w}\right)_k \left(\frac{p^{n+1}_{w,k+1}-p^{n+1}_{w,k}}{\Delta z} - \rho_{w,k}\, g\, \frac{D_{k+1}-D_k}{\Delta z}\right)^2 \end{aligned} \tag{D.14}$$

$$\begin{aligned} P6_{ijk} = & \left(-\rho_o \frac{kk_{ro}}{\mu_o}\right)_k \left(\frac{p^{n+1}_{o,k+1}-p^{n+1}_{o,k}}{\Delta z} - \rho_{o,k}\, g\, \frac{D_{k+1}-D_k}{\Delta z}\right) \frac{gD_k}{\Delta z} \\ & + \left(-\rho_o \frac{kk_{ro}}{\mu_o}\right)_{k-1} \left(\frac{p^{n+1}_{o,k}-p^{n+1}_{o,k-1}}{\Delta z} - \rho_{o,k-1}\, g\, \frac{D_k-D_{k-1}}{\Delta z}\right) \frac{gD_{k-1}}{\Delta z} \\ & \left(-\rho_w \frac{kk_{rw}}{\mu_w}\right)_k \left(\frac{p^{n+1}_{w,k+1}-p^{n+1}_{w,k}}{\Delta z} - \rho_{w,k}\, g\, \frac{D_{k+1}-D_k}{\Delta z}\right) \frac{gD_k}{\Delta z} \\ & + \left(-\rho_w \frac{kk_{rw}}{\mu_w}\right)_{k-1} \left(\frac{p^{n+1}_{w,k}-p^{n+1}_{w,k-1}}{\Delta z} - \rho_{w,k-1}\, g\, \frac{D_k-D_{k-1}}{\Delta z}\right) \frac{gD_{k-1}}{\Delta z} \end{aligned} , \tag{D.15}$$

$$P7_{ijk} = -\Delta x \Delta y \left[(1-\phi)\rho_s C_{p,s} + S_o \rho_o C_{p,o} + S_w \rho_w C_{p,w}\right]^n_{ijk} , \tag{D.16}$$

$$\begin{aligned} P8_{ijk} = -\Delta x \Delta y \Delta z \Bigg[& \left(\frac{S_o \beta_o \phi}{\Delta t}\right)^n_{ijk} \left(p^{n+1}_{w,ijk} + p^{n+1}_{c,ijk} - p^n_{w,ijk} - p^n_{c,ijk}\right) \\ & + \left(\frac{S_w \beta_w \phi}{\Delta t}\right)^n_{ijk} \left(p^{n+1}_{w,ijk} - p^n_{w,ijk}\right) \Bigg] , \end{aligned} \tag{D.17}$$

$$P9_{ijk} = -\frac{\Delta x \Delta y \Delta z}{\Delta t}\left[\left(S_o \rho_o gD + S_w \rho_w gD\right)^{n+1}_{ijk} - \left(S_o \rho_o gD + S_w \rho_w gD\right)^n_{ijk}\right], \tag{D.18}$$

NOMENCLATURE

Symbol	Description
c	compressibility of fluid
C_h	heat transfer coefficient
C_p	heat capacity
$\mathbf{D}$	weight matrix for observations
D	wellbore diameter
$\mathbf{d}$	derivative vector
$\mathbf{e}$	total energy flux
e	total energy
f_o	friction factor
f	friction factor with wall flux
$\mathbf{g}$	gravity acceleration vector
$\mathbf{g}$	gradient vector (Ch. 5)
g	gravity acceleration
$\mathbf{H}$	Hessian matrix
H	enthalpy
h	reservoir thickness
$\mathbf{I}$	identity matrix
$\mathbf{J}$	Jacobian matrix
J	productivity index
$\mathbf{k}$	permeability tensor
K	thermal conductivity
K_{JT}	Joule-Thomson coefficient

K_u	Kutateladze number
k	permeability
k_d	damaged permeability
L	well length
M	mass
N_{Re}	Reynolds number
$N_{\mathrm{Re},w}$	wall Reynolds number
N_{Pr}	Prandtl number
p	pressure
p_e	pressure at external boundary of reservoir
p_R	reservoir pressure
Q	heat transfer rate
$\mathbf{q}$	conductive heat flux
q	conductive heat flux (Ch. 2)
q	flow rate
R	pipe inner diameter
r_w	wellbore radius
r_d	damaged radius
s	skin factor
T	temperature
T_b	bulk temperature
T_e	temperature at external boundary of reservoir
T_I	inflow temperature
t	time
U	internal energy

$\mathbf{u}$	Darcy velocity vector
u	Darcy velocity
u_o	drift flux
V	specific volume
$\mathbf{v}$	velocity vector
v	velocity
v_{sg}	superficial velocity of gas
v_{sl}	superficial velocity of liquid
v_{so}	superficial velocity of oil
v_{sw}	superficial velocity of water
W	reservoir width
$\mathbf{w}$	parameter vector
w	mass flux
$\mathbf{x}$	observation space
$\mathbf{y}$	observations
y	holdup

Greek

α	overall heat transfer coefficient
α_I	combined overall heat transfer coefficient
β	coefficient of isobaric thermal expansion
γ	pipe open ratio
$\boldsymbol{\delta}$	Kronecker delta
ε	relative pipe roughness
η	upgrading parameter

$\mathbf{\Phi}$	combined convective and molecular momentum tensor
Φ	combined convective and molecular momentum
Φ	flow potential (Ch. 4)
ϕ	porosity
λ	Marquardt parameter
θ	wellbore inclination
μ	viscosity
ρ	density
σ	surface tension
$\boldsymbol{\tau}$	shear stress tensor
τ	shear stress

Subscripts

c	calculated (Ch. 5)
c	casing (Appendix A)
cem	cement
fl	fluid
g	gas
I	inflow
i	phase index
j,k	position index
l	liquid
m	mixture
m	measured (Ch. 5)
o	oil

T	total
TP	two phase
w	water

REFERENCES

1. Al-Hadhrami, A.K., Elliott, L., and Ingham, D.B.: "A New Model for Viscous Dissipation in Porous Media Across a Range of Permeability Values," *Transport in Porous Media* (October 2003) 117.
2. Bird, R.B., Stewart, W.E., and Lightfoot, E.N.: *Transport Phenomena*, second edition, John Wiley and Sons, New York (2002).
3. Brown, G. *et al*.: "Monitoring Horizontal Producers and Injectors During Cleanup and Production Using Fiber-Optic-Distributed Temperature Measurements," report SPE 84379 presented at the 2003 SPE Annual Technical Conference and Exhibition, Denver, 5-8 October.
4. Butler, R.M.: *Horizontal Wells for the Recovery of Oil, Gas, and Bitumen*, The Petroleum Society of the Canadian Institute of Mining, Metallurgy and Petroleum, Calgary, Canada (1994).
5. Carslaw, H.S. and Jaeger, J.C.: Conduction of Heat in Solids, Oxford U. Press, Amen House, London (1950).
6. Chaperon, I. : "Theoretical Study of Coning Toward Horizontal and Vertical Wells in Anisotropic Formations: Subcritical and Critical Rates," report SPE 15377 presented at the 1986 SPE Annual Technical Conference, New Orleans, 5-8 October.
7. Chauvel, Y. L., and Oosthoek, P.: "Production Logging in Horizontal Wells: Applications and Experience to Date," report SPE 21094 presented at the 1990 SPE Latin American Petroleum Engineering Conference, Rio de Janeiro, Brazil, 14-19 October.
8. Corey, A. T.: *Mathematics of Immiscible Fluids in Porous Media*, Water Resources Publication, Littleton, CO (1986).
9. Dawkrajai, P.: "Temperature Prediction Model for a Producing Horizontal Well," PhD report, U. of Texas, Texas (2006).
10. Dawkrajai, P., Lake, L.W., Yoshioka, K., Zhu, and D., Hill, A.D: "Detection of Water or Gas Entries in Horizontal Wells from Temperature Profiles," report SPE 100050 presented at the 2006 SPE/DOE Symposium on Improved Oil Recovery, Tulsa, 22-26 April.
11. Dikken, B.J.: "Pressure Drop in Horizontal Wells and its Effect on Production Performance," *JPT* (November 1990) 1426.
12. Duijndam, A.J.W.: "Bayesian Estimation in Seismic Inversion. Part II: Uncertainty Analysis," *Geophysical Prospecting* (November 1988) 899.
13. Falcone, G., Hewitt, G.F., Alimonti, C., and Harrison, B.: "Multiphase Flow Metering : Current Trends and Future Developments," *JPT* (April 2002) 77.
14. Flores, J.G., Sarica, C., Chen, T.X., and Brill, J.P.: "Investigation of Holdup and Pressure Drop Behavior for Oil-Water Flow in Vertical and Deviated Wells," presented at the 1998 Annual Energy-Source Technology Conference and Exhibition, Houston, 2-6 February.
15. Foucault, H. *et al*.: "A Successful Experience for Fiber Optic and Water Shut Off on Horizontal Wells with Slotted Liner Completion in an Extra Heavy Oil Field,"

report SPE 89405 presented at the 2004 SPE/DOE Symposium on Improved Oil Recovery, Tulsa, 17-21 April.

16. Franca, F. and Lahey, R.T.: “The Use of Drift-Flux Techniques for The Analysis of Horizontal Two-Phase Flows,” *Int. J. Multiphase Flow* (November 1992) 787.
17. Furui, K., Zhu, D., and Hill, A.D.: “A Rigorous Formation Damage Skin Factor and Reservoir Inflow Model for a Horizontal Well,” *SPEPF* (August 2003) 151.
18. Giger, F.: “Analytic 2D Models of Water Cresting Before Breakthrough for Horizontal Wells,” report SPE 15378 presented at the 1986 SPE Annual Technical Conference, New Orleans, 5-8 October.
19. Govier, G.W. and Aziz, K.: *The Flow of Complex Mixtures in Pipes*, Van Nostrand Reinhold, New York, New York (1972).
20. Haddad, S., Proano, E., and Patel, Y.: “A Method to Diagnose Depletion, Skin, kh, and Drive Mechanism Effects Using Reservoir Monitoring Data,” report SPE 90032 presented at the 2004 SPE Annual Technical Conference and Exhibition, Houston, 26-29 September.
21. Hagoort, J.: “Ramey’s Wellbore Heat Transmission Revisited,” *SPEJ* (December 2004) 465.
22. Hasan, A.R. and Kabir, C.S., Wang, X.: “Wellbore Two-Phase Flow and Heat Transfer During Transient Testing,” *SPEJ* (1998) 174.
23. Hasan, A.R. and Kabir, C.S.: “A Simplified Model for Oil-Water Flow in Vertical and Deviated Wellbores,” report SPE 49163 presented at the 1998 SPE Annual Technical Conference and Exhibition, New Orleans, 27-30 September.
24. Hill, A.D.: *Production Logging – Theoretical and Interpretive Elements*, Monograph Series, SPE, Richardson, Texas (1990) 14.
25. Hill, A.D. and Zhu, D.: “The Relative Importance of Wellbore Pressure Drop and Formation Damage in Horizontal Wells,” report 100207 SPE presented at the 2006 SPE Europec/EAGE Annual Conference and Exhibition, Vienna, Austria, 12-15 June.
26. Ingham, D.B., Pop, I., and Cheng, P.: “Combined Free and Forced Convection in a Porous Medium between Two Vertical Walls with Viscous Dissipation,” *Transport in Porous Media*, (August 1990).
27. Jayawardena, S.S. *et al.*: “A New Model for Dispersed Multi-Layer Oil-Water Flow,” presented at the 2001 Proceedings of the Engineering Technology Conference on Energy, Houston, 5-7 February.
28. Kim, D. and Ghajar, A. J.: “Heat transfer measurements and correlations for air-water flow of different flow patterns in a horizontal pipe,” *Experimental Thermal and Fluid Science* (February 2002) 659.
29. Kragas, T. K., Williams, B. A., and Myers, G. A.: “The Optic Oil Field: Deployment and Application of Permanent In-Well Fiber Optic Sensing Systems for Production and Reservoir Monitoring,” report SPE 71529 presented at the 2001 SPE Annual Technical Conference and Exhibition, New Orleans, 30 September-3 October.
30. Lake, L. W.: *Enhanced Oil Recovery*, Prentice Hall, Saddle River, New Jersey (1989).

31. Lanier, G. H., Brown, G., and Adams, L.: "Brunei Field Trial of a Fibre Optic Distributed Temperature Sensor (DTS) System in a 1,000m Open Hole Horizontal Oil Producer," report SPE 84324 presented at the 2003 SPE Annual Technical Conference and Exhibition, Denver, 5-8 October.
32. Li, H., Zhu, D., Lake, L. W., and Hill, A. D.: "A New Method to Interpret Two-Phase Profiles from Temperature and Flowmeter Logs," report SPE 56793 presented at the 1999 SPE Annual Technical Conference and Exhibition, Houston, 3-6 October.
33. Marquardt, D.W.: "An Algorithm for Least-Squares Estimation of Nonlinear Parameters," *J. of the Society for Industrial and Applied Mathematics* (June 1963) 431.
34. Maubeuge, F., Didek, M., Beardsell, M. B., Arquis, E., Bertrand, O., and Caltagirone, J. P.: "MOTHER: A Model for Interpreting Thermometrics," report SPE 28588 presented at the 1994 SPE Annual Technical Conference and Exhibition, New Orleans, 25-28 September.
35. McCain, W. D., Jr.: *The Properties of Petroleum Fluids*, second edition, PennWell Publishing Company, Tulsa, (1990).
36. Mills, A. F.: *Heat Transfer*, second edition, Prentice Hall, Saddle River, New Jearsey (1999).
37. Ouyang, L.-B., Arbabi, S., and Aziz K.: "General Wellbore Flow Model for Horizontal, Vertical, and Slanted Well Completions," *SPEJ* (June 1998) 124.
38. Ouyang, L.-B. and Aziz, K.: "A Homogeneous Model for Gas-Liquid Flow in Horizontal Wells," *J. Pet. Sci. and Eng.* (September 2000) 119.
39. Ouyang, L.-B. and Belanger, D.: "Flow Profiling by Distributed Temperature Sensor (DTS) System – Expectation and Reality," *SPEPO* (May 2006) 269.
40. Owodunni, A., Travis, T., and Dunk, G.: "The Use of Multilateral Technology to Arrest Production Decline in a West-Texas Gas Field," report SPE 84029 presented at the 2003 SPE Annual Technical Conference and Exhibition, Denver 5-8 October.
41. Ozkan, E., and Raghavan, R.: "A Breakthrough Time Correlation for Coning Toward Horizontal Wells," report SPE 20964 presented at Europec Conference, The Hague, Netherlands, 22-24 October, 1990.
42. Peaceman, D. W.: "Interpretation of Well-Block Pressure in Numerical Reservoir Simulation," *SPEJ* (1978) 183.
43. Peaceman, D. W.: "Interpretation of Well-Block Pressure in Numerical Reservoir Simulation With Nonsquare Grid Blocks and Anisotropic Permeability," *SPEJ* (June 1983) 531.
44. Peaceman, D. W.: "Interpretation of Wellblock Pressures in Numerical Reservoir Simulation: Part 3- Off-Center and Multiple Wells Within a Wellblock," *SPERE* (May 1990) 227.
45. Ramakrishnan, T. S., and Raghuraman, B.: "A Method for Continuous Interpretation of Permanent Monitoring Pressure Data," report SPE 90910 presented at the 2004 SPE Annual Technical Conference and Exhibition, Houston, 26-29 September.

46. Ramirez, R., Fernandez, V., and Barrios J.: Multilateral Field Experience in Developing an Extra Heavy Crude-Oil Reservoir, report SPE 86947 presented at the 2004 SPE International Thermal Operations and Heavy Oil Symposium and Western Regional Meeting held in Bakersfield, CA, USA, 16-18 March.
47. Ramey, H.J. Jr.: "Wellbore Heat Transmission," *JPT* (April 1962) 427.
48. Robles, Jorge: "Application of Advanced Heavy-Oil-Production Technologies in the Orinoco Heavy-Oil-Belt, Venezuela," report SPE 69848 presented at the 2001 International Thermal Operations and Heavy Oil Symposium held in Margarita Island, Venezuela, 12-14 March.
49. Romero, A.: "Temperature Behavior in the Build Section of Multilateral Wells," MS Report, Texas A&M University, Texas (2005).
50. Romero-Juarez, A.: "A Note on the Theory of Temperature Logging," *SPEJ* (December 1969) 375.
51. Sagar, R.K., Dotty, D.R., and Schmidt, Z.: "Predicting Temperature Profiles in a Flowing Well," *SPEPE* (November 1991) 441.
52. Sandler, S. I.: Chemical and Engineering Thermodynamics, Third Edition, John Wiley and Sons, New York, (1999).
53. Sensornet Limited, "DTS Advantages and Technology," www.sensornet.co.uk, 2007.
54. Shi, H. *et al.*: "Drift-Flux Parameters for Three-Phase Steady-State Flow in Wellbores," *SPEJ* (June 2005) 130.
55. Shook, M., Li, D., and Lake, L. W.: "Predicting Temperature Profiles in a Flowing Well," *SPEPE* (November 1991) 441.
56. Silva, M. I. D. O., and Kato, T.: "Reservoir Management Optimization Using Permanent Downhole Gauge Data," report SPE 90973 presented at the 2004 SPE Annual Technical Conference and Exhibition, Houston, 26-29 September.
57. Steffensen, R. J., and Smith, R. C.: "The Importance of Joule-Thomson Heating (or Cooling) in Temperature Log Interpretation," report SPE 4636 presented at the 1973 Annual Fall Meeting of the Society of Petroleum Engineers of AIME, Las Vegas, NV, 30 September - 3 October.
58. Stone, T.W. *et al.*: "Thermal Simualtion with Multisegment Wells," *SPERE* (June 2002) 206.
59. Taitel, Y. and Dukler, A.E.: "A Model for Predicting Flow Regime Transitions in Horizontal and Near Horizontal Gas-Liquid Flow," *AIChEJ* (January 1976) 47.
60. Tolan, M., Boyle, M., and Williams, G. : "The Use of Fiber-Optic Distributed Temperature Sensing and Remote Hydraulically Operated Interval Control Valves for the Management of Water Production in the Douglas Field," report SPE 71676 presented at the 2001 SPE Annual Technical Conference and Exhibition, New Orleans, 30 September-3 October.
61. Yoshioka, K. *et al.*: "A Comprehensive Model of Temperature Behavior in a Horizontal Well," report SPE 95656 presented at the 2005 SPE Annual Technical Conference and Exhibition, Dallas, 9-12 October.
62. Yoshioka, K. *et al.*: "Detection of Water or Gas Entries in Horizontal Wells from Temperature Profiles," report SPE 100209 presented at the 2006 SPE Europec/EAGE Annual Conference and Exhibition, Vienna, Austria, 12-15 June.

63. Yoshioka, K.: “Detection of Water or Gas Entry into Horizontal wells by Using Permanent Monitoring System,” PhD report, Texas A&M University, Texas (2007).
64. Yuan, H., Sarica, C., and Brill, J.P.: “Effect of Completion Geometry and Phasing on Single-Phase Liquid Flow Behavior in Horizontal Wells,” report SPE 48937 presented at the 1998 SPE Annual Technical Conference and Exhibition, New Orleans, 27-30 September.